Ion conduction in solid-state electrolytes

Investigating the fundamental conduction mechanism in Na_3PnS_4 (Pn = P, As, Sb) through computation and experiment

Author:

Timothy Joe Alders

to obtain the degree of Master of Science

at the Delft University of Technology,

to be defended publicly on February 18th 2022, at 13:00.

Student number: 4373278

Thesis Committee: Prof. dr. ir. M. Wagemaker

Dr. A. L. Smith

Dr. P. Braga Groszewicz

Dr. T. Famprikis

Abstract

Recent studies on various solid-state electrolytes showed that while improvements to the ionic conductivity are progressing swiftly, the understanding of the fundamental conduction mechanism is still lagging behind. We attempt to improve this understanding by providing a more complete overview of how different static (structural) and dynamic (lattice-ion interaction) properties relate to the ion diffusion mechanism, by investigating the differences between the Na_3PnS_4 isostructural compounds (Pn = P, As, Sb). The static bottleneck descriptors previously used in literature, based on the S-atoms coordinating the ion migration pathway, are found to not predict the ionic conductivities accurately. On the dynamic influences, we find that based on the melting points, Born Effective Charges, vibrational frequencies and dissociation energies, it seems that of the Pn-S bonds the P-S bonds are significantly stiffer than the As-S and Sb-S bonds and that based on the differences in electronegativities, Bader Charges and Electron Localization Functions the bonds are least polar for As-S, followed by P-S and Sb-S. The changes in the bond polarity were found to correlate more closely with the observed differences in ionic conductivity than the bond stiffness, and closer inspection of the differences in the bond polarity suggest that the Pn substitution in the PnS_4 anions (following the order As → P → Sb) causes a decrease in the Na-S bonding strength through electron transfer from the Na-ions to the S-ions. We quantified the conduction process further by determining the activation barrier with the Nudged Elastic Band method, with which we find that both the ionic conductivities and thus polarity correlate well with the activation barriers. Finally, we find that while the statis bottleneck descriptors are not great predictors of the overall conductivity, they do correlate with the activation volume, indicating an important role for these structural descriptors in studying pressure effects on conductivity.

Table of Contents

1. Introduction

With the growing need for decarbonization, research on battery materials has become increasingly important to facilitate a smooth and fast energy transition. Battery technologies are essential for enabling the electrification of transport as well as for the storage of intermittently produced renewable energy, such as by wind or solar power, and the expected demand for Li-ion batteries increases drastically in the upcoming years (Figure 1.1). At the same time, lithium-ion technologies are being developed with ever increasing performance characteristics and energy densities for applications in portable electronics. As a result of these immense recent advances in battery performance, the current state of the art lithium-ion battery technologies are reaching the fundamental limits in energy density and performance set by its core components[1].

To improve the performance of batteries even more and allow for large scale applications in transport and renewable energy storage, recent research efforts have been focused in two general directions: 1) incremental optimization of already mature Li-ion technologies (advanced Li-ion) and 2) rigorous changes to the core battery components and design (post Li-ion)[1]. Important directions of work focused on these post Li-ion technologies include the use of different mobile cations (e.g. Na^+ or Mg^{2+}), replacing the liquid electrolyte with solid state electrolytes (SSE) and enabling the use of pure metallic anodes. These approaches can even be combined in the design of metal-anode solid-state batteries (SSB), which boast significant theoretical improvements in energy density, safety, lifetime and cost[2]. Solid-state batteries are expected to promote a significant increase in safety, as a result of the absence of the flammable liquid electrolytes typically present in Li-ion cells[1]. Furthermore, with the potentially higher percentage of active material the solid-state battery is expected to have an increased specific energy, the ability to be designed in several different geometries and stability in excess of 10000 cycles[3].

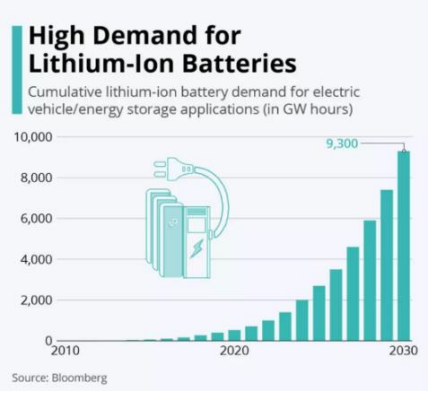

Figure 1.1. The demand for Li-ion batteries is growing increasingly fast, requiring significant improvements to current battery technologies. Adapted from [76].

Na- solid-state batteries (SSBs)

One potential design of a SSB utilizing a metal anode could make use of sodium metal as anode material. Because of the large sodium abundance in natural reserves, research efforts have been focused on Na-ion batteries for quite some time already[3]. Especially for static large-scale applications, such as the storage of renewable electricity, the lower costs of sodium could compensate the lower energy density of the Na-anode compared to the Li-anode[3]. The utilization of metal anodes in general is however very challenging as a result of so-called dendrite formation, where the inhomogeneous deposition of the metal leads to the growth of filament-like structures from the anode to the cathode. If such a dendrite were to cause a short-circuit between the cathode and anode, the results would be catastrophic for the battery. As such, in liquid-based cells it seems near to impossible to utilize solid-metal anodes. To allow for the use of metal anodes the combination with a solid-state electrolyte in a SSB could prove a viable solution.

To enable a good SSB design, the solid electrolyte requires a sufficiently high ionic conductivity. For crystalline structures, it has been noticed that body-centred cubic anionic frameworks are among the best ionic conductors (for example α-AgI)[4]. This is reasoned to be because this cubic framework allows for direct hops between adjacent sites, with a small associated activation energy, and a 3-dimensional conduction path[5].

Potential candidate electrolytes: the Na_3PnS_4-family

Over the past decade many different potential ionic conductors for both lithium and sodium have been discovered (Figure 1.2), with several indeed having a body-centred cubic anionic structure[1,6]. One class of very interesting Na-ion conductors is the sodium pnictogen-sulphides (Na_3PnS_4, Pn = P, As, Sb). The material Na_3PS_4 and its isostructural compounds (Na_3AsS_4 and Na_3SbS_4) have proven to be great candidates for solid electrolyte material, with Na_3PS_4 having a conductivity of $2 \cdot 10^{-4}$ S/cm (ref [7]) and Na_3SbS_4 a conductivity surpassing $1 \cdot 10^{-3}$ S/cm (ref [3]), comparable to the ionic conductivity of currently used liquid electrolytes.

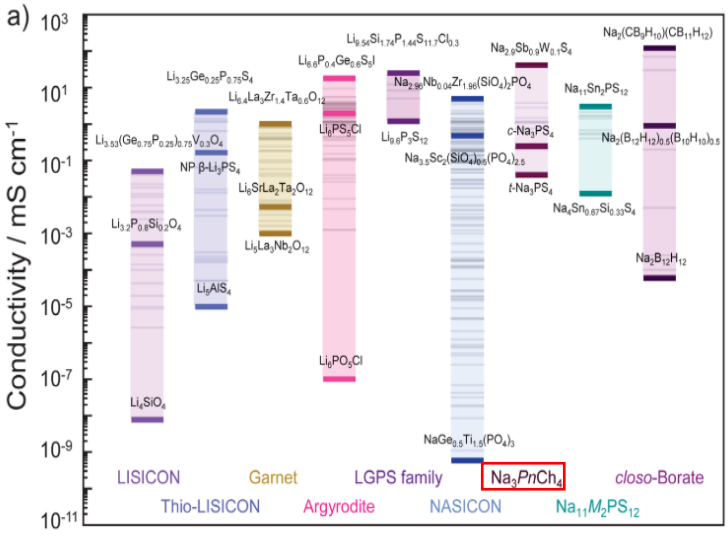

Figure 1.2. Reported conductivities for a variety of different solid-state electrolyte families. The Na_3PnS_4 family is a subfamily of the larger Na_3PnCh_4 class, highlighted in the figure. Adapted from [6].

Recent research efforts have identified various composite or doped structures of the Na_3PnS_4 family with even higher ionic conductivities[8,9], have found compounds with improved moisture stability[10] and have identified important aspects of the elastic and mechanical properties of the structures[11,12]. Especially the recently discovered Tungsten-doped thio-antimonate, $Na_{3-x}W_xSb_{1-x}S_4$, has received a lot of attention in recent studies: this compound has a reported ionic conductivity of up to ~$40 \cdot 10^{-3}$ S/cm (ref [3]), improved moisture and air stability and various different possible synthesis routes, opening up possibilities for economically feasible production methods[9,13,14,15]. However, despite the recent advances in the development of these solid-state electrolytes, a fundamental understanding of the ionic-conduction mechanism seems to be lacking. This poses a barrier for the further enhancement of these electrolytes, where it has already shown to be problematic when devising new doping strategies[16].

A lacking understanding of the fundamental conduction mechanism

Two recent studies illustrate the lack of understanding of the conduction mechanism in different members of the Na_3PnS_4 family. A study by Till et al (submitted)[17] on a 2-dimensional substitution series in $Na_3P_{1-x}Sb_xS_{4-y}Se_y$ (substituting P → Sb and S → Se) found that several of the commonly used descriptors of the conduction mechanisms (e.g. the structural bottleneck, see Figure 1.3) were insufficient to explain the found differences in ionic conductivity. In their experimental study they found that the static size of the conduction bottleneck, commonly used to predict ionic conductivity, was actually not a good predictor of the ionic conductivity of the $Na_3P_{1-x}Sb_xS_{4-y}Se_y$ structures. While the bottleneck size remained almost constant throughout the substitution of P → Sb, the activation energy decreased by a factor of almost 2.

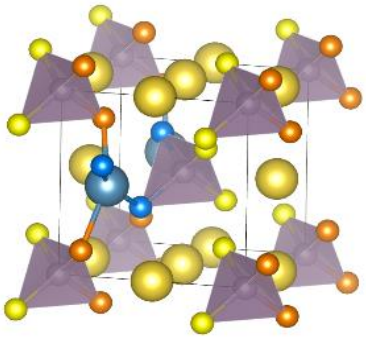

Figure 1.3. A schematic overview of the crystal structures of the Na_3PnS_4 structures during ion migration, with one Na-ion (blue) halfway along the conduction pathway. Ion migration occurs through Na-hopping between adjacent Na-sites; this conduction mechanism is often characterised by the size of the conduction bottleneck, the most narrow place the ion has to pass by.

Furthermore, while the static descriptors, such as cell volume, anion volume and bottleneck size where found to be inaccurate at predicting the activation energy, they also found that certain indicators of lattice rigidness (mainly the melting points and anharmonic bulk modulus) correlated much more strongly with the activation energy and ionic conductivity. This is one of several recent indications that the fundamental conduction mechanism cannot be explained purely through structural characteristics, but must be treated as a combination of static (bottleneck size) and dynamic (lattice rigidness / ion-phonon interactions) influences[18,19].

A recent study by Nishimura et al (pre-print)[20] also finds that the static bottleneck size is not an accurate predictor of ionic conductivity. In their study DFT calculations on the $Na_{3-x}W_xPn_{1-x}S_4$ (Pn = P, Sb) structure showed that the bottleneck size of Na_3PS_4 was actually larger than that of $Na_{3-x}W_xP_{1-x}S_4$, while the ionic conductivity of the latter was more than an order of magnitude higher. Contrary to their expectations they found that while the W-substitution does increase the anion-volume and cell-volume, the Na-S distance in the bottleneck (halfway between two adjacent Na-sites, Figure 1.3) actually became smaller. Like the 2-dimensional substitution series of Till et al, this points towards an insufficient structural definition of the bottleneck of diffusion for the Na_3PnS_4 (Pn = P, As, Sb) structures.

On top of that a study on a different solid-state electrolyte showed that the lack of understanding of the conduction mechanism can lead to ineffective doping strategies; in the Li-ion conductor $Li_{10}GeP_2S_{12}$ (LGPS) it was expected that the Sn doping at Ge sites would increase the cell volume and as such improve conductivity. Despite the increased cell volume however, Sn-doping was found to reduce the ionic conductivity of the electrolyte[18]. In a follow-up study, it was shown how the reduced ionic conductivity as the result of Sn-doping could be the result of two competing effects: an increased interatomic distance between the $Ge_xSn_{1-x}S_4$ anions and Li-ions, but also an increased attractive force between these groups as a result of a changed charge distribution[16] (visualised in Figure 1.4).

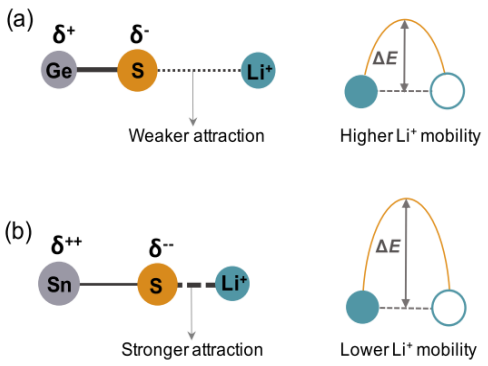

Figure 1.4. Schematic overview of the predicted difference in Li-S bonding in the Ge and Sn doped structures of LGPS, potentially explaining the difference in ionic conductivity. Adapted from [16].

These competing effects were further investigated in a study on the mechanochemical effects in LGPS (ref [21]), where the effects of pressure on the structure were used to show that the change in charge distribution and bond length between the anions and Li-ions affected the bond strength between the Li- and S-atoms of the anions. However, contrary to the mechanism as proposed in Figure 1.4, they found that the substitution of Ge by Sn caused an increased charge transfer from the $Ge_xSn_{1-x}S_4$ anions to the Li-ions during conduction, resulting in less negative S-charges, more covalent and stronger bonding between the anions and the migrating Li-ions in the Sn-doped structure and consequently more difficult conduction.

So, it seems that while improvements to the conductivity are progressing swiftly, the understanding of the fundamental conduction mechanism in solid-state electrolytes (among which the Na_3PnS_4 structures) is still lagging behind. We therefore require a more complete overview of how different structural and dynamical (lattice-ion interaction) properties relate to the ion diffusion mechanism and what descriptors are thus suitable to explain effects of isostructural changes or substitutions.

The aim of the project

In this study, we investigate three isostructural members of the Na_3PnS_4 family (namely Na_3PS_4, Na_3AsS_4 and Na_3SbS_4) in an attempt to better understand the fundamental Na-ion conduction mechanism in these structures. These structures are ideally suited for this endeavour, since they have very small structural difference and are chemically very comparable, yet have very different reported ionic conductivities (0.20 mS/cm for Na_3PS_4 (ref [8]), 0.027 mS/cm for Na_3AsS_4 (ref [8]) and 1.05 mS/cm for Na_3SbS_4 (ref [22])). On top of that, the crystal structures of the Na_3PnS_4 isostructural compounds are much less complicated than that of other solid electrolytes such as LGPS, making it easier to deconvolute different contributions to the conduction mechanism.

To investigate the fundamental ion-conduction mechanism in the Na_3PnS_4 isostructural compounds, we first investigate the structural parameters of the structures through density functional theory (DFT) and X-ray diffraction. We evaluate the interatomic distances, volumes of the PnS_4-anions and bottleneck size for all three isostructural compounds, to assess the effects of structural differences on the ionic conductivity. We go on to evaluate the bonding nature within the PnS_4-anions and between the Na- and S-atoms in the structures, to relate the bond strength to the energy barrier associated with ion migration. In order to do so, we determine the bulk moduli and melting points of the structures, both indicators of the lattice stiffness. Furthermore, we investigate the differences in the charge distribution in the three structures using three different metrics: the Bader charge, the Born Effective Charge and the Electron Localization Function. By combining the findings on the charge distributions with the known electronegativities of the atoms, we relate the differences in the charge distributions to different potential bonding interactions.

To relate the structural differences and differences in bond nature to the migration process, we determine the activation energy associated with the migration process. We perform Nudged Elastic Band (NEB) relaxations to calculate the energy landscape associated with the migration process. By further investigating the structural changes that occur in the structures as a result of ion migration using NEB, we get insight into how the small differences between the isostructural compounds relate to the differences in the activation barriers and the ionic conductivity. In order to get a more thorough understanding of these structural effects, we relate the structural changes as a result of pressure to changes in the energy barriers by performing NEB calculations under applied isostatic pressure.

Finally, in order to investigate the macroscopic conductivity, we perform electrochemical impedance spectroscopy (EIS) measurements to measure the ionic conductivity. By measuring the ionic conductivity at different temperatures and different pressures, we are able to determine the experimental activation energy and activation volume, to get insight into the additional factors that influence conductivity when thermal effects are present (non-0K).

The report is structured as follows. Chapter 2 describes the theoretical background of the Na_3PnS_4 structures and ion-conduction through solids. Chapter 3 covers the theory and methodology of the experimental work and chapter 4 focusses on the applied computational methods. Chapters 5 to 8 subsequently cover the main results of the study: chapter 5 covers the structural differences of the isostructural compounds, chapter 6 treats the bonding interactions, chapter 7 covers the activation barriers and chapter 8 covers the macroscopic conductivity. Finally, a general conclusion and future outlook is presented in chapter 9.

2. Background information on Na_3PnS_4 and ion-conduction

To follow the analyses and argumentation used to investigate the fundamentals of ion conduction, it is necessary to have a basic understanding of the various theoretical frameworks and experimental techniques applied in this work. For a fundamental understanding of how Na-ions move through the crystal structure, the first essential thing to know is what the crystallographic structure of the Na_3PnS_4 isostructural compounds is, combined with a basic understanding of several crystallographic elements. Then, a closer look at how ion-conduction through the crystalline structure works is required.

To relate differences between the Na_3PnS_4 structures to the process of conduction, there are many different descriptors that give indications on how well a structure conducts ions. In an attempt to find a more accurate description of the fundamental conduction mechanism in solid-state electrolytes, it is thus also necessary to get an overview of the most relevant of descriptors of the conduction process. How these descriptors can subsequently be quantified, will be covered in the next two chapters. The most important experimental techniques are outlined in chapter 3, whereas the required computational techniques are covered in chapter 4.

2.1 Elements of Crystallography

In crystallography, the structure of a material is generally described in terms of its unit cell: the smallest unit in which the unique crystal structure can be defined. For ionic compounds (such as the Na_3PnS_4 structures) this unit cell generally consist of a combination of positive ions (cations) and negative ions (anions). In the unit cell, a periodic lattice of ions at different locations is specified. A material as a whole can subsequently be described by copying the unit cell in all directions.

To illustrate this, we evaluate the simplest crystal structure: a simple cubic structure with atoms on the corners of the cube (Figure 2.1). The unit cell of this system can be described by a) looking at how long the sides of the cube are (the lattice parameter, in this case 'a') and b) which atoms are located at the corners. Based on this structure, it is easily imaginable how a crystal system could become more complicated by for example changing the length of one of the sides of the cube, the shape of the cell (by changing the angle between two of the sides), the coordinates inside the box at which the atoms are located, or which element the atoms are.

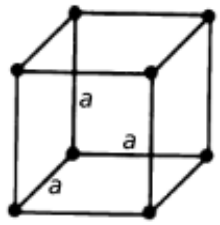

Figure 2.1. A simple cubic structure. Adapted from [23].

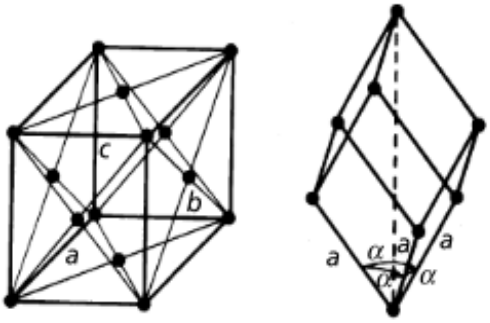

Figure 2.2. Face-centred ortho-rhombic (left) and rhombohedral (right) crystal structures. Adapted from [23].

Two of such variations are shown in Figure 2.2: a face-centred ortho-rhombic structure (with different lengths of the lattice parameters and atoms located in each face of the box) and a rhombohedral structure (where the angle between the sides of the box is no longer 90 °). The different combinations of lattice parameters and atom locations within the unit cell result in many different possible structures. Therefore, in order to describe the unit cell in a unique but straightforward way, different elements of symmetry are considered.

Examples of these symmetry elements are a mirror plane, where the atoms on opposing sides of the mirror plane are the same, or rotational symmetry, where the atoms in the lattice are the same when rotating about a specific axis by a certain angle (e.g. 90 ° or 120 °). Combining the different combinations of lattice parameters, atom locations and symmetry elements, a total of 230 unique three-dimensional ***space groups*** can be defined[23]. These space groups are one of the simplest 'complete' descriptors of a crystal structure; by identifying the space group of the material and indicating which type of atoms are located at which crystallographic location, the entire structure can be described. To analyse the structure of the Na_3PnS_4 solid-state electrolytes, it is thus necessary to know which space group described the structures and subsequently which atoms are located at the different sites.

A common method to describe which atoms are located where within a crystal structure is the ***Wyckoff notation***. The Wyckoff notation describes a position in the crystal lattice with a number and a letter, where the number shows the multiplicity of the site (how many times the site occurs in a single unit cell) and the letter is used to rank the sites from most symmetric to least symmetric. The Wyckoff notation is specific to a space group: Wyckoff positions for each space group are well documented and can for example be found on the Bilbao Crystallographic Server[24]. The Wyckoff notation of some space groups can be related to each other: in such a case the Wyckoff positions of high symmetry structures often split into unique positions for lower symmetry structures. This is relevant for the structures of Na_3PnS_4, since the materials have two distinct polymorphs (meaning it exists in two different crystal structures) which are closely related, as will be illustrated with an example in the next section.

By defining a space group and the Wyckoff positions, it is thus possible to accurately describe the crystal structure of an ionic compound such as the Na_3PnS_4 structures. Understanding the crystal structure of a material is essential for investigating the fundamentals of ion conduction, since the possible ion-conduction pathways and interatomic interactions determine the conductive properties of the material. To evaluate how this works in the isostructural compounds studied in this work, a closer look at the crystal structure of Na_3PnS_4 is needed.

2.2 The crystal structure of the Na_3PS_4

As Na_3PS_4 is a well-known material, the crystal structure is described in literature extensively and thus serves as a representative structure for the Na_3PnS_4 family. At room-temperature, two crystal phases are distinguished: a tetragonal phase (commonly referred to as "alpha") and a cubic phase (known as "beta")[3]. The difference between the two phases at room temperature is actually very small: the tetragonal phase crystallizes in space group $P\bar{4}2_1c$, with lattice parameters found in literature of a = b = 6.9520 Å and c = 7.0757 Å (ref [25]), while the cubic phase crystallizes in space group $I\bar{4}3m$, with a lattice parameter of 6.9965 Å (ref [26]). The largest difference between the lattice parameters is thus ~1.1%, and the difference in volume is only ~0.2%. The most significant difference between the two structures is the position of the Na-ions: the cubic Wyckoff site of 6b splits into two distinct sites for the tetragonal structure: 2b and 4d.

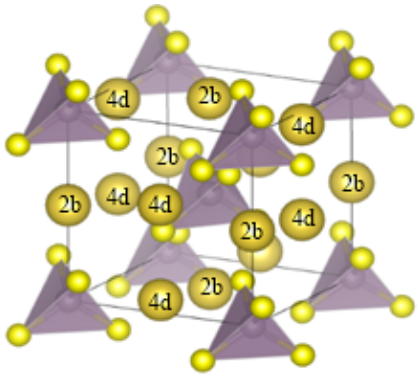

Figure 2.3. The tetragonal structure of Na_3PS_4 – space group $\mathbf{P\bar{4}2_1c}$. Na-atoms (gold) are in the 2b- and 4d-sites, the PS_4 anions (purple tetrahedra) with the P-atoms in the 2a-sites and S-atoms (yellow) in the 8e-sites. This tetragonal structure is only slightly distorted and comes very close to the cubic structure, where one cell parameter would be slightly shorter.

This site splitting can be seen in Figure 2.3, where the 2b and 4d sites are labelled. In the cubic structures, the 4d site is shifted about 0.5 Å, resulting in the 4d site ending up exactly on the sides of the unit cell.

The two crystal phases of Na_3PS_4 arise naturally at different temperatures: at room temperature the tetragonal phase is present, whereas the cubic phase arises when the material is heated to a temperature ~500 K (ref [27]). It is however possible to stabilize the cubic polymorph at room temperature, through means of mechanochemical synthesis (i.e. ball-milling)[7]. In the past, large differences in ionic conductivity between the cubic and tetragonal structure were reported, despite the small crystallographic differences[7]. However, recent studies showed that the differences in ionic conductivity between the cubic and tetragonal structures are more likely a result of synthesis method and treatment, rather than of the structural differences[3,11].

Recently, a third phase of Na_3PS_4 was found, referred to as the "gamma" phase[27]. This phase arises at a high temperature of ~775K and is indexed in space group Fddd. This phase exhibits plastic-crystal-like properties, where the Na-ions are very mobile within the anion-framework. With the high Na-ion mobility however, it becomes difficult to deconvolute the contributions of different structural aspects to the conductivity. Furthermore, given the high-temperature nature of the phase it is hard to access experimentally and it is to date unknown whether the other Na_3PnS_4 structures exhibits such a phase. Given these circumstances, it was decided not to investigate the gamma phase in this study.

2.2.1 The fundamental conduction pathway in Na_3PS_4

Ion conduction through crystal structures occurs by ions that move from a specific site to a neighbouring site in the structure. This process is commonly known as ***"hopping"***. Since a hop is associated with a displacement of charge (since the moving ion is charged), hopping is mechanism of conduction of charge. For conduction to occur in cubic Na_3PS_4 a Na-ion must hop from one 6b-site to a neighbouring 6b-site. For such a hop to happen, a vacancy (i.e. empty crystallographic site) for the Na-ion to move into must be present in the structure. This process of hopping in Na_3PS_4 is visualized in Figure 2.4 (made using VESTA[29]).

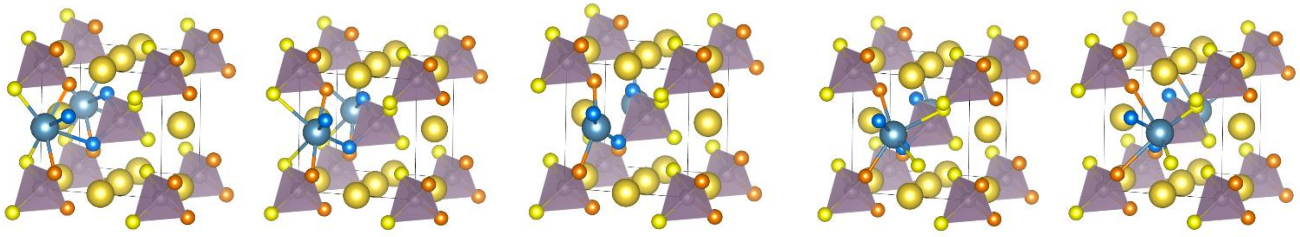

Figure 2.4. Visualisation of a Na-ion moving along the fundamental conduction pathway. The blue Na-ion moves from one 6b site (leftmost image) to another 6b site (rightmost image). Along the pathway, the Na-ion moves closely past 4 different S-atoms, commonly described as "the bottleneck" of diffusion. This bottleneck is here shown with the orange and blue S-atoms, to which the migrating Na-ion is bonded.

While in the tetragonal structure two different pathways can be distinguished (one along the a / b directions, one along the c direction), computational studies on the Na_3PnS_4 structures have shown that the difference in conductivity between these pathways is negligible[3,30]. For investigating the conduction mechanism through the structure, the most interesting characteristics are the interatomic distances between different atoms (notably the Na – S distances), the cell volume and the size of the PnS_4^{3-}-anions.

Ion conduction in Na_3PS_4 is often investigated by looking at the bottleneck of the conduction pathway: the place where it is most difficult for the migrating Na-ion to pass and the relative energy along the pathway reaches a maximum[30,31]. In literature, various descriptions of this bottleneck for Na_3PS_4 have been defined[17]. Two of these descriptors have so far seemed most accurate at predicting the conductive properties of Na_3PnCh_4 family (Pn = P, As, Sb; Ch = S, Se): the so-called Ch-Ch distance and the Ch_4-volume. The Ch-Ch distance refers to the distance between two S- or Se-atoms on opposing ends of the bottleneck (Figure 2.5, left, where the migrating Na-ion is placed in the bottleneck). The Ch_4-volume is defined as the volume of the distorted tetrahedron formed by the four S- or Se-atoms that coordinate the bottleneck (Figure 2.5, right). Since in the present study only the Na_3PnS_4 structures are considered, the Ch-Ch distance and Ch_4-volume always refer to S-atoms.

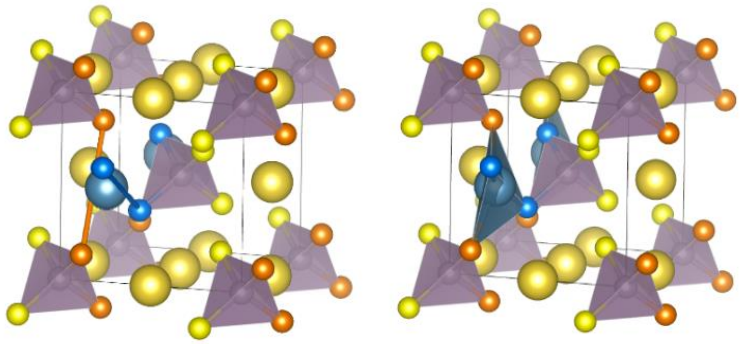

Figure 2.5. Visualisation of the Ch-Ch distance (left), between two opposing S-atoms coordinating the bottleneck and the Ch_4-volume (right), enclosed by the four S-atoms that coordinate the bottleneck, with the Na-ion in the middle of the conduction pathway (halfway between two 6b sites).

Both bottleneck descriptors have shown not to be perfect predictors of ionic conductivity[17,31]. Regardless, they can still provide valuable information about the conduction process: by investigating how the bottleneck changes when an ion moves through, we can get an indication of whether the energy required for migration is related to structural deformation. To illustrate: if the Ch-Ch distance needs to expand significantly to allow a Na-ion to pass through, this is likely associated with a higher energy of migration (thus a higher activation barrier). Especially when relating the changes in Ch-Ch distance to differences in the bonding interaction between Na and S during migration, the structural changes can be of great importance for understanding the conduction mechanism. It is important to note however such structural changes related to the migration of a single Na-ion are nearly inaccessible experimentally and that computational methods must be employed to investigate them.

2.3 Static and Dynamic influences on ion-conduction

To identify the different material properties that are related to the conduction process, it is of importance to take a closer look at how the hopping process works. For this, transition-state theory of ion conduction can provide an insight.

2.3.1 Transition state theory of ion-conduction

As seen when looking at the conduction pathway of Na_3PS_4, ion conduction through crystal structures occurs by ions that move between neighbouring sites. The Einstein-Smoluchowski equation[32] describes how ion-hopping can be used to calculate the diffusivity (D_J) of the ions through the structure:

$$\boldsymbol{D_J = \frac{\tau a^2}{2d}} \quad (1)$$

where τ is the ***mean hopping rate*** between sites, a is the ***distance between sites*** and d the number of diffusion dimensions. The effective diffusion of the ions is thus determined by how many hops occurs between different sites and how long these jumps are. From this diffusivity, the conductivity of the material can be determined through the Nernst-Einstein equation[32]:

$$\boldsymbol{\sigma = \frac{ne^2z^2D_J}{k_BT}} \quad (2)$$

with n the particle density, e the elementary charge, z the ionic charge, k_B Boltzmann's constant and T the temperature in Kelvin. From these equations we can deduce that the only two parameters that can potentially explain differences in the ionic conductivity between the Na_3PnS_4 structures are the interatomic distance and the mean hopping rate. The mean hopping rate however, is very dependent on the materials properties. The hopping rate is related to a different important quantity that is commonly used to qualify how difficult hopping between sites is: the activation energy E_a. We can relate the activation energy to the mean hopping rate (also referred to as the ***hopping frequency***) and ***attempt frequency*** (v_0) [32] by:

$$\boldsymbol{E_a = -k_BT \ln\left(\frac{\tau}{v_0}\right)} \quad (3)$$

From these equations it can be seen that all material properties that influence activation energy and the attempt frequency, impact the hopping frequency and therefore also impact conductivity. To study the fundamental conduction mechanism therefore becomes a question of studying the activation barrier and the attempt frequency.

Various rules for how the crystal structure impacts the activation energy and through it ionic transport have been derived in literature[33,34]. An important factor determining the energy barrier for the mobile ion is the coordination environment during migration. This coordination environment in the Na_3PnCh_4 family is reflected in for example the Ch-Ch distances and Ch_4 volumes as described in the previous section. Furthermore, the charge distribution around the ions in the structure can also affect the activation energy: as could be seen in Figure 1.4 for LGPS, differences in the charge on S-atoms can lead to a weaker or stronger bond with the mobile ion, thus resulting in easier or more difficult conduction. Since these effects of the coordination environment and static charge distribution on the activation energy can be derived from static evaluation of the structure, we summarize them under the term of static influences[17].

On the other hand, we see that the hopping frequency is directly impacted by the attempt frequency. This attempt frequency is generally interpreted as how often a mobile ion approaches the bottleneck, thus indicating "an attempt" at hopping. This attempt frequency is directly related to the vibrational modes of the migrating ion, showing that the phonon-lattice interactions are also related to the conduction process. Even more so, several studies have suggested that the lattice vibrations not only impact the attempt frequency, but also the height of the activation barrier[35–37]. Following the idea of "the softer the better", it is reasoned that by introducing ions with higher polarizability, the bonding interactions in the structure weaken. As a result, this would result in a flatter energy landscape, ultimately leading to a lower activation barrier[18,19]. This indicates that by evaluating the lattice softness we can get an indication of the phonons in the structure, which are directly related to the conduction mechanism.

Relating the lattice softness back to the attempt frequency, it can be reasoned that a soft lattice would allow for large lattice vibrations and low vibrational frequencies, which in turn could decrease the attempt frequency. All these effects of the lattice vibrations on the conduction mechanism we summarize under the term of dynamic influences[17].

It thus seems that the bonding interaction between the mobile ion and the framework is critical for explaining the conduction mechanism, both through the static influences (structural differences) and dynamic influences (lattice softness). The differences between the static and dynamic influences on conduction are visualised in Figure 2.6.

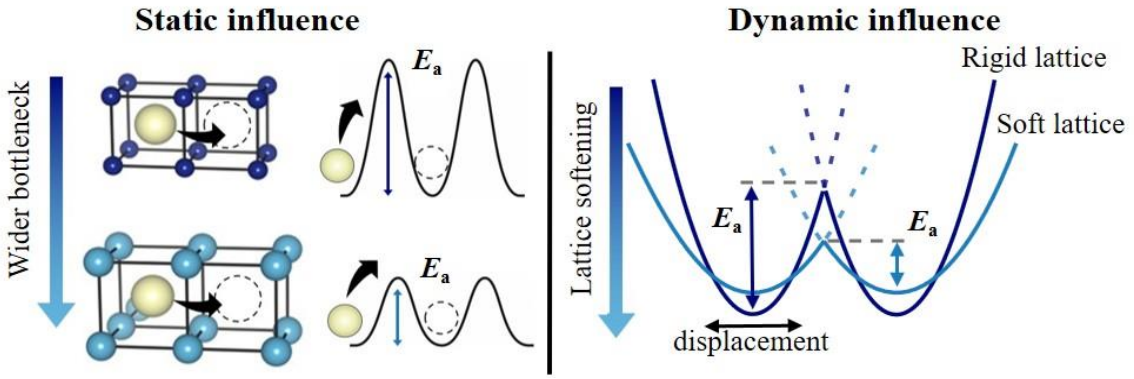

Figure 2.6. Visualisation of the static and dynamic influences on the activation energy. Static influences include the change in activation energy as a result of increasing bottleneck size or decrease electrostatic interaction with the host framework. Dynamic influences include the effects of lattice softness, where in a softer lattice the mobile ion has more freedom to move around its equilibrium position. Adapted from [17].

Distinguishing between these two different types of contributions to the conduction mechanism, the challenge now becomes how these influences can be deconvoluted and which metrics would be good at quantifying these descriptors.

2.3.2 The task at hand: comparing the Na_3PnS_4 isostructural compounds

To gain insight into how these static and dynamic properties influence the fundamental conduction mechanism, three Na_3PnS_4 structures are compared: Na_3PS_4, Na_3AsS_4 and Na_3SbS_4. These materials are excellently suited for this purpose because they are structurally very similar. The main difference between the structures, is the centre atom of the anion; for each of the structures, this is a different one of the pnictogens (P, As or Sb).

Separately, these different isostructural compounds have already been studied in literature (although Na_3AsS_4 not nearly as intensively as the other two). Because of the differences in approaches however (for example different synthesis methods[11,22], measurement conditions or computational tools[8]), the structural and dynamical data on the three structures are not directly comparable. One of the objectives of this work is therefore to provide accurate and comparable data on the structures of this family of materials. Since the ionic conductivities of the polymorphs are similar, both are suitable for studying the fundamental conduction mechanism. For symmetric simplicity, the cubic polymorph is used in the computational parts of this work. The tetragonal structure is studied in the experimental part because of the simpler synthesis recipe. An overview of several important properties of these materials from literature is provided in Table 2.1. From Table 2.1 it can be seen that there are several gaps in literature regarding the Na_3PnS_4 structures, such as incomplete knowledge on the bulk moduli and activation volumes. Furthermore, initial tests performed during this project have shown that the melting point of Na_3AsS_4 is likely above 600 °C, rather than the so-far reported 490 °C (ref [38]).

Table 2.1. Material properties of the isostructural compounds Na_3PS_4, Na_3AsS_4 and Na_3SbS_4, for both the cubic and tetragonal structures. Properties that have not been reported yet are denoted with x.

Isostructure	**Na_3PS_4**		**Na_3AsS_4**		**Na_3SbS_4**	
	Tetragonal	Cubic	Tetragonal	Cubic	Tetragonal	Cubic
Static descriptors:						
Space group	$P\bar{4}2_1c$	$I\bar{4}3m$	$P\bar{4}2_1c$	$I\bar{4}3m$	$P\bar{4}2_1c$	$I\bar{4}3m$
T_{XRD} / °C	25	25	25	300	25	250
a / Å	6.9520 [3]	6.9956 [3]	7.0389 [38]	7.1356 [38]	7.1676 [38]	7.2466 [38]
c / Å	7.0757 [3]	-	7.1385 [38]	-	7.2993 [38]	-
a / c ratio	1.018	-	1.014	-	1.018	-
Cell Volume / $Å^3$	341.971	342.354	353.685	363.321	374.998	380.542
ρ / $g \cdot cm^{-3}$	2.210 [38]	2.137 [38]	2.556 [38]	2.487 [38]	2.825 [38]	2.784 [38]
Activation Volume / $cm^3 \cdot mol^{-1}$	1.78 [11]	2.33 [11]	x	x	x	x
M / $g \cdot mol^{-1}$	228.2		272.1		319.0	
PnS_4^{3-}-anion Volume / $Å^3$	4.506 [38]		5.403 [38]		6.724 [38]	
Atomic Radius (Pn) / Å	0.52		0.6		0.76	
Ionic Radius (Pn) / Å	1.0		1.15		1.45	
Dynamic descriptors:						
σ_{RT} / $mS \cdot cm^{-1}$	0.2 – 0.46 [8]		0.027 [8]		1.05 [22]	
T_{phase} ($\alpha \rightarrow \beta$) / °C	227 [27]		200 [38]		227 [38]	
Melting Point / °C	765 [27]		490 [38]		621 [17]	
Bulk Modulus / GPa	25.3 [11] / 26.8 [12]	27.9 [11] / 21.5 [12]	x	x	46.0 [11]	x

To investigate the Na_3PnS_4 structures in detail and relate their characteristics to the conduction process, several static and dynamic descriptors are evaluated in this work. These descriptors are subsequently compared to different metrics that quantify the conduction process. More information on each descriptor can be found in the listed sections.

Static descriptors:

- Crystal structure (determined through X-Ray diffraction & DFT) - *(sections 3.2 & 4.1.2)*
- Bottleneck descriptors (Ch-Ch distance & Ch_4 volume (*section 2.2.1*))
- Charge distribution (quantified using Bader Charges & the Electron Localization Function) - *(section 4.2.3 & 4.2.4)*

Dynamic descriptors:

- Melting point - *(section 3.4)*
- Bulk modulus - *(section 4.1.2)*
- Born Effective Charges (as measure of polarizability) - (*section 4.2.2)*
- Electronegativity (Pauling & Allred-Rochow scale) - *(section 4.2.5)*

Quantifying the conduction process:

- Ionic conductivity (determined with impedance spectroscopy) - *(section 3.3)*
- Activation barrier (determined through the NEB method) - (*section 4.3)*

3. Theory and Methodology: experimental work

To understand how the various experimental techniques can help us to better understand the conduction mechanism, a basic understanding of each method is necessary. To this end, this chapter covers the basics of the synthesis method (solid-state synthesis) and material characterisation techniques (X-ray diffraction (XRD), electrochemical impedance spectroscopy (EIS) and differential scanning calorimetry (DSC)).

3.1 Solid-State Synthesis (*Sustainable Energy Technologies)*

Synthesis of the materials is a key element of every experimental study. Arguably the most straightforward method to synthesizing the Na_3PnS_4 solid electrolytes is by solid-state- / high-temperature synthesis[39]. Although for a while it was believed that mechanochemical synthesis (such as through ball-milling) of Na_3PnS_4 structures was preferential, a recent study by Famprikis et al showed that properly densifying the sample resulted in a similar conductivity for high-temperature and mechanochemical syntheses[11]. Furthermore, the synthesis of the W-doped $Na_{2.9}Sb_{0.9}W_{0.1}S_4$ with a record-high Na-conductivity of ~41 mS/cm was also achieved through solid-state synthesis[9], showing the potential of this synthesis route.

The first step in solid-state synthesis is ensuring stoichiometric mixing between the reagent powders, crucial due to the limited diffusivity of the atoms in solid state. Generally the processing of the reagents and resulting products is done in a protective atmosphere (glovebox filled with Argon), because of their sensitivity to air and moisture. By grinding the reagents, thus reducing particle size and creating physical contact between the reagent particles (by hand with a pestle and mortar or low speed ball-milling), the powders can be properly mixed. After grinding, the powder mixtures are typically pressed into pellets through mechanical pressing, to maximize physical contact between the particles. It is important not to use excessive pressure, since this could compromise the structural integrity of the resulting pellet, causing it to break.

Next, the pellet must be heated to a sufficient temperature to allow for reaction between the reagents: increasing the temperature leads to an increased reaction rate between the reagents and increased diffusivity of the ions through the mixture. To do this while keeping a protective atmosphere, the pellets are generally sealed in an ampoule. For the Na_3PnS_4 family, silica ampoules are suited because they do not react (to any appreciable degree) with the reagents or end product, even at high temperatures (at least 500 °C). It is important to control the heating rate during synthesis, since many reagents of solid-electrolytes have different volatile products that can evaporate if heated too quickly, which can result in a mismatch in stoichiometry of the resulting sample. Finally, after cooling, the ampoule can be opened again and the pellet can be ground into a powder which, if all went well, consists of the desired end product.

3.1.1 Experimental setup: synthesis

All sample preparations and treatments in this work were carried out in an Argon filled glove box. The electrolytes were prepared using sold-state synthesis (as described above), where stoichiometric amounts of the reagents were mixed by hand in an agate mortar for at least 10 minutes. Each sample was synthesized using a small sulphur excess, to compensate for the loss of sulphur that occurred during synthesis (as observed in initial Na_3PS_4 and Na_3SbS_4 synthesis attempts). The reagents used for the synthesis of the Na_3PnS_4 structures were Na_2S (Sigma Aldrich), P_2S_5 (Merck), As_2S_3 (Alfa Aesar, 99.9% metals basis), S (Acros Organics, 99.999%, trace metal basis), and Sb (Alfa Aesar, 99.9999, metals basis).

For the synthesis of Na_3PS_4, the reagents Na_2S and P_2S_5 were mixed stoichiometrically (3:1) with an additional 5 wt.% of sulphur. For Na_3AsS_4, the Na_2S, As_2S_3 and S reagents were mixed stoichiometrically, with a 10 wt.% sulphur excess. For the Na_3SbS_4 synthesis, two different synthesis routes were used. The first sample was made by first synthesizing Sb_2S_3; this was done by mixing of elemental Sb and S (grinding in an agate mortar for at least ten minutes). The Sb-S mixture was sealed in a silica ampoule and heated to 650 °C (rate 100 °C/h), dwelled for 20 minutes, then cooled down to 520 °C (rate 20 °C/h) and held there for 24 hours. The obtained crystal was ground into a powder and mixed stoichiometrically with Na_2S and S, including a 10 wt.% sulphur excess. The second sample of Na_3SbS_4 was made by directly mixing Na_2S, Sb and S stoichiometrically, again with a 10 wt.% sulphur excess.

The resulting powder mixtures were cold pressed into pellets at ~400MPa and kept at that pressure for at least 10 minutes, resulting in pellets of 10 mm in diameter and ~10 mm in thickness. The pellets were sealed in silica ampoules under a 500mbar Argon pressure, to inhibit the escape of gaseous S from the reagent mixture during heating. The ampoules were subsequently heated to 500 °C (rate 60 °C/h), kept there for 20 hours, and cooled to RT again (rate 60 °C/h). Finally, the resulting powders were ground again for at least 10 minutes, to ensure sufficiently small particle size for further characterisation.

3.2 X-Ray Diffraction (XRD)

One of the most useful and accessible tools to determine the crystal structure of a material is X-ray diffraction (XRD). To do so, X-ray diffraction utilizes the elastic scattering of X-rays on the lattice of the material: when a beam of X-rays is incident on a sample, the X-rays interact with the electron clouds of the atoms that make up the sample and get diffracted. How the X-rays are diffracted depends directly on the crystal structure of the irradiated sample (as shown schematically in Figure 3.1). The incident X-rays are diffracted by different atomic layers of the material. Based on the spacing between the atomic layers, there are certain angles for which constructive interference occurs between the diffracted X-rays. It is for this case that a significant contribution to the diffracted signal can be detected. This criterion is described by ***Bragg's law***:

$$\boldsymbol{\lambda = 2d_{hkl} sin\theta} \qquad (4)$$

where λ is the wavelengths of the incident X-rays, d_{hkl} is the distance between the planes and θ is the angle of incidence of the X-rays[40]. A Bragg diffractogram is then simply a plot of diffracted intensity versus 2θ. Thus: if the wavelengths and angle of incidence of the X-rays are known, the angles at which constructive interference occurs can be related to distances in the structure. To facilitate quick evaluation of which distance d_{hkl} is considered, crystallography provides a convenient way to denote specific planes in the crystal structure using three indices: h, k and l. These indices that describe the planes within the structure are commonly referred to as ***Miller indices***. As with regular geometry, the orientation of a certain plane in the unit cell can be described using the normal vector of that plane. When the size of this vector is subsequently scaled with the size of the unit cell, one obtains the Miller indices. Constructive interference thus occurs for a specific set of Miller planes in the structure, based on the space group and atom configuration of the underlying lattice. By measuring the diffracted intensity for various 2θ angles, it is thus possible to extract the structural information of the materials.

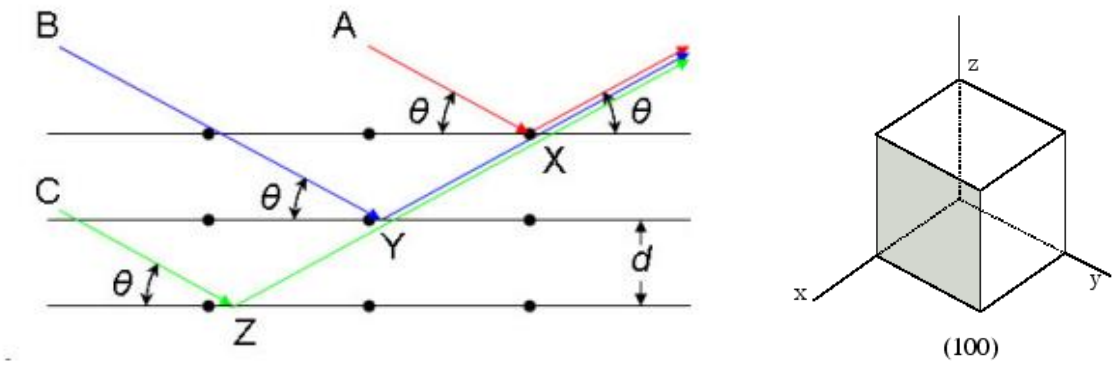

Figure 3.1. The diffraction of X-rays incident on the lattice of a crystal[40] (left) and an example of a Miller plane (100) (right).

There is one catch when considering XRD in this way: if a material consist of a single crystal, this results in different contributions to the interfering X-rays based on the orientation of the crystal. It is therefore easier to consider powder diffraction (used in this work): by grinding the crystal into small crystallites, we ensure that the orientation of the unit cells is arbitrary and that there is no preferential orientation for the crystal. Therefore, with powder diffraction we get a significant signal from all relevant Miller planes that contribute to constructive interference. In the end, a Bragg diffractogram offers three levels of information on the crystalline material[39]:

1) Geometrical: the positions of the Bragg peaks are directly related to the shape and size of the unit cell, as well as the symmetry of the unit cell.

2) Chemical: the intensities of the observed peaks are dependent on the type of atoms making up the structure and the exact locations of these atoms.

3) Microstructural: the shape of the peaks depends on the size of the crystallites contributing to diffraction, as well as potential micro strain in the structure (causing small, local deformation of the unit cells).

Based on Braggs law and crystallography, each of these levels can be related to attributes of the diffractogram: the geometrical information can be found in the peak positions, the chemical information in the peak intensities and the microstructural information in peak shape (illustrated in Figure 3.2).

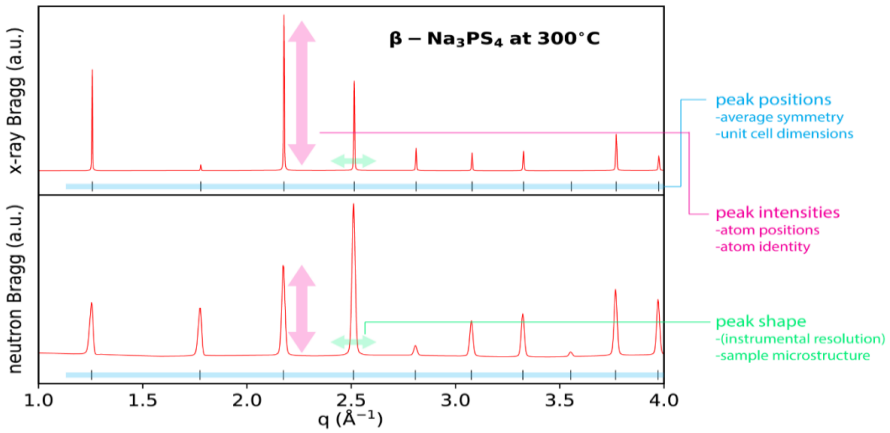

Figure 3.2. Exemplary neutron and X-ray diffractograms illustrating how the different types of information can be found in different aspects of the diffractograms. The diffracted intensity is plotted against q, where $q = \frac{4\pi \sin(\theta)}{\lambda}$. Adapted from [39].

One of the most common methods to get the structural information from a diffractogram is known as ***Rietveld refinement***. Rietveld refinement relies on calculating theoretical Bragg intensities based on a crystallographic model and comparing these to the experimental intensities. By iteratively changing the model parameters, a final structural model is created where the deviations between the theoretical and experimental observed intensities are minimized. This way, provided that the sample has a sufficiently crystallinity, the structure and structural characteristics of a sample can be determined.

3.2.1 Experimental setup: X-ray diffraction

In this work, powder XRD patterns were collected over an angular 2θ range of 10-90° with a step size of 0.017°, a total measurement time of 60 minutes and a fixed slit size of 0.5°, in order to identify the crystalline phases of the prepared Na_3PS_4, Na_3AsS_4 and Na_3SbS_4 samples. The measurements were performed on an X'Pert Pro X-ray diffractometer (PANalytical) using CuKα X-rays ($\lambda_1 = 1.540598$ Å, $\lambda_2 = 1.544426$ Å, at 45 kV and 40 mA). To prevent reaction with moisture and oxygen, the samples were prepared in an Argon filled glovebox and sealed in airtight XRD sample holders with a Kapton polyimide film[41].

Rietveld-refinements were carried out using the Jana2006 software package[42]. A manual background was selected and fitted with a Legendre polynomial function with 5 free coefficients. The peak shape was described using a pseudo-Voigt function and peak shape asymmetry was corrected for using a correction by divergence of HpS/L = ~0.05.

3.3 Electrochemical Impedance Spectroscopy (EIS)

To relate the structural characteristics of the three isostructural compounds to the conduction mechanism, it is necessary to determine the conductivity of the materials. Electrochemical Impedance Spectroscopy (EIS) is a technique that allows for the electrical characterization of materials through their response to an alternating current or potential over a range of different frequencies. It is a useful characterisation method that is applied widely in the field of battery technologies and perhaps the most common method to determine the ionic conductivity of solid-state electrolytes. In the general setup for solid-state electrolytes a polycrystalline powder is pressed into a solid pellet, generally with a thickness of several mm, and placed between two ion-blocking electrodes. For a potentiostatic impedance measurement, an AC potential of small (mV) amplitude is applied to the electrodes (covering a frequency range somewhere in the mHz to MHz range) while the current response is monitored. Because the solid-state electrolyte should be conductive ionically, but not electronically, the current through the electrolyte should only depend on the Na-ion conduction through the sample. With the known applied potential and measured current, the resulting impedance of the electrolyte and setup can be calculated.

To get the bulk resistance of the electrolyte from the measured impedance, the conducting behaviour of the entire setup has to be taken into account and modelled. To get the conductivity from the measurement, the impedance has to be separated into different contributions:

$$\boldsymbol{Z(\omega) = \frac{V(\omega)}{I(\omega)} = |Z|(\cos(\phi) + i \cdot \sin(\phi))} \qquad (5)$$

where $Z(\omega)$ is the impedance, $|Z|$ its modulus and ϕ its phase. Depending on the type of behaviour of the system, we can identify different contributions to the impedance: in the ideal case, we can distinguish between resistor-like behaviour ($Z = R$), capacitor-like behaviour ($Z = \frac{1}{i\omega C}$) or inductor-like behaviour ($Z = i\omega L$).

For a non-ideal case, it is also useful to define the ***Constant Phase Element (CPE)*** ($Z = \frac{1}{Q \cdot (i\omega)^{\alpha}}$): an element which acts like part of each of the aforementioned elements, depending on the power α (which range between -1 (inductor), 0 (resistor) and 1 (capacitor)).

To model the dynamics of a solid-state electrolyte using these elements, an ***equivalent circuit*** is used. The setup measuring the impedance of the solid-state electrolyte has several important contributions that need to be accounted for in the equivalent circuit:

1) The cables used to connect the cell to the measurement instrument show resistive and inductive behaviour. This contribution is only significant if the bulk resistance of the electrolyte is very small; if this is not the case, this element can be modelled using a series R.

2) The polycrystalline pellet that makes up the solid-electrolyte is best modelled by a combination of a CPE and R in parallel: the bulk resistance of the crystal gains behaves resistor-like, while charge separation that arises from the Na-migration contributes to capacitive behaviour (best modelled using a CPE to incorporate the non-ideality).

3) The blocking electrodes used for the measurement mainly show capacitive behaviour, best modelled using a CPE.

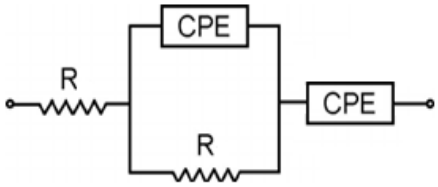

Figure 3.3. An example of an equivalent circuit of a solid-state electrolyte.

Because the impedance measurement is inherently a measurement with three different observable components (the magnitude of the impedance, the impedance phase and the frequency), the results can be visualized in three different plots: a ***Nyquist*** representation (where the complex impedance is decomposed into a real and imaginary part which are plotted against eachother), a ***Bode-magnitude*** plot (where the magnitude of the impedance is plotted against the frequency) and a ***Bode-phase*** plot (where the phase is plotted against the frequency). For the described equivalent circuit, these plots show distinct features which can be used to quickly evaluate the performance of the electrolyte (Figure 3.4).

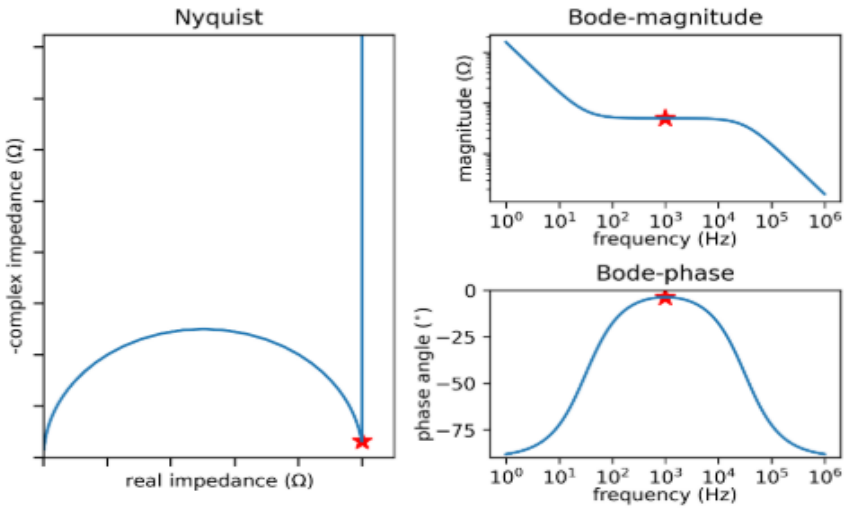

Figure 3.4. Examples of the Nyquist, Bode-magnitude and Bode-phase plots of an impedance measurement. The red star in the Nyquist plot indicates the end of the semi-circle, characteristic for the bulk resistance of a solid-electrolyte. Adapted from [39].

The different elements of the equivalent circuit can be best seen in the Nyquist representation, by looking at different aspects: (1) an offset on the real impedance axis would indicate a significant contribution of the resistive behaviour of the cables / measurement setup, (2) the semi-circle represents the solid-electrolyte (R-CPE) combination, where the end of the semi-circle gives an indication of the bulk resistance of the electrolyte and (3) the straight line at the end of the plot is the result of the capacitive behaviour of the blocking electrodes, where the angle of the line is indicative of the non-ideality of the CPE.

To get the conductive performance of the electrolyte, the measured impedance data can be fitted to the simulated data from the equivalent circuit. By iteratively updating the parameters of the model and using a least-squares method, the resistance of the solid-electrolyte pellet can be determined. Using this resistance (R) and the dimensions of the pellet (thickness d and area A), the ionic conductivity of the sample can be extracted ($\sigma = \frac{d}{RA}$).

It is important to note here that the performance of the electrolyte is directly dependent on several powder characteristics: for instance, if there are many imperfections within the crystal grains, their bulk resistance can be affected. Alternatively, depending on the size of the grains and densification of the pellet, the resistance (and capacitance) across the boundaries of the grains can affect the impedance. It is therefore important to take these factors into account when analysing the impedance spectra.

Changes in the conductivity as a function of temperature or pressure are commonly used to rate the performance of a solid-electrolyte. These changes are commonly referred to as the activation energy and activation volume. Mathematically, they can be described as:

$$\boldsymbol{E_a = -k_B \left(\frac{\partial \ln(\sigma T)}{\partial T^{-1}}\right)_P} \quad (6)$$

$$\boldsymbol{V_a = \left(\frac{dE_a}{dP}\right)_T = k_B T \left(\frac{\beta}{3} - \frac{\partial \ln(\sigma)}{\partial P}\right)_T} \quad (7)$$

where E_a and V_a are the activation energy and volume, respectively, k_B is the Boltzmann constant, T the temperature, P the pressure, σ the ionic conductivity and β the inverse of the bulk modulus [39]. So by measuring the conductivity as a function of temperature (at constant pressure) or as function of pressure (at constant temperature), we can determine the activation energy and volume.

3.3.1 Experimental setup: electrochemical impedance spectroscopy

For this study, the electrochemical impedance measurements were carried out using an Metrohm-potentiostat ("AUTOLAB-PGSTAT128N") instrument, with a frequency range from 1mHz to 10MHz. For the measurements special air-tight solid-state cells were used. These cells consist of two circular plates with each a stainless steel plunger of 10 mm in diameter attached, which go inside an aluminium mantel with the same inner diameter. Greased O-rings are placed on each side of the mantle to provide an airtight seal between the mantel and the circular plates (Figure 3.5).

The powder sample is placed in between the rods and pressed at a pressure of ~400 MPa for about 10 minutes, to densify the powder and reduce grain boundary resistance. To improve contact between the plungers and the powder, circular graphite electrodes with of ~0.5mm thickness were placed in between the plunger and the sample.

The EIS measurements in this work were performed after pressurising the cell to 500 MPa, to densify the powder even further. To determine the activation volumes, the impedance was measured for a series of pressures in the range of 0 to 500 MPa, applied using a manual hydraulic press. Because of the non-digital readout of the pressure gage, the effective pressure on the cell had an uncertainty in the order of 10 MPa. The plate and plunger of the manual press were coated in insulating tape to prevent short-circuiting of the cell. To determine the activation energy, the impedance of the samples was measured for a range of temperatures. The temperature series of Na_3PS_4 and Na_3AsS_4 were measured in an oven: the heating profile was set to range from 40 to 100 °C in steps of 10 °C, with a heating rate of 1 °C / min. The temperature was kept at every step for 1 hour, to allow the system to equilibrate. After equilibration, the error on the temperature based on the internal thermometer was in the order of 1.5 °C. At each step, several measurements were performed to ensure a maximum difference in the measured bulk resistance of ~2 Ω. The temperature series of the Na_3SbS_4 sample was measured in a freezer (at the temperatures of 0, -10, -30 and -50 °C), because the initial resistance of the Na_3SbS_4 sample was too small to be determined accurately with a high temperature setup. Based on fluctuations in the internal thermometers read-out, the error on the temperature of the freezer was determined to be 2 °C.

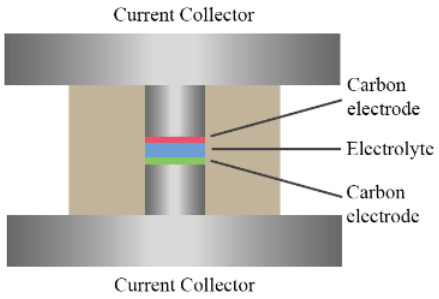

Figure 3.5. Graphical depiction of the cell design, with the current collectors, pistons, mantel, carbon electrodes and electrolyte. Adapted from [43].

The measurements were controlled using the NOVA software supplied with the AUTOLAB equipment and analysed using the *impedance.py* package[44]. The impedance spectra of the measurements at different pressures were fitted using a simple equivalent circuit of one series R, a R-CPE element and a series CPE. For the temperature series an equivalent circuit of a series R, two R-CPE elements in series and a series CPE was used. Errors on the conductivity measurements were estimated by finding the lowest point of the right side of the bulk resistance semicircles (see the red star in Figure 3.4) and comparing the real impedance at that point to the fitted resistance. A goodness of the fit was determined by calculating adjusted Pearson's R^2 values for both the real and the imaginary part of the impedance. The activation energy and volumes were calculated by fitting the resistance values determined through EIS and respectively the temperature and pressures to equations (6) and (7) using Matlab[45].

3.4 Differential Scanning Calorimetry (DSC)

The melting point of a material can be a useful indicator of the stiffness of the crystalline lattice, since the melting process is fundamentally connected to the forces acting on the different ions or atoms in the solid. The Lindemann criterion describes that a solid melts when the vibrational amplitudes of the relevant ions become so large that they interfere with the neighbouring atoms and so destabilize the lattice[46]. The thermally excited vibrations are connected to the binding strength between the ions, where stronger binding leads to a soft lattice and as such a higher melting point[47] (Figure 3.6).

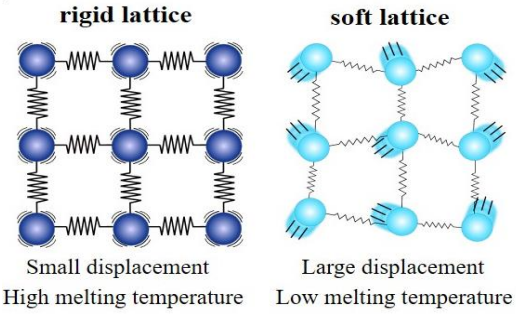

Figure 3.6. A soft lattice allows for much larger displacement as a result of weaker forces. Since the melting of the material is associated with displacements that are so large that the framework destabilizes, the larger displacements in the softer lattice are related to a lower melting point. Adapted from [17].

To determine the melting point of a material, differential scanning calorimetry (DSC) can be performed. DSC is a thermal analysis technique where the heat flow into and out of a sample are measured as a function of temperature and time, while the sample is exposed to a controlled temperature program[48]. By monitoring the heat flow, various different endo- or exothermic transitions of the material can be investigated, including phase transitions (provided a sufficient change in energy is associated with the transition). If a material undergoes a phase transition, such as melting, the rate at which the temperature changes compared to the controlled temperature program changes as well. This provides data on the heat flow into or out of the sample. Evaluating the onset temperature of the change in heat flow can provide one with the transition temperature. When performed with a reference material, of which the transition temperatures and energies are known, DSC can also be used to quantify the energy associated with the transition.

3.4.1 Experimental setup: differential scanning calorimetry

Differential scanning calorimetry (DSC) was performed with a Netzsch Simultaneous thermal analyzer STA 449F3 housed in an Ar-filled glovebox. For the measurement the samples were loaded into quartz crucibles and Ar gas flow was adjusted to 40 mL/min. For the Na_3PS_4 and Na_3SbS_4 samples the temperature was increased from 313 K to 1073 K and again cooled down to 313 K with 5 K per minute. For the Na_3AsS_4 sample the temperature was increased from 313 K to 973 K, due to the observed decomposition of the sample after melting.

It must here be noted that the DSC measurements were not performed or analyzed by the author. All measurements were performed at the Université de Picardie Jules Verne in Amiens by M. Courty. The Na_3PS_4 and Na_3SbS_4 measurements were performed on samples prepared by T. Famprikis, the Na_3AsS_4 measurement on the sample prepared for this work. Analysis of the thermograms was done by T. Famprikis.

4. Theory and Methodology: computational work

Following the description of the various experimental techniques used in this work, it is also important to have an understanding of the computational methods used for studying ion conduction. To this end, this chapter first covers the basics of density functional theory (DFT) Subsequently, a description is given of how DFT computations are performed using VASP, followed by an explanation of the various charge metrics used to investigate bonding nature (specifically Bader charge, Born Effective Charges (BEC), the Electron Localization Function (ELF) and the electronegativity[a]). Finally, it is explained how energy landscapes can be determined using the Nudged Elastic Band method (NEB).

4.1 Density Functional Theory (DFT) *(Applied Physics)*

Density Functional Theory (DFT) is a quantum mechanical modelling technique used to study the electronic structure of a material. It is applied in various different fields and has been recognized as the most successful way of studying many-body systems such as molecules, crystals and classical fluids [49,50]. Obtaining the wavefunction from the Schrödinger equation would provide all the necessary information to describe a system. However, solving the Schrödinger equation is only possible for very simple systems, such as the single electron hydrogen atom. To obtain an accurate solution for the many-body systems without having to treat all particles separately, density functional theory considers the electron density instead of separate electrons. Using this approximation allows for the calculation of the ground state of the systems and the computation of all fundamental material properties that arise from the electron distribution[49]. Because DFT calculations still require significant computational power, DFT simulations are best-suited for atomistic length-scales and studying systems in sizes ranging from Angstroms to nanometres.

To understand how we can use DFT to analyse the fundamental properties that are interesting for solid-electrolytes, such as the activation energy, charge distribution, bulk modulus and crystal structures, we require a basic understanding of the quantum mechanics behind DFT. For a more detailed description, please refer to Vasileiadis[49] or Sholl & Steckel[50].

4.1.1 Basic principles of DFT

To calculate the ground state of a collection of particles, the many-body Schrödinger equation needs to be solved:

$$\hat{\boldsymbol{H}}\boldsymbol{\psi}\left(\{\vec{\boldsymbol{r}}_{\boldsymbol{i}}\},\{\vec{\boldsymbol{R}}_{\boldsymbol{j}}\}\right) = \boldsymbol{E}\boldsymbol{\psi}\left(\{\vec{\boldsymbol{r}}_{\boldsymbol{i}}\},\{\vec{\boldsymbol{R}}_{\boldsymbol{j}}\}\right) \quad (8)$$

where $\hat{H}$ is the Hamiltonian energy, ψ the time-independent wavefunction (depending on the nucleus positions $\vec{R}$ and electron positions $\vec{r}$) and E the energy of the system. To simplify the many-body problem, DFT takes three important steps. The first step is the Born Oppenheimer approximation: by considering that the electron mass is about a thousand times smaller than the mass of the nucleus (causing the nucleus to react "sluggish" compared to the electrons), it is possible to separate the dynamics of the nuclei and the electrons:

$$\boldsymbol{\psi}\left(\{\vec{\boldsymbol{r}}_{\boldsymbol{i}}\},\{\vec{\boldsymbol{R}}_{\boldsymbol{j}}\}\right) = \boldsymbol{\psi}_{\boldsymbol{e}}(\{\vec{\boldsymbol{r}}_{\boldsymbol{i}}\}) \cdot \boldsymbol{\psi}_{\boldsymbol{N}}\left(\{\vec{\boldsymbol{R}}_{\boldsymbol{j}}\}\right) \quad (9)$$

[a] It must be noted that the electronegativity was not determined computationally or experimentally in this work. However, because the electronegativity is closely related to the charge metrics as described in this chapter, the concept of and theory behind electronegativity are very relevant to this work and thus covered in this section as well.

With this approximation, the electron part of the Hamiltonian becomes

$$\widehat{\boldsymbol{H}} = -\frac{\hbar^2}{2m_e}\sum_i^{N_e}\nabla_i^2 + \sum_i^{N_e} V_{ext}(\vec{r}) + \sum_{i=1}^{N_e}\sum_{j>1} U(\vec{r}_i, \vec{r}_j) \quad (10)$$

where m_e is the electron mass, N_e the number of electrons. The first term captures the kinetic energy, $V_{ext}(r)$ captures the nuclei-electron interactions and the $U(r_i,r_j)$ the electron-electron interactions. With a second approximation, known as the orbital approximation, solving the electron part of the Schrödinger equation becomes a lot simpler. By treating any electron as a point charge in the field created by the other electrons, we simplify the many electron problem into effectively many "one-electron" problems. Doing this, the electron density can be redefined in terms of single electron wavefunctions

$$n(\vec{r}) = 2\sum_i \psi_i^*(\vec{r})\psi_i(\vec{r}) \quad (11)$$

Now, the step that forms the heart of DFT has been reached: the two theorems of Hohenberg and Kohn. The first theorem states that the ground state energy E is a unique functional of the electron density. This implies that by solving for the electron density would directly also solve the ground state energy problem. The second theorem gives an indication as to where to find the energy functional. The second theorem states that the electron density that minimizes the energy of the overall functional is the true ground state electron density. This indicates that when the true energy functional form is known, one can iteratively vary the electron density until the energy becomes minimum.

Based on these approximations and theorems, Kohn and Sham proposed a way of obtaining the ground state electron density: the Kohn-Sham scheme. This approach is based on solving the set of single-electron wave functions that only depend on the three spatial dimensions. This is done by separating the interactions between the single-electron wavefunctions and accounting for those in different potentials:

$$\left[-\frac{\hbar^2}{2m_e}\nabla^2 + V_{ext}(\vec{r}) + V_H(\vec{r}) + V_{XC}(r)\right]\psi_i(\vec{r}) = \varepsilon_i(\vec{r})\psi_i \quad (12)$$

where again the kinetic and electron-nuclei interaction contributions can be seen, as well as the Hartee potential (V_H) and an unknown exchange correlation potential (V_{XC}). The Hartee potential is defined by the electron density and captures the interactions of the electrons with the electron density. The exchange correlation (XC-) functional includes all other quantum mechanical interactions between the single electrons. The exact form of this functional is unknown: throughout the years, many different approximations have been developed to calculate this exchange correlation functional, all differing significantly from each other. The choice of XC-functional is thus of great importance when performing DFT calculations, and generally depends on the properties of interest.

Ultimately, the point has been reached where the problem has to be implemented into a computer: we need to define a loop where a trial electron density is selected, from which a Hartee and XC- potential can be calculated. With this, the Kohn-Sham equations can be solved to get the single-particle wavefunctions. To make working with the wavefunctions computationally feasible, we need to define the electron wavefunction in a suitable numerical way. Perhaps the most used approximation is the plane wave approximation: a basis set of plane waves is defined in which the electronic wavefunction can be expanded (also known as Bloch's theorem). Because this expansion can theoretically be infinite, a cut-off energy of the plane-

wave basis set needs to be defined. By numerically modelling the wavefunctions in this way, we can use them to calculate the electron density. This calculated electron density can be compared to the trial electron density and once self-consistency is reached, the electron density can be used to compute the total ground state energy of the system. This Kohn-Sham scheme is visualized in Figure 4.1.

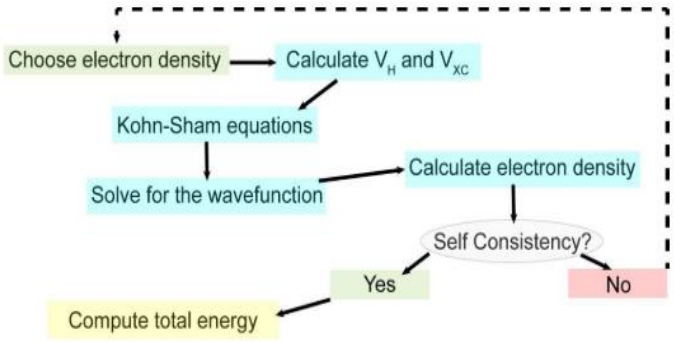

Figure 4.1. Schematic overview of the Kohn-Sham scheme. Adapted from [49].

Thus, using DFT allows for the calculation of the energy of a system in a quantum mechanical manner. This can in turn be used to calculate many different other material properties: by for example iteratively moving ions and calculating the energy for each step, we have a way to find the minimum energy state of a certain collection of atoms, or by calculating changes in energy resulting from small perturbations to the system, we can calculate higher order properties such as the polarizability or the bulk modulus.

It is in the Kohn-Sham scheme that many commercial packages have implemented DFT and there is a wide variety of commercial source codes available that can run DFT calculations. For this work, we consider DFT as implemented in the Vienna Ab-Initio Simulation Package (VASP), using the wavefunction approximation as implemented by the Projector Augmented Wave method (PAW). Further details on the implementation are found in the next sections.

4.1.2 Geometry optimization and pressure relaxations

For calculating interatomic distances through DFT simple "geometry relaxations" suffice. These relaxations consist of an iterative loop where the ions (provided through an initial structure) are moved and for each loop the energy is calculated. By using an iterative scheme focused on minimizing the energy (or forces on the ions) the ion-configuration with the lowest possible energy can be found. This type of relaxation therefore consist of two loops for each iteration: firstly the lowest energy of the electron distribution is found (using DFT) and afterwards the ions are moved in an attempt to find a configuration where the electron distribution has a lower energy. As evident from this approach, this results in a loop where the ions can infinitely be moved in order to possibly reduce the total energy. Therefore, DFT relaxations have certain settings implemented to end the calculation once specific criteria have been met. The most important features of the relaxation are the accuracy (which can be interpreted as "step size") with which the ions are moved, the convergence criteria for the electron distribution and ion-configuration and the scheme that describes the way in which the ions are moved.

To perform a DFT calculation in VASP there are four key elements required: a file containing an initial structure (called the POSCAR file), a file containing pseudopotentials that model the XC-functional and determine which electrons are treated as valence electrons (the POTCAR file), a file containing the sampling distribution of the structure in reciprocal space (the KPOINTS file) and a file containing the settings of the relaxations, where among other things the accuracy, ion-scheme and convergence criteria are specified (the INCAR file).

It might seem counterintuitive to relax a structure of which the structure is already known; after all, the crystal structure of Na_3PS_4 and its isostructural compounds is already well-known.

Nonetheless, relaxing these structures using DFT has several advantages. Firstly, it is possible to relax the structures under specific conditions: it is for example possible to isotropically apply pressure to the structure and relax the structure again. This way, the structural evolution and effects of pressure on the structure can be investigated. Furthermore, it is possible to calculate many different material properties through these structure relaxations: DFT can be used to calculate the charge distribution around atoms, bulk moduli, phonon modes and many more properties. Of these properties, the different charge metrics (as covered in the next section) and the bulk moduli are the most interesting for the study of the conduction mechanism.

The ***bulk modulus*** of a material *B* is a macroscopic measure for the compressibility of the material. It can serve as a descriptor of lattice softness, since it is directly influenced by all force constants present in the structure. The bulk modulus of a material can be calculated using the Birch-Murnaghan equations of state[51]. These equations relate the change in volume and energy of the structure to the applied pressure. The equation for the pressure (P) - volume (V) relation is given by

$$\boldsymbol{P(V) = \frac{3B_0}{2}\left[\left(\frac{V_0}{V}\right)^{\frac{7}{3}} - \left(\frac{V_0}{V}\right)^{\frac{5}{3}}\right]\left\{1 + \frac{3}{4}(B_0' - 4)\left[\left(\frac{V_0}{V}\right)^{\frac{2}{3}} - 1\right]\right\}} \qquad (13)$$

where B_0 is the bulk modulus, B_0' the derivative of the bulk modulus with respect to pressure and V_0 the equilibrium volume. The relation between the internal energy (E) and pressure is given by

$$\boldsymbol{E(V) = E_0 + \frac{9V_0B_0}{16}\left\{\left[\left(\frac{V_0}{V}\right)^{\frac{2}{3}} - 1\right]^3 B_0' + \left[\left(\frac{V_0}{V}\right)^{\frac{2}{3}} - 1\right]^2\left[6 - 4\left(\frac{V_0}{V}\right)^{\frac{2}{3}}\right]\right\}} \qquad (14)$$

with E_0 as the equilibrium energy (at 0 pressure). Compared to the melting point, the bulk modulus is a less direct indicator of vibrations of the lattice. The bulk modulus does however bear a strong relation with the concept of the activation volume: if we interpret the activation volume as the change in local volume required for ion migration, then a material with a low bulk modulus should easily deform and thus allow for large changes in the local structure during ion conduction. However, applying pressure to a material with a low bulk modulus should cause the structure to be compressed significantly, which in turn should cause the activation barrier to increase (since compression would result in a more narrow bottleneck of conduction).

So, it becomes clear that simple DFT relaxations can be used to investigate the static structure as well as the dynamics of the material. To get direct information on the conductive behaviour of the structure however, simple DFT relaxations do not suffice. For this, two different DFT methods are available which are more successful at estimating activation barriers and ionic conductivity. For assessing the activation barrier, the Nudged Elastic Band (NEB) method can be used, and for evaluating ion migration *ab initio* Molecular Dynamics (AIMD) is ideally suited. The NEB method is used extensively in this work to assess activation barriers and will be covered later on (section 4.3). AIMD simulations were considered for this work, but due to time constraints were not incorporated in this study. A short outline of the potential uses of AIMD for studying ion conduction and preliminary results can be found in "Appendix E. – Ab Initio Molecular Dynamics". A complete guide on how DFT calculations can be performed in VASP, including a detailed description of all input files, as well as specific notes on DFT calculations under pressure or for charge analysis (on which more information is found in the next section), is included in "Appendix F. – Guideline DFT using VASP".

4.1.3 Computational setup: geometry optimization and relaxations under pressure

All DFT calculations in this work were performed using the Vienna Ab-initio Simulation Package (VASP) code[52]. The projector augmented wave (PAW) method was employed to create the plane wave basis set. The selected pseudopotentials for the different atoms Na, P, Sb, As and S considered respectively the $2p^6 3s^1$, $3s^2 3p^3$, $4s^2 4p^3$, $5s^2 5p^3$ and $3s^2 3p^4$ electrons as valence. For all atoms except for Na these are considered the standard forms of the pseudopotentials[53]. For the Na-atom, the Na_pv pseudopotential was selected because the semi-core like $2p^6$ states have a small role in the Na-S bond nature and therefore need to be included.

The Perdew-Burke-Ernzerhof specified for solids (PBEsol) version of the generalized gradient approximation (GGA) was adopted as the exchange correlation functional. The PBEsol XC-functionals have been found to underestimate the cell volume compared to the PBE XC-functionals and experimental data[11]. However, when taking the thermal expansion coefficient into account and compensating for the fact that the DFT calculations are run at 0K, the PBEsol XC-functionals were found to model the cell volume most accurately. An energy cut-off of 520 eV was set for the plane wave expansion. For the geometry optimizations and relaxations under pressure, a Γ-centered Monkhorst-Pack k-point mesh of 5 x 5 x 5 was used to sample the Brillouin zone. Convergence criteria of 10^{-6} eV/cell in energy and 10^{-2} eV / Å in force were adopted for the electronic and ionic loops, similar to previous studies[52,21]. The tetrahedron method with Blöchl corrections was used for the smearing of the partial occupancies across the orbitals, with a 0.002 eV smearing width.

With these settings, the error on the calculated energies became < 0.0005 eV for the entire structure. The error on the calculated cell volumes was significantly larger, as a result of residual pressure in the structure after relaxation. The residual pressure for each calculation was ensured to be below 0.6 kB. Based on calculated bulk moduli, the error in the calculated volumes as a result of the residual pressures became < 1 $Å^3$.

The initial structures of Na_3PS_4 and Na_3SbS_4 were based on experimental CIFs acquired through the ICSD[54], the initial structure of Na_3AsS_4 on the work of Pompe[38]. All computational work was performed on the cubic polymorphs of the materials, since this allowed for easier comparison between the isostructural compounds and analysis of the fundamental conduction pathway. The structures under pressure were relaxed by controlling the Pulay-stress, covering a range of isostatic pressures of – 2.5 GPa to 5 GPa. The bulk moduli were calculated by fitting the relaxations data to the Birch-Murnaghan equations of state[51] and fitted using MATLAB[45]. For this, only the pressures in the range of -1 GPa to 1 GPa were considered, since the larger pressures showed significant residual external pressures after relaxation (> 0.6 kB).

4.2 Charge analysis in crystal structures

DFT is a powerful tool for evaluating the charge distribution in the structure. The distribution of charge is a key element that determines the nature of bonds between atoms, which in turn has large effects on the energy landscape within the structure and as such the conduction mechanism. Four interesting metrics for analysing charge in solid electrolytes are the Born Effective Charge, the Bader Charge, the Electron Localization Function (ELF) and the electronegativity. Before it is possible to discuss which information these charge indicators can provide us with, it is important to note that the output of charge analysis is very dependent on the choice of pseudopotential. This therefore needs to be discussed first.

4.2.1 Pseudopotentials

The information on the electron density used in VASP is initially provided through the POTCAR file. Herein, the pseudopotentials and default exchange correlation functionals are specified. The exchange correlation functional can be defined through many different approaches: of these, the Local Density Approximation (LDA) or different versions of the Generalized Gradient Approach (GGA) are most common[55]. Within the GGA approach, the Perdew-Burke-Ernzerhof (PBE) scheme or the PBE scheme for solid (PBEsol) are common choices when studying solid-electrolytes[12]. Which exchange correlation functional is set is by default determined by which pseudopotentials are used to create the POTCAR file. The choice of XC-functional can however be manually overwritten using the INCAR file.

To use the pseudopotentials to construct the all-electron charge density, it is essential to know which electrons in the structure have to be considered in this charge density. For many types of atoms, the electrons in the lower shells are core like, meaning they do not or hardly participate in bonding. When creating the all-electron charge density, it is therefore most interesting to consider the self-consistent valence electrons (which do participate in bonding). In the different pseudopotentials that are used for DFT calculations using VASP, different electrons are considered as valence electrons[53]. Most of the pseudopotentials contain a subscript of either pv or sv, indicating whether the primary valence electrons or secondary valence electrons are considered. For a sodium atom (Na), there are three different pseudopotentials available:

1) The “Na” pseudopotential considers only the 3s electron as a valence electron.
2) The “Na_pv” pseudopotential considers the 3s and 2p electrons as valence electrons.
3) The “Na_sv” pseudopotential considers the 3s, 2p and 2s electrons as valence electrons.

As can be seen from the trend in the pseudopotentials, the amount of electrons treated in the all-electron charge density increases as more electron shells are treated as valence shells. This has two important consequences: firstly, the charge density will be more complete and thus the calculated energies of the relaxation will be more accurate and secondly, the calculation will be more computationally demanding since more electrons have to be evaluated. As such, the pseudopotential should be carefully chosen depending on which of these characteristics of the computation is important.

For the other pseudopotentials necessary to model Na_3PS_4, Na_3AsS_4 and Na_3SbS_4, namely the P, As, Sb and S pseudopotentials, only the outermost s-shell and p-shell electrons are considered in the POTCAR files. This means that respectively 5, 5, 5 and 6 s- and p-shell electrons are treated as valence electrons for these atoms. The nature of the different electrons shells and their valence or core like nature has a direct impact on the bonding interactions between the atoms; this will be discussed in more detail in the upcoming sections.

4.2.2 Born Effective Charges

The first method to quantify charge are the Born Effective Charges (BEC). The Born charges describe the phonon-electric field coupling[56] and are defined as the change in polarizability of an atom as a result of an atomic displacement. Since the polarizability in turn is a measure of induced dipole moment per unit strength of applied electric field, it can be interpreted as a measure for the shift of the electron distribution around an atom (Figure 4.2).

To be exact, the Born Effective Charge of atom k is defined as

$$\boldsymbol{Z^*_{k,\gamma\alpha}} = \boldsymbol{V}\frac{\boldsymbol{\delta P_\gamma}}{\boldsymbol{\delta \tau_{k,\alpha}}} = \frac{\boldsymbol{\delta F_{k,\alpha}}}{\boldsymbol{\delta \xi_\gamma}} = -\frac{\boldsymbol{\partial^2 E}}{\boldsymbol{\partial \xi_\gamma \partial \tau_{k,\alpha}}} \quad (15)$$

where $Z^*_{k,\gamma\alpha}$ is the Born Effective Charge, P_γ the polarizability, τ_α the displacement, $F_{k,\alpha}$ the force on the atom, E the energy and ξ_γ the electric field[58]. From this definition of the Born charge, it can be seen that the Born charge is dependent on both the local displacements of the atoms as well as the change in the electric field (or local electron density). Since these properties are directional, the Born charges can be different for each direction. This can be imagined by comparing the system to a macro-scale parallel plate capacitor: if one moves the plates of the capacitors parallel to each other, there will be no resulting force on the plates (even though there is a displacement). However, if one moves the plates towards each other, a force will arise as a result of the electric field that exists between the two plates. The resulting force is dependent on both the magnitude of the electric field and the displacement. In practice, when using a Cartesian system, the Born effective charges are given in a 3 x 3 matrix.

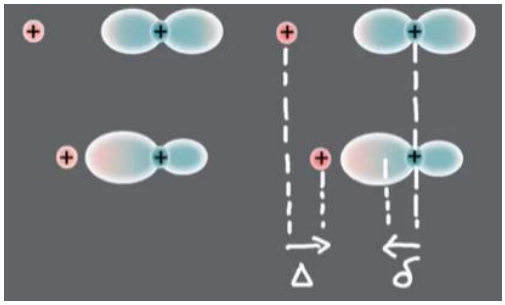

Figure 4.2. The Born Effective Charge is a measure of the shift in the electron distribution (**δ**) as a result of a displacement (**Δ**). Adapted from [57].

While the origin of Born Effective Charges are somewhat indirectly related to the quantification of charge on atoms, they are important quantities elucidating the physical understanding of bonding, as they describe the coupling between lattice displacements and the electric field. Because of this relation to the lattice dynamics, the Born Effective Charge can be seen as an indicator of the dynamic lattice influences on the conduction mechanism. Specifically, the Born charges are indicative of how stiff the bonds forming the lattice are, since the Born charges are only strongly affected by atom positions if the resulting electric field change is significant. If the force constant of the bond is high, thus indicating a stiff bond, the effects of displacement on the polarizability will be large. Born charges can also serve as indicators of bonding nature. For ionic bonds, where the atoms in questions have a more closed shell-like nature, the Born charge carried by an ion would be close to its nominal charge, as the electron shell is less affected by the displacement of ions[59]. On the other hand, if a covalent character is present, a significant amount of charge flows through the bond when ions are displaced and the resulting change in electric field is significant. The Born charge of an atom participating in a covalent bond is therefore usually significantly different from its nominal charge[59].

4.2.3 Bader Charges

A different way to get an estimate of the amount of charge on an atom (sometimes also referred to as the Net Atomic Charge, or NAC) is to devise a method to split the charge density up in different sections and attribute the charge in a certain volume to a specific atom. However, where the charge density should be split is not an arbitrary choice. There are several different approaches to do so; there are different electrostatic potential fitting methods, several versions of a Density Derived Electrostatic and Chemical approach (the newest of which is known as DDEC6), and Bader's Quantum Chemical Topology (QCT)[60,61,62]. In this study the Bader approach, where the integrated charge inside the calculated volume is known as Bader charge, is used to split the charge density and determine the Net Atomic Charge.

The Bader approach uses what are called zero flux surfaces to divide the electron density into volumes[62]. A zero flux surface is a 2D surface where the gradient of the charge density perpendicular to the surface is zero (Figure 4.3). Typically, the charge density reaches a minimum somewhere in between the atoms and this is therefore a natural place to separate atoms from each other. The charge subsequently enclosed within the Bader volume is a good approximation for the total electronic charge belonging to the atom. Comparing the Bader charge to the nominal ionic charge also gives a reasonable indication of the nature of a bond between two atoms, yet it is important to take the Bader volume into account when doing so, since differences in Bader volume result in differences in Bader charge. While both the Born and Bader charge can be used to investigate bonding nature, the Bader charge is a more accurate descriptor of the net atomic charge than the Born charge.

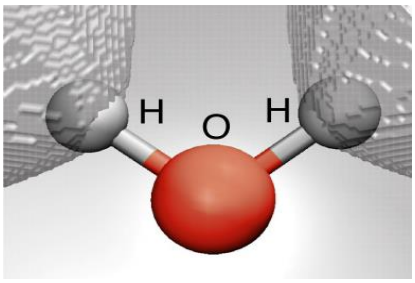

Figure 4.3. The zero flux surfaces for an H_2O molecule, with which the shifted electron distribution as a result of the polar covalent bond can be observed. Adapted from [62].

4.2.4 Electron Localization Function

A less quantitative but more qualitative way of quantifying charge is the so-called Electron Localization Function (ELF). The ELF is a function of the electron localization in the system and is defined as:

$$\boldsymbol{n}(\vec{\boldsymbol{r}}) = \frac{\mathbf{1}}{\mathbf{1}+\boldsymbol{\chi}(\vec{\boldsymbol{r}})} \qquad (16)$$

where n(**r**) is the ELF and χ(r) is the ratio between the electron localization in the system and the electron localization in a uniform electron gas (fully delocalized)[63]. The ELF is a number between 0 and 1 and expresses the probability of finding another Pauli exclusive electron (same spin) near a chosen reference electron.

Since the ELF is a direct measure of the localization of electrons in the system, it is very useful for identifying shared-electron and unshared-electron interactions. The ELF is close to unity in regions occupied by paired electrons; these electrons have opposite spin and as such a third reference electron would be Pauli exclusive with one of the paired electrons. In general, the rule of thumb applies that where the ELF is high (> 0.7), the electrons are characterized as localized, meaning they constitute core, bonding or paired electrons. On the other hand, when the ELF is between 0.7 and 0.2, the electron localization is similar to that of an electron gas and is characteristic of metallic or ionic bonds. In the absence of electron density, the ELF becomes 0 (ref [63]).

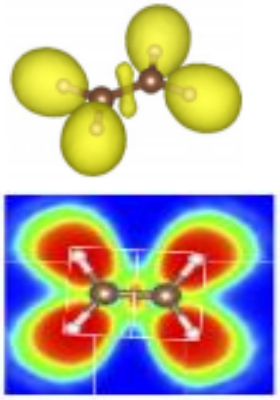

Figure 4.4. The charge distribution (top) and the ELF (bottom) of an ethene (C_2H_4) molecule.

The relation to the Bader charge can be seen when one realises that the Bader charge is based on partition of the electron density based on the criterion $\nabla n(\vec{r}) = (0, 0, 0)$ (ref [64]). The Bader charge and ELF can therefore function as complementary methods, where the Bader charge quantifies the charge on an atom and the ELF provides a deeper understanding of the bonding interactions in the structure.

4.2.5 Electronegativity and bonding nature

In bonding theory the electronegativity is one of the most important characteristics that defines the nature of a bond [65]. Electronegativity can somewhat loosely be defined as the ability of atoms to attract the electrons in covalent bonds towards themselves. The charge distribution in a structure is what determines what type of bond exists between two atoms. When both atoms have the same electronegativity, both atoms pull equally on the electrons in the bond: in this way a covalent bond is formed [66]. When atoms differ in electronegativity, the electrons in the bond will be slightly shifted towards the atom with the higher electronegativity: this results in a shifted charge distribution, which is known as a polar bond. In an ionic bond, the differences in electronegativity are so large that one atom actually becomes ionized, and the electron is transferred from one atom to the other. As a result, in an ionic bond the nuclei are bound by the forces exerted by the charge density localized on a single nucleus [66].

Figure 4.5. How the electrons are shared between the atoms depends on the electronegativity. If the electronegativity of two atoms is the same, a covalent bond arises (left), if one atom has a slightly higher electronegativity that atoms pulls the electrons slightly towards it, resulting in a polar bond (middle) and if the electronegativities differ significantly, this can result in the electrons being pulled towards one atom to such an extent that the other atom ionizes and an ionic bond arises (right).

The electronegativity (χ) is often quantified using the Pauling scale. The Pauling scale is based on the observation that polar bonds are generally stronger than the average of their homopolar counterparts [65]. Pauling devised a measure where the difference in electronegativity between two binding atoms is calculated based on the binding energies between the two atoms and their homopolar combinations:

$$|\chi_A - \chi_B| = \sqrt{E_{A-B} - \frac{E_{A-A}+E_{B-B}}{2}} \qquad (17)$$

where $E_{A\text{-}B}$ is the binding energy between atom A and B, $E_{A\text{-}A}$ and $E_{B\text{-}B}$ are the homopolar binding energies and χ_A and χ_B the respective electronegativities. Since Pauling's system can only be used to determine differences in electronegativity, the value of 4.00 was assigned to the most electronegative element on the scale (fluor) as reference value. Pauling's scale is commonly used to determine the nature of bonds: in Pauling's ionic bonding criterion a bond has a somewhat covalent character as long as the difference in electronegativity is below 1.7 and is classified as polar covalent bond when the differences is between 0.4 and 1.7 (ref [21]).

The actual electronegativity of atoms generally depend on the natural electron configuration of the atom, the oxidation state and the hybridization of orbitals of the binding electrons. The effects of the electron configuration on the electronegativity can easily be illustrated by considering a Na-Cl bond; a bond between two elements from the 3rd period of the periodic table. Both Na and Cl have their bonding electrons in the 3rd electron shell. Also, in both elements this binding electron-pair is screened by the 1s, 2s and 2p electrons in their lower shells. However, the Cl atom has a nucleus with 6 more protons than the Na atom; as a result, the attractive force on the binding electrons in the third shell is much larger for the Cl atom than for the Na atom. As a result of this large difference in "attractive force" (the electronegativity), the Cl-atom pulls much more strongly on the electrons in the bond than the Na-atom, resulting in an ionic bond instead of a covalent bond. The screening effect of the lower orbital electrons thus has a significant impact on the electronegativity of an atom.

Based on the screening effects of the non-binding orbitals, Allred and Rochow considered that the electronegativity should be related to the effective charge of the nucleus as experienced by the electrons, rather than the absolute charge [65]. For this, they used the effective nuclear charge Z_{eff} as estimated by Slater's rules to correct the values of the electronegativity. With Slater's rules the effective nuclear charge is calculated by subtracting the shielding constant (specific for each electron configuration) from the actual nuclear charge [65]. With this effective nuclear charge they came up with a new equation for the electronegativity:

$$\chi^{AR} = \left(\frac{3590 \cdot Z_{eff}}{r_{cov}^2}\right) + 0.744 \qquad (18)$$

where r_{cov} is the covalent radius of the atom and 3590 and 0.744 are parameters they used to correct for the fact that the covalent radii at the time were inaccurate. This resulted in the Allred-Rochow scale of electronegativity. This scale of electronegativity has been used in different solid-electrolyte studies to investigate bonding natures[18,21]. Besides the electron configuration, the oxidation state and orbital hybridization have an impact on the electronegativity. Allred tried to include the effects of oxidation state in his theory of electronegativity, but was not entirely successful due to a lack of data on binding energies with different oxidation states[67]. The effect on orbital hybridization on electronegativity have been studied in extensive detail, but are less relevant for the study at hand since all PnS_4^{3-} tetrahedra are thought to utilize the same hybridized sp^3 orbitals (for more detail, see "Appendix A. – Orbital hybridization in bonding"). Given the highly oxidized nature of the Pn-atoms in the PnS_4^{3-}-anions, the Allred-Rochow scale will be used to investigate the bonding nature in the Na_3PnS_4 structures instead of the Pauling scale.

Each of the described charge metrics has specific advantages for analysing the nature of bonds between atoms. Combined with the structural data, these charge metrics provide valuable insight into the factors that determine the energy landscape of ion migration, and through that the fundamental conduction mechanism.

4.2.6 Computational setup: charge analysis computations

The charge analysis computations were performed with similar settings to those described in section 4.1.3. Contrary to those relaxations, the charge analysis runs were performed using Gaussian smearing to set the partial occupancies of the orbitals, with a smearing width of 0.05, in order to facilitate faster convergence. The Bader charges were calculated using the Bader script from the Henkelman group from Austin, Texas[62], the ELFs were visualized using VESTA[29]. Errors on the Bader and Born charges were estimated by comparing the charges on different atoms within a 2 x 2 x 2 supercell. This resulted in an estimated error on both types of charge of ~0.002. It must be noted that the exact relaxation parameters (e.g. precision settings Medium or Accurate) had a larger impact on the values of the Bader and Born charges. Therefore, the relative differences between the values of relaxations performed with the same settings were investigated in more detail than the absolute charge values.

4.3 The Nudged Elastic Band (NEB) method

To relate the structural data and charge distribution to the conduction mechanism, it is important to know what the activation barrier looks like. The Nudged Elastic Band (NEB) method is a useful tool to investigate this energy landscape between two different states of a system.

4.3.1 The basics of the Nudged Elastic Band method

NEB can be applied to a variety of systems; from investigating the energy profile of a reaction from reagents to products, to ion migration through a crystal lattice. To find the minimum energy path between two states, in order to construct an energy landscape, a first step is to simply "guess" the intermediate states that could exist. Especially when there is some understanding of what the reaction path might look like, it is fairly straightforward to construct several intermediate "guessed states" (Figure 4.6). The easiest way to construct such states is through linear interpolation between the initial and final state. In most scenarios this will prove an apt approximation to continue with, although one must ensure that the guessed states are physically possible. If for example ion migration through a lattice is studied, the linear interpolation is only a good method as long as the guessed states do not coincide with other particles in the system.

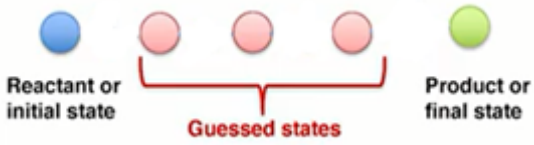

Figure 4.6. By constructing guessed states and calculating the energy of these states, the minimum energy path can be modelled. Adapted from [68]

While useful, the states guessed through linear interpolation are usually still far away from the minimum energy path. It is therefore necessary to relax the guessed states, so that they fall in the minimum energy positions along the guessed path. However, it is impossible to relax the states directly: since it is known that the initial and final states are stable states, the guessed states will likely simply fall back to either the initial or final state. It is therefore important to include a measure to prevent the guessed states from falling back to the end states. To do so, the guessed states are connected to each other with springs that keep them at fixed distance. This approach is known as the Elastic Band method, because the resulting string of states (also referred to as images) behaves similar to an elastic band (Figure 4.7).

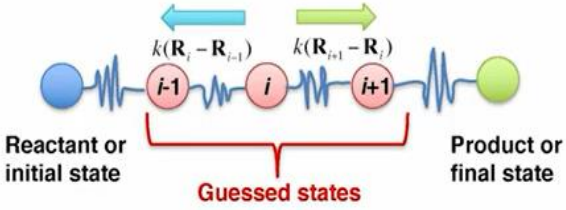

Figure 4.7. Connecting the images with strings prevents them from falling back to the initial or final state. Adapted from [68]

By adding the springs a component is added to the effective force on the ion (i)[68]:

$$\vec{F}_i^{EB} = \vec{F}_i^{potential} + \vec{F}_i^{spring} \quad (19)$$

where

$$\vec{F}_j^{spring} = k(\vec{R}_{i+1} - \vec{R}_i) - k(\vec{R}_i - \vec{R}_{i-1}) \quad (20)$$

$$\vec{F}_i^{potential} = -\nabla V(\vec{R}_i) \quad (21)$$

with k the spring constant, R the position vectors of the different images and V the potential energy landscape. By relaxing the images connected through the springs, they relax to the minimum energy path.

The Elastic Band method comes with two potential pitfalls. Firstly, if the spring constant is set too rigid, the springs will pull on the images "too strongly", causing them to cut corners in the energy path (Figure 4.8, left). Alternatively, if the spring constant is set too soft, the springs will not keep the images spaced equidistantly, causing the images to slide back down towards the end states (Figure 4.8, right).

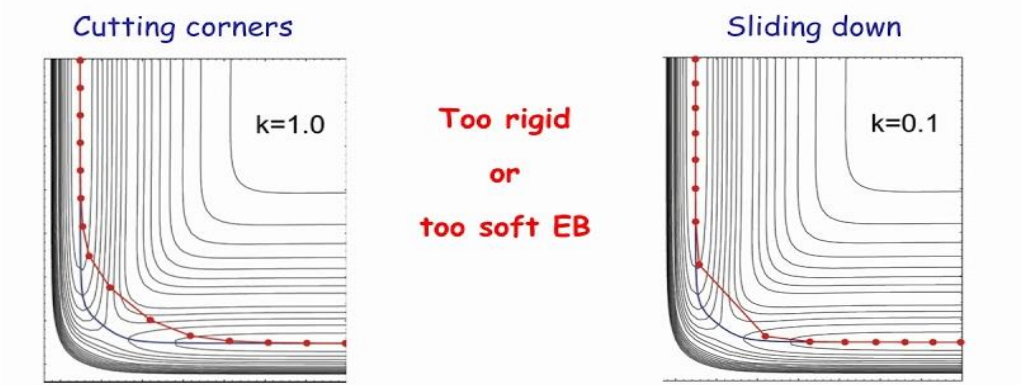

Figure 4.8. The two shortcoming from the Elastic Band method are based on a too rigid spring constant (left) or too soft spring constant (right). Adapted from [69]

Investigating the forces, we find that the cutting of corners and sliding down are the result of respectively a) the force of the spring perpendicular to the path being too high and b) the force of the potential along the spring being too strong. To solve this problem, the Nudged Elastic Band (NEB) method was developed. With the NEB method, the perpendicular component of the spring force and the parallel component of the potential energy force are projected out of the total force. Through this, the energy minimisation (now dependent on the potential force) and the image distribution (now dependent on the spring force alone) are effectively decoupled. The NEB force then becomes:

$$\vec{F}_i^{NEB} = -\nabla V(\mathbf{1} - (\vec{\tau}_i)\vec{\tau}_i) + \left(\vec{F}^{spring} \cdot \vec{\tau}_i\right)\vec{\tau}_i \qquad (22)$$

where we define the tangent:

$$\vec{\tau}_i = \frac{\vec{r}_{i+1} - \vec{r}_{i-1}}{|\vec{r}_{i+1} - \vec{r}_{i-1}|} \qquad (23)$$

The images will now relax to the point where the sum of these forces is zero (or drops below a given convergence criterion), giving an accurate estimate of the minimum energy path. The decoupling of the forces and subsequent NEB relaxation are visualised in the Figure 4.9.

In summary, the NEB method is a suitable method for finding the minimum energy path between an initial and final state. The resulting energies of the images along the path provide an insight into the energy landscape and quantify the activation barrier. How the NEB method can be applied using VASP can be found in "Appendix G. – Guideline NEB using VASP".

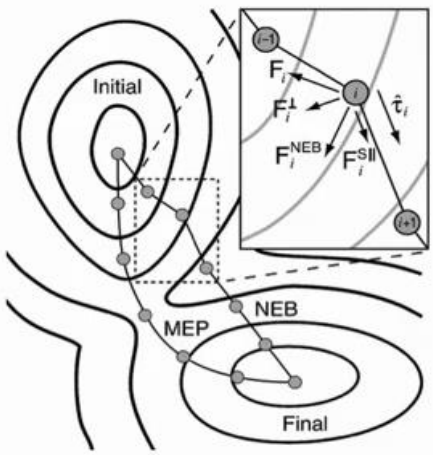

Figure 4.9. Using the NEB method, the guessed states are relaxed to the minimum energy path, with which the transition state energy can be found. Adapted from [68]

4.3.2 Computational setup: NEB calculations

The NEB calculations were performed using a 2 x 2 x 2 supercells with a single vacancy, for all three isostructural compounds. No background charge compensation or removal of different ions was done, in order to prevent interactions between the additional vacancies and the moving Na-ion. The initial and final images were relaxed using a Γ-centered k-point mesh of 1 x 1 x 1 to sample the Brillouin zone. Strict convergence criteria of 10^{-6} eV/cell in energy and $5 \cdot 10^{-3}$ eV / Å in force were adopted for the electronic and ionic loops, to ensure the initial and final states were completely relaxed before introducing the spring forces. The spring force constant was set to -5.0 eV / $Å^2$, where the negative sign sets the "nudge" algorithm. Gaussian smearing was used with a 0.05 eV smearing width. The images for the NEB run were created using the nebmake.pl script from the Henkelman group[70]; 9 images were chosen to allow for reasonable computations times, whilst ensuring an image was located in the middle of the transition path to provide an accurate estimate of the energy barrier. NEB calculations were performed for a series of applied pressures on all three isostructural compounds, in order to allow for the calculation of an activation volume. The selected pressures covered a range of -1000 MPa to 2500 MPa, with more selected pressures around 0 MPa.

The force convergence criterium for the NEB calculations (not to be confused with the relaxations of the initial and final structures) was set to 0.05 eV and the precision to accurate. This force criterium is higher than the force criteria used for the simple DFT calculations and the initial and final state relaxations. This was done because it was found that stricter criteria led to significantly longer computation times and was less strict criteria were thus necessary considering the available computational resources[b]. For getting detailed information on the charge distribution and structural changes throughout the process of hopping, DFT charge calculations were performed on each separate image of the relaxed NEB runs (at P = 0 MPa). These relaxations were performed with the same settings as the relaxations of the initial and final states of the NEB calculations, without ionic steps.

[b] To check for the effects of the force convergence criteria on the outcomes of the relaxations, NEB calculations with stricter force convergence criteria (0.02 eV) were performed on the Na_3PS_4, Na_3AsS_4 and Na_3SbS_4 supercells with 0 applied pressure. This showed that while the calculated activation energies changed with ~16 meV (~20% change), the relative differences between the isostructures remained nearly the same. In a further investigation, it was found that the calculated values of the activation energies also changed significantly with the precision settings of the relaxations, with a difference of ~12 meV (~15% change) between the medium and accurate precision. It must therefore be noted that also for the activation energies, the relative difference between the isostructures was paid more attention than the absolute values of the activation energies.

5. Results - The Na_3PnS_4 structures and conduction bottlenecks

In this study, we compare the Na_3PnS_4 (Pn = P, As, Sb) isostructural compounds through computation and experiment. For the computational work we compare relaxations of the cubic polymorphs of the materials (space group $I\bar{4}3m$). The experimental work is performed on the ground-state tetragonal structures (space group $P\bar{4}2_1c$), prepared by high-temperature solid-state synthesis.

To improve our understanding of the conduction mechanism, we first investigate the static structures of the three materials (through X-Ray diffraction (XRD) and density functional theory (DFT)) (this chapter). Subsequently, we analyse several static (Bader charges, ELF) and dynamic (melting points, bulk moduli and Born Effective Charges) influences on the lattice, to get a thorough understanding of the bonding interactions in the structure (chapter 6). Then, we quantify the conduction process through the activation barrier (using with the Nudged Elastic Band method (NEB)) and relate these to the structural characteristics and the bonding interactions. We combine this with a more thorough investigation of the structural changes during the ion-migration process, through DFT charge calculations on the separate images of NEB runs and NEB calculations of the structures at different pressure (chapter 7). Finally, we evaluate the macroscopic conductivity through electrochemical impedance spectroscopy, and quantify the effects of temperature and pressure on the conductivity with the experimental activation energy and volume (chapter 8).

5.1 XRD Measurements of the Na_3PnS_4 samples

To determine the ionic conductivity of the samples made in this work, it is necessary to know the purity of the synthesized materials. For the structural characterisation of the samples, XRD measurements were performed. All diffractograms were analysed with Rietveld refinements; the results and extracted structural parameters can be found in "Appendix D. – Fit Parameters".

5.1.1 Na_3PS_4 Diffractogram

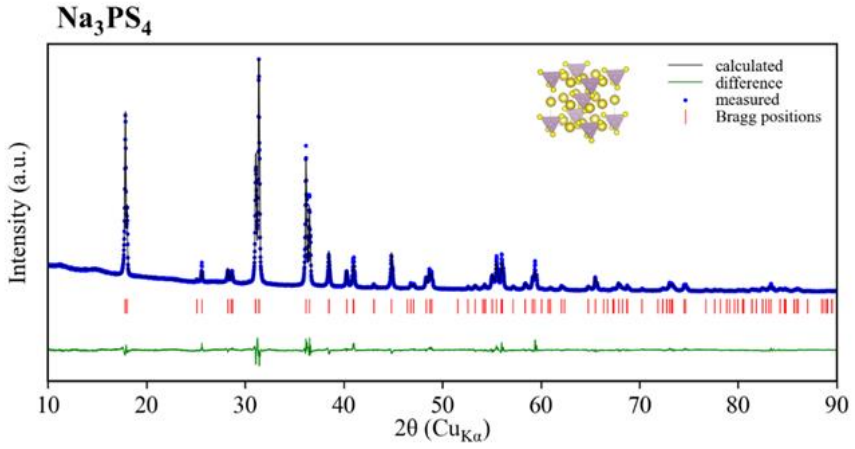

Figure 5.1. Diffractogram of the Na_3PS_4 sample. Bragg positions of the $\mathbf{P\bar{4}2_1c}$ space-group are included for reference.

The Na_3PS_4 diffractogram revealed no observable crystalline contaminations. The determined lattice parameters (a = 6.953(7) Å, c = 7.087(9) Å) are very close to those from other studies (e.g. Pompe[38] found values of a = 6.952(0) Å, c = 7.075(7) Å).

5.1.2 *Na_3AsS_4 Diffractogram*

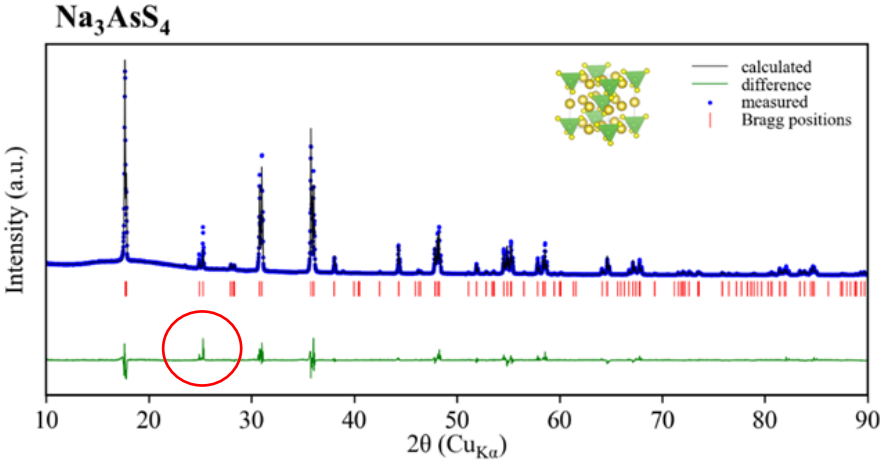

Figure 5.2. Diffractogram of the Na_3AsS_4 sample. Bragg positions of the $\mathbf{P\bar{4}2_1c}$ space-group are included for reference. The refinement of the atomic positions resulted in a negative value for the atomic displacement factor U(iso) of the As atom. Both with the negative value of U(iso) and with a fixed U(iso) of 0.016, the diffractogram showed missing intensity on specific peaks (e.g., red circle).

The refinement of the Na_3AsS_4 sample showed no significant contaminations; unidentified trace contaminations of <0.1% of the max intensity could be noticed on close inspection. The found lattice parameters are in agreement with reported values in literature, although seemingly slightly larger (<0.05%): a = 7.040(8) Å, c = 7.141(7) Å compared to a = 7.038(9) Å, c = 7.0138(5) Å as reported by Pompe[38]. During the refinement process the initial fits resulted in a negative value for the atomic displacement factor U(iso). To correct for this, the refinement was attempted with a fixed U(iso) of 0.016, selected as representative value based on the U(iso) values of the Na_3PS_4 and Na_3SbS_4 samples (respectively 0.0164 and 0.0162). The final refinement however was very similar to the fit with the negative U(iso), with no observable changes to the difference plot and goodness of fit parameters.

Compared to the LeBail fit, the final Rietveld refinement showed significant missing intensity on specific peaks. This can be seen in the diffractogram at for example 2θ ~25°, circled in red. Because this deviation was not present in the LeBail fit, we expect that this missing intensity in the Rietveld refinement could be related to the strange fitting of atomic displacement factor of the As atom. One possible explanation is that this strange refinement could have to do with the modelled ionic radius of the As-atom: in the Jana2006 software used for the refinements, the ionic radius of As used is 1.21 Å. The reported value for the Shannon radius of As in the 5^+ oxidation state (IV coordination) is significantly smaller: 0.335 Å [71]. Quick investigation of diffractograms of other synthesized Na_3AsS_4 samples showed similar attributes. Whilst deserving of further investigation, we did not have any indication that the strange behaviour of the refinements of the As U(iso) was related to potential contaminations in the sample. Since the purity of the sample seemed sufficient, the Na_3AsS_4 sample was used for further characterisation (impedance spectroscopy). Nonetheless, when comparing the crystal structures of the Na_3PnS_4 structures as determined through XRD, the potential inaccuracy of the atomic positions in the Na_3AsS_4 has to be taken into account.

5.1.3 Na_3SbS_4 Diffractogram

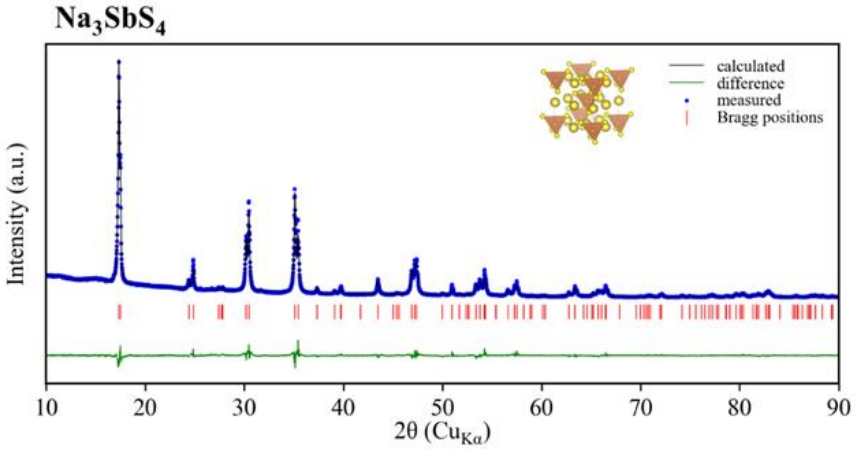

Figure 5.3. Diffractogram of the Na3SbS4 sample synthesized using metallic Sb and elemental S as reagents. Bragg positions of the $\mathbf{P\bar{4}2_1c}$ space-group are included for reference.

Two different synthesis recipes were used to make the Na_3SbS_4 samples in this study. In the first recipe an intermediate synthesis step was used where Stibnite (Sb_2S_3) was made from metallic Sb and elemental S, before further mixing with Na_2S and S to make Na_3SbS_4. The diffractogram of this sample (shown in "Appendix C. – Additional Figures Data Analysis") revealed a significant amount of another phase was present. Upon further investigation this phase was identified as Na_3SbS_3, estimated to be approximately 1% (rough estimation based on comparing peak intensities). The presence of Na_3SbS_3 in the sample suggests a sulphur deficit during synthesis: reaction energies calculated using DFT show that there are only very small differences between the energies of Na_3SbS_4 and that of Na_3SbS_3 + S [30]. The second recipe used in this work combined stoichiometric amounts of Na_2S, metallic Sb and elemental S in a single step. This recipe resulted in a pure Na_3SbS_4 sample whose diffractogram is shown in Figure 5.3. It is possible that because only a single synthesis step occurred during this synthesis, less sulphur loss occurred throughout the entire synthesis process. The found lattice parameters (a = 7.167(6) Å, c = 7.299(3) Å) were in good agreement with literature (a = 7.164(0) Å, c = 7.292(7) Å[38]). Since no observable contaminations were present, this sample was used for the further characterisation of the properties of Na_3SbS_4.

5.2 Investigating the structural differences through DFT geometry optimizations

To investigate the different structural properties and bottleneck sizes in the Na_3PnS_4 structures, DFT geometry optimizations were performed. The cubic structure of Na_3PS_4, illustrative for the crystal lattices of the Na_3PnS_4 structures, is shown in Figure 5.4.

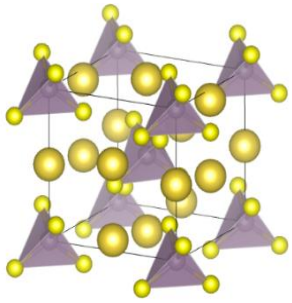

Figure 5.4. The cubic structure of Na_3PS_4 as used as input of the DFT calculations (gold: Na, purple: P, yellow: S).

Comparing the different isostructural compounds, we can see that the lattice parameters and cell volumes increase monotonically with the Pn substitution P → As → Sb, with cell volumes of respectively 332.49, 342.28 and 358.50 Å^3. This is not unexpected; if the size of the central atom increases, it is logical that the sizes of the PnS_4^{3-}-tetrahedra and unit cell also increase. In the simplest approach, this expanded lattice should allow for a larger bottleneck of ion migration and therefore easier conduction.

Assuming easier ion conduction purely based on lattice expansion would however be an oversimplification: the effects of the lattice expansion on the conduction pathway are directly dependent on how the tetrahedral expansion causes the cell volume to expand and subsequently on how this changes the conduction bottleneck. To investigate to what extent the changes in interatomic distances and cell volume are a result of the volumetric expansion of the tetrahedron, it is important to accurately define the PnS_4^{3-} tetrahedral volume.

Based on a geometrical approach, it is possible to define the tetrahedral volume as a shape enclosed by the four sulphur atoms at the corners of the PnS_4^{3-}-tetrahedron. With this definition, the tetrahedral volume can be calculated using

$$\boldsymbol{V_{ABCD} = \frac{1}{6}(\overline{AB} \times \overline{AC}) \cdot \overline{AD} = \frac{1}{6}\begin{vmatrix} X_B - X_A & Y_B - Y_A & Z_B - Z_A \\ X_C - X_A & Y_C - Y_A & Z_C - Z_A \\ X_D - X_A & Y_D - Y_A & Z_D - Z_A \end{vmatrix}} \quad (24)$$

where V_{ABCD} is the tetrahedral volume and X, Y and Z are the Cartesian coordinates of the respective atoms A, B, C and D. The tetrahedral volumes calculated using this method are listed in

Table 5.1. However, this approach does not take into account the ionic radius of the S-atoms on the corners of the tetrahedron. As such, a different proposed method for describing the tetrahedral volume is by defining an average ionic radius of the tetrahedron, using

$$\boldsymbol{R_{mean} = \left(\frac{1 \cdot r_{Pn} + 4 \cdot r_S}{5}\right)} \quad (25)$$

with R_{mean} the average ionic radius and r_{Pn} and r_S the ionic radii of the pnictogens and sulphur atoms. For this calculation, the listed Shannon radii of S^{2-} (1.84 Å), P^{5+} (0.17 Å in IV coordination) and As^{5+} (0.335 in IV coordination) were used[71]. Since for Sb^{5+} no ionic radius in an IV coordination is reported in literature, the Sb^{5+} radius was estimated by comparing the Sb-S bond length (2.335 Å) to the S^{2-} radius, resulting in a ionic radius of 0.495 Å for Sb^{5+}. With these radii, the average ionic radii of the PnS_4^{3-} tetrahedra were determined to be 1.506 Å, 1.539 Å and 1.571 Å for the P, As and Sb structures respectively.

While the increased PnS_4^{3-}-anion size as a result of the Pn substitution can be expressed through these two metrics, it does not directly relate the substitution to the structural changes in the whole crystal. It was noted recently by Till[17] (submitted) that for substitution in the $PnCh_4^{3-}$ tetrahedra in Na_3PnCh_4 (Pn = P, Sb; Ch = S, Se), the expansion of the lattice as a result of the substitutions was accompanied by a change in the S-coordination of the Na-sites (Figure 5.5). The S-coordination of the Na-sites can be described as an eight-coordination, with four S-atoms located at a shorter distance (referred to as Na-S-1) and four S-atoms located at a longer distance (referred to as Na-S-2).

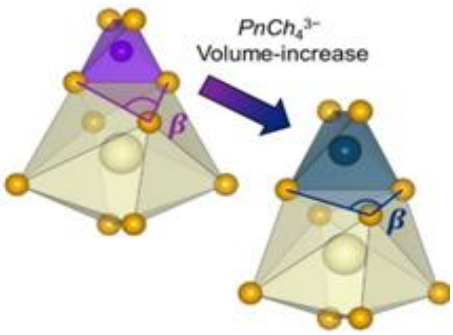

Figure 5.5. Illustration showing how the increase of a $PnCh_4^{3-}$ tetrahedron can cause a change in coordination environment of a Na-site. This can best be seen by the change in the angle $\boldsymbol{\beta}$ between different S-atoms surrounding the Na-site. Adapted from [17]

By comparing the Na_3PnS_4 structures, we found that as a result of the Pn substitution the Na-S-1 increases monotonically, but that the Na-S-2 actually decreases with the Pn substitution P → As → Sb (see "Appendix C. – Additional Figures Data Analysis").

It thus seems that comparable to the findings of Till the coordination environment around the Na-site changes as a result of the increased PnS_4^{3-} tetrahedral volume, resulting in smaller differences between the short and long Na-S distances in the octahedral Na-site. This change in coordination environment must be considered when evaluating the effects of the tetrahedral volume increase on the conduction pathway.

The tetrahedral volume and average ionic radius are plotted against the cell volume in Figure 5.6, to evaluate to what extent the expansion of the cell volume can be explained based on these changes in the PnS_4^{3-} tetrahedral volume. It can be seen that the cell volume increases linearly with both descriptors of the PnS_4^{3-} tetrahedral volume. As such, based on these structural elements, there is no indication that the expanded cell volume is caused by something other than the volumetric expansion of the PnS_4^{3-} tetrahedra.

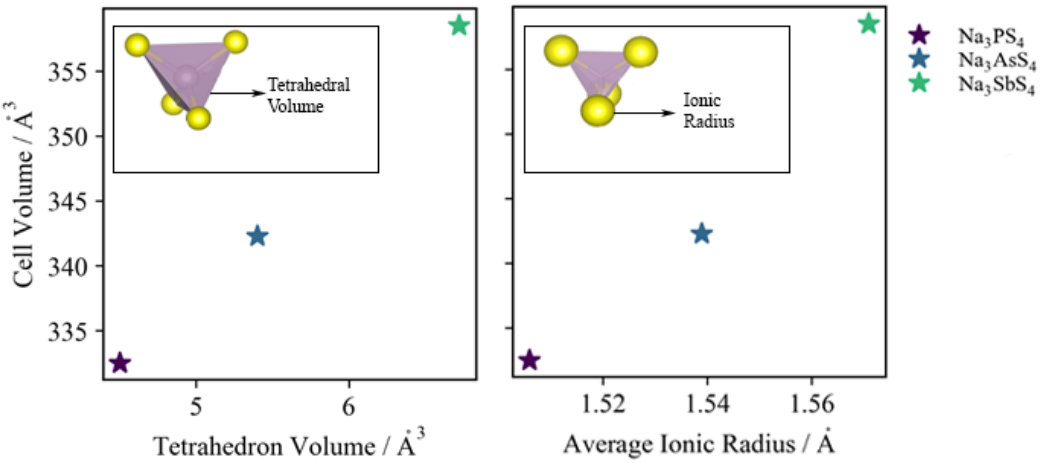

Figure 5.6. The cell volume of the three isostructural compounds versus the tetrahedron volume (left) and the average ionic radius (right). The cell volume increases monotonically with both descriptors, indicating that the increased cell volume is primarily caused by a volumetric expansion of the PnS_4^{3-} tetrahedra.

5.3 Describing the bottleneck of the conduction pathway

These findings do however not mean that the conduction bottleneck also scales monotonically with the cell volume. From our analysis of the Na-S-1 and Na-S-2 distances we find that the β angle increases with the P → As → Sb substitution, indicating that the coordination environment of the conduction pathway is altered. To see whether the substitution has effects on the conduction mechanism through structural changes, it is therefore important to investigate what happens to the bottleneck of the conduction pathway. Two descriptors of the bottleneck for the Na_3PnS_4 structures are the distance between the S-atoms that coordinate the bottleneck (referred to as the Ch-Ch distance, since this distance is characteristic in all members of the Na_3PnCh_4 family (Pn = P, As, Sb and Ch = S, Se)) and the volume enclosed by these same S-atoms (referred to as the Ch_4 volume)[17]. It has been found in literature that changes to the bottleneck can have a large impact on the coordination environment during conduction, and as such are key to understanding the fundamental conduction mechanism[33,34].

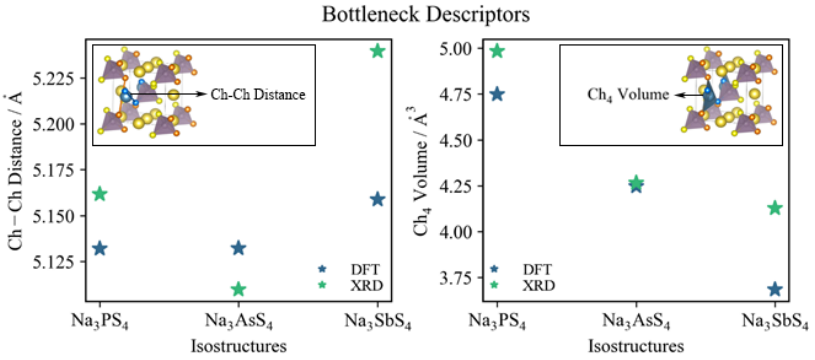

Figure 5.7. The structural descriptors of the bottleneck of conduction in the Na_3PnS_4, the Ch-Ch distance and Ch_4 volume. The values from the DFT computations and XRD measurements are compared: while slightly different, both show a clear deviation from the monotonic trend for the Ch-Ch distance.

When analysing the bottleneck descriptors, we see that the Ch-Ch distance deviates from the monotonic trend observed in the other structural descriptors (such as the cell volume) for both the DFT results and the XRD measurements (Figure 5.7, left). While the differences in the Ch-Ch distances do not relate monotonically to the conductivities in literature (Na_3PS_4 0.2 mS / cm (ref [8]), Na_3AsS_4 0.027 mS/cm (ref [8]) and Na_3SbS_4 1.05 mS / cm (ref [22])), they do provide an initial insight: we see that the Ch-Ch distance is approximately the same for the Na_3PS_4 and Na_3AsS_4 structures (DFT), while the cell volume of the latter is 3.1% larger. This would indicate that if a difference in the Na-S bonding strength exists between the isostructural compounds, this would have a direct impact on the conduction mechanism, since these differences would not be compensated by differences in the Na-S distance in the bottleneck.

When looking at the Ch_4 volumes (Figure 5.7, right), we do observe a monotonic trend (P → As → Sb). As such, the Ch_4 volume seems to provide little insight into why the ionic conductivities do not scale monotonically with cell volume. Contrary to the cell volume however, the Ch_4 volume decreases with increasing Pn-size. This decrease can be related to the changes in the different Na-S-1 and Na-S-2 distances and the coordination environment of the Na-sites. We see that as the size of the Pn atom increases, the difference between Na-S-1 and Na-S-2 becomes smaller. Close inspection of the eight-S-coordination of the Na-site shows that the Ch_4 volume depends on the differences between the Na-S-1 and Na-S-2 distances, thus explaining the decrease in the Ch_4 volume with the Pn substitution.

The bottleneck descriptors as determined with XRD show slightly different trends from the values obtained through DFT. It must be noted however, that a direct comparison between the DFT and XRD results is not possible, since the DFT calculations are performed at 0K and the XRD measurements at 298K. Furthermore, it must be noted that the DFT results were obtained based on the cubic structures whereas the XRD measurements were performed on the tetragonal structures. Evaluating the tetragonal distortion of the structures (c / a ratio) we see that the distortion of the Na_3AsS_4 structure deviates from the other two isostructural compounds, with a factor of 0.5%. When calculating the relative difference in Ch-Ch distances between the DFT and XRD measurements between the Na_3PS_4 and Na_3AsS_4 we notice that this change, from cubic to tetragonal structure, is also 0.5%. It is thus not unlikely that the differences in Ch-Ch distance and Ch_4 volume trends (P → As → Sb) between the DFT and XRD results are indeed the result of the different tetragonal distortions of the structures.

5.4 Summary: the static influences on the conduction pathway

From the results of our XRD measurements we can conclude that (nearly) pure phases of all three materials were obtained. It was found that for the synthesis of Na_3SbS_4, the synthesis recipe without the intermediate step of making Sb_2S_3 yielded better results, possibly due to less loss of sulphur in the synthesis process. To investigate the conductive properties of the materials, these samples must be further characterized using electrochemical impedance spectroscopy.

When investigating the structural differences between the isostructural compounds (summarized in Table 5.1), it was found that the expansion of the cell volume with increasing pnictogen size is likely a direct result of the increased PnS_4^{3-} tetrahedral volume, based on the observed monotonic relation between the cell volume and the tetrahedral volume and average ionic radius.

The descriptors of the bottleneck size used in this work, the Ch-Ch distance and the Ch_4 volume, showed no monotonic relation with the trend in ionic conductivities observed in literature. However, it was noted that the Ch-Ch distance remained constant for the P → As substitution (DFT) and even showed a lower value for Na_3AsS_4 than for the Na_3PS_4 and Na_3SbS_4 structures in the XRD results, despite the increase in cell volume associated with the substitution. This would indicate that if a difference in the Na-S bonding strength exists between the isostructural compounds, this would have a direct impact on the conduction mechanism, since these differences would not be compensated by differences in the Na-S distance in the bottleneck.

So, a purely structural evaluation of the $NaPnS_4$ isostructural compounds was found to be insufficient to explain the so far reported differences in ionic conductivities between the structures. It is therefore important to investigate the dynamic lattice influences of the structures, to get a better understanding of the possible differences in the bonding interactions between the atoms and subsequently the effects on the energy landscape of ion migration.

Table 5.1. The structural characteristics of the Na_3PnS_4 structures; comparison between the structural data retrieved from DFT calculations (simply geometry optimization) and structural data from the Rietveld Refinements of the XRD measurements.

Isostructure	**Na_3PS_4**		**Na_3AsS_4**		**Na_3SbS_4**	
	DFT	XRD	DFT	XRD	DFT	XRD
Space group	$I\bar{4}3m$	$P\bar{4}2_1c$	$I\bar{4}3m$	$P\bar{4}2_1c$	$I\bar{4}3m$	$P\bar{4}2_1c$
a / Å	6.9277	6.9537	6.9951	7.0408	7.1039	7.1640
c / Å	-	7.0879	-	7.1417	-	7.2927
c / a ratio	-	1.019	-	1.014	-	1.018
Cell Volume / Å^3	332.49	342.73	342.28	354.03	358.50	374.28
Ch-Ch Distance / Å	5.1321	5.1616	5.1320	5.1096	5.1587	5.2394
Ch_4 Volume/ Å^3	4.7495	4.9831	4.2478	4.2658	3.6832	4.1287
PnS_4^{3-} Anion Volume / Å^3	4.5058	4.5216	5.4030	5.5416	6.7240	6.5948
PnS_4-Anion Average Ionic Radius / Å	1.506		1.539		1.571	

6. Results - Investigating bonding in Na_3PnS_4 through static and dynamic influences

To investigate the dynamic influences on the conduction process, we report findings on several different indicators of the lattice dynamics and stiffness. Together with the described structural differences, we use these indicators to identify the nature of bonds within the Na_3PnS_4 structures, to shed more light on the fundamental conduction mechanism.

6.1 Bulk Moduli

The bulk modulus of a material (*B*) is a macroscopic measure for its resistance against compression. Since it is directly influenced by all force constants present in the structure, it is also a measure of the stiffness of the lattice. To determine the bulk moduli of the Na_3PnS_4 structures DFT relaxations at different pressures were performed. Relaxations were performed using the PSTRESS method to apply isostatic pressure on the unit cell during relaxation; for the analysis a pressure range of 36 pressures between -2.5 GPa to 5 GPa was considered. Applying a negative pressure is not a realistic manipulation of the structure (since applying such large tensile stresses would be physically (nearly) impossible to achieve) but can still provide insight into how the structure would evolve if the lattice expanded. The energies and cell volumes calculated in the relaxations were plotted against the pressure and fitted to the Birch-Murnaghan equations of state[51] (see "Appendix D. – Fit Parameters" for details of the fit). The relation between the cell volumes and the applied pressures can be seen in Figure 6.1. For the final fitting only the pressures in the range of -1 GPa to 1 GPa were taken into account, to prevent biasing as a result of extreme values. As can be seen from the figure however, even the more extreme pressures fall on the fitted line. The bulk moduli of the isostructural compounds were found to decrease monotonically with Pn substitution: for Na_3PS_4, Na_3AsS_4 and Na_3SbS_4 respectively 26.55, 25.65 and 24.72 GPa. The fit and plot of the energy-volume relation were in good agreement with the ones obtained through the pressure-volume relation can be found in "Appendix C. – Additional Figures Data Analysis".

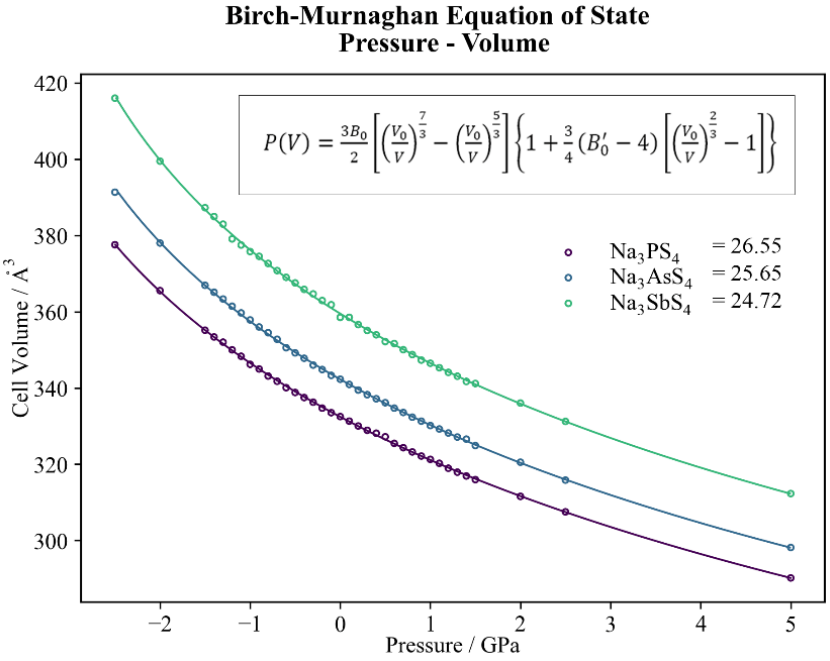

Figure 6.1. Pressure-volume plot and fit of the different DFT relaxations under pressure for the three isostructural compounds. The Birch-Murnaghan equation of state shows the relation between the applied pressure and resulting volume change.

The decreasing trend in bulk moduli for P → As → Sb indicates that the lattice becomes softer with the Pn substitution, resulting in higher compressibility. To see whether any interesting structural changes under pressure could be noticed, the different interatomic distances (the Na-S-1, Na-S-2, Pn-S and Na-Pn distances) were also evaluated. For both the tensile and compressive pressures, no deviations from isotropic expansion / compression (as set by the bulk modulus) could be noticed for any of these bond lengths. When investigating the bottleneck distances, a similar isotropic expansion / compression was observed. Noteworthy, it could be seen that the Ch-Ch bottleneck distances of $NaPS_4$ and $NaAsS_4$ were not only the same for 0 MPa, but that this behaviour held for both tensile and compressive pressures (see "Appendix C. – Additional Figures Data Analysis").

Although the monotonic trend in the bulk moduli does not directly offer an explanation for the non-monotonic trend in conductivities, it matches the monotonic changes in cell volume and lattice parameters. A challenge with interpreting the relation between the bulk modulus and the lattice stiffness is that the bulk modulus depends on all bond strengths and forces within the structure. It is therefore not possible to draw conclusions on how pressure affects specific bond strengths (e.g., the Na-S bond, which is the most related to Na-ion migration) based on the bulk modulus alone: for that more specific information on the bonding energy or specific interatomic forces is required.

6.2 Melting Point

A different indicator of the stiffness of the crystalline lattice is the melting point. The melting process is directly connected to the forces acting on the different ions in the structure: the Lindemann criterion describes that a solid melts when the vibrational amplitudes of the relevant ions become so large that they interfere with the neighbouring atoms. As a result, the thermally excited vibrations destabilize the lattice[46]. These vibrations are directly connected to the binding strength between the ions: the stronger the binding, the stiffer the lattice and the higher the melting point[47].

While the melting points of the Na_3PnS_4 structures have been studied before[17,27,38,25,33], initial melting tests of our synthesized samples showed that the only reported melting point for Na_3AsS_4 of 490 °C (ref [33]) was likely inaccurate. To investigate the melting point pellets of Na_3AsS_4 of a 10 mm diameter and 10 mm in height were made and sealed into silica ampoules. Upon heating of the ampoules from 300 °C to 750 °C, in steps of 50 °C whilst leaving the samples for 1 hour at each step, no melting of the compound was observed until a temperature of 650 °C was reached. These initial findings on the melting point of Na_3AsS_4 are reminiscent of earlier contradictions in the reported melting point of Na_3PS_4: for years it was thought that the melting point of Na_3PS_4 was around 500 °C, until a recent study[24] showed with temperature dependent XRD and DSC measurements that at this temperature a first-order phase transition (beta → gamma) occurred instead of melting. Through comparisons with the melting of the sample sealed in silica ampoules they established the actual melting point of Na_3PS_4 at 765 °C. In a similar set-up the melting point of Na_3SbS_4 was also investigated: for this structure however, no "gamma" phase was observed, and found the melting point was to be at 621 °C.

To further investigate the melting point of Na_3AsS_4, DSC measurements were performed. The resulting thermogram, as well as the thermograms of Famprikis on his Na_3PS_4 and Na_3SbS_4 samples measured in the same setup, are shown in "Appendix B. – DSC Thermograms".

In the Na_3AsS_4 thermogram a small event could be observed with an onset temperature of 506 °C. It is possible that Pompe[33], the only other author who reported on the Na_3AsS_4 melting point to our knowledge, observed this event in his DSC measurements and ascribed it to the melting process. Next to the small even at 506 °C, a much more energetic event was observed at 636 °C. It is likely that this event was the result of the melting of the sample, based on the energy associated with the event and the match of the temperature with our initial melting tests. The nature of the event at 506 °C is at the moment of writing still unknown. Drawing a comparison with the Na_3PS_4 structure, the event could be indicative of a similar beta → gamma transition, but further investigation of the thermal behaviour of Na_3AsS_4 is needed [c].

With the newly determined melting point of Na_3AsS_4, it becomes clear that the melting points of the Na_3PnS_4 structures do not follow a monotonic trend. Based on the relation between lattice stiffness and melting point, the results indicate that the lattice of the Na_3PS_4 structure is more rigid than that of the Na_3AsS_4 and Na_3SbS_4 structures. It is difficult to say what the role of the existence of an additional gamma-phase in the Na_3PS_4 structure (and perhaps the Na_3AsS_4 structure) in this trend is. The nature of the gamma-phase, which is described as plastic-crystal-like, where the Na-ions move freely through the PS_4-framework, gives a small indication that the PS_4-framework could play a larger role in the melting point than the Na-S bonds. Investigating the bond dissociation energies of the P-S, As-S and Sb-S bonds we observe a trend very similar to that of the melting points: the P-S bond has a much higher dissociation energy (442 ± 10) than the As-S (379.5 ± 6.3) and Sb-S (378.7 ± ?) bonds[72]. This trend supports the reasoning that the PnS_4^{3-}-framework plays a large role in setting the melting point and as such the lattice stiffness.

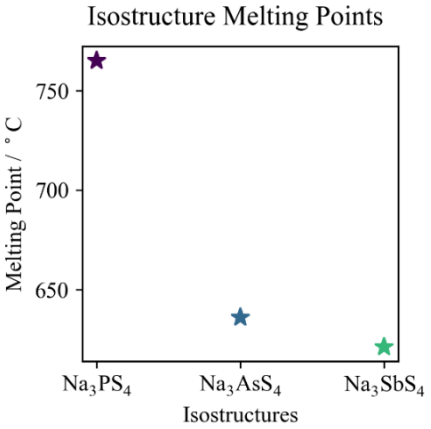

Figure 6.2. The melting points of the different isostructures: the trend of decreasing melting point suggest softer lattices for the Na_3AsS_4 and Na_3SbS_4 structures.

6.3 Electronegativity

To investigate the bonding nature in the PnS_4^{3-} tetrahedra, and through that the Na-S bonding nature, it is necessary to take a close look at the Pn-S bonds. One of the most commonly used indicators of bond nature and strength is the electronegativity. The charge distribution in the bond is in the end what determines the type of bond between two atoms. When both atoms have the same electronegativity, both atoms pull equally on the electrons in the bond: in this way a covalent bond is formed. When atoms differ in electronegativity, the electrons in the bond will be slightly shifted towards the atom with the higher electronegativity, resulting in what is known as a polar bond. When the differences in electronegativity become so large that one atom actually becomes ionized, and the electron is transferred from one atom to the other, we consider it an ionic bond. Fundamentally, there is nothing different in the interaction for the three bonds: all forces are the result of electrostatic interactions. However, the exact charge distribution, so how the electrons are shared, has a large impact on the forces: in bonding theory, covalent bonds are generally considered to be strongest and ionic bonds weakest. This is the result of the large attractive forces of the nuclei on the shared electron pair in the covalent bond.

[c] While such a gamma phase would be very interesting from the perspective of ion-dynamics, it is beyond the scope of this work and will have to be studied further in future research.

Perhaps the most commonly used scale of electronegativity is the Pauling scale. This scale is defined on the basis that the binding energy between two different atoms, A and B, is larger than that of the average of the homopolar bonds A-A and B-B. By comparing the electronegativities of two different elements, the nature of a bond can be estimated: according to Pauling's ionic bonding criterium, bonds with a difference in electronegativity smaller than 1.7 are covalent in nature, where values between 0.4 and 1.7 indicate polar covalent bonding. One large disadvantage of the Pauling scale however, is that it does not take the effects of electron shielding into account. As a result, the values of the electronegativity on Pauling scale can be inaccurate for atoms in an oxidized state. To correct for the effects of electron shielding, Allred and Rochow developed a new scale of electronegativity, where the effective nuclear charge is used to correct for the shielding effects by the inner electron shells[65]. Since the ions in consideration in the Na_3PnS_4 structures are in an oxidized state, especially the Pn^{5+} ions, the Allred-Rochow scale is more appropriate for analysing bonding strength in Na_3PnS_4. This scale is also the one that has been used to estimate bonding effects in the LGPS solid-state electrolyte[21]. When comparing the electronegativity values of the two scales, it can indeed be noticed that mainly the values for the Pn atoms are significantly different (Figure 6.3). Since it is exactly the substitution of this atom (in oxidized state) that we are interested in, the Allred-Rochow scale is more suited for analysing the bonding nature in the PnS_4^{3-}-anions.

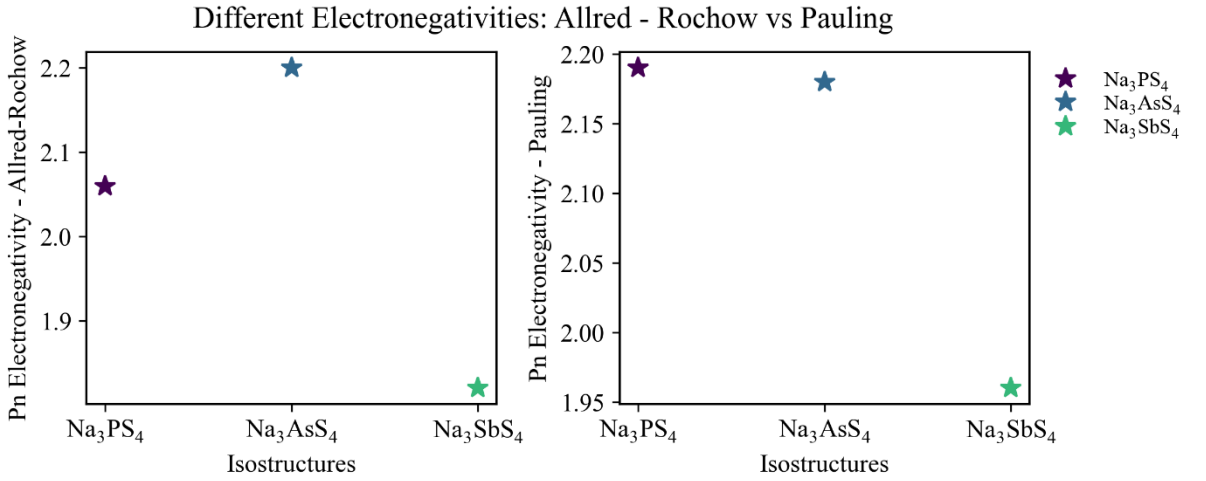

Figure 6.3. Side by side comparison of the electronegativity of the Pn atoms in the Na_3PnS_4 structures of the Allred-Rochow and Pauling scales.

Comparing the Pn electronegativities, we notice the trend is not monotonic for either scale. In fact, the trend in Allred-Rochow electronegativities seems similar to that of the ionic conductivities as reported in literature (where $Na_3AsS_4 < Na_3PS_4 < Na_3SbS_4$). To relate the Pn electronegativities to the bonding in the structure, we compare the values to those of the S-atoms (2.44), in order to investigate the Pn-S bond nature. Although for the Allred-Rochow scale no unique bonding criteria were established, it is safe to assume that since the difference in electronegativity between the pnictogen and the sulphur atoms are all < 0.7, all three bonds can be considered covalent in nature. The P-S and As-S bonds would be classified as non-polar covalent bonds using both scales, whereas the Sb-S bond would be classified as polar covalent bond on both. Following the reasoning "more covalent = stronger", when using the difference in electronegativity as a measure for bond strength we would expect the As-S bond to be strongest, followed by the P-S bond and then the Sb-S bond. A study on the effects of substitutions in the GeS_4-anion in LGPS report similar findings: they find that the larger

difference in electronegativity between Sn (1.7) and S (2.44) results in weaker bonding than between Ge (2.0) and S (2.44). There is an important difference however: in their study on LGPS, Krauskopf et al relate the weaker intramolecular bonding in the SnS_4-anions to a larger negative charge on the S-ions, which in turn leads to a stronger Li-S bond and therefore lower ionic conductivity (Figure 6.4). While nothing can be said yet about a potentially shifted charge distribution in the PnS_4^{3-}-anions, the opposite relation between the bond polarity and the trend in conductivities is observed for the Na_3PnS_4 structures. Furthermore, the trend of "stronger bonding" as a result of the smaller differences in electronegativity seemingly contradicts recent findings on the stretching force constants (calculated using DFT) of the As-S and P-S bonds, where the stretching force constant of the P-S bond was found to be higher than that of the As-S bond[8].

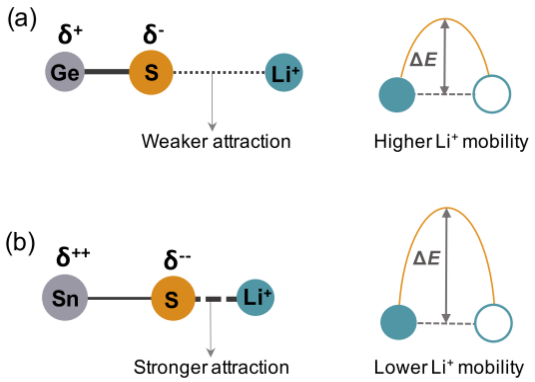

Figure 6.4. The changed bonding interaction in the $Ge_xSn_{1-x}S_4$ tetrahedra in LGPS: the less more polar Sn-S bond results in a more negative S-ions, which causes a stronger Li-S bonding interaction and therefore a lower Li^+ mobility. Adapted from [16].

To find an explanation for these different findings, we consider two different qualities of the Pn-S bonds: their stiffness and their polarity. The polarity of the bond can be assessed using the electronegativity. If the difference in electronegativity becomes larger, the resulting shift in the charge distribution also becomes larger. The stiffness in turn is more directly related to the nature of the bonding electrons and the vibrational properties of the bond. If the valence electrons that participate in bonding have a more core-like nature (e.g., the 3p electrons of the P-atom compared to the 4p electrons of the As-atoms), the resulting bond will be "stronger" in the sense that it is less easily deformed (since the core-like electrons are more tightly bound to the nucleus). As a measure of how rigid the bonds / lattice are, this bond stiffness can be related to the bond dissociation energy and melting points. For the $NaPnS_4$ structures we then indeed observe that the P-S bond are strongest, in line with findings on the stretching force constants. Investigating the bond stiffness through the vibrational modes of the bond (as determined through Raman spectroscopy by Pompe[38], see Figure 6.5), we observe that the characteristic frequency of symmetric stretching of the P-S bond (ν_1 = 411 cm^{-1}) is significantly higher than that of the As-S bond (ν_1 = 376 cm^{-1}) and Sb-S bond (ν_1 = 367 cm^{-1}). This is in line with our reasoning that the P-S bond is more rigid than the As-S and Sb-S bonds and the observed trend closely resembles that of other indicators of the stiffness of the Pn-S bond.

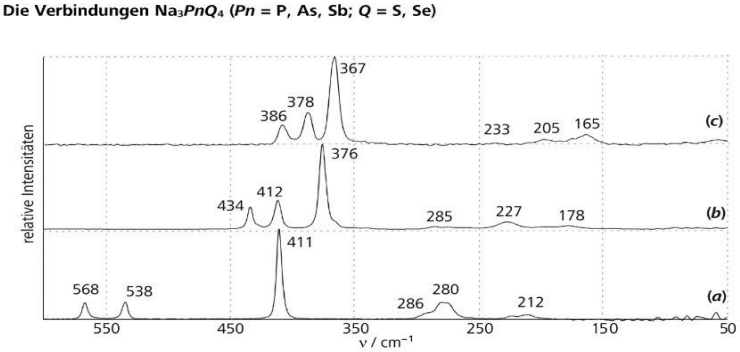

Figure 6.5. The Raman spectra of the tetragonal polymorphs show a systematic redshift for the order (a) Na_3PS_4, (b) Na_3AsS_4 and (c) Na_3SbS_4. The largest peak is attributed to the Pn-S stretching vibrational mode.

Turning back towards bond polarity, we observe that contrary to the bond stiffness the bond polarity follows the trend As-S < P-S < Sb-S. Since this bond polarity is directly related to the charge on the S-atoms (which influences the Na-S bond), it seems logical that the bond polarity correlates more strongly with the reported ionic conductivities than the bond stiffness. It also seems however that in the covalent limit (difference in electronegativity < 0.4, as for the Pn-S bonds), the qualification that "more covalent bonding = stronger" might not hold. Nevertheless, the question that still remains is why the ionic conductivities of the Na_3PnS_4 structures seem to increase with Pn-S bond polarity, whereas for the LGPS substitution the ionic conductivity decreased with the more polar bonds. These findings indicate that the relation between the bonding interactions in the structure and the conductivity cannot be captures by structural characteristics or bonding interactions alone. To gain more insight into this relation and move from the Pn-S bonding interaction to the Na-S bonding interaction, we must quantify the charges on the Na and S atoms, in order to evaluate the interactions in this bond.

6.4 Charge analysis in the Na_3PnS_4 structures

To investigate the Na-S bonds, as well as further analyse the Pn-S bonds, it is essential to quantify the charge distribution in the structures. For this, three different means of charge analysis are employed: the Bader Charge, where the charge density is divided based on the zero-flux surfaces, the Electron Localization Function, which expresses the probability that a Pauli exclusive electron is found near a reference electron, and the Born Effective Charge, which is a measure for the change in the polarizability of an atom as a result of a small perturbation.

6.4.1 Bader Charges

Perhaps the most direct way of quantifying the net atomic charge on the different atoms in the structure is through the Bader charge. With the Bader method, the charge density is split into different regions based on zero-flux surfaces (where the change in charge density is at a minimum) and subsequently attributed to specific atoms. The Bader charge generally provides a more accurate estimation of the net atomic charge of an atom than simply through investigating its nominal oxidation state. Since the Bader charge is based on the zero-flux surface, its relation with the electronegativity is strong: it a covalent bond is of a more polar nature, the charge distribution will shift towards the more electronegative element and as a result the Bader charge of the atom will increase.

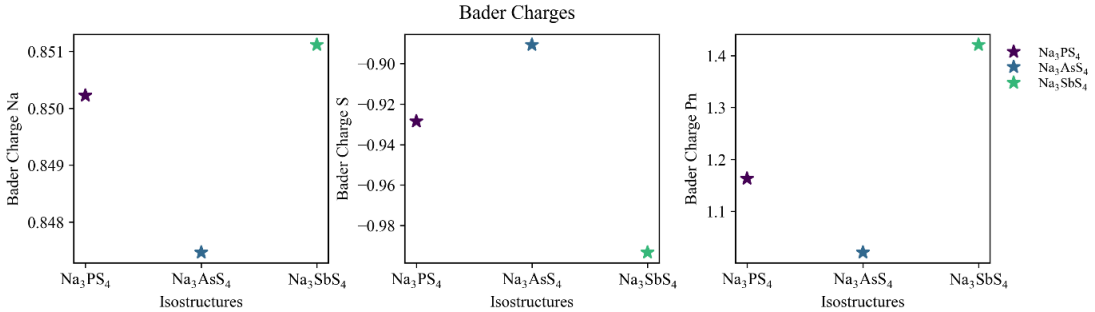

Figure 6.6. The Bader charges of the different atoms in the isostructural compounds. Notice the y-axis: the choice of Pn-atom has a large effect on the Pn Bader charge and with it a smaller effect on the S Bader charges. A resulting change in the Na Bader charge can be observed, but this difference is much smaller than the respective changes of the Pn and S Bader charges.

The Bader charges of the different atoms of the Na_3PnS_4 structures are shown in Figure 6.6. Since the cut-off of the Bader volumes is dependent on the exact charge distribution, it is important to compare the changes in Bader charge to the potential changes in Bader volume associated with the charge.

To this extent, we define a pseudo "Bader density", where

$$\rho_{Bader} = \frac{e_{Bader}}{V_{Bader}} \quad (26)$$

with ρ the density, e the charge and V the volume. When compensating for the potential changes in volume in this way, we found that the differences in Bader charges between the isostructural compounds remained nearly the same. As such, we assume that the changes in Bader charges are not the result of volumetric changes in the Bader volumes.

When evaluating the Pn-Bader Charges we observe the same (but inversed) trend as with the Allred-Rochow Pn Electronegativity: following the theory of electronegativity, it indeed seems that the differences in electronegativity between the pnictogen have resulted in more polar bonds in the order As-S < P-S < Sb-S. The Bader charge on the Sb atom is significantly more positive than that of the P and As atoms, indicating electrons have shifted from the Sb atom towards the S-atoms. This is verified by looking at the S Bader charge in the Na_3SbS_4 structure, which is significantly more negative than in the Na_3PS_4 and Na_3AsS_4 structures. Interestingly, the change in the charge distribution inside the PnS_4^{3-}-anions only had a small impact on the Na Bader charge: where the largest difference in Pn Bader charges is 40% (between As and Sb), the equivalent difference in Na Bader charges is only 0.5%. This indicates that any changes in the Na-S bonding interactions are likely the result of the change in the charge of the S-atoms.

6.4.2 Electron Localization Function

To further elucidate the differences in the charge distribution in the Na_3PnS_4 structures, the Electron Localization Function (ELF) was analysed. This charge metric expresses the probability with which a Pauli exclusive electron can be found near a reference electron and as such is ideally suited for identifying the type of environment in which an electron is located. In general, the rule of thumb applies that where the ELF is high (> 0.7), the electrons are characterized as localized, meaning they constitute core, bonding or paired electrons. On the other hand, when the ELF is between 0.7 and 0.2, the electron localization is similar to that of an electron-gas and is characteristic of metallic or ionic bonds. In the absence of electron density, the ELF becomes 0.[63] In the ELFs determined by DFT, only the valence electrons are considered. For the Na, P, Sb, As and S atoms the $2p^6 3s^1$, $3s^2 3p^3$, $4s^2 4p^3$, $5s^2 5p^3$ and $3s^2 3p^4$ electrons are considered as valence, respectively.

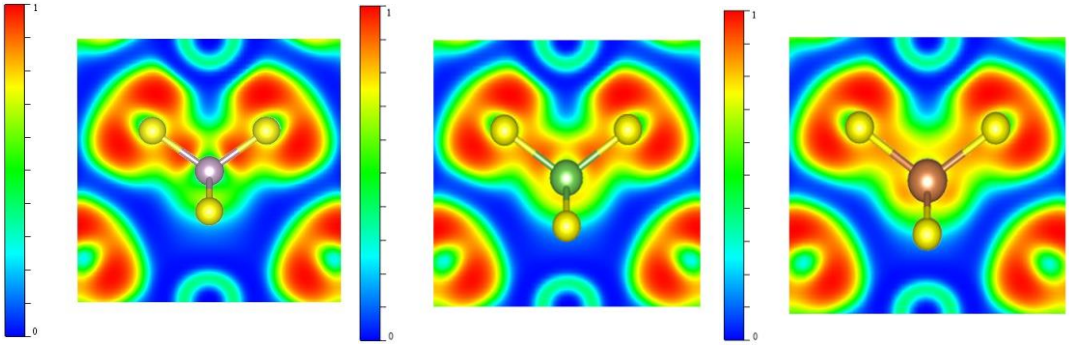

Figure 6.7. The ELFs of the Na_3PnS_4 structures: cross sections of the PnS_4^{3-}anions through two of the Pn-S bonds. The electrons in the bond are more localized for the Na_3PS_4 structure (left) than for the Na_3AsS_4 (middle) or Na_3SbS_4 structure (right).

Looking at the ELFs of the Na_3PnS_4 structures, we observe that the electrons are most localized in the P-S bond and least in the Sb-S bond. Based on the value of the ELF (~1) this indicates clear covalent bonding for the P-S structure, with a slightly less covalent nature for the As-S

and Sb-S bonds. The differences in this bonding interaction can potentially be linked to the electronic structure of the shielding electron shells. For the P-atom, the valence electrons participating in bonding are the $3s^2 3p^3$ electrons. The shielding core electrons thus constitute of the 1s, 2s and 2p shells. For the As and Sb atoms, the valence electrons participating in bonding are respectively the $4s^2 4p^3$ and $5s^2 5p^3$ electron. This means that the outermost shell below the valence electrons consists of d-shell electrons in both cases (filled $3d^{10}$ and $4d^{10}$ shells respectively). With more electron shells there is a larger shielding effect of the effective nuclear charge for the As and Sb structures, resulting in a less tight binding of the valence electrons and as such weaker bonding interactions in these structures than for the P structure.

Following this reasoning, the difference in electron configuration can potentially be related to the large differences in bonding energies and melting points of the Na_3PS_4 structure compared to the Na_3AsS_4 and Na_3SbS_4 structures. Since the electrons participating in bonding are more strongly bound to the nucleus for the Na_3PS_4 structure, the resulting bonds are stronger / stiffer. This reasoning based on the valence electron nature also suggests that using the covalent bonding criterion (differences in electronegativity) as a measure for bond strength is inappropriate when considering electrons from different shells. This illustrates there is an important distinction in bonding nature between the polarity of a bond and its strength. As such, it is possible that while the difference in electronegativity in the As-S bond is smaller than the difference in the P-S bond, resulting in a less polar As-S bond, the As-S bond is also weaker than the P-S bond.

This line of thought can be extended to the Na – S bond nature. Looking at the valence electrons of the Na-ions, it is generally assumed that the 3s valence electron plays the largest role in bonding. For the S-ions, the 3p electrons are assumed to participate in bonding. Because in all isostructural compounds the same electrons participate in bonding, Pauling's bonding criterion can potentially be applied to investigate bond nature. This means that if the Na-S bonds has any sort of covalent nature, a larger difference in Na and S charge would indicate a less covalent bond nature and as such a weaker bond. With a Na electronegativity of 1.01, the difference in Na and S electronegativities becomes 1.43. Since this falls in the range of $0.4 < 1.7$, it means that according to the Pauling bonding criterion we can treat the bond to a certain extent as covalent in nature. This must be interpreted with caution however, since the difference is not far from the cut-off value of 1.7.

From the Bader charges, it can be seen that the difference in charge between Na and S follows the trend $Na_3AsS_4 < Na_3PS_4 < Na_3SbS_4$. If we follow the reasoning on the strength of the covalent bonds, this could mean that the Na-S bonds are weakest in the Na_3SbS_4 structure and strongest in the Na_3AsS_4 structure. This could provide a potential explanation for the differences in ionic conductivity as observed in literature: since the Na-ion is more tightly bound in the Na_3AsS_4 framework than in the Na_3PS_4 and Na_3SbS_4 frameworks, the energy associated with ion migration becomes larger.

This reasoning on the changing Na-S bond strength is directly opposite of the conclusion that would be drawn based on the electrostatic interaction. In the electrostatic approximation, as used by Krauskopf et al to explain the differences in conductivity in LGPS, a larger difference in charge would suggest a stronger bonding interaction and thus lower conductivity. It thus seems that there is more to the relation between the Na-S bond nature and the conduction mechanism than initially thought.

6.4.3 Born Effective Charges

To shed more light on the different potential effects of the Na – S bonding interaction on the conductivity, the Born Effective Charges (BEC) can be analysed. The Born charge of atom k is defined as

$$Z^*_{k,\gamma\alpha} = V\frac{\delta P_\gamma}{\delta \tau_{k,\alpha}} = \frac{\delta F_{k,\alpha}}{\delta \xi_\gamma} = -\frac{\partial^2 E}{\partial \xi_\gamma \partial \tau_{k,\alpha}} \quad (27)$$

where $Z^*_{k,\gamma\alpha}$ is the Born Effective Charge, P_γ the polarizability, τ_α the displacement, $F_{k,\alpha}$ the force on the atom, E the energy and ξ_γ the electric field[58]. As can be noticed from this equation, the Born Effective charges are a measure for how the electron distribution around an atom (related to the polarizability) changes as a result of a displacement. Since it is a directional property, the BEC can be expressed in a 3 x 3 matrix of Cartesian coordinates. The Born Effective Charges are a good measure for the stiffness of a bond, as can be seen from the second definition of the Born charge in equation 27, where the force is defined as the partial derivative of the force on the ion to the change in electric field. So: when an ion is moved along a direction that coincides with a bond, the change in electric field is larger than when the ion is moved in a different direction. If the bond in question is a stiff bond (large spring constant), the effective change in force is then larger than for a soft bond.

In the Na_3PnS_4 structures, the Born Effective Charges of the Pn and S atoms are isotropic, meaning that the change in polarizability is the same for all diagonal components (xx, yy and zz). For the S-atom is it noticed that as a result of the local environment, the off-diagonal components of the matrix have a constant value of approximately -0.3. The Born Effective Charge of the Na-atom however, is not isotropic and has a higher value in one of the three directions. The reason for this altered BEC component is the coordination of other Na-atoms and PnS_4^{3-}-anions surrounding the Na-site. It can be seen from the structure than in 4 directions (+x, -x, +y, -y) the Na-site has neighbouring Na-sites, and in 2 directions (+z, -z) the Na-site is enclosed by PnS_4^{3-} anions. This coordination around the Na-site causes a different change in polarization in the direction of the PnS_4^{3-} neighbours than for the Na-neighbours. This effect is illustrated by the Na-density map of Na_3PS_4 as obtained through *ab initio* Molecular Dynamics (see Figure 6.8).

Na-BEC	**x**	**y**	**z**
	1.0818	*0.0*	*0.0*
y	*0.0*	*1.0818*	*0.0*
z	*0.0*	*0.0*	*1.4255*

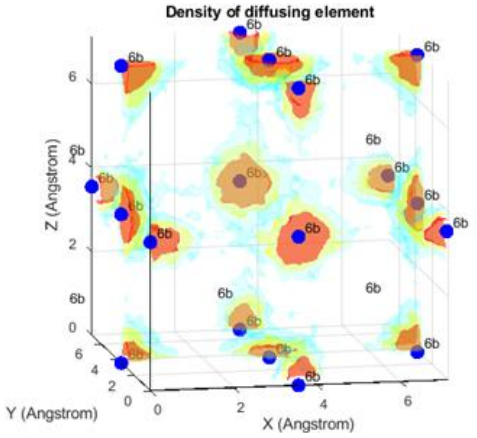

Figure 6.8. The Born Effective Charge matrix of the Na-atom in Na_3PS_4 structure (left) and density map of the diffusing element Na from *ab initio* Molecular Dynamics in the Na_3PS_4 structure (right). In the density map it can be seen that the Na-ion moves much more freely in a specific plane than in the third direction. Comparing the density map to the crystal structure shows that the neighbours in this plane are four different Na-atoms, and the third direction is coordinated by the two PnS_4 anions.

The anisotropy of the Na Born Effective Charge is interesting from the perspective of bonding interactions; since the Na-ion is theoretically not bound to the neighbouring Na-atoms, the BEC in those direction should be close to the nominal charge of the ion (as is the case for the BEC if no bonding is present). However, since the Na-ion is bound to the PnS_4^{3-} anions, the Born Effective Charge in the direction of these anions provides a direct estimate of the bond stiffness of the bond between the Na-atoms and PnS_4^{3-} tetrahedra.

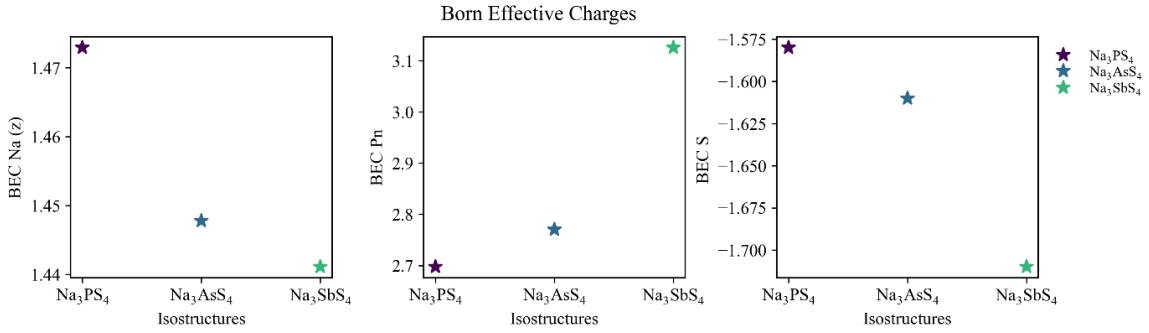

Figure 6.9. BEC of the Na-ion in the (zz) direction (towards the PnS_4^{3-} anions), the Pn BEC and the S BEC, for all isostructural compounds. As with the Bader charges, the changes in the Pn BEC are larger than those of the Na and S BEC.

When comparing the Born Effective Charges of the three isostructural compounds (Figure 6.9) it can indeed be observed that in the direction of the neighbouring Na-atoms, the Na BEC (xx/yy) of the Na_3PnS_4 structures are close to +1 (between 1.085 and 1.138), indicating no bonding, and in the direction of the PnS_4^{3-}-anions deviate from 1 (between 1.441 and 1.473), indicative of a bonding interaction. Contrary to the Bader charges, the Born Effective Charges scale more monotonically with the Pn-substitution. We observe that the BECs change significantly more for the Pn and S atoms than for the Na atoms. This is in line with the findings on the Bader charge and is to be expected given that the fundamental change in the structures occurs in the PnS_4^{3-} anions. The BEC of the Pn and S atoms seem to change proportionally to each other: the small increase in the Pn BEC from P to As is associated with a small decrease of the S BEC from P to As. It is observed that while the Na BEC (zz) changes less between the structures than the Pn and S BEC, the trend in the Na BEC (zz) is very similar to that of the melting points and indicators of lattice stiffness: a larger decrease in the Na BEC (z) from P → As and a smaller decrease from As → Sb. Whilst small, based on the definition of the BEC these changes suggest that the Na – S bond is stiffer for the Na_3PS_4 structure than for the Na_3AsS_4 and Na_3SbS_4 structures (as the spring constant depends on $\frac{\delta F}{\delta \xi_\gamma}$), and are in line with the other indications on bond stiffness in the Na_3PnS_4 structures.

While the bond stiffness and polarity shed light on the fundamental differences in the chemistry at play in the isostructural compounds, based on the contradicting findings of the effects of S-charge on ion migration in LGPS and Na_3PnS_4, these metrics alone seem insufficient to explain the complex differences in the Na – S bonding interaction and the ionic conductivity. It is therefore important to relate the static and dynamic influences on the conduction process directly to the conduction mechanism, specifically to the activation energy required for ion migration.

6.5 Summary: on the bonding interaction in the Na_3PnS_4 structures

In an attempt to better understand the conduction mechanism in Na_3PnS_4, we evaluated several indicators of lattice rigidness, which act as descriptors of how the lattice dynamics can influence ion conductivity. It is often thought that a softer lattice, containing weaker bonds, facilitates easier ion migration. When studying the bonding nature in the Na_3PnS_4 structures, we find several seemingly contradicting findings on bond strength. Based on the melting points, vibrational frequencies (Raman) and dissociation energies, it seems that the P-S bonds are significantly stiffer / stronger than the As-S and Sb-S bonds. However, when investigating the differences in electronegativities in the Pn-S bonds, we note that the As-S bonds are of the least polar nature, which according to the Pauling ionic bonding criterium suggest that this bond is actually more covalent than the P-S and Sb-S bonds.

To explain these findings in bond "strength", we considered two different qualities of the Pn-S bonds: their stiffness and their polarity. Combining the various findings of the dynamical lattice descriptors with different charge metrics in the structure, we find that the stiffness of the bond is best described by the melting points, the vibrational modes, the dissociation energies and the Born Effective Charges. These metrics suggest that the Pn-S bonds in the Na_3PS_4 structure are significantly stiffer than the Pn-S bonds in the Na_3AsS_4 and Na_3SbS_4 structures. The polarity of the bond is best captured by the Allred-Rochow electronegativities, the Bader charges and the Electron Localization Function. These descriptors show that the As-S bond is the least polar bond, followed by the P-S bond and finally the Sb-S bond.

To investigate the effects of these bonding natures on the conduction process, it is important to see how they affect the Na – S bonding interaction. We see from the Bader and Born charge analysis that changes in the electron distribution of the Na atoms are present, but very small compared to the changes in the PnS_4^{3-}-anions. It is therefore to be expected that the largest effects of the substitution on the Na-S bonding interaction are a direct result of the changes in the S-ion charge. Based on the electrostatic interaction, the more negatively charges S-ions in the Na_3SbS_4 structure would the strongest bond with the Na-ions in the structure, which should result in more difficult ion migration. However, the values for the conductivity in literature indicate that ion migration is actually easiest in the Na_3SbS_4 structure and most difficult in the Na_3AsS_4 structure, which has the lowest S-charge. We find that it is important to not only consider the pure electrostatic interaction in the Na-S bond, but also the fundamental nature of the bond. Taking the difference in electronegativity into account, we observe that the Na-S bond can be said to have a somewhat covalent character. Since for covalent bonds the general trend goes towards weaker bonding the larger the charge for the seemingly weaker Na-S bonding in the Na_3SbS_4 structures.

The main findings on the different dynamical lattice descriptors and charge data are summarized in respectively Table 6.1 and Table 6.2. To truly understand the effects of bonding on conduction, it is important to directly relate these difference in dynamical influences and bonding interactions to the energy barrier, in order to more accurately explain the trend in ionic conductivities.

Table 6.1. A summary of the dynamical lattice influences as determined in this study. The values for the electronegativity were not measured but come from literature[65].

Isostructure	**Na_3PS_4**	**Na_3AsS_4**	**Na_3SbS_4**
Bulk Modulus / GPa	26.55	25.65	24.72
dB/dP	4.77	4.97	5.12
Pn Electronegativity (Pauling)	2.19	2.18	1.96
Pn Electronegativity (Allred-Rochow)	2.06	2.20	1.82
Melting Point / °C	765 [24]	636 [24]	621
Bond Dissociation Energy (Pn-S) / eV	442 ± 10 [72]	379.5 ± 6 [72]	378.7 ± ? [72]
Raman $\boldsymbol{\nu_1}$ / cm^{-1}	411 [33]	376 [33]	367 [33]

Table 6.2. Summary of the different charge metrics (Bader and Born charges) used to describe the effective charge distribution.

Isostructure	**Na_3PS_4**	**Na_3AsS_4**	**Na_3SbS_4**
Bader Charges			
Na	0.850	0.847	0.851
Pn	1.163	1.021	1.421
S	-0.928	-0.891	-0.993
Born Effective Charges			
Na (xx / yy)	1.085	1.109	1.138
Na (zz)	1.473	1.448	1.441
Pn	2.697	2.771	3.125
S	-1.584	-1.609	-1.709

7. Results – Quantifying the activation barrier and investigating the fundamental conduction pathway with NEB

To relate the static and dynamic influences on ion migration directly to the conduction process, it is necessary to quantify the energy associated with ion migration. One of the most direct methods to quantify the migration energy for a single ion hop is the so-called Nudged Elastic Band (NEB) method. In this method, two states of a system are taken (e.g., a before and after state of an ion hop) between which a linear interpolation is performed. By subsequently minimizing the energy on each image, an accurate representation of the energy landscape between the end states can be obtained. Applying this to the process of ion migration, the activation barrier of the hopping process can be quantified. In this chapter we utilize the NEB method to quantify this energy barrier. Furthermore, we use the different images along the transition pathway to investigate the structural changes and changes in the electron distribution during the process of migration. Finally, to shed a different light on these structural effects on the activation barrier, the effects of pressure on the activation energy are studied.

7.1 Investigating the activation barrier with the Nudged Elastic Band method

To determine the energy landscape of ion migration, NEB calculations were performed on the transition of a single Na-ion to a (vacant) neighbouring Na-site. To do so, the initial and final state of the migration were generated and 9 intermediate images interpolated to create the initial guess of the migration path (Figure 7.1 illustrates the NEB method with the initial state, three images and the final state). To ensure accurate energies of the migration path, the initial and final states of the structure were relaxed after a vacancy was introduced into the structure. To prevent the interaction of the vacancy with itself in the DFT calculation, a 2 x 2 x 2 supercell was used for the calculations. When investigating the relaxed structures of the initial and final states before the NEB run, it could already be observed that as a result of introducing the vacancy, the energetically lowest location for the Na-ions next to the vacancy had shifted. As a result of the generated vacancy, the Na-ions in the sites adjacent to the vacancies were drawn in the direction of the vacancy. As a result, the effective migration distances in the NEB runs differed from the crystallographic 6b – 6b distance (as will be discussed later).

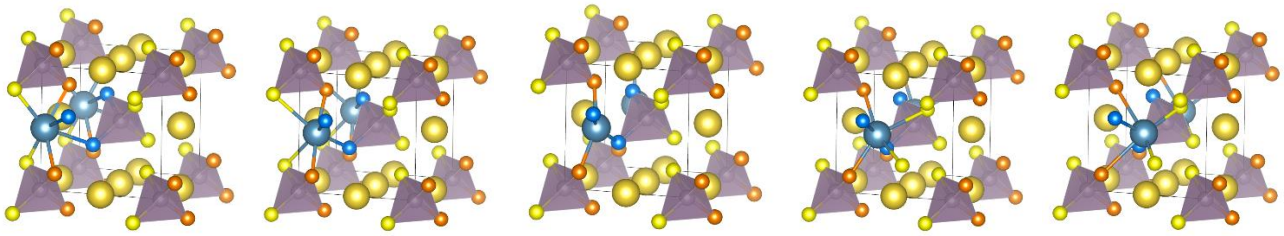

Figure 7.1. NEB can be used to study a Na-ion moving along the fundamental conduction pathway. The blue Na-ion moves from one 6b site (leftmost image) to another 6b site (rightmost image). Along the pathway, the Na-ion moves past a constellation of 4 S-atoms, commonly described as “the bottleneck” of diffusion. This bottleneck is here shown with the orange and blue S-atoms to which the migrating Na-ion is bonded.

By calculating the ground state energies of the images along the migration path, the energy landscape of migration was obtained (Figure 7.2). With the NEB analysis it was found that the activation energies of the three isostructural compounds follow the exact same trend as the ionic conductivities as reported in literature: for the Na_3PS_4, Na_3AsS_4 and Na_3SbS_4 structures the activation energies were found to be respectively 69.2 meV, 75.9 meV and 58.6 meV. The values of the E_a found in this study are quite close to those in other studies of the Na_3PnS_4 structures that utilize NEB[30,73]. While these energies are much smaller than some of the activation energies as found using impedance spectroscopy or molecular dynamics[3,28,30], this is not unreasonable since with NEB only the energy of a single ion hop at a temperature of 0K is calculated (thus all effects not related to the static and electronic structure are ignored). It therefore makes more sense to compare the values of the activation barriers to each other than to the different ways of quantifying the E_a.

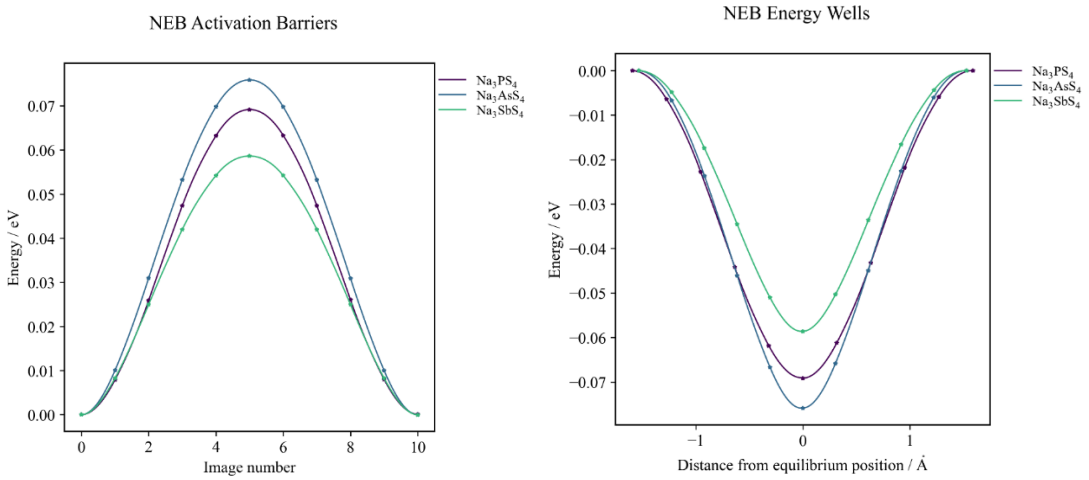

Figure 7.2. The NEB activation barrier showing the energies of the different images along the migration path, with an interpolated spline fit (left). The energy barrier was also transformed into an "energy well", where the relative energy with respect to the initial / final structure is plotted against the displacement from the equilibrium distance (right).

To investigate the local energy landscape surrounding the Na-site, we plot the relative energy of the images against the displacement from the equilibrium position. Here is becomes important to take into account the exact locations of the Na-ions in the initial and final states. Since introducing the vacancy caused a shift of the ideal Na-site in the relaxed initial and final states, the "equilibrium position" of the NEB run is not directly relatable to the equilibrium 6b-position in the ideal Na_3PnS_4 structures (no vacancies). It is important to take note of this displacement, since from the energy wells in Figure 7.2 it can be seen that the effective migration path is actually shorter for the Na_3SbS_4 structure than for the Na_3AsS_4 structure, while in reality the lattice of the Na_3SbS_4 structure is larger and with it the 6b-6b distance between the Na-sites as well. Despite this important difference, it can be seen that not only the total increase in energy is higher for the Na_3AsS_4 structure compared to the others, but also that the degree with which the energy changes as the result of a small displacement from the "equilibrium" position is much larger (indicated by the slope of the well). This behaviour could be directly related to the attempt frequency: if the energy well within the ion is located is more narrow, the ion has a smaller vibrational amplitude, and as such less "attempts" at hopping occur. It must be noted that this conclusion cannot be drawn from the current results alone, and a different study of the energy landscape in the vicinity of the Na-site would be required to investigate this further.

7.2 The relation between static / dynamic influences and ion migration

To identify which of the static and dynamic indicators correlate with the activation energy, we compared the various descriptors of the static and dynamic influences from the previous chapters to the activation energies. Whilst all of the previously described indicators hold a relation to the conduction process, the objective was to find which of the descriptors is seemingly the best at predicting the conductive behaviour. Of all indicators, the Pn electronegativity and the Pn Bader charges correlate best with the activation barrier (Figure 7.3). Neither the bottleneck descriptors (Ch-Ch distance and Ch_4 volume) , nor any of the other dynamic descriptors (bulk moduli, melting points, BEC) showed a clear monotonic relation with the activation energy.

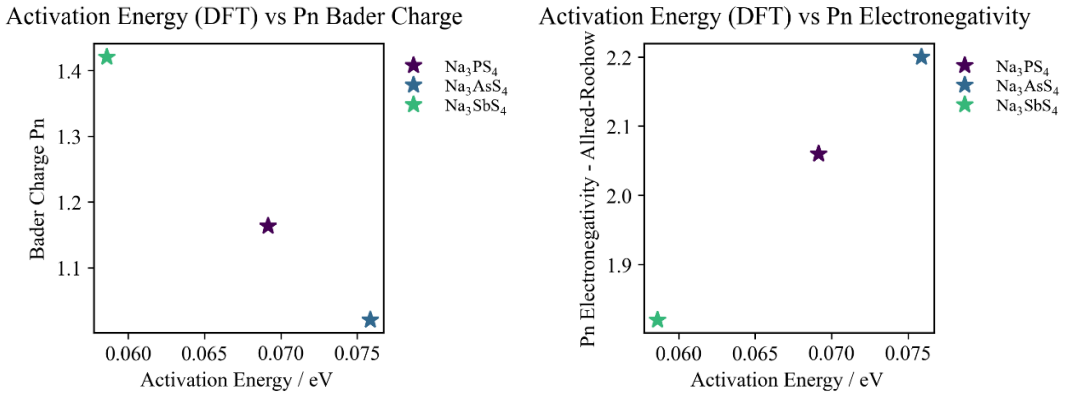

Figure 7.3. The activation energies of the three isostructural compounds as determined through NEB plotted against the Pn Bader charge (left) and the Pn Electronegativity (Allred-Rochow, right). Of all investigated indicators, the different Bader charges and electronegativities showed the most promising predictive capacity.

This observation provides an important insight for the future development of solid-state electrolytes: where the different dynamic descriptors (melting points, bulk moduli, BEC) capture the lattice stiffness accurately, it seems that the conduction process is more dependent on the bond polarity in the structure than the bond stiffness. The changes in the bond polarity result in a shift in the charge distribution, where the bonds with lowest polarity result in most electrons on the S-atoms, directly affecting the Na-S bonding interaction. However, how the Na-S bonding interaction relates to the conduction mechanism also depends on the coordination environment of the conduction pathway. It is thus necessary to relate the findings on the bonding interactions to the structural characteristics of the materials.

7.2.1 The Coulombic interaction approach

Since the Na – S bonding interaction is dependent on both the changes in Na and S charge, as well as the interatomic distances, it would be ideal to express a metric that captures both influences. Especially since in the Na_3PnS_4 structures the Na and S Bader charges and the interatomic distances both change, it is important to capture both effects. From the bonding analysis in the previous chapter, we know that a purely electrostatic approach is insufficient at explaining the bond strength between the Na and S in the structures. However, since in the covalent bonding framework the bond strength is also dependent on the Na and S charge, but inversely to the electrostatic approach, describing the Coulombic interaction between the Na and S atoms could still provide a new perspective on the bonding interaction. To this end, based on Coulombs law, we investigate whether a pseudo “Coulombic interaction” can be related to the activation barrier in the structures.

Following Coulombs law, we base this Coulombic interaction on the product of the Na and S Bader charges, capturing the change in magnitude of both charges at once

$$\vec{F} = \sum_i \frac{q_{Na} \cdot q_S}{R^2_{Na-S_i}} \quad (28)$$

where q is the measure of respective Bader charges and $R_{Na\text{-}Si}$ the interatomic distance between a Na atom and a specific S atom (i). To properly capture the Coulombic interaction between the Na and the lattice, we combine the interactions of the eight S-atoms coordinating a single Na-site. The combined Na · S charge and the calculated Coulombic Interaction are plotted against the activation energies in Figure 7.4.

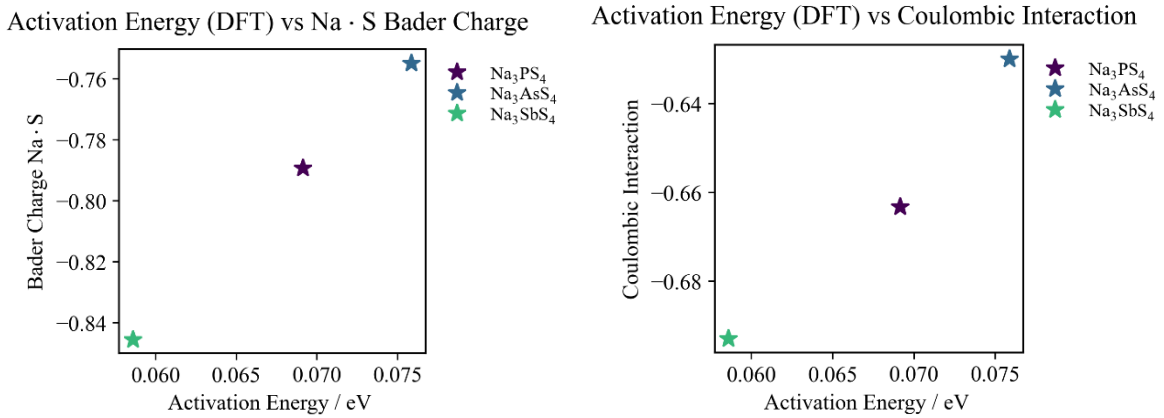

Figure 7.4. The Na-S Bader charge product shows a similar relation to the activation energy as the Pn electronegativity and the Pn Bader charge (left). Even when the Na-S interaction is corrected for the differences in interatomic distance, in a pseudo Coulombic interaction, the relation between the changed Bader charges and the activation energy holds.

From this comparison it becomes clear that the Na-S Bader charge product holds a very similar relation to the activation energy as the Pn electronegativity and the Pn Bader charge. This confirms that as expected the changes in the Pn Bader charge can directly be related to the changed Na-S interaction. Even when correcting for the changed interatomic distances, we see that the "Coulombic interaction" still correlates with the activation energy. It is interesting that even when correcting for the differences in bond lengths, the proxy for the Coulombic force shows that the electrostatic interaction is smallest for the Na_3AsS_4 structures. Purely based on the electrostatic interaction, this would imply the weakest force on the Na-ions in the Na_3AsS_4 structures and as such the weakest bonds. Given the highest activation energy and lowest ionic conductivity of the Na_3AsS_4 structure, this indicates that the bonding strength between the Na and S atoms is indeed more than a pure electrostatic interaction and likely needs to be considered as a somewhat covalent bond. However, an alternative explanation is available: since the Coulombic interaction as calculated is based on the static structure, it is possible that this Coulombic interaction is significantly different during the process of ion migration. It was found that the bottleneck sizes (Ch-Ch distances) differ for the three isostructural compounds, and as such the combined effects of the differences in the bottlenecks and Na-S interaction could be at the heart of the differences in the activation barrier and conductivity. As such, it is important to not only consider the differences in charge distribution and interatomic distances in the equilibrium structure, but also their changes along the conduction pathway.

7.3 Diving deeper into the fundamental conduction pathway with NEB

In an attempt to investigate the changes along the conduction pathway, we investigate ion migration by analysing the structural and electrochemical changes in the Na_3PnS_4 structures along the conduction pathway. We do so by performing separate electronic optimizations on the different images of the NEB calculation, where the ions are fixed in the energetically optimal positions based on the NEB run.

7.3.1 Definitions of specific atoms

Since the NEB calculations were performed in 2 x 2 x 2 supercells with only a single ion hop, it is necessary to define specific Na-, Pn- and S-atoms within the structure that are located along the migration pathway. Based on the structures used as input for the NEB calculations, we refer to the migrating Na ion as the Na_{26} ion (shown as the blue Na ion in Figure 7.5). The bottleneck of conduction is coordinated by four different S-atoms: the S_{65}, S_{82}, S_{106} and S_{121} atoms. These S-atoms are coordinated in such a way that the S_{106} and S_{121} atoms coordinate one side of the bottleneck (visible as the two orange S-atoms bound to the migrating Na-ion in Figure 7.5), and the S_{65} and S_{82} atoms coordinate the other side of the bottleneck (shown as the blue S-atoms in Figure 7.5). To investigate potential changes in the PnS_4^{3-} anions connected to the bottleneck, we define the Pn_{58} atom as the Pn-atom at the centre of the PnS_4^{3-} anions connected to the S_{106} atom (directly below the migrating Na-ion in Figure 7.5). Using these definitions, we can assess the changes in the interatomic distances and charge distribution of specific ions directly related to the conduction pathway.

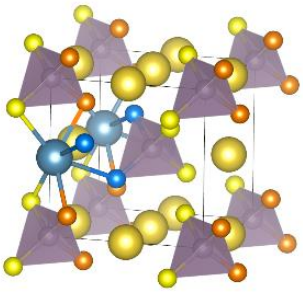

Figure 7.5. 1 x 1 x 1 unit cell showcasing the different atoms along the path of conduction.

7.3.2 The structural changes of the bottleneck

As the ion moves through the conduction pathway, it moves closer to the S-ions coordinating the bottleneck. This can clearly be seen when inspecting the distances between the migrating Na_{26} ions and the bottleneck ions S_{65} and S_{106} (shown in Figure 7.6) for each image.

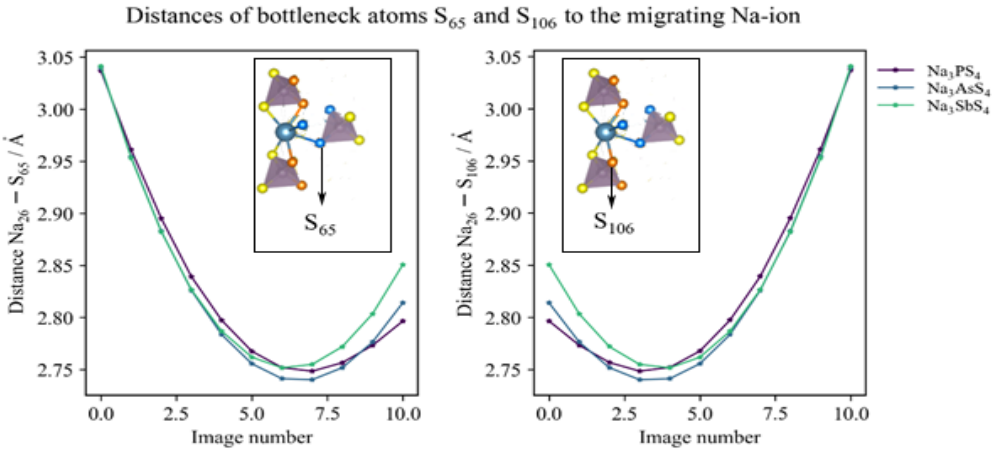

Figure 7.6. The distances between Na_{26} and S_{65} (left) and S_{106} (right) for the images along the conduction pathway.

From these distances is becomes clear that at approximately one-third and two-third of the conduction pathway, the Na_{26} ion is closest to the bottleneck S-ions. When combining these Na-S distances into a combined "average Na-S" distance, we observed that the average Na-S distance reaches a minimum halfway through the migration pathway. It thus seems that the

'competing' effects of the expansion / contraction of the two sides of the bottleneck are potentially related to the energy maximum in the middle of the conduction path. It can be noted that while the changes in these distances are very similar for the three isostructural compounds, it seems that at each end of the pathway the interatomic distance is larger for the Na_3SbS_4 structure, followed by the Na_3AsS_4 structure and then the Na_3PS_4 structure. This observation is related to the relative differences in the 2 distinct Na-S distances in the structures: at both ends of the pathway, the respective S-atom coordinating that side of the bottleneck is in a position close to the Na-site (thus at the Na-S-1 distance from the Na-ion). In this position, the Na-S bond length scales directly with the cell volume, and as such is largest for the Na_3SbS_4 structure.

To further investigate the structural changes along the conduction pathway, we inspect the changes in the bottleneck through the Ch-Ch distance and the Ch_4 volume (Figure 7.7).

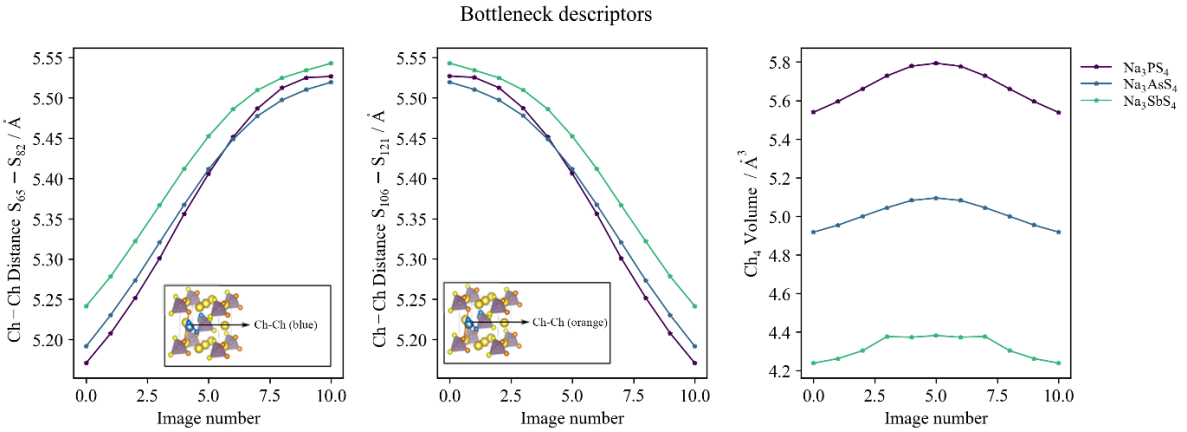

Figure 7.7. The Ch-Ch distance for the two ends of the bottleneck: the S_{65}-S_{82} distance (left) and the S_{106} – S_{121} distance (middle). These distances can be seen in Figure 7.5 as the distance between the two orange S-atoms and the two blue S-atoms. The Ch_4 volume seems to increase as the ion moves through, although a plateau can be observed for Na_3SbS_4 (right).

In the figure we can observe two trends: firstly, we note that as the Na-ion starts moving through the bottleneck, the two S-ions coordinating the "far" side of the bottleneck start moving apart from each other (Figure 7.7, left). Secondly, we also observe that after the Na-atom passes the bottleneck atoms, the S-atom start to move towards each other again (Figure 7.7, middle). Comparing the bottleneck S_{65}-S_{82} and S_{106}-S_{121} distances to the Na_{26}-S_{65} and Na_{26}-S_{106} distances we observe that when the Na-ion is closest to the S atoms, the bottleneck distance is nearly the sum of the two Na-S distances, indicating that the Na-atom passes almost exactly in between the bottleneck S-atoms. This can clearly be seen when inspecting the bottleneck, including the Ch_4 volume, when the Na_{26} ion is in this position (Figure 7.8). These observations on the Na-S distances and Ch-Ch distances indicate that to accurately describe the size of the conduction bottleneck, both of the Ch-Ch distances need to be taken into account at the same time.

Figure 7.8. The bottleneck of the Na_3SbS_4 structure for the 3rd image.

Next to the changes in the Ch-Ch distance, we observe that as a result of the combined expanding and contracting effects of the Ch-Ch distance the Ch_4 volume increases up until the middle of the migration path is reached, and afterwards starts decreasing again (Figure 7.7, right). From Figure 7.8 however, we see that during ion migration the Ch_4 tetrahedron is almost flat. As a result, the changes in the Ch-Ch distances that occur as the Na_{26} ion moves through the bottleneck hardly affect the enclosed volume. As a result, the Ch_4 volume is not capable of capturing the structural changes during migration in a meaningful way and thus might not be a suitable descriptor of bottleneck size.

7.3.3 Charge analysis: changes in bonding along the conduction pathway

To relate the structural changes to the conduction mechanism, it is important to consider how the charge distribution changes. Investigating the changes in the Bader charges along the pathway (visualised in "Appendix C. – Additional Figures Data Analysis") leads to two observations. Firstly, we observe that the same absolute trends in the Pn and S Bader charges as we did for the perfect crystal lattice: the Pn Bader charge is lowest for Na_3AsS_4, followed by Na_3PS_4 and finally Na_3SbS_4, and the S Bader charge follows the opposite trend. Secondly, the most noteworthy difference between the Bader charges in the perfect lattice and along the conduction pathway is that we observe that the S-Bader charge seems to decrease significantly and the Pn-Bader charge increases as the Na_{26} ion moves closer to the respective S-atoms. Meanwhile, the Na_{26} Bader charge decreases as the Na-ion approaches the bottleneck and increases again once the Na-ion has passed the middle of the migration path. This implies that as the Na-ion moves through the bottleneck, electrons are transferred from Pn atoms to the S-ions coordinating the bottleneck (making the S-ions more negative), while at the same time electrons are transferred from the S-ions to the migrating Na-ion (making the Na-ion less positive). The combined effects can be captured by considering the product of the Na and S charges (Figure 7.9).

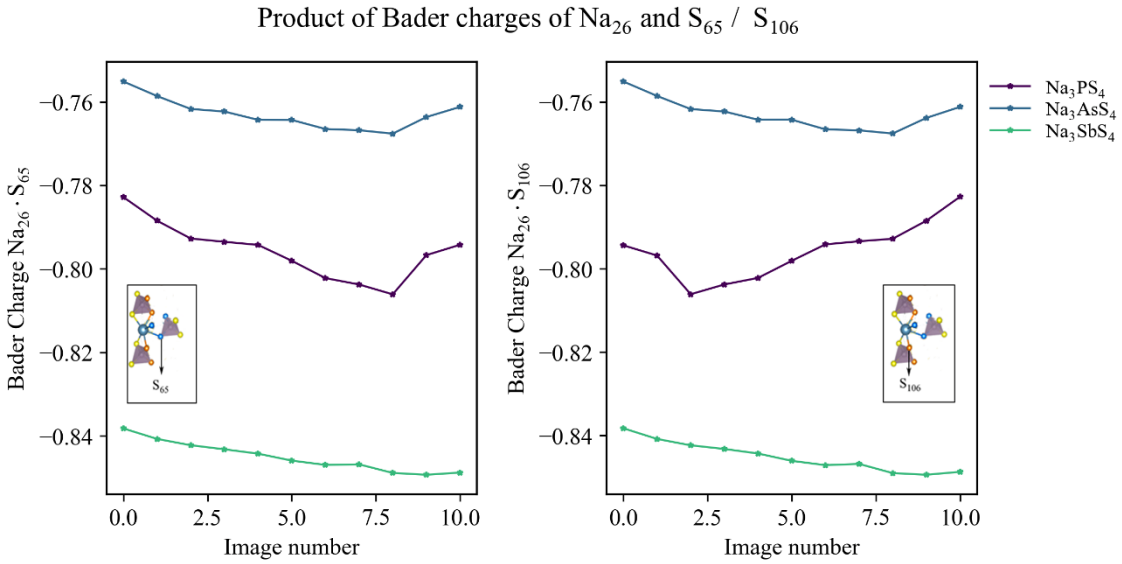

Figure 7.9. The changes in the Na x S Bader charge along the conduction pathway of two S-atoms (S_{65} and S_{106}) with the migrating Na_{26}-ion. It can be seen that as the Na-ion moves closer to the bottleneck atoms, the product of the Bader charges increases slightly in absolute value.

Because we observe both significant changes in the Bader charges along the pathway as well as changes in the bottleneck distances, we go back to our earlier defined "Coulombic Interaction" term to investigate the effects simultaneously. However, instead of defining the term based on the eight S-atoms coordinating the Na-site we now consider the interactions with the four S-atoms coordinating the bottleneck. Furthermore, based on the relaxation on the ideal structures, the absolute trend in "Coulombic Interaction" is already known (Figure 7.4). To compensate for this and isolate the changes in the "Coulombic Interaction" along the pathway, we subtract the value for the "Coulombic Interaction" of the initial image from the calculated interactions. With this, we end up with a measure that expresses directly both the changes in the Na and S Bader charges as well as the changes in the distance of the Na-ion to the bottleneck atoms.

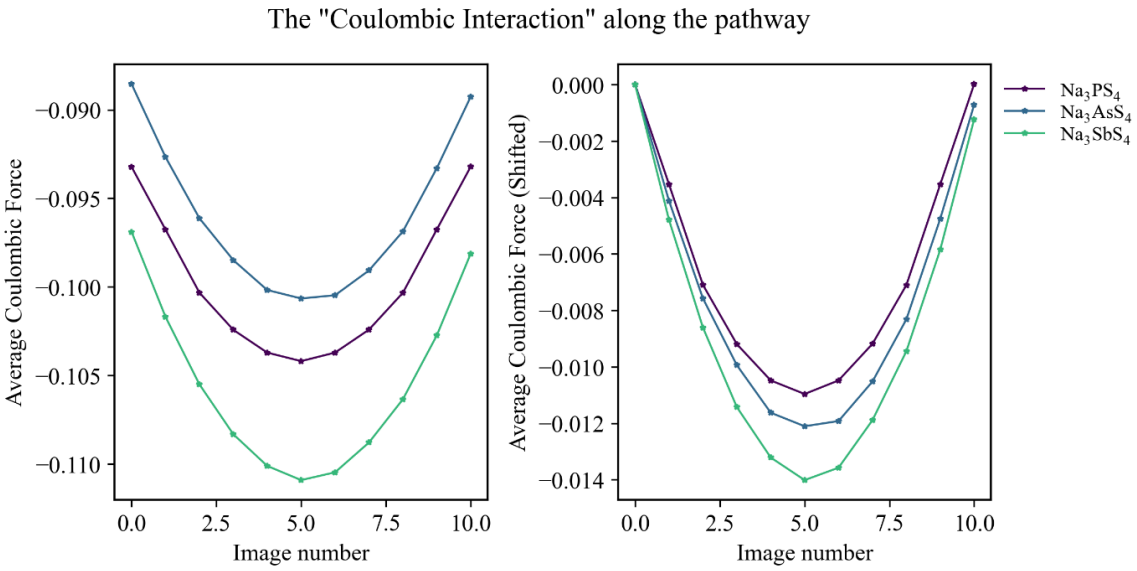

Figure 7.10. Side by side comparison of the absolute Coulombic interaction between the migrating Na-ion and the S-ions coordinating the bottleneck along the pathway (left) and the shifted Coulombic interaction.

Contrary to what one would expect based on the absolute trend in Coulombic Interactions, it is observed that the relative changes in the Coulombic interaction follow the trend of P → As → Sb. This indicates that the bond strength as quantified by the Coulombic interaction actually changes most during ion conduction for the Na_3SbS_4 structure and least for the Na_3PS_4 structure. The absolute Coulombic interaction on the other hand does seem to follow the trend of the activation energies. These findings indicate that it is not necessarily the changes in the bond strengths along the pathway that are the best predictor of the activation energy, but the bonding interactions in the structure in general.

Since the changes in the Coulombic interaction are not the only factor that impact the energy landscape, it is important to look at other aspects, including indicators of the lattice dynamics. To get a better understanding of the lattice dynamics during the migration, the Born Effective Charges of the ions in the vicinity of the conduction pathway were investigated. However, while it was noticed that the BEC charges showed significant fluctuations along the pathway, the complex dimensionality of the PnS_4^{3-} tetrahedra and coordination environment of the conduction pathway made it impossible to differentiate all factors and forces contributing to the changes in the BEC. The changes in the BEC along the pathway are reported in "Appendix C. – Additional Figures Data Analysis".

A different attribute related to the lattice dynamics that was observed in the NEB analysis, was a change in the PnS_4^{3-}-anions close to the bottleneck. It was found that while the volumes of the tetrahedra coordinating the bottleneck didn't change, the bond between the Pn-atoms and the respective S-atoms next to the bottleneck stretched (Figure 7.11). While this effect was very small, it is worthy to take note of since this change is directly related to the main stretching mode of the PnS_4^{3-} tetrahedra.

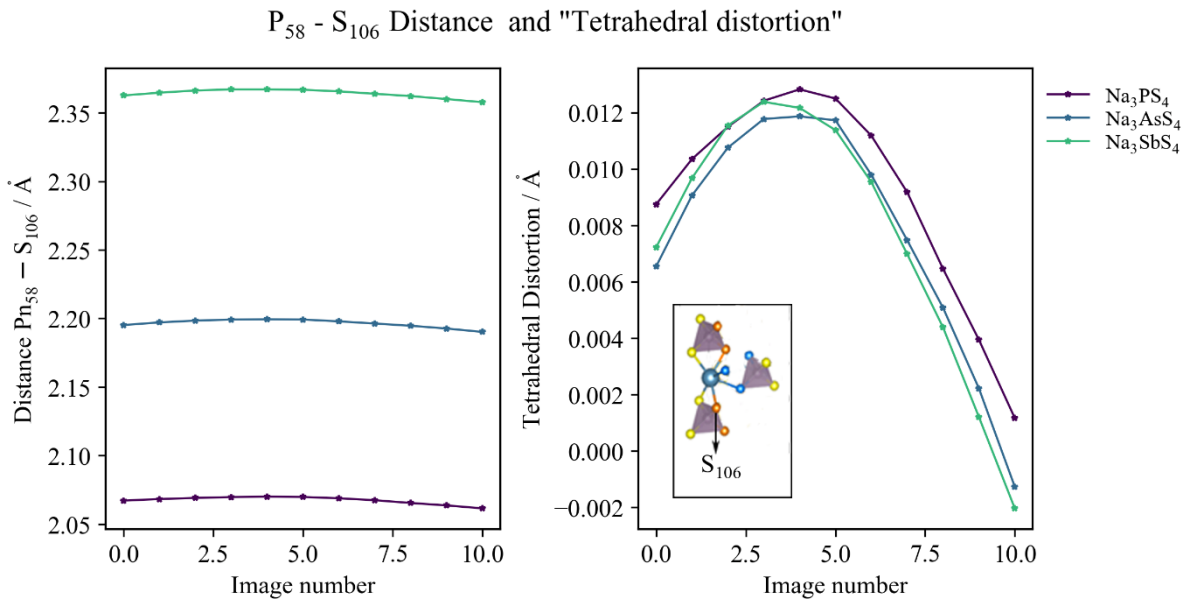

Figure 7.11. The changes in the bond length between the Pn_{58} atom and the S_{106} atom, which is coordinating the bottleneck (left). While the absolute changes in the bond lengths are very small, the difference between this specific bond length and the other Pn-S bond lengths in the anion is relatively large (right).

From the measure for the tetrahedral distortion (Pn_{58}-S_{106} compared to the other Pn_{58}-S distances, Figure 7.11) it becomes clear that this effect occurs in a similar manner for all three isostructural compounds. As such, it is not possible to relate this effect to the differences in activation energies between the isostructural compounds. Nevertheless, it is striking that this change in the PnS_4^{3-} configuration can be observed in the NEB calculation. This implies that there is an energetically favourable synergy between the process of ion migration and the stretching mode of the Pn-S bond. It is worthwhile to investigate this relation in further detail in future studies.

From our analysis of the fundamental conduction pathway, it becomes clear that significant structural changes occur during the process of conduction. To allow for the ion to move through the pathway, the bottleneck needs to open up significantly. On the other hand, investigating the bottleneck descriptors in the perfect crystal structure showed that these descriptors are not sufficient to predict the differences in ionic conductivity between the structures. It is therefore important to further investigate in what way the structural characteristics are related to the activation barrier, if not solely through the bottleneck of conduction.

7.4 Changes to the activation barrier under pressure

To further investigate how the structural characteristics of the structures relate to the conductivity, we performed NEB calculations under pressure. Since we observe distinct structural changes as a result of pressure (see section 6.1), we can try to relate these structural differences to the activation barrier.

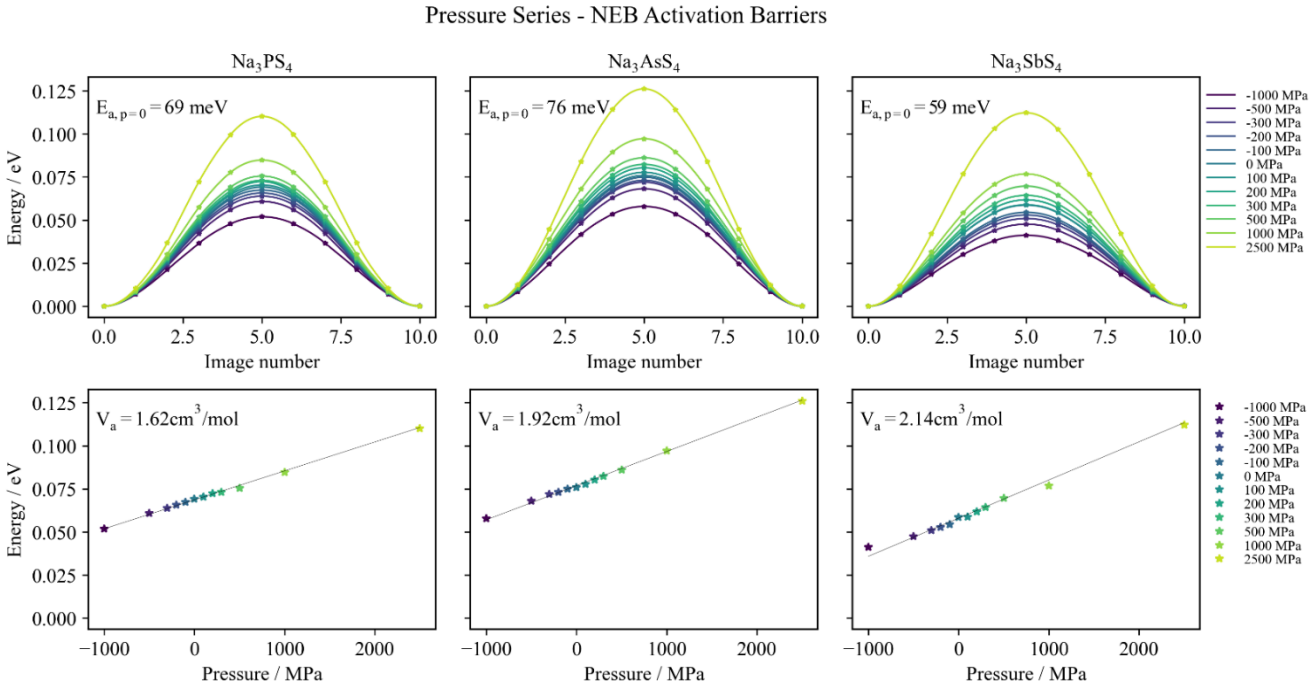

Figure 7.12. The energy profiles of the isostructures under pressure (top). Using these activation energies we can determine the activation volume, which increase with the substitution P → As → Sb (bottom).

By investigating the changes of the activation barrier under pressure, we can determine the activation volume. This metric is defined as the change of the activation energy by applying pressure and can be described using

$$\boldsymbol{V_a = \left(\frac{dE_a}{dP}\right)_T = k_B T \left(\frac{\beta}{3} - \frac{\partial \ln(\sigma)}{\partial P}\right)_T} \qquad (29)$$

where E_a and V_a are respectively the activation energy and volume, k_B is the Boltzmann constant, T the temperature, P the pressure, σ the ionic conductivity and β the inverse of the bulk modulus. An interpretation of the activation volume is that it signifies the increase / decrease in the volume required for ion migration and would as such be related to local structural changes to the conduction environment. Looking at the activation volumes of the Na_3PnS_4 structures reveals that these increase linearly with the size of the Pn-atom. This signifies that pressure has a larger effect on the conductivity in the Na_3SbS_4 structure and a smaller effect in the Na_3AsS_4 and Na_3PS_4 structures. By looking at the trend in bulk moduli, which are inversely related to the activation volume, it makes sense that the activation volume increases linearly: as the Na_3SbS_4 structure is most compressible (lowest bulk modulus), pressure has the largest effect on the structural bottleneck and decreases ion migration the most. Purely based on the mathematics however, the change to the bulk modulus term in equation 29 ($\Delta\left(\frac{\beta}{3}\right) = 0.011\ cm^3/mol$) is much smaller than the change the activation volumes. The activation volumes therefore imply that pressure affects the conductivity more than only mediated through the compressibility of the lattice.

To investigate the structural changes in more detail, we plot the different interatomic distances and bottleneck descriptors against the activation energies. While no significant differences between the isostructural compounds can be observed in the short Na-S-1 distance and the Pn-S distance, nor in the bottleneck descriptors Ch-Ch distance and Ch_4 volumes, see "Appendix C. – Additional Figures Data Analysis"), the relations between the cell volume and the Na-S-2 bond length and the activation energy show interesting trends (Figure 7.13).

When looking at the relation between activation energy and cell volume, it appears as if the Na_3AsS_4 and Na_3SbS_4 structure follow a very similar trend in activation energy as function of cell volume. This could be related to the very similar valence electron configuration of the two structures: in both the As and Sb structure shell directly below the valence shell consists of a filled d-shell. For the P structure this is the 2p-shell. As such, this could mean that the bonding interaction in the As-S and Sb-S is of a very similar nature, where the latter has only a larger difference in electronegativity (more polar bonds). However, the stiffness of the bonds and dissociation energies of the As-S and Sb-S bonds are very comparable. This suggests that if we correct for the differences in cell volume (as done by applying pressure), the bonding strength in the structure become more similar.

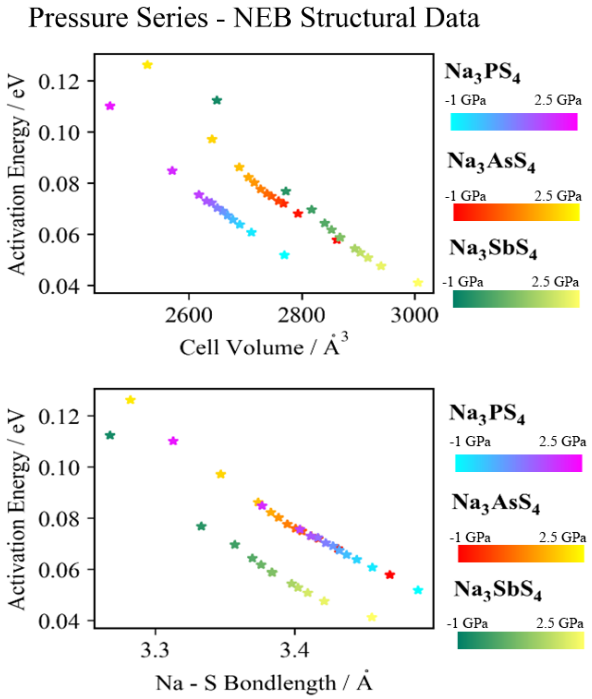

Figure 7.13. The relations between the cell volume and the activation energy (top) and between the Na-S-2 bond length and the activation energy (bottom).

The Na-S-2 distances of the octahedral coordination of the Na-sites on the other hand show a similar length for the P and As structures when we apply pressure to the system. It seems that the this can be directly related to the changes in the beta-angle, as shown in Figure 5.5: by increasing the size of the anion, not only the Na-Pn distance increases, but also the shape of the eight-S-coordination of the Na-sites is affected. It seems that this difference in Na-S-2 it directly related to why the Ch-Ch distance seems to remain constant under pressure ("Appendix C. – Additional Figures Data Analysis"). The fact that the Na-S-2 bond length is smaller for the Na_3AsS_4 structure than for the Na_3PS_4 structure can therefore be an indication of a more narrow effective bottleneck of conduction, given that the Na-S bonding interaction at the same distance is weaker for the Na_3AsS_4 structure.

Despite the noticeable trends in the structures under pressure, we find no conclusive relations between the structural changes as a result of pressure and the activation volume. Since the effects of the cell volume on the conductivity seem in some way related to the bond dissociation energies and bond stiffness, we require more information on how these dynamic qualities affect the activation energy. These descriptors are however fundamentally inaccessible through NEB, given its static nature and 0K optimizations. To get more insight into the dynamics, AIMD or EIS data is required.

7.5 Summary: a close look at the conduction pathway

In order to relate the static and dynamic characteristics of the Na_3PnS_4 structures to the conduction mechanism, we quantified the energy landscape of ion-migration through NEB. We found that the activation energies of the three isostructural compounds follow the exact same trend as the ionic conductivities as reported in literature: for the Na_3PS_4, Na_3AsS_4 and Na_3SbS_4 structures the activation energies were found to be respectively 69.2 meV, 75.9 meV and 58.6 meV. When relating the activation energies to the different materials characteristics, we found that the best predictors of the activation barrier were the Pn Electronegativity and the Pn Bader charge. This observation provides an important insight into the conduction process: while the different dynamic descriptors (melting points, bulk moduli, BEC) capture the lattice stiffness of the structure, the conduction process seems more directly related to the bond polarity. It seems that the change in S-charge as a result of the Pn substitution lies at the heart of the differences in the activation energies.

To investigate how these changes in S-charge affect the Na-S interaction, we defined a pseudo "Coulombic interaction", where both the changes in Na- and S Bader charges and differences in Na-S bond lengths between the structures are captured. We observe that like the Pn-electronegativity and Pn-Bader charges this "Coulombic interaction" correlates with the activation energy. Interestingly, even when correcting for the differences in bond lengths, the proxy for the Coulombic force shows that the electrostatic interaction is smallest for the Na_3AsS_4 structures. This indicates that the bonding strength between the Na and S atoms is indeed more than a pure electrostatic interaction and likely has a somewhat covalent nature.

The Na-S bonding interaction during ion migration was studied in more detail by investigating the structural changes and changes in the charge distribution along the conduction pathway, through DFT charge calculations on the separate images of the NEB runs. From the structural data we found that the bottleneck of conduction, as coordinated by the four characteristics S-atoms, opens and closes as the ion moves through. As the ion moves closer to the bottleneck atoms, this opening and closes of the bottleneck is accompanied by a shift in charge from the Pn-atoms to the S-atoms surrounding the bottleneck, and subsequently a shift from electrons from the S-atoms to the Na-atoms (as indicated by the Bader charges). Contrary to expectations, the Coulombic interaction between the Na-ion and the S-atoms around the bottleneck increases most for the Na_3SbS_4 structures, followed by the Na_3AsS_4 structure and finally the Na_3PS_4 structure. It thus seems that it is not the change in Coulombic interaction but the absolute values of the interaction predict the energy barrier most accurately.

From the analysis of the fundamental conduction pathway, it becomes clear that significant structural changes occur during the process of conduction. To investigate these structural changes in more detail we performed NEB analyses on the crystal structures under applied pressure. We find that the activation volumes, defined as the derivative of the activation energy with respect to pressure, increases linearly with the Pn substitution (P → As → Sb). While not in line with the trend in activation energies, this trend can be interpreted based on the cell volumes and bulk moduli of the structures: it is found that as the cell volume and the bulk modulus increase, the activation volume decreases. Since a lower bulk modulus implies a more easily deformable lattice, it makes sense that the effects of pressure on the energy barrier become larger. Despite our attempts at quantifying the dynamic lattice contributions through NEB, this method fundamentally lacks the dynamical and temperature effects. A more thorough study of the dynamic qualities through AIMD or EIS is therefore necessary.

8. Results – Towards macroscopic conduction with impedance spectroscopy

So far, we have seen that the different bonding interactions within the Na_3PnS_4 structures (quantified using different static and dynamic lattice descriptors) have a large impact on the energy barrier experienced during ion migration. Despite these interesting findings, the time independent nature of the DFT analyses make it fundamentally impossible to directly investigate the molecular dynamics in the structure during conduction. To get an estimate of quantities such as the hopping rate and the attempt frequency, it is therefore necessary to move beyond static calculations and introduce temperature and time components.

This can be achieved through either *ab initio* molecular dynamics (AIMD) or experimentally through impedance spectroscopy: by investigating how the structure behaves in a time-dependant matter, we can get a much more accurate view on how the ion dynamics influence conduction. Both methods were considered for studying the meso-/macroscopic conduction process in the Na_3PnS_4 structures in this work. However, because of the time-consuming nature of the AIMD simulations (a single computation can take over 2 weeks), it was not possible to include the results from thorough AIMD analyses in the timeframe set for this study. The results from initial MD tests are included in "Appendix E. – Ab Initio Molecular Dynamics" as reference for potential future MD studies on the Na_3PnS_4 structures. To investigate the ion dynamics in the structures, impedance spectroscopy measurements were performed in this study: with these, it is possible to investigate various important qualities of the conduction process not accessible through static calculations, such as the ionic conductivity and the experimental activation energy and volume.

8.1 Macroscopic conduction in the Na_3PnS_4 structures

The ionic conductivity of the synthesized Na_3PS_4, Na_3AsS_4 and Na_3SbS_4 samples was determined through impedance spectroscopy. The impedance measurements were fitted to an equivalent circuit of a series R, a CPE-R combination and a series CPE (the fit parameters can be found in "Appendix D. – Fit Parameters"). For determining the bulk ionic conductivity from the impedance measurements, the characteristic resistance of the CPE-R was used. With this resistance, the ionic conductivity can be calculated using

$$\boldsymbol{\sigma = \frac{d}{RA}} \qquad (30)$$

where σ is the ionic conductivity, d the thickness of the electrolyte layer, A the electrolyte area and R the fitted resistance. To illustrate this process, the Nyquist, Bode-phase and Bode-magnitude representations of the impedance measurement of the Na_3PS_4 sample are shown in Figure 8.1 (measurements of the Na_3AsS_4 and Na_3SbS_4 samples are included in "Appendix C. – Additional Figures Data Analysis"). From these representations, several characteristics of the conductive behaviour of the samples can be inferred. The ideality factor of the series CPE elements for example gives an indication of the capacitive behaviour of the blocking electrode; this ideality factor can directly be related to the characteristic frequency ats which the phase plateaus in the Bode-phase plot. Furthermore, the shape of the semi-circle gives a direct indication of the ideality factor and Q of the CPE element in the CPE-R combination. It is evident that these impedance measurements contain a lot of valuable information that could provide insight into the conductive properties. Whilst these characteristics are not studied in this work, for further studying of the fundamental conduction mechanism in Na_3PnS_4 a detailed study of these different qualities could provide valuable information.

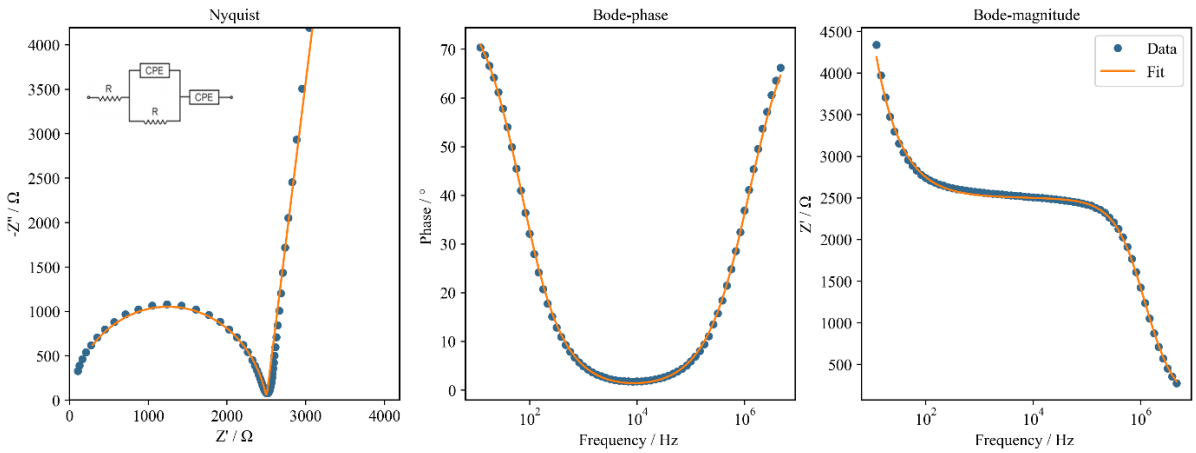

Figure 8.1. The Nyquist, Bode-phase and Bode-magnitude plots for the main impedance measurement of the Na_3PS_4 sample. The data points (blue) are compared to the fit (orange line).

The ionic conductivities of the samples were determined to be 0.0447 mS / cm^3 for Na_3PS_4, 0.0527 mS / cm^3 for Na_3AsS_4 and 1.79 mS / cm^3 for Na_3SbS_4. Comparing these ionic conductivities to the values found in literature, we notice that the ionic conductivities of the Na_3AsS_4 and Na_3SbS_4 samples are comparable to the reported values of 0.027 mS / cm^3 (ref [8]) and 1.05 mS / cm^3 (ref [22]) respectively. The ionic conductivity of the Na_3PS_4 sample however is nearly an order of magnitude smaller than some values reported in literature (0.2 – 0.46 mS / cm^3 (ref [8])). Figure 8.2 shows a comparison between the ionic conductivities found in literature and the ones determined in this work. It is uncertain where the difference in ionic conductivity of the Na_3PS_4 sample comes from. It is possible that the higher resistance of the Na_3PS_4 sample is the result of improper densification of the pellet. The work of Famprikis et al[11] shows the importance of densification on the conductivity of Na_3PS_4 samples synthesized using high-temperature solid-state synthesis. While the cell was put under pressure in order to densify the electrolyte powder, the applied pressure did not reach the 1 GPa used by Famprikis et al[11] (as pressures higher than 500 MPa caused the mantle in the solid-state cell to break). Why this effect of pressurization would only have such detrimental effects on the conductivity of the Na_3PS_4 sample however is unclear.

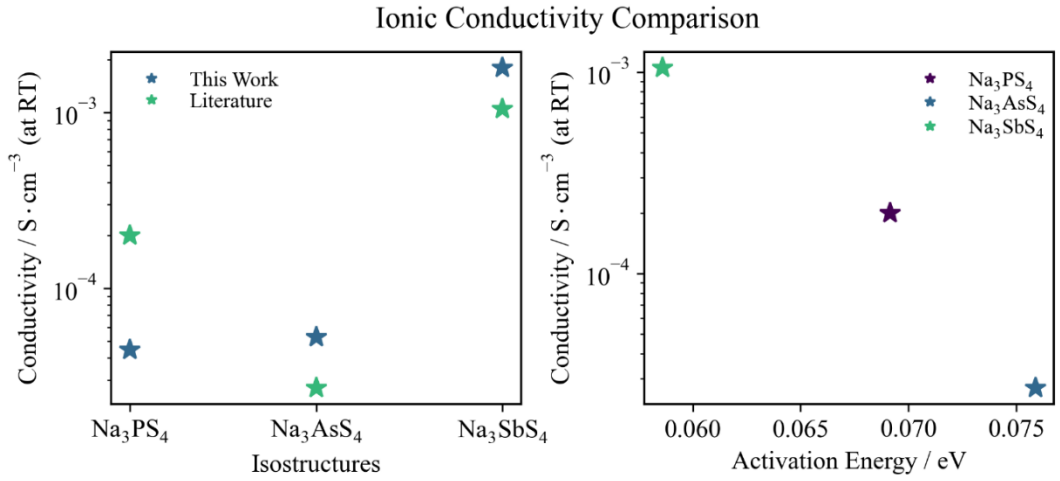

Figure 8.2. Comparison between the different descriptors of the ease of conduction: the ionic conductivities and the NEB activation energy. The ionic conductivities in this work for the Na_3AsS_4 and Na_3SbS_4 samples are close to literature values; the conductivity of the Na_3PS_4 sample is nearly an order of magnitude smaller (left). The activation energies from NEB are related to the conductivities reported in literature and show a monotonic relation (right).

To properly compare the macroscopic conductivity to the activation barrier, the activation energies as determined through NEB were plotted against the ionic conductivities found in literature (Figure 8.2). This showed a monotonic trend with the substitution of the Pn atom: for the Na_3AsS_4 sample the ionic conductivity was lowest and the energy barrier highest, for Na_3SbS_4 the ionic conductivity was highest and the energy barrier lowest and for the Na_3PS_4 sample both the ionic conductivity and the energy barrier were in between the values of the other samples. This is an important finding, since it shows that the different static and dynamic descriptors that correlate with the activation barrier also correlate with the ionic conductivities. As such, studying these static and dynamic descriptors for potential candidate structures can help the endeavour to enhance and improve current solid-state electrolytes.

8.2 Pressure effects on the conductivity – the activation volume

To get a deeper understanding of the differences in ionic conductivity between the Na_3PnS_4 isostructural compounds, the changes in the conductivity as a function of pressure and temperature were investigated (all measurements and fits are reported in "Appendix C. – Additional Figures Data Analysis" and "Appendix D. – Fit Parameters"). To determine the effects of pressure on the conductivity, the impedance was measured for a series of pressures from 0 GPa to 0.5 GPa. By investigating the conductivity under pressure (fitted to the same equivalent circuit of one series R, one parallel CPE-R combination and one series CPE as the standard conductivity measurements), we were able to calculate an experimental activation volume using

$$V_a = \left(\frac{\boldsymbol{dE_a}}{\boldsymbol{dP}}\right)_{\boldsymbol{T}} = \boldsymbol{k_B}T\left(\frac{\beta}{3} - \frac{\partial \ln(\sigma)}{\partial P}\right)_T \qquad (31)$$

where the compressibility β was calculated using the values for the bulk modulus obtained in section 6.1.

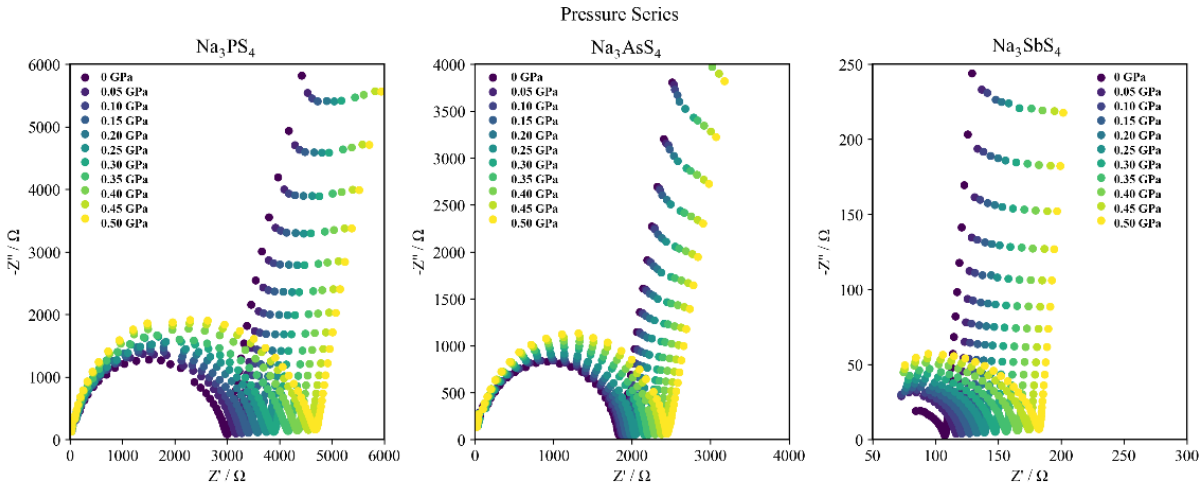

Figure 8.3. Nyquist plots of the impedance measurements under pressure for the three different isostructural compounds: Na3PS4 (left), Na3AsS4 (middle) and Na3SbS4 (right).

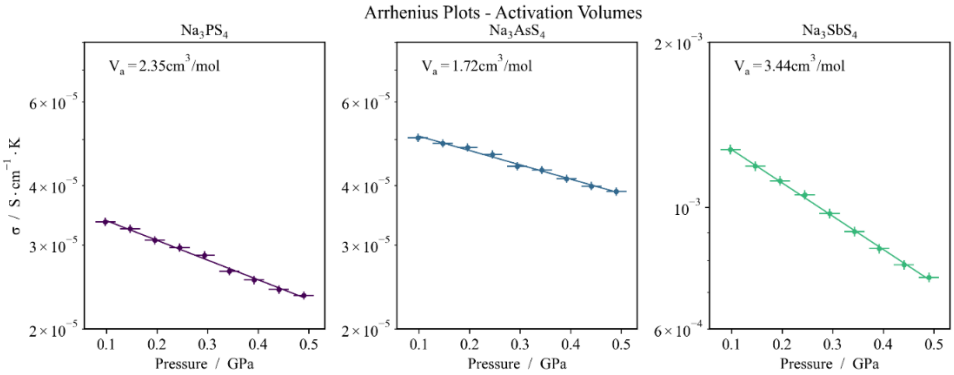

Figure 8.4. The ionic conductivities are plotted against the pressure, to determine the experimental activation volumes.

Inspecting the ionic conductivities under pressure, we observe a clear decrease in the conductivity as a result of applied pressure. This is relatable to the findings on the activation volume from NEB where the activation barrier increased as a result of applied pressure. This signifies that as the lattice is compressed, ion migration becomes more difficult and thus the bulk resistance of the electrolyte decreases. Contrary to the activation volumes of the NEB calculations, we observe a non-monotonic trend in experimental activation volumes, where the V_a of Na_3SbS_4 is highest (3.44 cm^3/mol), followed by Na_3PS_4 (2.35 cm^3/mol) and finally Na_3AsS_4 (1.72 cm^3/mol). While we need to take caution in interpreting these results, since we found that the ionic conductivity of the Na_3PS_4 sample might not be representative for literature findings on this material, the activation volume of the Na_3PS_4 sample is actually very close to the reported value by Famprikis et al in their study of Na_3PS_4 under pressure (2.33 cm^3/mol) [11].

From the negative value of the activation volumes, we can deduce that in some way the applied pressure is inhibiting ion hopping. Considering the findings on the Na-ion migration pathway (NEB), from which we know that the process of ion conduction through the lattice is associated with an expanded Ch-Ch bottleneck size, it is possible that the reduced conductivity under pressure is a direct result of a more narrow bottleneck of conduction. When investigating the bottleneck distances at RT, as determined through XRD, we observe that for the synthesized samples the bottleneck descriptor (Ch-Ch distance) follows the same trend as the found activation volumes. This could imply that at room temperature conditions, taking into account the bulk moduli of the samples, the bottleneck distance of the Na_3SbS_4 sample is compressed more than the bottleneck distance of the Na_3AsS_4 and Na_3PS_4 distance, explaining the larger activation volume. Similar analyses of the conduction pathway to those shown in section 7.3 could be employed in future studies to investigate the relation between the activation volume and the conduction bottleneck in more detail.

It must be noted that solely based on these impedance measurements, it is difficult to exactly explain the differences in activation volumes. When comparing the impedance values to the NEB results, there are many factors present in the impedance measurement that are not considered in the calculations, including particle size, particle stacking, effects of the electrode electrolyte interface, micro-strain and local lattice defects. To truly investigate the effects of pressure on the ionic conductivity, it is therefore worthwhile to combine measurements of the impedance of the structures with a detailed structural analysis of the sample through SEM or TEM, to relate the aforementioned characteristics to the differences in ionic conductivity.

8.3 Temperature effects on the conductivity – the activation energy

To investigate the effects of temperature on the ionic conductivity, impedance measurements on a series of temperatures were performed for the three isostructural compounds. For the Na_3PS_4 and Na_3AsS_4 samples, measurements were performed for a temperature range of 40 to 100 °C, whereas for the Na_3SbS_4 sample a temperature range of -50 to 0 °C was measured. The Na_3SbS_4 sample was measured at low temperatures to allow for accurate fitting of the bulk-conductivity semi-circle in the Nyquist plots, because with the high conductivity of the sample this became difficult at higher temperatures. It was noticed that for temperatures above 70 °C an additional effect arose in the impedance measurements of the Na_3PS_4 and Na_3AsS_4 samples, as seen by the additional semi-circle in the Nyquist plot (partially visible in the 100 °C measurement of Na_3AsS_4 in Figure 8.5, yellow). As such, the temperature measurements of the Na_3PS_4 and Na_3AsS_4 were fitted with an additional CPE-R element in series, to account for the extra semi-circle. The origin of why this occurred is unclear; it is possible that the semi-circle is a result of an decreased resistance in the blocking electrodes used on each side of the electrolyte, but further investigation is necessary to confirm this.

Activation energies were calculated from the impedance measurements using

$$\boldsymbol{E_a = -k_B \left(\frac{\partial \ln(\sigma T)}{\partial T^{-1}}\right)_P} \qquad (32)$$

The results of the temperature series are shown in Figure 8.5 and Figure 8.6.

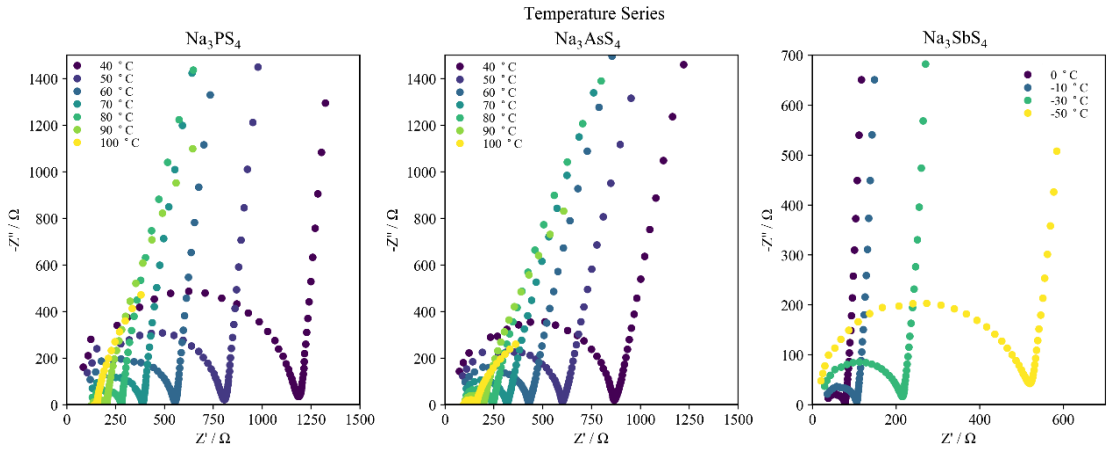

Figure 8.5. Nyquist plots of the impedance measurements at different temperatures for the three different isostructural compounds: Na_3PS_4 (left), Na_3AsS_4 (middle) and Na_3SbS_4 (right). In the 100 °C line on the Na_3AsS_4 a clear example can be seen of the additional semi-circle that arose at high temperature measurements.

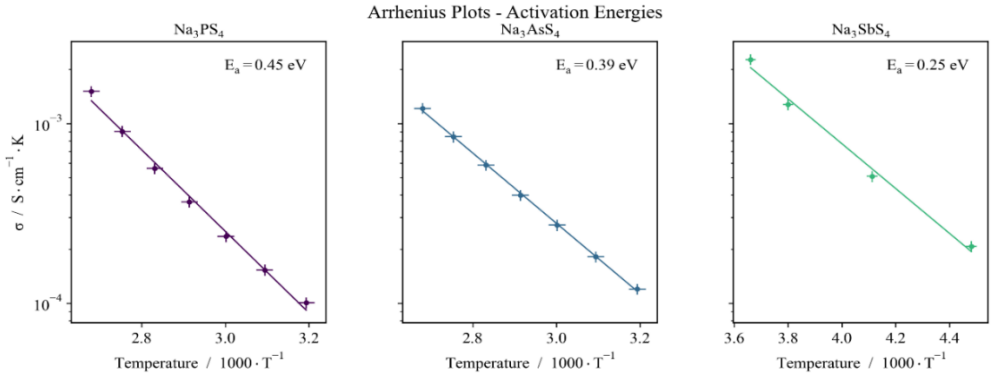

Figure 8.6. The ionic conductivities are plotted against T^{-1}, to determine the experimental activation energies.

The activation energies determined through EIS show a significantly different trend from the activation barriers as determined through NEB: where the NEB activation barrier was highest for Na_3AsS_4 (0.076 eV), follow by Na_3PS_4 (0.069 eV) and finally Na_3SbS_4 (0.059 eV), the experimental activation energies followed a decreasing trend from Na_3PS_4 (0.45 eV) to Na_3AsS_4 (0.39 eV) to Na_3SbS_4 (0.25 eV).

The large differences in the activation energies in general and between the NEB activation barriers and the impedance values highlight several important differences between the two types of activation energy. The positive values of the experimental activation energy indicate that as temperature increases, so does conductivity. Given the influence of temperature on the kinetic energies of the atoms making up the structure, there are several different consequences of the increased temperature that can cause the increased conductivity, all which are captured in the activation energy. For instance, the experimental activation energy is explicitly related to the process of thermal activation, where the increased kinetic energy allows the Na-ion to pass the energy barrier much more easily (more successful ion hops). Furthermore, the increased vibrational frequency of the ions at higher temperature are fundamentally related to the concept of the attempt frequency, where at a higher temperature the increased vibrational frequency of the ion increases the amount of times the ion approaches the conduction bottleneck. This indicates that it might be more appropriate to systematically differentiate between the activation energies from EIS and NEB, in terms of the activation barrier and the thermal activation energy. The different effects of temperature on the lattice dynamics unfortunately also make it very difficult to deconvolute their effects on the activation energy, and therefore explain the differences between the isostructural compounds. For this, an intermediate approach that can more directly relate the thermal effects (vibrational modes, attempt frequency) to the conduction process is required. *Ab initio* molecular dynamics simulations could provide an outcome for this, since in *ab initio* molecular dynamics both a temperature and time component are introduced in the DFT calculations, making it possible to calculate the ion-dynamics at the quantum mechanical level.

The many different macroscopic effects at play in impedance measurements provide yet another perspective on the conduction process. The most important findings on the activation energies, volumes and conductivities are summarized in Table 8.1. We find that the ionic conductivities from literature relate accurately to the activation barriers found in NEB and that while the bottleneck of diffusion is not a great predictor of the overall conductivity, it might hold a strong relation to the activation volume.

Table 8.1. Summary of the different descriptors that are used to quantify the ease of ion migration in this work: the activation volume, the activation energy and the ionic conductivity.

Isostructure	**Na_3PS_4**		**Na_3AsS_4**		**Na_3SbS_4**	
	DFT - NEB	EIS	DFT - NEB	EIS	DFT - NEB	EIS
Activation Energy / eV	0.0692	0.4638	0.0759	0.3719	0.0586	0.2475
Activation Volume / $cm^3 \cdot mol^{-1}$	1.62	2.35	1.92	1.72	2.14	3.44
Ionic Conductivity (this work) / $mS \cdot cm^{-3}$	-	0.0447	-	0.0527	-	1.79
Ionic Conductivity (literature) / $mS \cdot cm^{-3}$	-	0.2 – 0.46[8]	-	0.027[8]	-	1.05[22]

8.4 Summary: on macroscopic ionic conductivity

To quantify the ionic conductivity of the samples and get more information on the ion-dynamics at finite temperatures, impedance measurements on all three isostructural compounds were performed. Through these measurements, the ionic conductivities of the samples were determined to be 0.0447 mS / cm^3 for Na_3PS_4, 0.0527 mS / cm^3 for Na_3AsS_4 and 1.79 mS / cm^3 for Na_3SbS_4. Comparing these results to literature we find that the ionic conductivities of the Na_3AsS_4 and Na_3SbS_4 samples are close to other reported values[8,22], but that the ionic conductivity of the Na_3PS_4 sample is smaller than in literature[8]. It is possible that this effect is the result of improper densification of the electrolyte powder, but further investigation is required to confirm this.

A monotonic trend was found when comparing the activation barriers from NEB to the ionic conductivities from literature: the lower the activation barrier in NEB, the higher the ionic conductivity. This is an important finding, since it shows that the different static and dynamic descriptors that predict the activation barrier are also predictive of the trend ionic conductivities, which could help when attempting to find potential candidate structures for enhancing and improving current solid-state electrolytes.

When measuring the ionic conductivities under pressure, we observe a non-monotonic trend in experimental activation volumes, where the V_a of Na_3SbS_4 is highest (3.44 cm^3/mol), followed by Na_3PS_4 (2.35 cm^3/mol) and finally Na_3AsS_4 (1.72 cm^3/mol). While these differences in activation volume must be interpreted with caution (since the Na_3PS_4 sample might not be representative), it is possible that these differences are related to the observed bottleneck sizes: the larger bottleneck in the Na_3SbS_4 sample might be compressed more than the others as a result of pressure, which could lead to a larger decrease in conductivity.

Temperature dependant impedance measurements show a clear decrease in activation energy with the Pn substitution: from Na_3PS_4 (0.45 eV) to Na_3AsS_4 (0.39 eV) to Na_3SbS_4 (0.25 eV). While this trend does not match with the trend in calculated energy barriers through NEB, it is not unlikely given the different natures of the two activation energies: in NEB only the electron distribution and static forces are considered, whereas in EIS many different thermal effects (such as changes in the vibrational frequencies) are present. It is therefore important to systematically differentiate in analyses on ion conductivity between these two activation energies: the activation barrier and the thermal activation energy.

The different macroscopic effects (thermal effects, microstructural characteristics) provide yet another perspective on the conduction process. Through EIS, we find that the ionic conductivities relate accurately to the activation barriers found in NEB and that while the bottleneck of diffusion is not a great predictor of the overall conductivity, it might hold a strong relation to the activation volume. What is still lacking to complete our understanding of ion conduction in the Na_3PnS_4 structures, is an intermediate approach that can more directly relate the thermal effects of being at non 0K to the conduction process, whilst not having the effects of microstructure present. For this, we recommend future studies to also employ *ab initio* molecular dynamics simulations to study the fundamental conduction mechanism, since in *ab initio* molecular dynamics both a temperature and time component are introduced, making it possible to investigate the ion-dynamics at the most fundamental level.

9. Conclusions and future outlook

Recent studies on various solid-state electrolytes showed that while improvements to the ionic conductivity are progressing swiftly, the understanding of the fundamental conduction mechanism in is still lagging behind. In an attempt to provide a more complete overview of how different static (structural) and dynamic (lattice-ion interaction) properties relate to the ion diffusion mechanism, we investigated the fundamental conduction mechanism in the Na_3PnS_4 structures (Pn = P, As, Sb). For the static influences it was found that with the Pn substitution, the cell volume expands monotonically as a direct result of the increased PnS_4^{3-} tetrahedral volume. This monotonic trend however is unpredictive of the ionic conductivity found in literature, which follow the trend $Na_3AsS_4 < Na_3PS_4 < Na_3SbS_4$. The Ch-Ch distance bottleneck descriptor showed a distinct non-monotonic trend with the substitution, hinting towards a potential effect of the structural differences on the ionic conductivity. The relation was however not strong enough to explain the large differences in ionic conductivity between the structures.

For the dynamic influences on the conductivity, expressed through the lattice stiffness, it was found that none of the indicators of the lattice stiffness showed a clear correlation with the ionic conductivity either. Investigating the bonding nature in the Na_3PnS_4 structures we found several seemingly contradicting findings on bond strength. Based on the melting points Born Effective Charges, vibrational frequencies (Raman) and dissociation energies, it seems that the P-S bonds are significantly stiffer / stronger than the As-S and Sb-S bonds. However, when investigating the differences in electronegativities, Bader Charges and Electron Localization Functions we find that the bonds are least polar (thus "strongest") for As-S, followed by P-S and Sb-S, showing the importance of distinguishing between these two qualities of the Pn-S bonds. Linking these bonding interactions to the conduction mechanism, it was found that the Pn-S bond polarity correlates more strongly with the ionic conductivities than the Pn-S bond stiffness. By investigating the Bader and Born Charges, it was found that the changes in the Na-S bonding interaction are most likely dominated by changes in the S-charge, through a relation inversely related to the electrostatic interaction: for the largest difference in the Na-S charges, which would indicate the largest electrostatic interactions, the ionic conductivity was also largest. This was related to the partial covalent nature of the Na-S bonds, which according to the Pauling Bonding criterion become weaker the larger the charge difference.

By quantifying the activation barriers of the isostructural compounds through NEB, we found that the activation energies of the three isostructural compounds follow the exact same trend as the ionic conductivities as reported in literature: for the Na_3PS_4, Na_3AsS_4 and Na_3SbS_4 structures the activation energies were found to be respectively 69.2 meV, 75.9 meV and 58.6 meV, whereas the ionic conductivities in literature are 0.0447 mS / cm^3 for Na_3PS_4, 0.0527 mS / cm^3 for Na_3AsS_4 and 1.79 mS / cm^3 for Na_3SbS_4. When relating the activation energies to the different materials characteristics, we found that the best predictors of the activation barrier were the Pn Electronegativity and the Pn Bader charge. This observation provides an important insight into the conduction process: while the different dynamic descriptors (melting points, bulk moduli, BEC) capture the lattice stiffness of the structure, the conduction process seems more directly related to the bond polarity.

By investigating the structural changes and changes in the charge distribution along the conduction pathway, we found that the bottleneck of conduction, as coordinated by the four characteristics S-atoms, opens and closes as the ion moves through. As the ion moves closer to

the bottleneck atoms, this opening and closes of the bottleneck is accompanied by a shift in charge from the Pn-atoms to the S-atoms surrounding the bottleneck, and subsequently a shift from electrons from the S-atoms to the Na-atoms (as indicated by the Bader charges). Contrary to expectations, the Coulombic interaction between the Na-ion and the S-atoms around the bottleneck increases most for the Na_3SbS_4 structures, followed by the Na_3AsS_4 structure and finally the Na_3PS_4 structure. It thus seems that it is not the change in Coulombic interaction that predicts the energy barrier most, but the absolute values of the interaction.

Through NEB calculations under pressure we quantified the activation volumes, which increase linearly with the Pn substitution (P → As → Sb). While not in line with the trend in activation energies, this trend can be interpreted based on the bulk moduli of the structures: it is found that as the bulk modulus increases, the activation volume decreases. Since the lower bulk modulus implies a more easily deformable lattice, it makes sense that the effects of pressure on the energy barrier are highest for this structure. The actual ionic conductivity of the samples was quantified using impedance measurements, where the ionic conductivities of the samples were determined to be 0.0447 mS / cm^3 for Na_3PS_4, 0.0527 mS / cm^3 for Na_3AsS_4 and 1.79 mS / cm^3 for Na_3SbS_4. Comparing these results to literature we find that the ionic conductivities of the Na_3AsS_4 and Na_3SbS_4 samples are close to other reported values of 0.027 mS / cm^3 (ref [8]) and 1.05 mS / cm^3 (ref [22]) respectively, but that the ionic conductivity of the Na_3PS_4 sample is much smaller than in literature (0.2 – 0.46 mS / cm^3 (ref [8])).

A monotonic trend was found when comparing the activation barriers from NEB to the ionic conductivities from literature: the lower the activation barrier in NEB, the higher the ionic conductivity. This is an important finding, since it shows that the different static and dynamic descriptors that predict the activation barrier are also predictive of the trend ionic conductivities, which could help us when attempting to find potential candidate structures for enhancing and improving current solid-state electrolytes.

When measuring the ionic conductivities under pressure, we observe a non-monotonic trend in experimental activation volumes with increased Pn-size, where the V_a of Na_3SbS_4 is highest (3.44 cm^3/mol), followed by Na_3PS_4 (2.35 cm^3/mol) and finally Na_3AsS_4 (1.72 cm^3/mol). Temperature dependant impedance measurements show a clear decrease in activation energy with the Pn substitution: from Na_3PS_4 (0.45 eV) to Na_3AsS_4 (0.39 eV) to Na_3SbS_4 (0.25 eV). While this trend does not match with the trend in calculated energy barriers through NEB, it is not unlikely given the different natures of the two activation energies: in NEB only the electron distribution and static forces are considered, whereas in EIS many different thermal effects (such as changes in the vibrational frequencies) are present. It is therefore important to systematically differentiate in analyses on ion conductivity between these two activation energies: the activation barrier and the thermal activation energy.

We thus find that the ionic conductivities correlate with the activation barriers found in NEB and that while the bottleneck of diffusion is not a great predictor of the overall conductivity, it might hold a strong relation to the activation volume. The most accurate predictors of the ionic conductivity seem to be the indicators of bond polarity in the PnS_4^{3-} anions, through the Pn Bader charge and Pn electronegativity. What is still lacking to complete our understanding of ion conduction in the Na_3PnS_4 structures, is an intermediate approach that can more directly relate the thermal effects of being at non 0K to the conduction process. For this, *ab initio* molecular dynamics simulations could provide an outcome.

Acknowledgements

This thesis would never have been possible without the help of many different people. Firstly, I would like to thank Marnix for his role as my supervisor, his constructive approach in the meetings we had and being a part of my thesis defence committee, together with Pedro and Anna, to whom I am also very grateful. Secondly, I would like to thank all the people who've helped me to get a hold of the different techniques applied in this work, both experimentally and computationally. Work in the lab wouldn't have been possible without the assistance of Frans and Esther, and I'd be completely lost in the world of DFT without Tammo, Alexandros, Piero and Jouke.

There are several people who deserve special thanks, not only because of their great assistance with the work, but also because of their contributions to life at the RID in general.

Thanks to Victor, as part-time co-supervisor; without you I would never even have been able to perform a single VASP run, and given the high concentration of DFT related findings I'm pretty sure that would have been quite detrimental for the project.

Thanks to Hanan, for being the most joyful guide in both the lab and at the coffee corner: without my beautiful (sometimes somewhat philosophical) conversations with you I'd never have enjoyed working on the project this much.

Thanks to Jan, for well, being the best co-masterstudent-masterprenker-Na_3SbS_4-king-physicist-torrentlord-andmuchmore that I could have wished for.

Thank to Dennis, for printing, printing, printing, so-much carpool karaoke and always casually waiting whenever I was once again working 15 minutes longer than I said I would.

Thanks to John Cleese, because well, you know.

And finally ***thanks to Theo***, for being the Gandalf to my Bilbo: the perfect guide to help me through the project, always there when needed and never there when not expected. May he, much like Gandalf, listen to his own advice for many years to come.

References

1. Famprikis, T., Canepa, P., Dawson, J. A., Islam, M. S. & Masquelier, C. Fundamentals of inorganic solid-state electrolytes for batteries. *Nat. Mater.* **18**, 1278–1291 (2019).

2. Janek, J. & Zeier, W. G. A solid future for battery development. *Nat. Energy* **1**, 16141 (2016).

3. De Klerk, N. J. J. & Wagemaker, M. Diffusion Mechanism of the Sodium-Ion Solid Electrolyte Na_3PS_4 and Potential Improvements of Halogen Doping. *Chem. Mater.* **28**, 3122–3130 (2016).

4. Jansen, M. Volume Effect or Paddle-Wheel Mechanism—Fast Alkali-Metal Ionic Conduction in Solids with Rotationally Disordered Complex Anions. *Angew. Chemie Int. Ed. English* **30**, 1547–1558 (1991).

5. Wang, Y. *et al.* Design principles for solid-state lithium superionic conductors. *Nat. Mater.* **14**, 1026–1031 (2015).

6. Ohno, S. *et al.* Materials design of ionic conductors for solid state batteries. *Prog. Energy* **2**, 022001 (2020).

7. Hayashi, A., Noi, K., Sakuda, A. & Tatsumisago, M. Superionic glass-ceramic electrolytes for room-temperature rechargeable sodium batteries. *Nat. Commun.* **3**, (2012).

8. Yu, Z. *et al.* Exceptionally High Ionic Conductivity in Na 3 P 0.62 As 0.38 S 4 with Improved Moisture Stability for Solid-State Sodium-Ion Batteries. (2017) doi:10.1002/adma.201605561.

9. Fuchs, T., Culver, S. P., Till, P. & Zeier, W. G. Defect-Mediated Conductivity Enhancements in $Na_{3-x}Pn_{1-x}W_xS_4$ (Pn = P, Sb) Using Aliovalent Substitutions. *ACS Energy Lett.* **5**, 146–151 (2020).

10. Shang, S.-L., Yu, Z., Wang, Y., Wang, D. & Liu, Z.-K. Origin of Outstanding Phase and Moisture Stability in a Na 3 P 1– x As x S 4 Superionic Conductor. *ACS Appl. Mater. Interfaces* **9**, 16261–16269 (2017).

11. Famprikis, T. *et al.* Under pressure: Mechanochemical effects on structure and ion conduction in the sodium-ion solid electrolyte Na3PS4. *J. Am. Chem. Soc.* **142**, 18422–18436 (2020).

12. Deng, Z., Wang, Z., Chu, I.-H., Luo, J. & Ong, S. P. Elastic Properties of Alkali Superionic Conductor Electrolytes from First Principles Calculations. *J. Electrochem. Soc.* **163**, A67–A74 (2016).

13. Hayashi, A. *et al.* A sodium-ion sulfide solid electrolyte with unprecedented conductivity at room temperature. *Nat. Commun.* **10**, 5266 (2019).

14. Yubuchi, S. *et al.* Aqueous solution synthesis of Na_3SbS_4–Na_2WS_4 superionic conductors. *J. Mater. Chem. A* **8**, 1947–1954 (2020).

15. Tsuji, F., Nasu, A., Sakuda, A., Tatsumisago, M. & Hayashi, A. Mechanochemical synthesis and characterization of Na3–xP1–xWxS4 solid electrolytes. *J. Power Sources* **506**, 230100 (2021).

16. Culver, S. P. *et al.* Evidence for a Solid-Electrolyte Inductive Effect in the Superionic

Conductor Li10Ge1-xSnxP2S12. *J. Am. Chem. Soc.* **142**, 21210–21219 (2020).

17. Till, P. *et al.* Two-dimensional substitution series highlighting the insufficient description of structural bottlenecks on the Na+ ionic transport in Na3P1−xSbxPS4−ySey.

18. Krauskopf, T., Culver, S. P. & Zeier, W. G. Bottleneck of Diffusion and Inductive Effects in Li10Ge1- xSnxP2S12. *Chem. Mater.* **30**, 1791–1798 (2018).

19. Kraft, M. A. *et al.* Influence of Lattice Polarizability on the Ionic Conductivity in the Lithium Superionic Argyrodites Li6PS5X (X = Cl, Br, I). *J. Am. Chem. Soc.* **139**, 10909–10918 (2017).

20. Nishimura, S., Hayashi, A., Sakuda, A. & Yamada, A. *Vacancy-Stabilized Superionic State in Na*.

21. Fu, Z. *et al.* Stress Regulation on Atomic Bonding and Ionic Diffusivity: Mechanochemical Effects in Sulfide Solid Electrolytes. *Energy & Fuels* acs.energyfuels.1c00488 (2021) doi:10.1021/acs.energyfuels.1c00488.

22. Wang, H. *et al.* An Air-Stable Na 3 SbS 4 Superionic Conductor Prepared by a Rapid and Economic Synthetic Procedure. *Angew. Chemie Int. Ed.* **55**, 8551–8555 (2016).

23. Hammond, C. *The Basics of Crystallography and Difraction*. (Oxford University Press, 2009).

24. Kroumova, E., Perez-Mato, J. M. & Aroyo, M. I. WYCKSPLIT: a computer program for determination of the relations of Wyckoff positions for a group-subgroup pair. *J. Appl. Crystallogr.* **31**, 646–646 (1998).

25. Jansen, M. & Henseler, U. Synthesis, structure determination, and ionic conductivity of sodium tetrathiophosphate. *J. Solid State Chem.* **99**, 110–119 (1992).

26. Tanibata, N. *et al.* X-ray Crystal Structure Analysis of Sodium-Ion Conductivity in 94 Na 3 PS 4 ·6 Na 4 SiS 4 Glass-Ceramic Electrolytes. *ChemElectroChem* **1**, 1130–1132 (2014).

27. Famprikis, T. *et al.* A New Superionic Plastic Polymorph of the Na+Conductor Na3PS4. *ACS Mater. Lett.* **1**, 641–646 (2019).

28. Famprikis, T. *et al.* Under Pressure: Mechanochemical Effects on Structure and Ion Conduction in the Sodium-Ion Solid Electrolyte Na 3 PS 4. *J. Am. Chem. Soc.* **142**, 18422–18436 (2020).

29. Momma, K. & Izumi, F. VESTA 3 for three-dimensional visualization of crystal, volumetric and morphology data. *J. Appl. Crystallogr.* **44**, 1272–1276 (2011).

30. Rush, L. E., Hood, Z. D. & Holzwarth, N. A. W. Unraveling the electrolyte properties of Na_3SbS_4 through computation and experiment. *Phys. Rev. Mater.* **1**, 075405 (2017).

31. Feng, X. *et al.* Heavily Tungsten Doped Sodium Thioantimonate Solid State Electrolytes with Exceptionally Low Activation Energy for Ionic Diffusion. *Angew. Chemie Int. Ed.* (2021) doi:10.1002/anie.202110699.

32. Stoneham, A. M. (Ed. . *Ionic solids at high temperatures (Vol. 2)*. (World Scientific, 1989).

33. Lin, Y.-Y. *et al.* Toward design of cation transport in solid-state battery electrolytes: Structure-dynamics relationships. *Curr. Opin. Solid State Mater. Sci.* **24**, 100875 (2020).

34. Ohno, S. *et al.* Materials design of ionic conductors for solid state batteries. *Prog. Energy* **2**, 022001 (2020).

35. Vineyard, G. H. Frequency Factors and Isotope Effects in Solid State Rate Processes. *J. Phys. Chem. Solids* **3**, 121–127 (1957).

36. Allen, S. J.; Remeika, J. P. Direct Measurement of the Attempt Frequency for Ion Diffusion in Ag and Na Beta-Alumina. *Phys. Rev. Lett.* **33 (25)**, 1478–1481 (1974).

37. Wakamura, K. Roles of phonon amplitude and low-energy optical phonons on superionic conduction. *Phys. Rev. B* **56**, 11593–11599 (1997).

38. Pompe, C. Strukturchemie und elektrische Leitfähigkeiten von Natriumchalkogenometallaten. *Dissertation* (Universität Regensburg, 2016).

39. Famprikis, T. *Thèse de Doctorat Studies on inorganic solid electrolytes for batteries: Focus on Na3PS4. Doctoral Thesis* (2020).

40. LibreTexts. Bragg's Law. (2021).

41. Yu, C., Ganapathy, S., de Klerk, N. J. J., van Eck, E. R. H. & Wagemaker, M. Na-ion dynamics in tetragonal and cubic Na3PS4, a Na-ion conductor for solid state Na-ion batteries. *J. Mater. Chem. A* **4**, 15095–15105 (2016).

42. Petříček, V., Dušek, M. & Palatinus, L. Crystallographic Computing System JANA2006: General features. *Zeitschrift für Krist. - Cryst. Mater.* **229**, 345–352 (2014).

43. Schwietert, T. K. Ab initio molecular dynamics simulations and experimental study on Li6PS5Cl interfaces for future solid-state Li-ion batteries. *Master Thesis* (Delft University of Technology, 2017).

44. Murbach, M., Gerwe, B., Dawson-Elli, N. & Tsui, L. impedance.py: A Python package for electrochemical impedance analysis. *J. Open Source Softw.* **5**, 2349 (2020).

45. MATLAB. Version 9.10 (R2021a). (2021).

46. F. A. Lindemann. No Title. *Phys. Zeitschrift* **11**, 609 (1910).

47. Rabinovich, S., Voronel, A. & Peretzman, L. Generalisation of the lindemann criterion for disordered mixed crystals. *J. Phys. C Solid State Phys.* **21**, 5943–5952 (1988).

48. Intertek. Differential Scanning Calorimetry (DSC) Analysis. https://www.intertek.com/analysis/dsc/ (2021).

49. Vasileiadis, A. *Modeling Electrode Materials Bridging Nanoscale to Mesoscale. TU Delft University* (2018).

50. Sholl, D. S. & Steckel, J. A. *Density Functional Theory. Electrocatalysis: Computational, Experimental, and Industrial Aspects* (John Wiley & Sons, Inc., 2009). doi:10.1002/9780470447710.

51. Katsura, T. & Tange, Y. A Simple Derivation of the Birch–Murnaghan Equations of State (EOSs) and Comparison with EOSs Derived from Other Definitions of Finite Strain. *Minerals* **9**, 745 (2019).

52. Kresse, G. & Hafner, J. Ab initio molecular dynamics for liquid metals. *Phys. Rev. B* **47**, 558–561 (1993).

53. VASP. The VASP Manual. https://www.vasp.at/wiki/index.php/The_VASP_Manual.

54. Bergerhoff, G., Hundt, R., Sievers, R. & Brown, I. D. The inorganic crystal structure data base. *J. Chem. Inf. Comput. Sci.* **23**, 66–69 (1983).

55. Fuchs, M. Comparison of exchange-correlation functionals : from LDA to GGA and beyond. (2005).

56. Tulip, P. R. Phonon-Electric Field Coupling: Born Effective Charges. http://cmt.dur.ac.uk/sjc/thesis_prt/node56.html (2004).

57. Spaldin, N. The Beginner's Guide to the Modern Theory of Polarization. Module 7: The Born Effective Charge. https://www.youtube.com/watch?v=_hoYTuu9GvA (2020).

58. Roy, A. *et al.* Electronic structure, Born effective charges and spontaneous polarization in magnetoelectric gallium ferrite. *J. Phys. Condens. Matter* **23**, 325902 (2011).

59. Roy, A., Prasad, R., Auluck, S. & Garg, A. First-principles calculations of Born effective charges and spontaneous polarization of ferroelectric bismuth titanate. *J. Phys. Condens. Matter* **22**, 165902 (2010).

60. Manz, T. A. & Limas, N. G. Introducing DDEC6 atomic population analysis: part 1. Charge partitioning theory and methodology. *RSC Adv.* **6**, 47771–47801 (2016).

61. Khaledialidusti, R. Bader Charge Analysis using VASP and Charge Density Difference Plot using VESTA. https://www.youtube.com/watch?v=UxPrN7KcswA (2020).

62. Tang, W., Sanville, E. & Henkelman, G. A grid-based Bader analysis algorithm without lattice bias. *J. Phys. Condens. Matter* **21**, 084204 (2009).

63. Koumpouras, K. & Larsson, J. A. Distinguishing between chemical bonding and physical binding using electron localization function (ELF). *J. Phys. Condens. Matter* **32**, 315502 (2020).

64. Walsh, A., Sokol, A. A., Buckeridge, J., Scanlon, D. O. & Catlow, C. R. A. Oxidation states and ionicity. *Nat. Mater.* doi:10.1038/s41563-018-0165-7.

65. Miessler, G., Fischer, P. & Tarr, D. *Inorganic Chemistry*. (Pearson).

66. Bader, R. F. W. *An Introduction to the Electronic Structure of Atoms and Molecules*. (Clarke, Irwin & Co. Ltd., 1970).

67. Allred, A. L. Electronegativity values from thermochemical data. *J. Inorg. Nucl. Chem.* **17**, 215–221 (1961).

68. Kunaseth, M. Transition State Calculation Using Nudge Elastic Band (NEB). https://www.youtube.com/watch?v=2PotR4_sV_0&t=226s (2019).

69. Iannuzzi, M. CP2L: NEB & Free Energy Calculations. https://www.youtube.com/watch?v=t8jxq4e0Qtw&t=1s (2019).

70. Sheppard, D., Xiao, P., Chemelewski, W., Johnson, D. D. & Henkelman, G. A generalized solid-state nudged elastic band method. *J. Chem. Phys.* **136**, 074103 (2012).

71. London, I. C. Shannon Radii - Database of ionic radii.

http://abulafia.mt.ic.ac.uk/shannon/ptable.php (2022).

72. Luo, Y. R. Comprehensive handbook of chemical bond energies. *Compr. Handb. Chem. Bond Energies* 1–1656 (2007) doi:10.1201/9781420007282.

73. Yu, Z. *et al.* Exceptionally High Ionic Conductivity in Na3P0.62As0.38S4 with Improved Moisture Stability for Solid-State Sodium-Ion Batteries. *Adv. Mater.* **29**, 1605561 (2017).

74. Liao, Y. Practical Electron Microscopy and Database. https://www.globalsino.com/EM/page2118.html (2006).

75. Jain, A. *et al.* Commentary: The Materials Project: A materials genome approach to accelerating materials innovation. *APL Mater.* **1**, 011002 (2013).

76. Statista. High Demand for Lithium-Ion Batteries. (2021).

Appendix A. – Orbital hybridization in bonding

One of the elements that affects the electronegativity is the hybridization of orbitals. Following a similar logic to how electronegativity scales with group and period, it is easy to see how orbital hybridization results in a change in electronegativity. In hybridized orbitals, electrons that participate in bonding come from different orbitals. In for example the ground state of a carbon atom ($1s^2$, $2s^2$, $2p^2$) the 2s and 2p electrons could participate in bonding. However, in this scenario binding would require much less energy for the 2p electrons than the tightly bound 2s electrons. It turn out that the energy released by bonding makes that it is energetically favourable for the C-atom to excite one 2s electron to a 2p state and then make four different bonds. This would mean still mean however that 3 of the 2p electrons and a single 2s electron are the valence electrons participating in bonding. Quantum mechanics shows that a linear superposition of the three 2p and one 2s electrons actually leads to the lowest energy state: it is this effect of mixing binding orbitals that is known as orbital hybridization. This orbital hybridization is visualised in Figure A.1. An hybrid orbital can have more p-character (sp^3, consisting of 1 s-orbital and 3 p-orbitals) or more s-character (e.g. sp, consisting of a hybridization of 1 s-orbital and 1 p-orbital). Since the s-shell electrons are more tightly bound to the nucleus, an atom that employs p-character hybrid orbitals will be more heavily polarized than an atom with a more s-character hybrid orbital. The electronegativity of hybridized orbitals thus follows the trend p-character hybrid orbitals < s-character hybrid orbitals. This is important to account for each structure where orbital hybridization plays a large role in the bonding interactions.

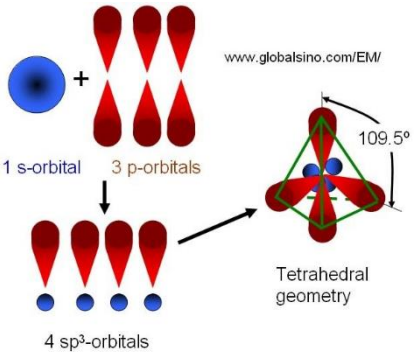

Figure A.1. Orbital hybridization between 1 s-orbital and 3 p-orbitals; the resulting structure would have a tetrahedral geometry due to the equality of the sp^3 bonds. [74]

Appendix B. – DSC Thermograms

This appendix contains the thermograms of the different DSC measurements used to determine the melting points in this work. All measurements are performed by M. Courty and analysed by T. Famprikis. The measured Na_3PS_4 and Na_3SbS_4 samples were synthesized by Famprikis as well, whereas the measured Na_3AsS_4 sample was one synthesized for this work.

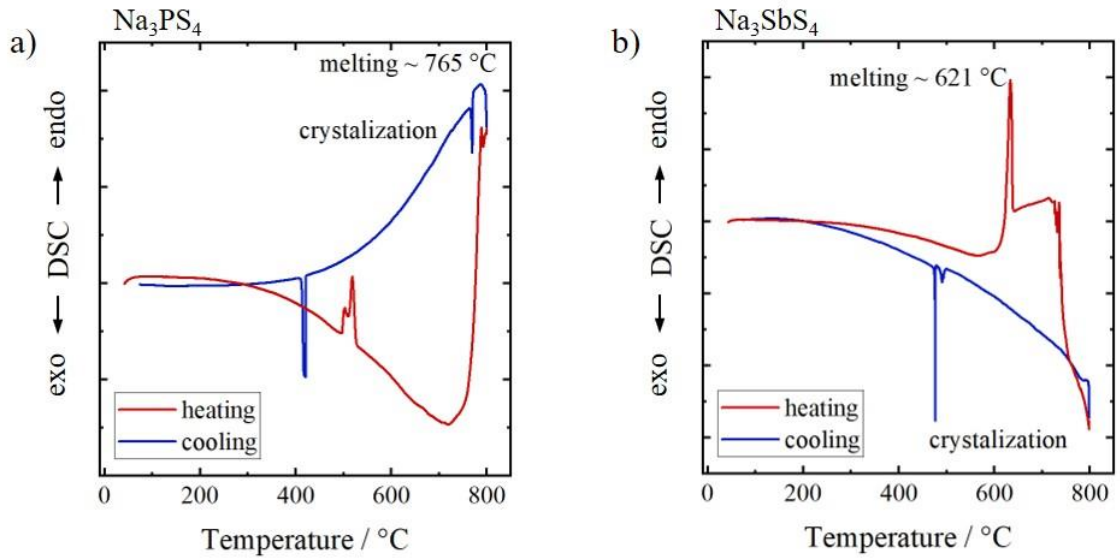

Figure B.1. The thermograms of the Na_3PS_4 and Na_3SbS_4 samples showing the melting point of the materials.The most intense peaks are attributed to the melting process respectively. Determined enthalpies for these processes match those of a melting process.

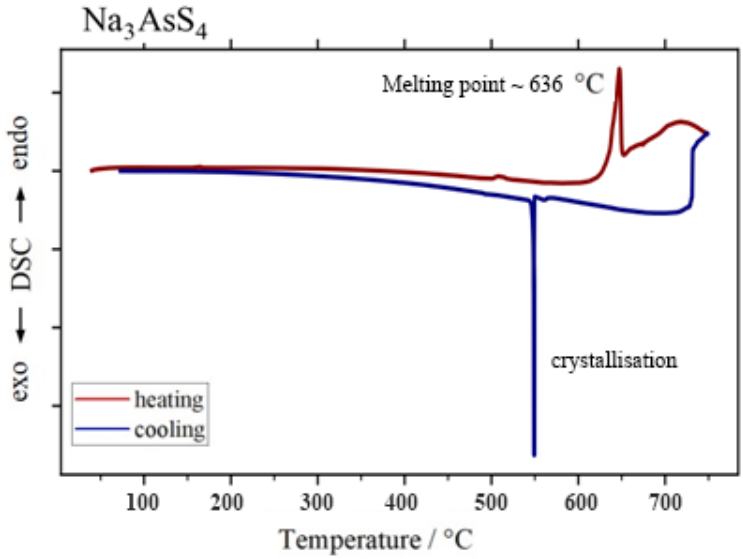

Figure B.2. The thermogram of the Na_3AsS_4 sample showing the melting point 636 °C instead of the previously reported 490 °C. At ~506 °C a small event can be observed.

Appendix C. – Additional Figures Data Analysis

This appendix contains various figures containing supplementary information.

XRD – Different synthesis recipe Na_3SbS_4 diffractogram

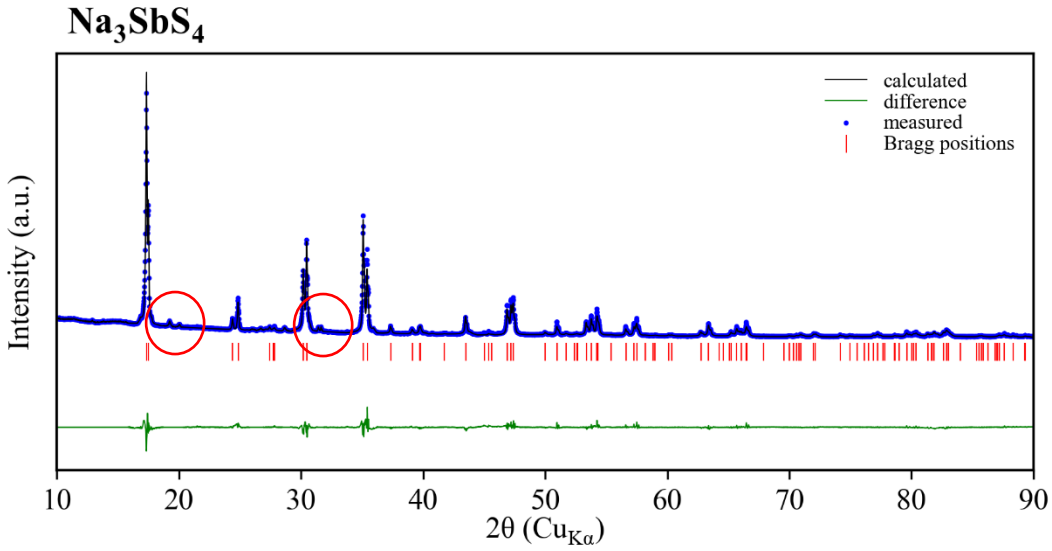

Figure C.1. Diffractogram of the other Na_3SbS_4 sample. The red circles peaks could be matched to Na_3SbS_3, indicating a S-deficit.

Static Descriptors – Bond length Distances Na-S

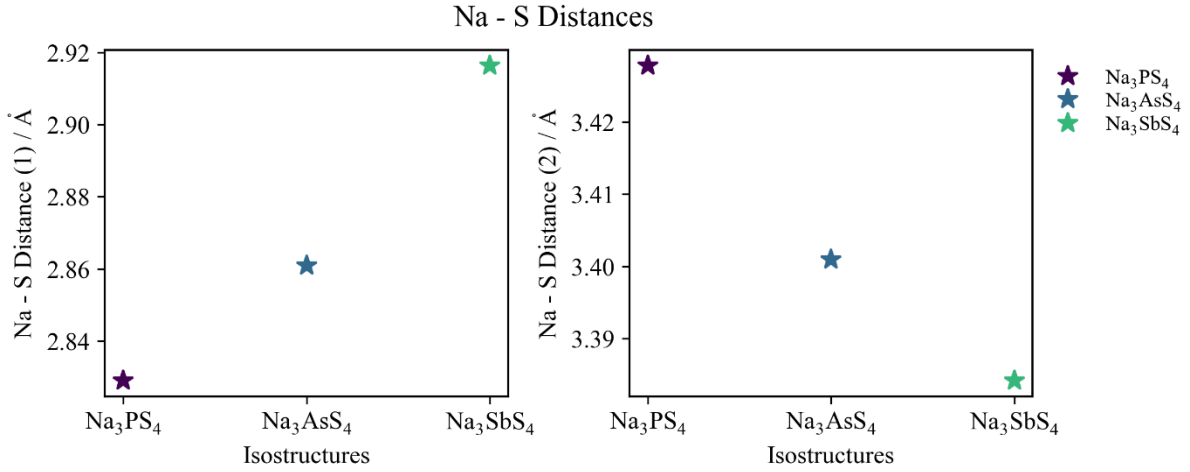

Figure C.2. The Na-S-1 and Na-S-2 bond length distances in the Na_3PnS_4 structures. It can be seen that while the Na-S-1 distance increases with cell volume, the Na-S-2 distance actually decreases.

Bulk Modulus - Energy Fits

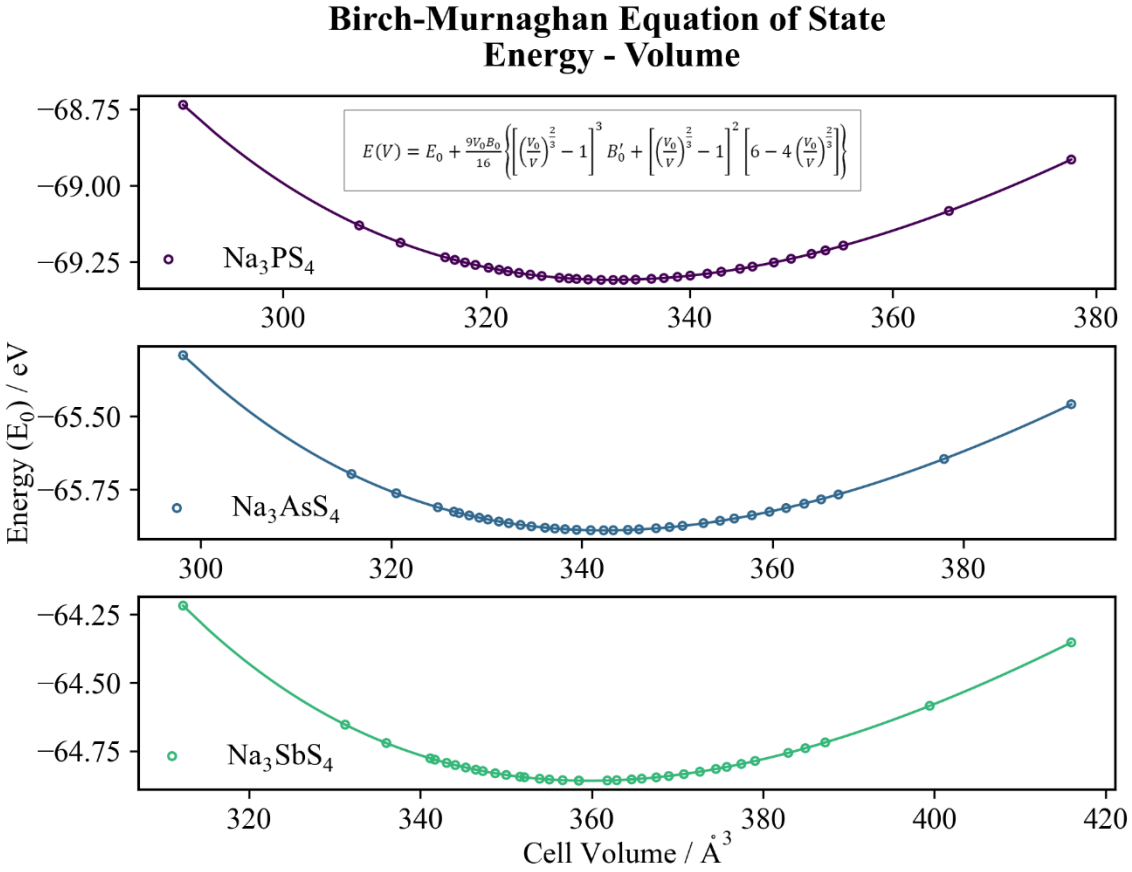

Figure C.3. The energy of the different structures relaxed under pressure plotted against the cell volumes. These energies and volumes were fitted to the Birch Murnaghan equation of state, to calculate the bulk modulus.

Bulk Modulus - Evolution of the bottleneck under pressure

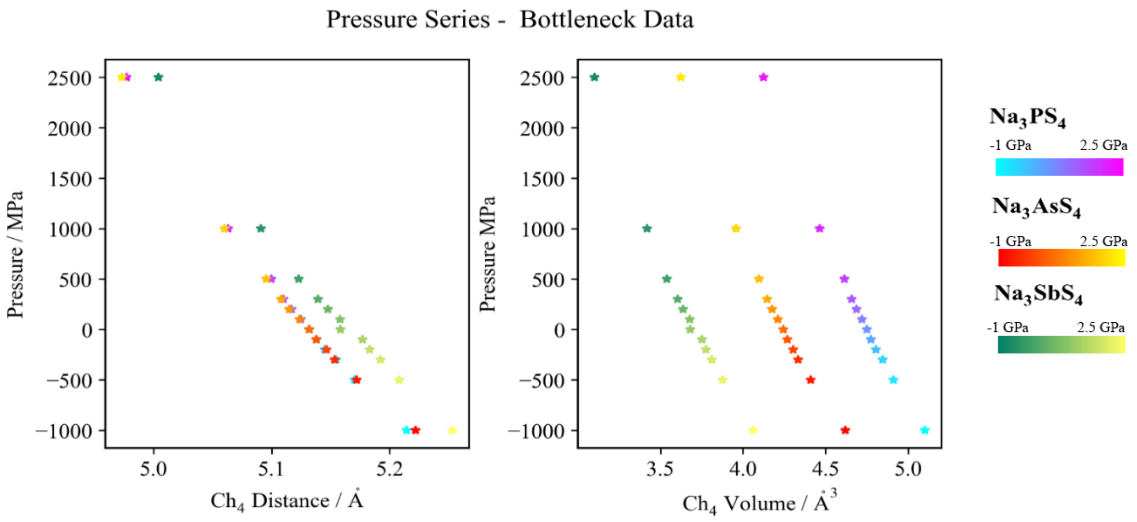

Figure C.4. To relate the differences in the bulk modulus to the conduction process, the bottleneck descriptors were plotted against the pressure. It can be seen that the changes in the bottleneck descriptors (Ch_4 distance, or Ch-Ch distance and Ch_4 volume) are comparable for the three structures.

NEB under pressure - relationship between the bottleneck and activation energies

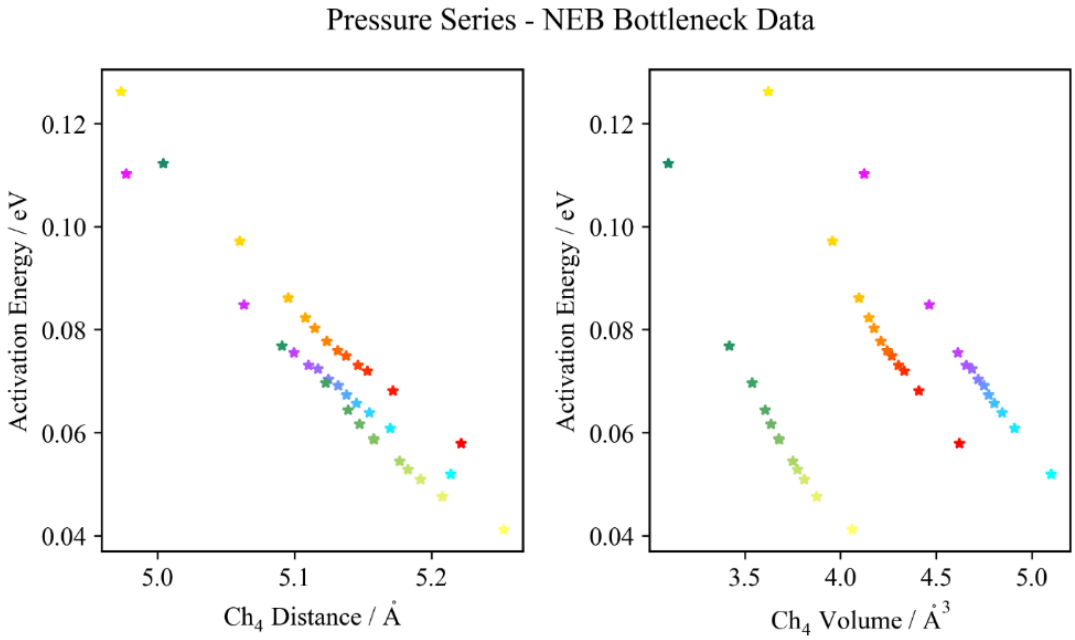

Figure C.5. To check for a relation between the bottleneck and the activation volumes, the bottleneck descriptors were plotted against the activation energies. No specific trend in the isostructural compounds could be identified linking to the fundamental conduction mechanism.

NEB into the Run - Bader Charge data

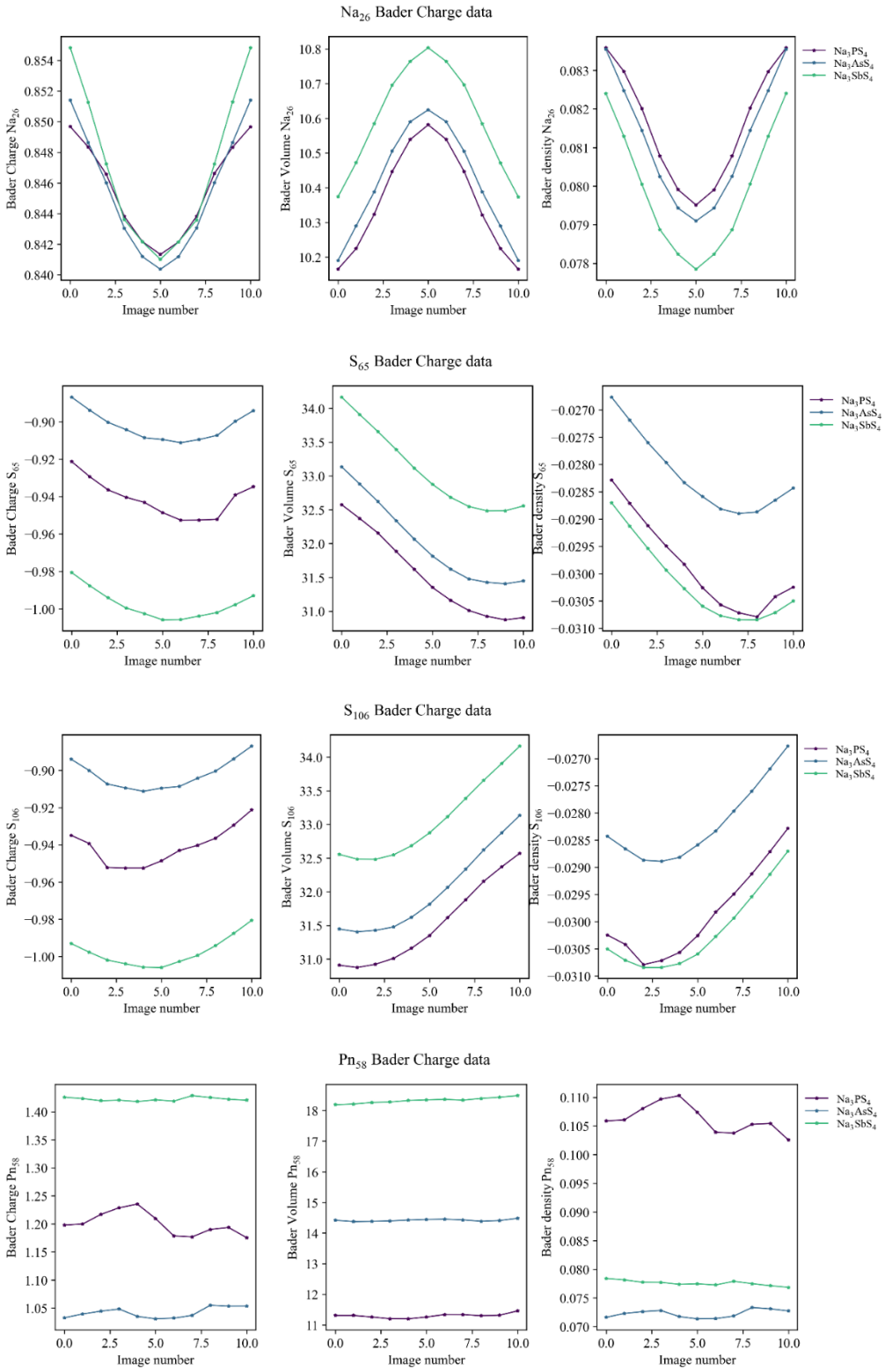

Figure C.6. The changes in the Bader charges along the fundamental conduction pathway for the most important ions, namely the Na_{26}, S_{65}, S_{106} and Pn_{58} ions.

NEB into the Run - Born Effective Charge Data

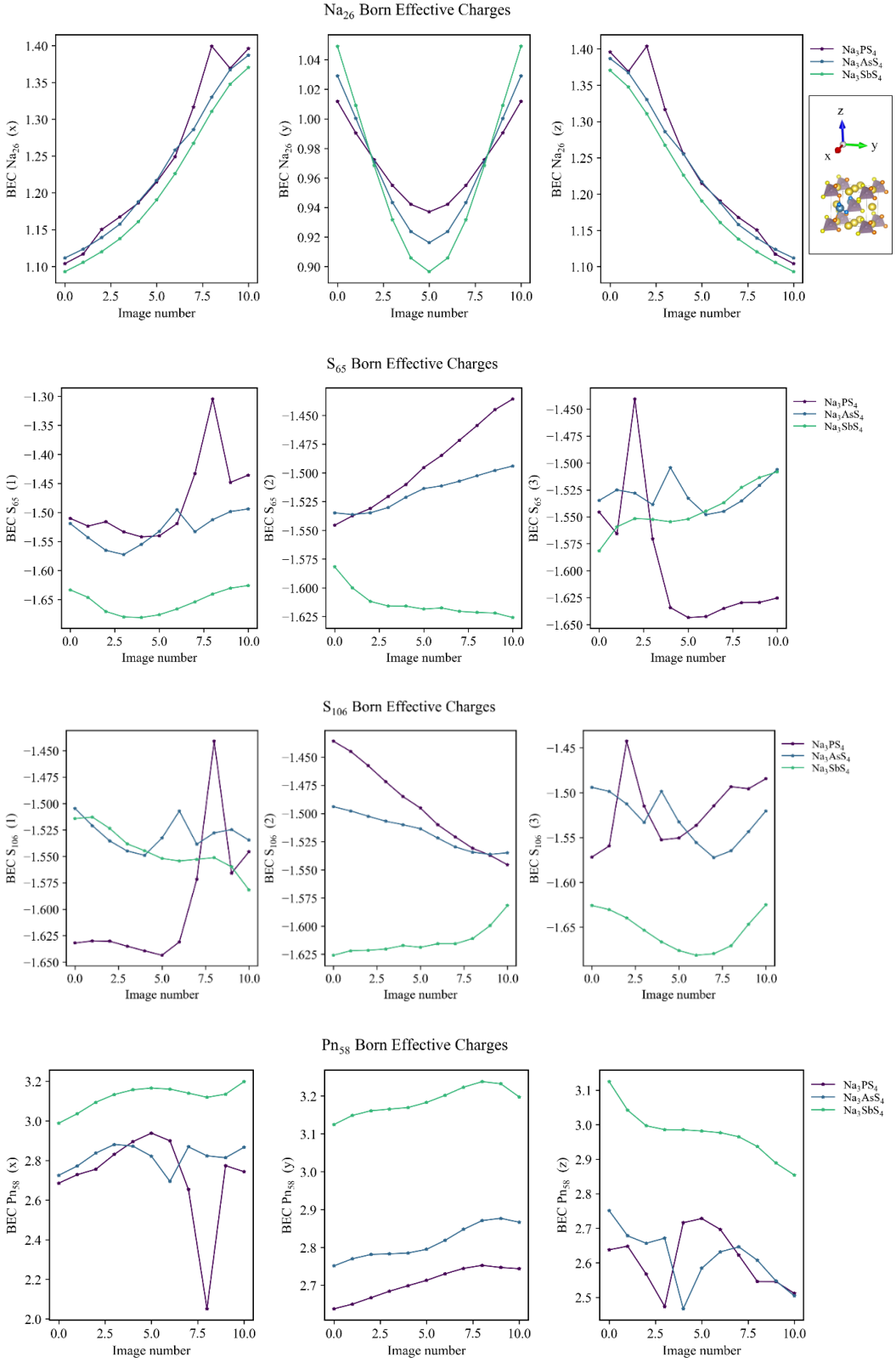

Figure C.7. The changes in the Born Effective Charges along the fundamental conduction pathway for the most important ions, namely the Na_{26}, S_{65}, S_{106} and Pn_{58} ions.

Impedance measurements: fits of the main Na_3AsS_4 and Na_3SbS_4 measurement

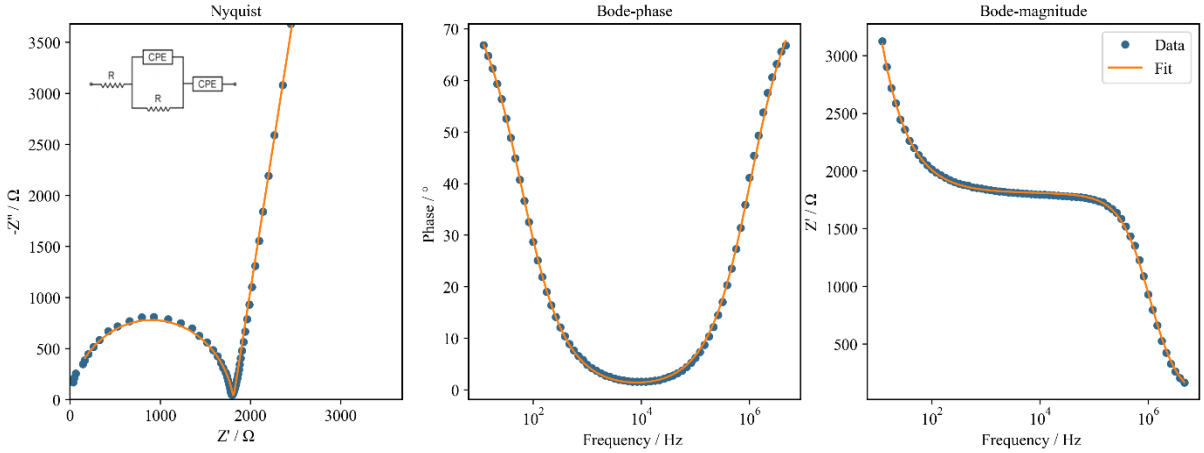

Figure C.8. The Nyquist, Bode-phase and Bode-magnitude representations of the main impedance measurement of the Na_3AsS_4 sample.

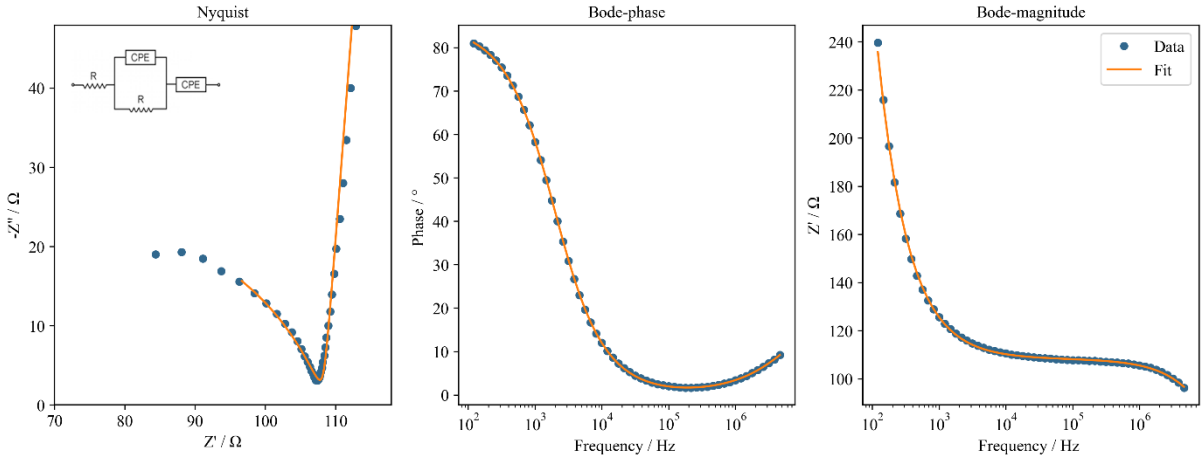

Figure C.9. The Nyquist, Bode-phase and Bode-magnitude representations of the main impedance measurement of the Na_3SbS_4 sample.

Impedance measurements: complete series up and down

Na_3PS_4

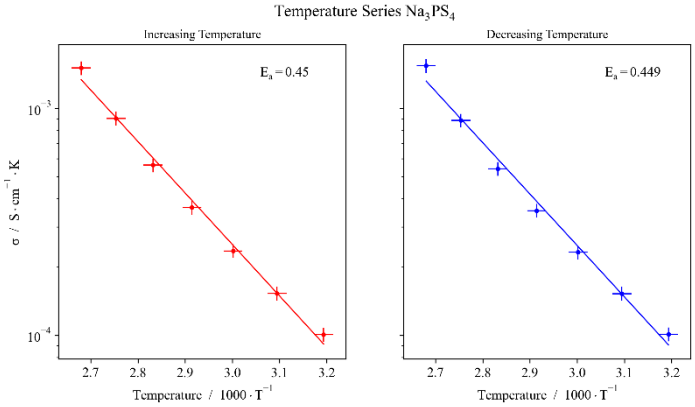

Figure C.10. The conductivity plotted against the inverse of the temperature for the complete temperatures series of the Na_3PS_4 sample, both on the way up (increasing temperature, left) and down (decreasing temperature, right).

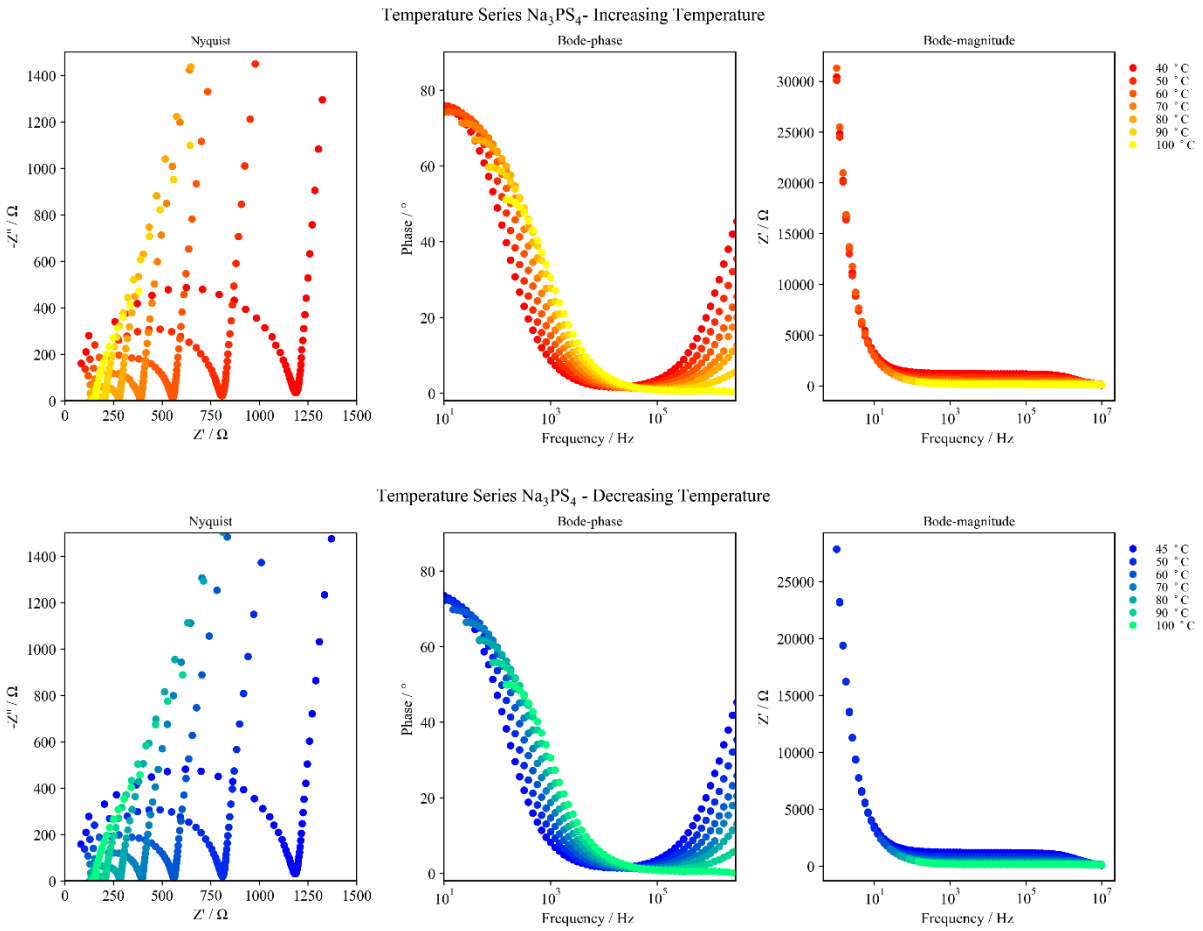

Figure C.11. The Nyquist, Bode-phase and Bode-magnitude representations belonging to the impedance measurements of the temperature series of Na_3PS_4.

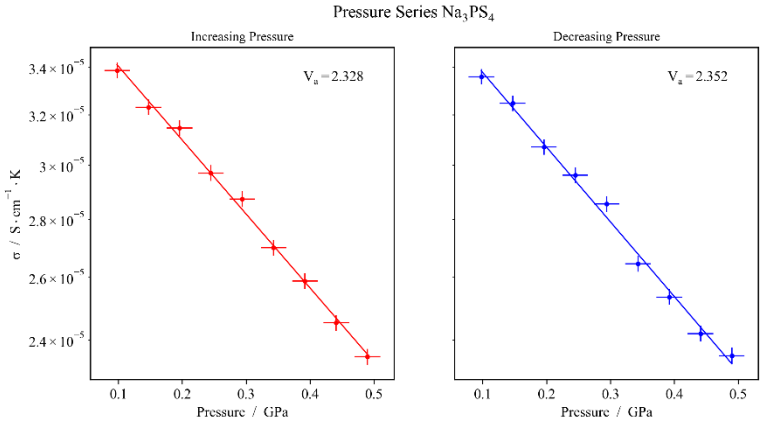

Figure C.12. The conductivity plotted against the pressure for the complete pressure series of the Na_3PS_4 sample, both on the way up (increasing pressure, left) and down (decreasing pressure, right).

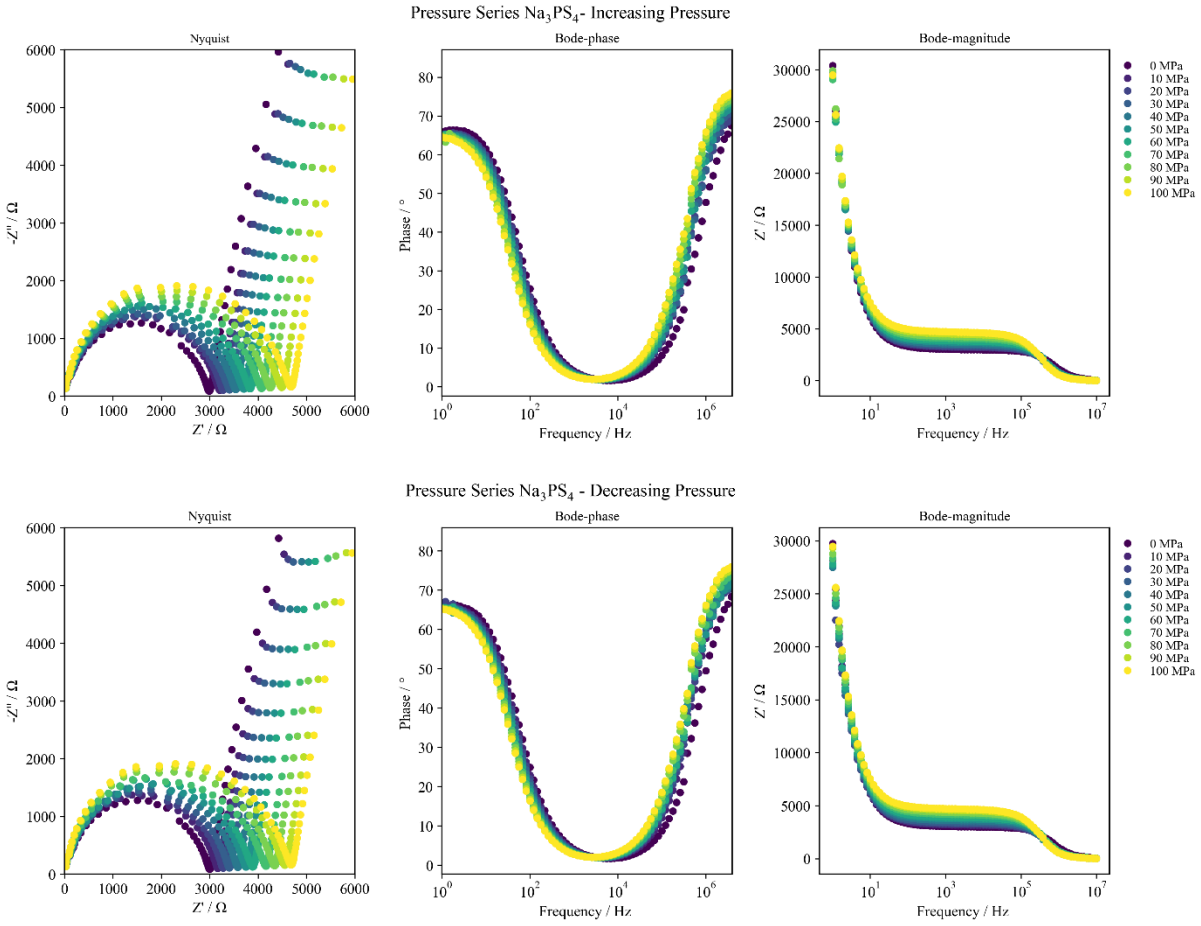

Figure C.13. The Nyquist, Bode-phase and Bode-magnitude representations belonging to the impedance measurements of the pressure series of Na_3PS_4.

Na_3AsS_4

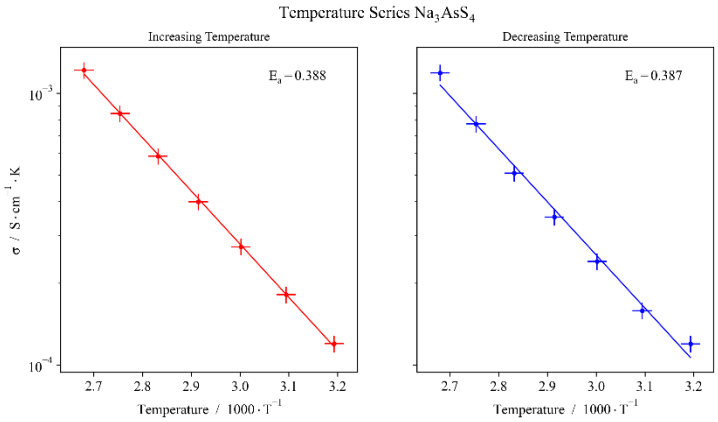

Figure C.14. The conductivity plotted against the inverse of the temperature for the complete temperatures series of the Na_3AsS_4 sample, both on the way up (increasing temperature, left) and down (decreasing temperature, right).

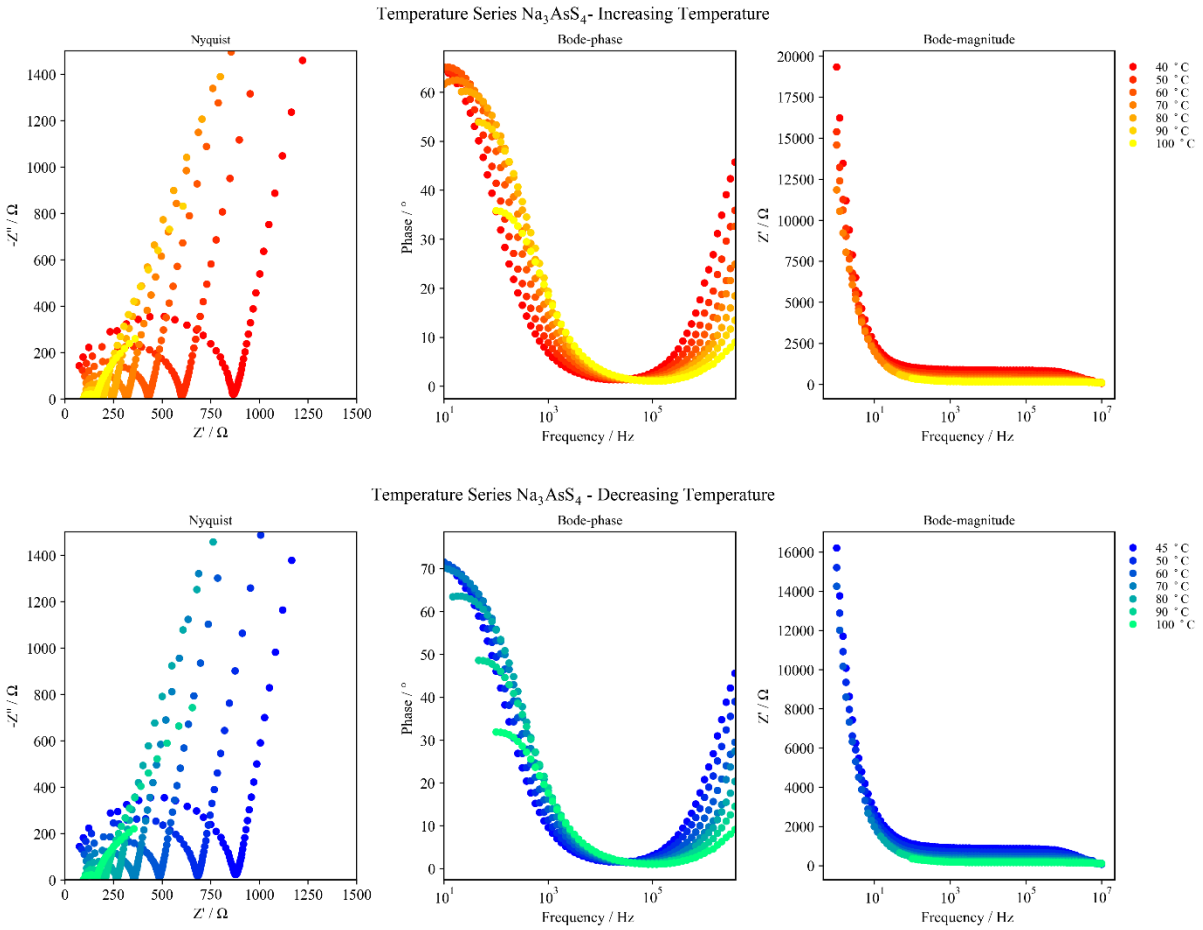

Figure C.15. The Nyquist, Bode-phase and Bode-magnitude representations belonging to the impedance measurements of the temperature series of Na_3AsS_4.

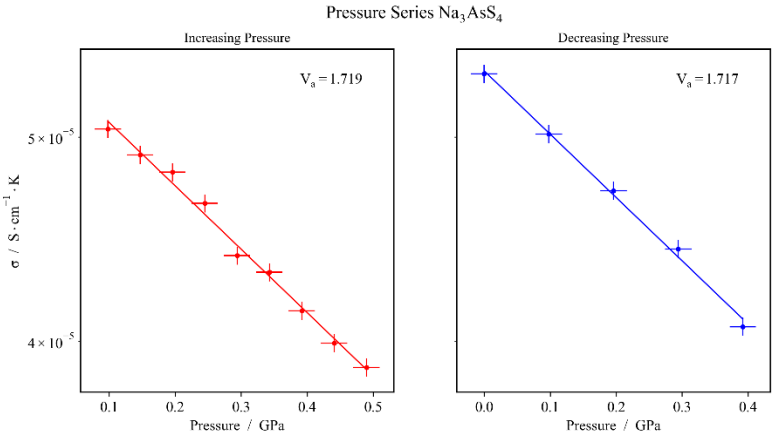

Figure C.16. The conductivity plotted against the pressure for the complete pressure series of the Na_3AsS_4 sample, both on the way up (increasing pressure, left) and down (decreasing pressure, right).

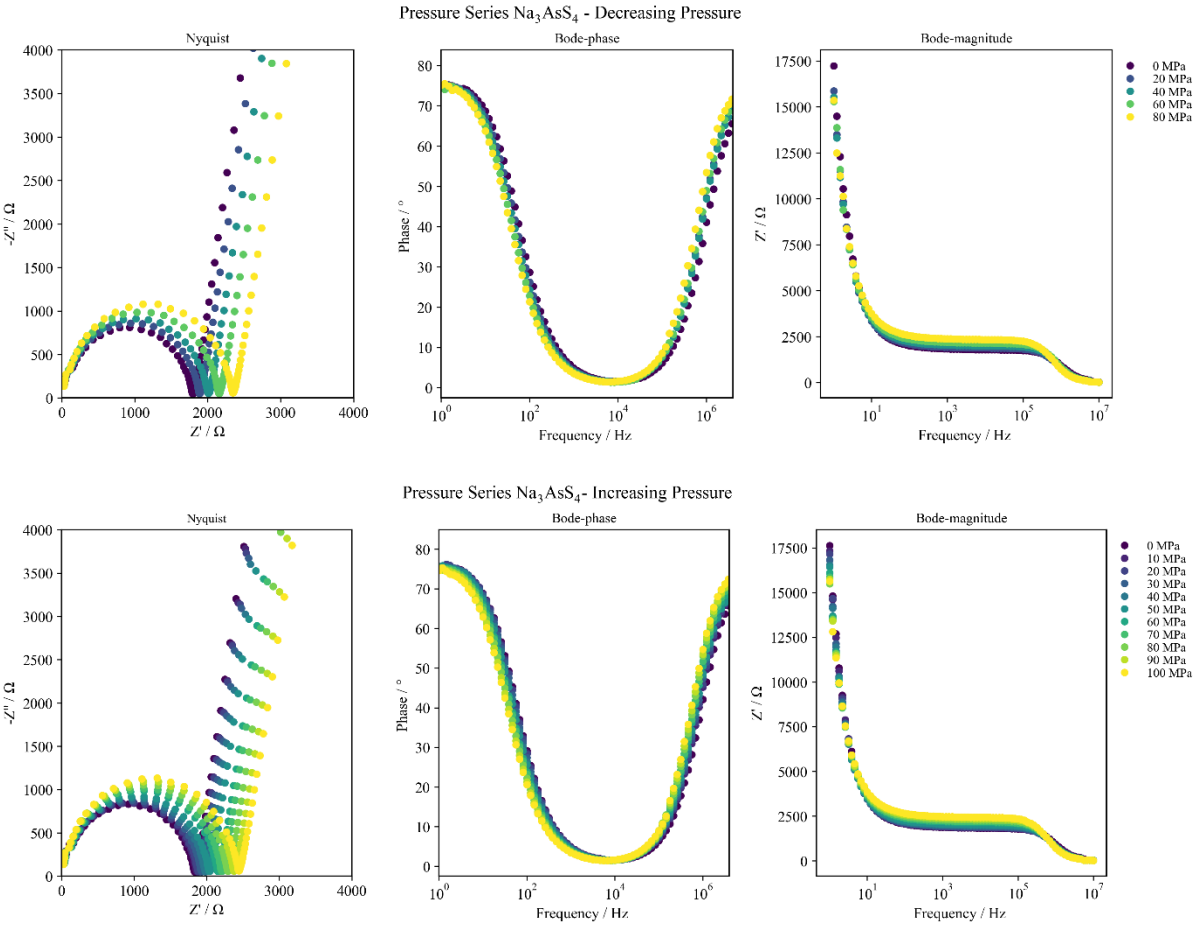

Figure C.17. The Nyquist, Bode-phase and Bode-magnitude representations belonging to the impedance measurements of the pressure series of Na_3AsS_4.

Na_3SbS_4

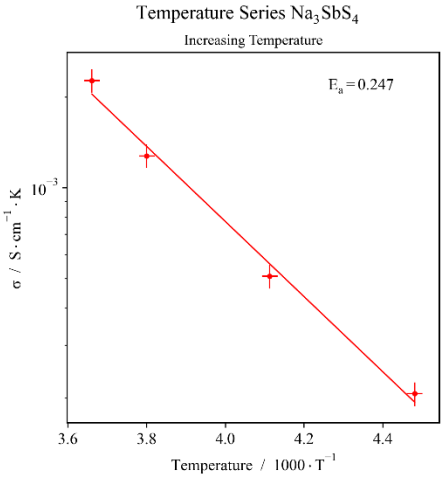

Figure C.18. The conductivity plotted against the inverse of the temperature for the complete temperatures series of the Na_3SbS_4 sample. Since this sample was measured at low temperatures, only a series on the way up way measured.

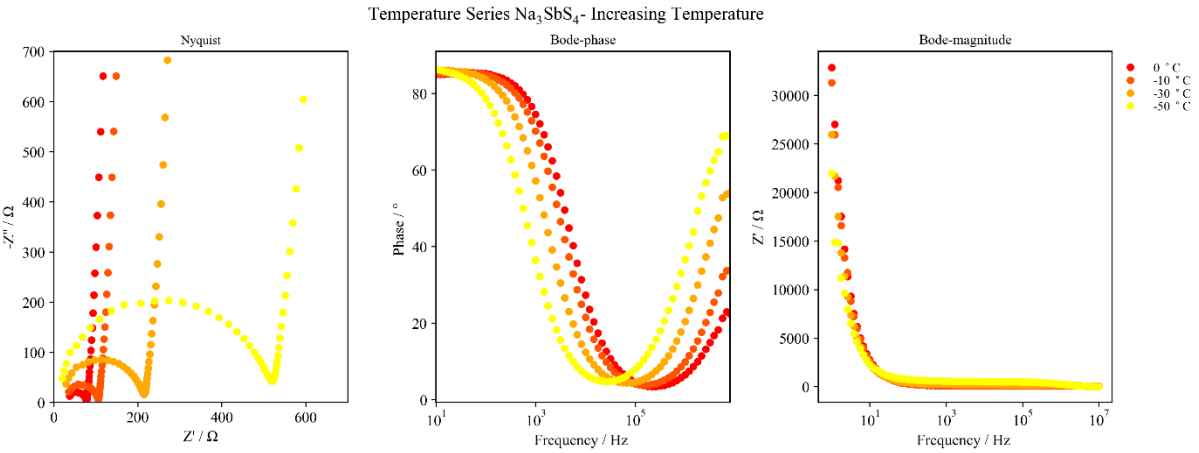

Figure C.19. The Nyquist, Bode-phase and Bode-magnitude representations belonging to the impedance measurements of the temperature series of Na_3SbS_4.

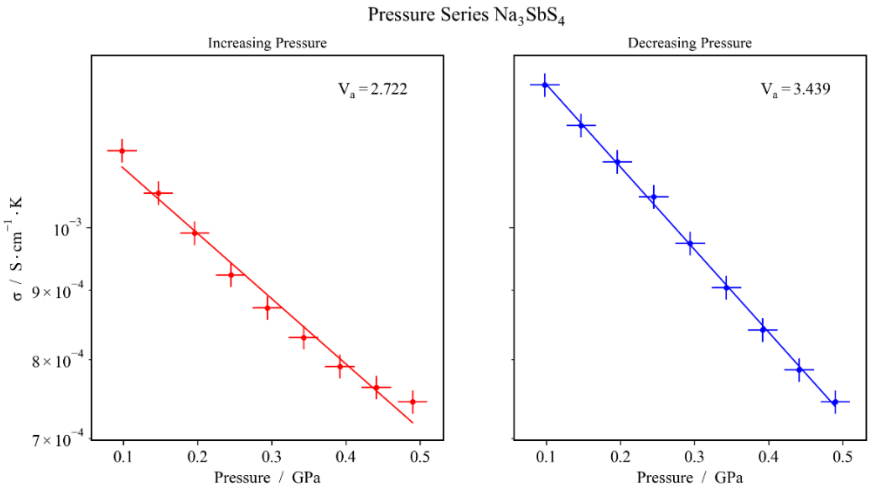

Figure C.20. The conductivity plotted against the pressure for the complete pressure series of the Na_3SbS_4 sample, both on the way up (increasing pressure, left) and down (decreasing pressure, right). It is likely that the sample wasn't properly compressed before measuring the increasing series, leading to a different activation volume for this measurement series.

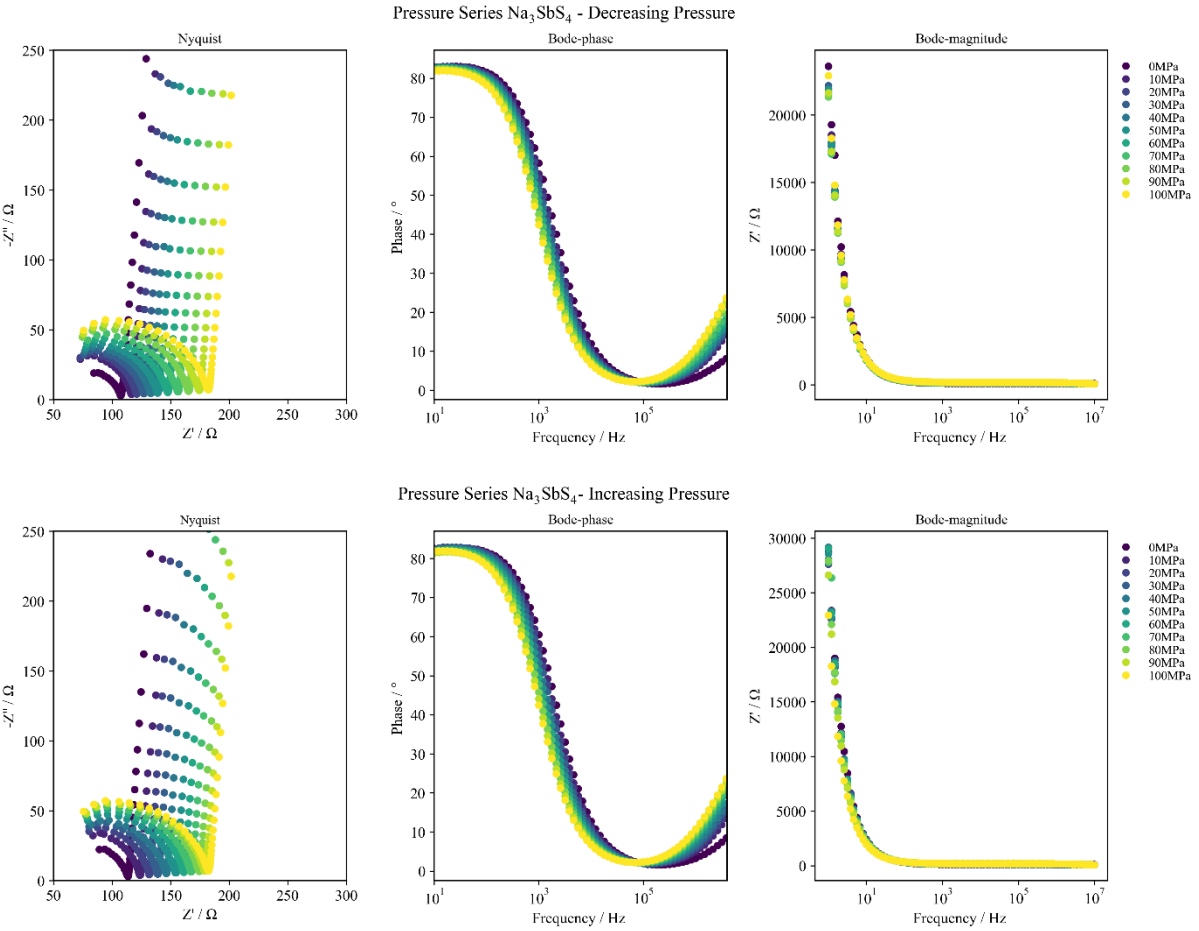

Figure C.21. The Nyquist, Bode-phase and Bode-magnitude representations belonging to the impedance measurements of the pressure series of Na_3SbS_4.

Appendix D. – Fit Parameters

This appendix contains all the relevant fit parameters and data used for the fits in this work.

Bulk Modulus – Fit Tables

Table D.1. The fit parameters from the fits of the pressure data to the Birch Murnaghan equations using the CFTOOL of MATLAB.

Isostructure	**Na_3PS_4**	**Na_3AsS_4**	**Na_3SbS_4**
Space group	$I\bar{4}3m$	$I\bar{4}3m$	$I\bar{4}3m$
Energy-Volume fit			
• **B / GPa**	26.403	25.606	24.641
• **dB/dP**	4.772	4.922	5.0496
• **V_0 / Å^3**	332.429	342.330	359.713
• **R-Squared**	1	0.9999	1
• **Adj. R-Squared**	1	0.9999	1
Pressure-Volume fit			
• **B / GPa**	26.553	25.653	24.719
• **dB/dP**	4.774	4.969	5.120
• **V_0 / Å^3**	332.426	342.261	359.488
• **R-Squared**	0.9998	0.9998	0.9997
• **Adj. R-Squared**	0.9998	0.9998	0.9996

Activation Energy and Activation Volume (DFT) – Fit Tables

Table D.2. Fit data for the calculations of the activation energy and volumes. For the activation volumes the pressures were plotted against the logarithm of the conductivity, for the activation volumes the inverse temperatures were plotted against the logarithm of the conductivity.

Isostructure	**Na_3PS_4**		**Na_3AsS_4**		**Na_3SbS_4**	
Space group	$I\bar{4}3m$		$I\bar{4}3m$		$I\bar{4}3m$	
	Up	*Down*	*Up*	*Down*	*Up*	*Down*
Activation Energy fit						
• **E_a / eV**	0.45(0)	0.44(9)	0.38(8)	0.38(7)	-	0.24(7)
• **P1 (coefficient)**	5222.1	5213.8	4503.0	4494.5	-	2872.3
• **P2 (intercept)**	7.377	7.342	5.323	5.205	-	4.323
• **R-Squared**	0.9638	0.9814	0.9995	0.9956	-	0.9912
• **Adj. R-Squared**	0.9608	0.9799	0.9994	0.9952	-	0.9867
Activation Volume fit						
• **V_a / cm^3 mol^{-1}**	2.32(8)	2.35(2)	1.71(9)	1.71(7)	2.72(2)	3.43(9)
• **P1 (coefficient)**	-0.943	-0.954	-0.693	-0.692	-1.105	-1.399
• **P2 (intercept)**	-10.194	-10.201	-9.818	-9.831	-6.697	-6.525
• **R-Squared**	0.9956	0.9951	0.9914	0.9916	0.9853	0.9990
• **Adj. R-Squared**	0.9970	0.9967	0.9902	0.9888	0.9832	0.9989

X-Ray Diffraction – Fit Tables

Table D.3. Structural parameters of Na_3PS_4 at 293 K as obtained from Rietveld refinements of X-Ray diffraction data.

Na_3PS_4 at 293 K

Lattice Parameter: $a = b = 6.95367(5)$ $c = 7.0878(8)$

$R_{wp} = 5.26$ %, $R_p = 3.88$ %, Goodness of fit: 2.43

Space group: $P\bar{4}2_1c$ Impurity phase: -

Atom	**Wyckoff position**	**Atomic coordinates**			***Occ.***	U_{iso} / Å^2
		x	***y***	***z***		
Na1	2*b*	0	0	1/2	1	0.055826
Na2	4*d*	0	1/2	0.069497	1	0.043053
P	2*a*	0	0	0	1	0.016431
S	8*e*	0.187147	0.154817	0.167732	1	0.020887

Table D.4. Structural parameters of Na_3AsS_4 at 293 K as obtained from Rietveld refinements of X-Ray diffraction data.

Na_3AsS_4 at 293 K

Lattice Parameter: $a = b = 7.04062(8)$ $c = 7.141619(9)$

$R_{wp} = 7.16$ %, $R_p = 4.57$ %, Goodness of fit: 3.97

Space group: $P\bar{4}2_1c$ Impurity phase: unknown

Atom	**Wyckoff position**	**Atomic coordinates**			***Occ.***	U_{iso} / Å^2
		x	***y***	***z***		
Na1	2*b*	0	0	1/2	1	0.01657
Na2	4*d*	0	1/2	0.067707	1	0.036078
As	2*a*	0	0	0	1	0.016022
S	8*e*	0.200161	0.166293	0.17376	1	0.011105

Table D.5. Structural parameters of Na_3SbS_4 at 293 K as obtained from Rietveld refinements of X-Ray diffraction data (sample synthesized from elemental Sb and S).

Na_3SbS_4 at 293 K

Lattice Parameter: $a = b = 7.16399(2)$ $c = 7.29265(5)$

$R_{wp} = 5.47$ %, $R_p = 3.99$ %, Goodness of fit: 2.35

Space group: $P\bar{4}2_1c$ Impurity phase: -

Atom	**Wyckoff position**	**Atomic coordinates**			***Occ.***	U_{iso} / Å^2
		x	***y***	***z***		
Na1	2*b*	0	0	1/2	1	0.047629
Na2	4*d*	0	1/2	0.063897	1	0.053283
Sb	2*a*	0	0	0	1	0.016189
S	8*e*	0.201077	0.174426	0.186501	1	0.020535

Table D.6. Structural parameters of Na_3SbS_4 at 293 K as obtained from Rietveld refinements of X-Ray diffraction data (sample made through intermediate synthesis of Sb_2S_3).

Na_3SbS_4 at 293 K

Lattice Parameter: $a = b = 7.16320(1)$ $c = 7.29373(3)$

$R_{wp} = 8.1$ %, $R_p = 6.09$ %, Goodness of fit: 3.79

Space group: $P\bar{4}2_1c$ Impurity phase: unknown

Atom	**Wyckoff position**	**Atomic coordinates**			***Occ.***	U_{iso} / Å^2
		x	***y***	***z***		
Na1	2*b*	0	0	1/2	1	0.048742
Na2	4*d*	0	1/2	0.067141	1	0.037689
Sb	2*a*	0	0	0	1	0.009067
S	8*e*	0.203953	0.173461	0.185142	1	0.022514

Electrochemical Impedance Spectroscopy – Fit Tables

Table D.7. Na_3PS_4 impedance fits of the temperature series, fit with a constant R_{series} of 80 Ω.

T / °C	first semicircle			second semicircle			series CPE		Adj. R-Squared	
	R	i_1	Q_1	R	i_2	Q_2	i_3	Q_3	Z’	Z’’
Up:										
40	1111.1	0.889	4.25E-10	17216.8	0.865	5.55E-06	1.000	1.78E-06	0.9996	1.0000
50	731.0	0.868	6.35E-10	16239.2	0.866	5.43E-06	1.000	2.04E-06	0.9997	1.0000
60	475.1	0.867	7.11E-10	11460.8	0.877	6.02E-06	0.961	2.66E-06	0.9997	1.0000
70	305.9	0.889	5.78E-10	10870.2	0.875	5.58E-06	0.938	4.04E-06	0.9998	1.0000
80	198.8	0.818	2.14E-09	1763.6	0.861	7.03E-06	1.000	2.66E-06	0.9974	1.0000
90	123.8	0.652	3.48E-08	1275.0	0.866	6.37E-06	0.995	4.06E-06	0.9981	1.0000
100	74.2	0.275	1.44E-05	1080.6	0.875	5.48E-06	0.947	1.15E-05	0.9987	0.9999
Down:										
100	72.5	0.242	2.52E-05	1065.5	0.874	5.34E-06	0.947	1.32E-05	0.9988	0.9999
90	126.3	0.657	3.14E-08	1064.0	0.878	5.92E-06	0.948	5.75E-06	0.9984	1.0000
80	206.2	0.745	6.91E-09	1939.4	0.890	5.5E-06	0.929	5.28E-06	0.9964	0.9999
70	315.4	0.877	7.27E-10	1859.6	0.859	6.77E-06	0.985	2.45E-06	0.9975	0.9999
60	481.2	0.872	6.66E-10	3936.2	0.868	5.65E-06	0.985	2.38E-06	0.9951	0.9999
50	732.7	0.877	5.57E-10	7960.7	0.870	5.7E-06	0.986	2.28E-06	0.9986	0.9998
45	1105.7	0.890	4.27E-10	26018.1	0.826	8.29E-06	1.000	1.75E-06	0.9981	0.9996

Table D.8. Na_3PS_4 impedance fits of the pressure series, fit with a constant R_{series} of 80 Ω.

Pressure / bar	first semicircle			series CPE		Adj. R-Squared	
	R	i_1	Q_1	i_3	Q_3	Z’	Z’’
Up:							
0	2967.97	0.878	4.66E-10	0.847	2.56E-06	0.9981	0.9997
10	3179.26	0.881	6.08E-10	0.844	2.69E-06	0.9979	0.9997
20	3249.65	0.900	4.44E-10	0.845	2.67E-06	0.9985	0.9998
30	3406.23	0.900	4.44E-10	0.845	2.67E-06	0.9986	0.9996
40	3497.86	0.904	4.29E-10	0.845	2.72E-06	0.9988	0.9997
50	3704.57	0.904	4.27E-10	0.845	2.76E-06	0.9980	0.9991
60	3830.02	0.904	4.27E-10	0.845	2.76E-06	0.9989	0.9997
70	4074.28	0.904	4.27E-10	0.845	2.76E-06	0.9991	0.9997
80	4252.78	0.904	4.27E-10	0.845	2.76E-06	0.9992	0.9996
90	4485.35	0.904	4.27E-10	0.845	2.76E-06	0.9992	0.9996
100	4683.84	0.904	4.27E-10	0.845	2.76E-06	0.9993	0.9995
Down:							
90	4547.86	0.896	4.67E-10	0.845	2.85E-06	0.9989	0.9989
80	4339.79	0.896	4.67E-10	0.845	2.85E-06	0.9988	0.9991
70	4159.82	0.896	4.67E-10	0.845	2.85E-06	0.9992	0.9992
60	3853.19	0.896	4.67E-10	0.845	2.85E-06	0.9990	0.9997
50	3715.07	0.894	5.17E-10	0.844	2.87E-06	0.9990	0.9998
40	3583.23	0.896	5.17E-10	0.843	2.88E-06	0.9988	0.9998
30	3388.75	0.896	5.17E-10	0.843	2.88E-06	0.9987	0.9998
20	3275.81	0.899	4.64E-10	0.841	2.84E-06	0.9986	0.9998
10	3136.74	0.899	4.64E-10	0.841	2.84E-06	0.9986	0.9998
0	2966.99	0.890	4.22E-10	0.840	2.71E-06	0.9982	0.9997

Table D.9. Na_3AsS_4 impedance fits of the temperature series, fit with a constant R_{series} of 65 Ω.

T / °C	first semicircle			second semicircle			series CPE		Adj. R-Squared	
	R	i_1	Q_1	R	i_2	Q_2	i_3	Q_3	Z’	Z’’
Up:										
40	796.51	0.869	7.59E-10	21967.02	0.873	7.55E-06	0.859	1.32E-05	0.9968	0.9998
50	526.38	0.829	1.55E-09	22348.87	0.840	8.38E-06	0.897	1.64E-05	0.9948	0.9999
60	350.80	0.820	2.67E-09	21499.51	0.835	8.46E-06	0.896	2.02E-05	0.9972	0.9998
70	239.49	0.829	3.07E-09	20444.1	0.836	7.37E-06	0.897	1.46E-04	0.9989	0.9999
80	162.91	0.856	1.78E-09	19997	0.837	7.52E-06	0.900	7.25E-03	0.9984	0.9999
90	113.31	0.844	2.9E-09	4007.69	0.837	8.25E-06	0.826	2.00E-04	0.9991	0.9999
100	78.61	0.762	1.82E-08	392.28	0.827	1.39E-05	0.869	3.29E-05	0.9928	0.9957
Down:										
100	80.41	0.771	1.18E-08	324.26	0.824	1.43E-05	0.851	4.19E-05	0.9991	0.9999
90	123.91	0.863	1.89E-09	5012.13	0.796	1.11E-05	0.900	3.19E-02	0.9962	0.9998
80	188.00	0.868	1.4E-09	18716.58	0.851	5.86E-06	0.901	1.45E-03	0.9989	0.9999
70	272.62	0.827	2.33E-09	37209.36	0.868	8.13E-06	0.819	1.33E-05	0.9983	0.9999
60	397.38	0.811	2.52E-09	24000.49	0.932	6.71E-06	0.802	9.54E-06	0.9953	0.9999
50	602.98	0.866	6.21E-10	20000	0.900	2.5E-06	0.900	4.00E-04	0.9924	0.9887
45	798.79	0.902	4.27E-10	20000	0.886	2.76E-06	0.886	6.33E-04	0.9982	0.9996

Table D.10. Na_3AsS_4 impedance fits of the pressure series, fit with a constant R_{series} of 80 Ω.

Pressure / bar	first semicircle			series CPE		Adj. R-Squared	
	R	i_1	Q_1	i_3	Q_3	Z’	Z’’
Up:							
0	1850.59	0.906	3.75E-10	0.890	2.76E-06	0.9995	0.9999
10	1883.24	0.908	4.05E-10	0.891	2.76E-06	0.9996	0.9999
20	1890.08	0.908	4.05E-10	0.891	2.76E-06	0.9995	0.9999
30	1944.12	0.909	4.06E-10	0.891	2.84E-06	0.9995	0.9999
40	1981.19	0.909	4.06E-10	0.891	2.84E-06	0.9995	0.9998
50	2049.89	0.915	3.75E-10	0.890	2.97E-06	0.9997	0.9999
60	2170.48	0.920	3.42E-10	0.888	3.09E-06	0.9997	0.9999
70	2210.11	0.920	3.42E-10	0.888	3.09E-06	0.9997	0.9998
80	2305.13	0.928	3.14E-10	0.886	3.2E-06	0.9998	0.9998
90	2388.23	0.928	3.08E-10	0.884	3.29E-06	0.9998	0.9998
100	2452.48	0.933	2.95E-10	0.880	3.41E-06	0.9998	0.9998
Down:							
80	2345.69	0.916	3.95E-10	0.884	3.33E-06	0.9994	0.9996
60	2155.00	0.915	3.54E-10	0.884	3.28E-06	0.9995	0.9998
40	2021.68	0.915	3.54E-10	0.884	3.28E-06	0.9997	0.9999
20	1900.55	0.920	3.54E-10	0.886	3.15E-06	0.9997	0.9999
0	1779.31	0.931	2.82E-10	0.880	2.99E-06	0.9988	0.9997

Table D.11. Na_3SbS_4 impedance fits of the temperature series, fit with a constant R_{series} of 65 Ω.

T / °C	first semicircle			series CPE		Adj. R-Squared	
	R	i_1	Q_1	i_3	Q_3	Z'	Z''
Up:							
-50	532.83	0.830	4.26E-09	0.954	5.75E-07	0.9976	0.9999
-30	217.07	0.840	4.24E-09	0.964	5.52E-07	0.9948	1.0000
-10	86.42	0.865	4.18E-09	0.964	5.81E-07	0.9964	1.0000
0	48.61	0.883	4.78E-09	0.963	5.85E-07	0.9974	1.0000

Table D.12. Na_3SbS_4 impedance fits of the pressure series, fit with a constant R_{series} of 50 Ω.

Pressure / bar	first semicircle			series CPE		Adj. R-Squared	
	R	i_1	Q_1	i_3	Q_3	Z'	Z''
Up:							
0	78.56	0.795	4.23E-09	0.946	1.08E-06	0.9973	1.0000
10	89.24	0.816	4.13E-09	0.946	1.1E-06	0.9983	1.0000
20	96.77	0.858	2.07E-09	0.947	1.09E-06	0.9980	1.0000
30	103.98	0.870	1.75E-09	0.947	1.11E-06	0.9983	1.0000
40	111.27	0.850	2.46E-09	0.946	1.15E-06	0.9982	1.0000
50	119.46	0.856	2.33E-09	0.946	1.17E-06	0.9986	1.0000
60	126.33	0.859	2.26E-09	0.944	1.22E-06	0.9986	1.0000
70	132.77	0.849	2.73E-09	0.944	1.27E-06	0.9988	1.0000
80	139.48	0.847	2.86E-09	0.942	1.33E-06	0.9987	1.0000
90	144.56	0.831	3.79E-09	0.942	1.38E-06	0.9990	1.0000
100	148.06	0.821	4.58E-09	0.943	1.43E-06	0.9995	1.0000
Down:							
90	140.28	0.824	4.46E-09	0.943	1.42E-06	0.9995	1.0000
80	131.10	0.828	4.18E-09	0.944	1.41E-06	0.9995	1.0000
70	122.06	0.820	4.57E-09	0.944	1.4E-06	0.9993	1.0000
60	113.20	0.826	4.15E-09	0.945	1.38E-06	0.9995	1.0000
50	104.62	0.831	3.82E-09	0.945	1.37E-06	0.9993	1.0000
40	98.61	0.833	3.69E-09	0.946	1.35E-06	0.9994	1.0000
30	92.72	0.833	3.83E-09	0.946	1.34E-06	0.9993	1.0000
20	86.56	0.843	3.31E-09	0.946	1.32E-06	0.9994	1.0000
10	82.12	0.848	3.04E-09	0.947	1.3E-06	0.9994	1.0000
0	73.37	0.758	9.05E-09	0.946	1.24E-06	0.9994	1.0000

Appendix E. – *Ab Initio* Molecular Dynamics

Perhaps the most powerful tool for analysing ion-dynamics that DFT has to offer is *ab initio* Molecular Dynamics. With Molecular Dynamics, a temperature is introduced to the DFT calculation. This results in thermal motion of the particles, which produces a random motion of the ions in the structure. By determining how the kinetic energies should be scaled and how the system must keep to the same temperature, this technique allows the ion optimization step of each cycle to mimic the dynamical behaviour of the structure. With AIMD it is possible to determine different lattice vibrations and distributions of ionic motion. Furthermore, it is possible to induce the process of ion-diffusion through the lattice: by introducing vacancies in the structure, thermal excitation can cause ions to hop from one site to the other, thus simulating the process of ionic conduction. It thus becomes clear that AIMD is a very useful tool when analysing the fundamental of ion conduction, since important determinants of the conductivity such as the vibrational distributions and hopping frequency can directly be probed using this technique.

There is however a large drawback to using AIMD for modelling ion conduction: because of the stochastic nature of the diffusion process and thermally induced lattice vibrations, significant computation times are required to get sufficient statistics. Generally, simulations times of several ps are required to get sensible MD data. With the current computational power this will involve real computational time in the range of days or weeks, depending also on the ion mobility in the studied material. Furthermore, analysing the large amounts of output resulting from an MD analysis is not in any way trivial and on top of that a time-consuming task. As such, it was decided not to include a detailed AIMD analysis in this study of the fundamental conduction mechanism in Na_3PnS_4. Initial findings from pilot AIMD calculations (shorter simulation times) are presented as outlook for future studies in this appendix.

Table E.1. The initial output from an attempted MD analysis.

Isostructure	Na_3PS_4	Na_3AsS_4	Na_3SbS_4
Activation Energy	0.396 (+/- 0.022)	0.407 (+/- 0.027)	0.397 (+/- 0.015)
Jumps	126	115	125
Transition Rate	$2.750 \cdot 10^{10}$ (+/- $8.80 \cdot 10^{9}$)	$2.510 \cdot 10^{10}$ (+/- $7.44 \cdot 10^{9}$)	$2.728 \cdot 10^{10}$ (+/- $5.37 \cdot 10^{9}$)
Attempt Frequency	$4.498 \cdot 10^{12}$ (+/- $5.15 \cdot 10^{11}$)	$4.776 \cdot 10^{12}$ (+/- $6.36 \cdot 10^{11}$)	$4.469 \cdot 10^{12}$ (+/- $5.31 \cdot 10^{11}$)
Jump Diffusivity	$5.498 \cdot 10^{-10}$	$5.116 \cdot 10^{-10}$	$5.736 \cdot 10^{-10}$
Atom Percentage	0.9608	0.9567	0.9735
Site Radius	1.1851	1.1168	1.1856
Vibrational Amplitude	0.5926	0.5584	0.5928
Tracer Diffusion	$3.936 \cdot 10^{-10}$	$3.513 \cdot 10^{-10}$	$9.670 \cdot 10^{-10}$

Guideline DFT using VASP

T. J. Alders

➔ Introduction

This document describes how different types of structural analysis are performed using Density Functional Theory (DFT). The computations are performed using the Vienna Ab-initio Simulation Package (VASP)[75], using the projected augmented wave (PAW) approach.

Density Functional Theory (DFT) is a very useful tool for modelling materials at the atomic scale. It is a quantum mechanical approach where the electrons are treated in an electron density approximation, so that the many-body Schrödinger equation can be solved without having to treat all electron-electron interactions separately. DFT thus makes it possible to find the lowest total energy state of a system and subsequently evaluate the structural properties as accurately as computationally possible. DFT can be used to model many different system and assess many different properties. This guideline is focussed on how to use VASP to perform DFT calculations where crystal structures are relaxed and optimized. Besides these structure or geometry optimizations, additional attention is paid to how relaxations can be performed under simulated hydrostatic pressure and how the charge and electron density in the structure can be quantified.

In this guideline, a very basic understanding of how to perform actions on a Linux terminal is assumed. If necessary, appendix A contains a list of useful Linux commands which are necessary to perform the calculations.

The first section of this document treats the basics of VASP and simple geometry optimizations. In this section the four key files, POSCAR, KPOINTS, POTCAR and INCAR will be covered, together with how to submit folder to VASP. In the second section, the focus will be on how to perform relaxations under applied hydrostatic pressure: two different approaches to do so, one using the Pulay Stress and another using Volume Fixing, will be explained. Finally, the third section will focus on performing charge analysis. Three different metrics that describe charge in the structure, the Born Effective Charges, Bader Charges and the Electron Localization Function, will be explained, as well as how to calculate these using VASP. [d]

[d] All information in this guideline (without reference) comes from the VASP manual, VASP wiki or personal experience.

➔ Simple Relaxations

A simple geometry relaxation in VASP requires five steps. To run the simulation in VASP a folder containing four different files needs to be submitted to the program. These files are the POSCAR file (containing information about the atomic positions of the to-be-investigated structure), the POTCAR file (containing information on how the electron-density and electronic distribution should be modelled for the structure), the KPOINTS file (containing the details of with what approach and grid the Brillouin zone should be sampled) and the INCAR file (containing information on in what way and under what conditions the computation must be performed). How these files should be prepared is described below. For preparing your KPOINTS and INCAR file, it is useful to get a template file from someone with experience with VASP in the group.

➔ 1) POSCAR

Getting the POSCAR, or structural information, is usually fairly straightforward. It is possible to make a POSCAR file from many structure files, including the CIF format. An easy approach to getting an initial POSCAR file is to get an experimental CIF file of the structure from a database (e.g. ICSD, PCD) or a simulated one from the Materials Project. It is usually desirable to get the primitive cell: this is the version of the unit cell with the least possible atoms. Alternatively, for visualisation or relaxations, the symmetrized cell is also a good option.

Once a CIF of the structure is acquired, it is possible to open the CIF with the VESTA software for visualisation of crystal structures and to subsequently save it again as POSCAR. This option can be found under "export data". It is important that the file is ultimately saved under the name "POSCAR", since VASP will be looking for a file with this exact name. If no initial CIF of the structure exists yet, it is possible to make your own CIF using VESTA. Simply put in all the relevant crystallographic information on the structure and VESTA will be able to create a CIF file for you.

➔ 2) KPOINTS

Although there are many approaches with which VASP can sample the Brillouin zone, generally generating a KPOINTS grid using the Monkhorst-Pack method is a good approach. In this approach, the integral over the Brillouin zone is solved for a rectangular grid of points in three dimensions, spaced evenly through the reciprocal space. The larger the grid, the finer and more accurate the sampling will be. To find a sufficient k-point sampling density, it is useful to calculate an estimate for how many k-points will be needed. To do so, calculate the length of the unit-vectors in reciprocal space. A k-point sampling of one k-point per 0.2 A^{-1} is usually sufficient. A denser k-point grid will provide more accurate simulations but will also be computationally much heavier. It is therefore recommended to do a k-points convergence test.

To do a k-point convergence test: first, we should determine what a reasonable k-point distribution is (for cubic cells this is evenly distributed 1x1x1, but for a tetragonal cell an asymmetrical distribution could be better, e.g., 1x1x2). Once we have a suitable distribution, we must make a range of different k-points densities (1x1x1, 2x2x2, etc.) and perform a simple electronic relaxation for each. We can plot the final values in Excel (preferable energy and

pressure versus k-point density, perhaps the lattice parameters versus k-point density) and evaluate the trends. When the difference in energy becomes smaller than 1 meV / atom from 1 KPOINTS grid to the next, you have found convergence. For pressure and lattice parameters, convergence criteria of 0.1 kB for pressure and 0.01 Angstrom can be used respectively. It is however unlikely that these criteria will not already be met when the energy convergence criterium is met.

➔ 3) POTCAR

The POTCAR file contains information on the electronic structure of the materials and how VASP should treat this. Perhaps the most important characteristics determined with the POTCAR choice are the choice of pseudopotential and exchange correlation functional. In the pseudopotential it is determined which electrons of the atom are to be treated as valence electrons. In the section "pseudopotentials" of the charge analysis chapter an example is provided of what this means for the structure of Na_3PS_4. The exchange correlation functional describes how quantum mechanical properties of the electron-electron interactions should be approximated. This can be done through many different approaches, although the Local Density Approximation (LDA) or different versions of the Generalized Gradient Approach (GGA) are common. Within the GGA approach, the Perdew-Burke-Ernzerhof (PBE) scheme or the PBE scheme for solid (PBEsol) are common choices. Which exchange correlation functional is set is by default determined by which pseudopotentials are used to create the POTCAR file. However, is desired this can be overwritten by specifying the choice of exchange correlation functional in your INCAR file (see below).

To create a POTCAR file, one must have access the relevant pseudopotential files. These can usually be obtained from someone else working with VASP in the group and are provided with the software. Each type of atom in the structure has its own pseudopotential. It is thus necessary to concatenate these different pseudopotentials into one POTCAR file. To do so, select which pseudopotentials should be used for the POTCAR and copy these to a directory. The VASP manual and the Materials Project list which pseudopotentials they recommend using for certain analyses (for simple relaxations the pseudopotential containing only primary valence electrons will suffice, but for more detailed relaxations you'll need to treat more of the electrons in the structure as valence electrons). Then, concatenate the pseudopotentials in the order in which they are listed in the POSCAR file. This is usually the same order as the molecular formula. This way, the POTCAR for the simulation can be prepared.

➔ 4) INCAR

The INCAR file is the heart and soul of your DFT analysis. Here you determine which additional input parameters VASP should take into account, how VASP should perform the relaxation and what output should be generated. This is done by specifying certain parameters in your INCAR file. For almost all settings VASP has a predefined value which is selected if not specifically specified. The most important tags for performing a simple geometry

optimization are listed below.[e] In appendix B and example INCAR file for a simple geometry relaxation can be found.

Key INCAR tags

NSW: NSW sets the maximum number of ionic steps taken in the relaxation. The default is set to 0. Common settings for NSW: 0 = electronic relaxation, 1+ = ionic relaxation

ISIF: ISIF determines which principal degrees-of-freedom are allowed to change in the relaxation or molecular dynamics (MD) run. The default is set to 0 for MD runs and 2 for other runs. Common settings for ISIF: 2 = only positions allowed to change, 3 = positions, cell shape and cell volume allowed to change.

EDIFF & EDIFFG: EDIFF and EDIFFG specify the global break conditions for respectively the electronic relaxation loop and ionic relaxation loop. Default settings are 10^{-4} eV for EDIFF and EDIFF x10 eV for EDIFFG. EDIFFG can also be specified as negative value: the break condition then becomes a norm for the force, and the relaxation is stopped when all forces becomes smaller than |EDIFFG|. Common settings for EDIFF and EDIFFG: EDIFF = 0.0001 and EDIFFG = -0.01.

LREAL: LREAL determines whether the projection operators are evaluated in real-space or in reciprocal space. The default value of LREAL is .FALSE, meaning the projection operators are evaluated in reciprocal space. Evaluating the projection operators in reciprocal space provides more accurate energy calculations, yet also requires more computational power. If the projection operators are evaluated in real space, it is valuable to specify the precision settings with which the projection is performed with PREC and ENCUT. Common settings for LREAL: LREAL = Auto or LREAL = .FALSE (for calculations where accurate energies are required).

PREC: PREC specifies which precision mode for the projection operators should be used. This determines several settings including ENCUT, ENAUG and which fast Fourier transform (FFT) grids are used. The default setting for PREC is Normal. Common settings for PREC: PREC = Normal or PREC = Accurate (essential for convergence with calculations where the stress tensor is modified).

ENCUT: ENCUT specifies the cut-off energy for the planewave basis set (in eV). The default setting of ENCUT is the largest ENMAX that is in the POTCAR file. For more accurate calculations it can be important to specify a larger ENCUT however. The VASP manual suggests an ENCUT for each selected pseudopotential. Common settings for ENCUT: ENCUT = 520.

IBRION: IBRION determines which what algorithm the ions are moved and manipulated during the computation. IBRION is one of the most important and powerful settings in VASP. IBRION = 0 is used for MD runs and IBRION = 1 / 2 is used for ionic relaxations. From IBRION = 5 onwards, the Hessian matrix (and thus the second derivatives of the energy with respect to atomic positions) is calculated. From IBRION 7 onwards a perturbation matrix is applied to the system to calculate additional second derivates, such as the stiffness matrix and

[e] Some other tags are important for a geometry optimization as well, such as ISTART, ICHARG and ISPIN, yet understanding what these tags specify is less important. These are therefore not explained until the next section.

dielectric matrix. Common settings for IBRION: IBRION = 0 (MD run), IBRION = 2 (Ionic Relaxation), IBRION = 8 (Charge Analysis).

GGA: GGA specifies which exchange correlation functional is selected. The default GGA is the exchange correlation functional specified in the POTCAR file. Common settings for GGA: GGA = PE (PBE exchange correlation functional) or GGA = PS (PBEsol exchange correlation functional).

➔ 5) Submit the folder to VASP

Once all four files have been prepared, the only thing that remains is letting VASP perform the simulation. For this, make sure that the selected directory contains all four files with the names exactly as listed above and no extensions. VASP will look for these files and a simulation will not be possible if one of them is missing. It is also important to ensure that no other files exist in the folder yet. Once these boundary conditions have been met, submit the folder to VASP and congratulate yourself, because you've just finished a DFT computation!

For submitting the folder to VASP on Linux, ensure that a vasp executable is in your home directory. This could for example be vasp8. To submit the folder using vasp8, simply go to the directory with your files and type qsub ~/vasp8. This will submit your folder to VASP.

Note: the 8 in vasp8 signifies that this executable will submit the input to 8 cores. It is possible, and sometimes even necessary, to submit the folder to a different amount of cores. For this, open the vasp8 executable in a text editor and change the ppn = 8 to ppn = x (x being the desired value). Save this as vaspx and submit to this new executable.

➔ Other important INCAR tags

Besides the INCAR tags that are important for (almost) all calculations, several tags are required for specific analyses. To get a better understanding of what these different tags that can / need to be specified in the INCAR file entail, the most relevant tags are outlined below. This overview specifically also includes tags which are important for performing ionic relaxations under external pressure and charge analysis.

General Tags

ISMEAR: ISMEAR determines how the partial occupancies are set for each orbital. The occupancy is smeared across the different states using a specific approach and width of smearing in eV (set by SIGMA). For semiconductors and very accurate total energy calculations the use of ISMEAR = -5 (tetrahedron method with Blöchl corrections) is recommended. For large cells, metals or unknown structures the use of ISMEAR = 0 (Gaussian smearing) is recommended: this setting generally converges more easily.

SIGMA: SIGMA determines the width of smearing (approach set by ISMEAR) in eV. Common settings for SIGMA: SIGMA = 0.002 for the use of ISMEAR = -5 or SIGMA = 0.05 for the use of ISMEAR = 0.

ISPIN: ISPIN specifies whether spin polarized calculations are used or not. ISPIN = 1 specifies that non spin polarized calculations are performed and ISPIN = 2 specifies that spin polarized calculations are performed.

ISTART: ISTART specifies whether a job should start from scratch or be a continuation of a previous job. ISTART = 0 defines that the job should run from scratch. ISTART = 1 or ISTART = 2 will continue the run from an existing WAVECAR file. The default choice is to always start a new job from scratch (ISTART = 0).

ICHARG: ICHARG determines how VASP constructs the initial charge density. If a completely new run is started (ISTART = 0), the standard ICHARG is ICHARG = 2, which indicates that the initial charge density is calculated from the superposition of atomic charge densities. This is also the default choice of VASP. For ICHARG = 0, the charge density is determined from the initial wave functions. For ICHARG = 1, the charge density is read from a readily existing CHGCAR file.

NELM: NELM sets the maximum number of electronic relaxation steps. The default value of NELM = 60. In general, there is no reason to change the NELM setting: if the self-consistency electronic loop does not converge within 40 steps, it is likely that the loop will not converge at all.

NELMIN: NELMIN sets a minimum number of electronic relaxation steps. The default is set to NELMIN = 2. In general, it is not necessary to specify NELMIN. For MD runs it can be useful to set NELMIN to a slightly higher value, e.g., 4 or 8.

ALGO: ALGO sets the electronic minimisation algorithm. The default of ALGO = Normal (blocked Davidson iteration scheme), which is sufficient for most optimizations.

ISYM: ISYM determines the way VASP treats symmetry. The default of ISYM is ISYM = 1 or 2 (considers symmetry of charge density) or ISYM = 0 (no symmetry) for MD runs.

Relaxations under pressure

PSTRESS: PSTRESS determines whether or not Pulay corrections are added to the stress tensor. The Pulay stress arises from the fact that the plane wave basis set is not complete with respect to changes in the volume of the cell. As a result, the diagonal components of the stress tensor are incorrect unless absolute convergence with regards to the basis set has been achieved. For very large values of the energy cut-off and strict energy convergence criteria, the remaining Pulay stress is usually negligible.

Forcing the system to stick to a specified Pulay stress has useful applications: since the Pulay stress is the correction between the real and computed stress, setting the Pulay stress acts like applying an isotropic hydrostatic pressure on the system. It is evident from the origin of the Pulay stress however that to use PSTRESS to set an external pressure, the stress tensor needs to be converged properly. To this end, there are several settings that are important to take into account when using PSTRESS to set an external pressure on the system (see Relaxations under pressure).

PSTRESS can be specified to have any value both positive and negative and is set in kbar. Generally, stresses over or under 25 kbar do not result in accurate computations and applying larger pressures should be done with caution.

*Note: it is important to note that as a result of the forced Pulay stress an energy correction is required. The calculated energies have to be corrected with a factor of Cell Volume * PSTRESS.*

Charge analysis

LELF: LELF determines if the ELFCAR file is created or not. The ELFCAR file contains the structural information of the cell as well as the ELF (electron localization function). The default setting of LELF = .FALSE. For computations where the ELF needs to be calculated it is therefore necessary to specify LELF = .TRUE.

Note: it is recommended to set NPAR = 1 when calculating the ELF for accurate results.

NPAR: NPAR determines the number of bands that are treated in parallel on multi-core systems. On high power multi-core machines it is recommended to set NPAR to the number of cores per node (e.g., 4 or 8).

Note: for calculations with IBRION set to 7 or higher, it is essential not to specify NPAR: doing so can cause the system to crash and provide you with a fairly angry error message in your OUTCAR.

LAECHG: LAECHG determines whether the all-electron charge density will be reconstructed explicitly and written out in different files. The general CHGCAR file that is generated in a VASP run contains the information on the complete all-electron charge density. It can however be useful to be able to separately evaluate the core density and self-consistent (SC) valence density, for example in Bader charge analysis. The default setting of LAECHG = .FALSE. Setting LAECHG to .TRUE will result in the computation of three separate files: AECCAR0, AECCAR1 and AECCAR2. These files contain respectively the all-electron core density, the proto-atomic valence density and the SC valence density. For Bader analysis, both AECCAR0 and AECCAR2 are required.

LEPSILON: LEPSILON determines whether or not the static dielectric matrix, ion-clamped piezoelectric tensor and the Born effective charges are calculated using density functional perturbation theory. The default setting of LEPSILION = .FALSE. For calculation of the Born effective charges it is therefore necessary to specify LEPSILON = .TRUE.

For computing the static dielectric matrix and Born effective charges, it is necessary to have a fully relaxed structure beforehand. Furthermore, it is important to perform the computation using IBRION set to 8, since several of the second derivatives of the energy with respect to position are essential for calculating the these metrics.

➔ Relaxations Under Pressure

While general geometry optimizations can be very insightful, it can be even more interesting to see how a certain structure changes under external pressure. To do so, it is necessary to know how to perform an ionic relaxation under pressure. Although there are several different ways to do so, only the most common two methods applied in material characterisation are outlined below: fixing the volume and setting the Pulay stress. Independent of the selected method, the same three steps should always be taken to get accurate output of relaxations under pressure:

1) Perform a standard geometry optimization (with accurate energy calculations). This is essential because the stress tensor needs to be properly converged before it can be altered using the Pulay stress or before changes in the lattice parameters for volume fixing can be calculated.
2) Perform an ionic relaxation "under pressure". To do this, start from the CONTCAR obtained in step 1 and follow either method 1 or method 2 described below.
3) Perform an electronic relaxation on the structure obtained in step 2. This is essential to get accurate energies, because the final basis set of an ionic relaxation might not be isotropic. Perform this electronic relaxation with a precision set to accurate and a sufficiently high ENCUT (minimally 1.3 times ENMAX). It is also possible to perform this relaxation with IBRION set to 8, so that charge analysis can be performed on the relaxed structure (see Charge Analysis).

With these three steps, accurate energy values should be obtained for all structures under pressure.

Performing the relaxation "under pressure"

Method 1: The Pulay Stress

The Pulay stress is a correction factor in DFT calculations resulting from the fact that the plane wave basis set is not complete with respect to changes in the volume of the cell. As a result, the diagonal components of the stress tensor are incorrect unless absolute convergence with regards to the basis set has been achieved. In general, remaining Pulay stress means there is leftover pressure and stress in a relaxed structure, and is as such indicative of inaccurate cell volumes and energies. Forcing the system to stick to a specified Pulay stress however has useful applications. Because the Pulay stress is the correction between the real and computed stress, setting the Pulay stress acts as an isotropic hydrostatic pressure on the system. The real pressure in the system can subsequently easily be calculated by evaluating the difference between the Pulay stress and external pressure as calculated by VASP. Through this method it is therefore possible to obtain the optimized geometry of the structure under hydrostatic pressure.

It is evident from the origin of the Pulay stress however that to use PSTRESS to set an external pressure, the stress tensor needs to be converged properly. The general recommendation is therefore to perform the initial structure relaxation and the relaxations under pressure with an ENCUT value of at least 1.3 times ENMAX. In practise, 520 eV is sufficient for most relaxations. Furthermore, it is <u>essential</u> that the precision setting is set to Accurate (High in older versions of VASP). Not doing so can lead to the computation not converging. Furthermore, to ensure the stress tensor is converged, it is recommended to use a slightly stricter k-point density.

In general, the external pressure can be set to any desired value. PSTRESS can be specified to have any value both positive and negative and is set in kbar. A positive PSTRESS indicates a compressive pressure on the cell, whereas for a negative PSTRESS value the applied pressure can be seen as "tensile stress" on the system: the cell is being "pulled apart". Generally, stresses over 25 kbar or under negative 25 kbar do not result in accurate computations and applying larger pressures should be done with caution.

It is important to note that as a result of the forced Pulay stress an energy correction is required. The calculated energies have to be corrected with a factor of Cell Volume * PSTRESS. This correction is not performed by VASP and therefore needs to be accounted for after the final energy relaxation.

Method 2: Fixing the Volume

Applying a hydrostatic pressure (compressive or tensile) generally results in a decrease or increase in cell volume. Comparably, a structure where the volume is fixed at something other than the equilibrium volume, has residual stress in the structure. By fixing the volume and lattice parameters and subsequently calculating the residual pressure in the structure, it is therefore possible to "mimic" the behaviour of applying external pressure. This method of "volume fixing" is also a common method to get information on the pressure / volume relation of a certain material.

The most essential question when applying the volume fixing method is in what way the lattice parameters change as a result of pressure. In the easiest scenario occurs when a cubic structure is considered and the change is isotropic: here the lattice parameters can directly be scaled with the cube root of the volume. To apply the volume fixing method, like with the Pulay stress method, the starting point must be a fully relaxed structure at no applied pressure. Subsequently, based on set volumes, the different cell parameters at these different volumes must be computed.

With these lattice parameters, the POSCAR of the structure can be manually updated. By performing an electronic relaxation on this "POSCAR under pressure", the residual pressure in the structure can be calculated (listed as "external pressure" in the OUTCAR).

This method of performing a relaxation under pressure has two distinct disadvantages. Firstly, it is very difficult to utilize this method on structures that have low symmetry since the change in lattice parameters is very unlikely to be isotropic. Secondly, even for cubic or tetragonal structures, it is not always possible to assume that the change in lattice parameters will be isotropic. This can be the result of for example complex anion frameworks which lower the symmetry of the overall structure. Using the volume fixing method for relaxations under pressure must therefore be used carefully and only when the changes in unit cell parameters can be predicted accurately.

➔ Charge Analysis

Analysing the charge on atoms in a structure provides valuable structural information and can be done in various different ways. Three interesting metrics for analysing charge in solid electrolytes are the Born Effective Charge, the Bader Charge and the Electron Localization Function (ELF). All three can be calculated through DFT and the methodology to do so is outlined below for each method. For each method of charge analysis, it is essential to start from a fully relaxed structure. It is important to note that the output of charge analysis is very dependent on the choice of pseudopotential. Therefore, this section will highlight the characteristics of the different pseudopotentials before looking at how to perform the charge analyses.

➔ Pseudopotentials

To create the all-electron charge density (which is key in density functional theory), it is essential to know which electrons in the structure have to be considered in this charge density. For many types of atoms, the electrons in the lower shells are core like, meaning they do not or hardly participate in bonding and hardly contribute to the interatomic forces that create the structure. When creating the all-electron charge density, it is therefore most interesting to consider the self-consistent valency electrons (which do participate in bonding). In the different pseudopotentials that are used for DFT calculations using VASP, different electrons are considered as valence electrons. Most of the pseudopotentials contain a subscript of either pv or sv, indicating whether the primary valence electrons or secondary valence electrons are considered. For a sodium atom (Na) for example, there are three different pseudopotentials available:

4) The “Na” pseudopotential, which considers only the one 3s electron as a valence electron.
5) The “Na_pv” pseudopotential, which considers the 3s electron and the 2p electrons as valence electrons.
6) The “Na_sv” pseudopotential, which considers the 3s electron, the 2p electrons and the 2s electrons as valence electrons.

As can be seen from the trend in the pseudopotentials, the number of electrons treated in the all-electron charge density increases as more electron shells are treated as valence electrons. This has two important consequences: firstly, the charge density will be more complete and thus the energies will be more accurate and secondly, the calculation will be much more computationally demanding. As such, the pseudopotential should be carefully chosen depending on which of these characteristics is important.

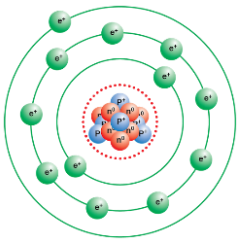

Figure F.1. Model of the Na atom, including the different electron shells.

To determine which pseudopotential is most suitable for your computation, refer to the recommendations by the Materials Project[75]:
http://docs.materialsproject.org/methodology/pseudopotentials/

To see which electrons are considered in which pseudopotential, refer to the VASP manual[53]:
https://cms.mpi.univie.ac.at/vasp/vasp/Pseudopotentials_PAW_potentials_supplied_with_VASP_package.html

➔ Born Effective Charges

The first method to quantify charge are the Born Effective Charges (BEC). The Born charges describe the phonon-electric field coupling[56]. The Born charge is defined as the change in polarizability of an atom as a result of an atomic displacement. The polarizability in turn is a measure of induced dipole moment per unit strength of applied electric field; it can be interpreted as a measure for the shift of the electron distribution around an atom (visualized in the figure). To be exact, the Born charge of atom k is defined as

$$Z^*_{k,\gamma\alpha} = V\frac{\delta P_\gamma}{\delta \tau_{k,\alpha}} = \frac{\delta F_{k,\alpha}}{\delta \xi_\gamma} = -\frac{\partial^2 E}{\partial \xi_\gamma \partial \tau_{k,\alpha}} \quad (33)$$

where $Z^*_{k,\gamma\alpha}$ is the Born Effective Charge, P_γ the polarizability, τ_α the displacement, $F_{k,\alpha}$ the force on the atom, E the energy and ξ_γ the electric field[58]. From this definition of the Born charge, it can easily be seen that the Born charge is dependent on both the local displacements of the atoms as well as the change in the electric field (or local electron density). Since these properties are directional, the Born charges can also differ per direction. This is most easily imagined by comparing the system to a macro-scale parallel plate capacitor: if you move the plates of the capacitors parallel to each other, there will be no resulting force on the plates (even though there is a displacement). However, if you move the plates towards each other, a force will arise as a result of the electric field that exists between the two plates. The resulting force is therefore dependent on both the electric field and the displacement. In practice, when using a Cartesian system, the Born effective charges are given in a 3 x 3 matrix.

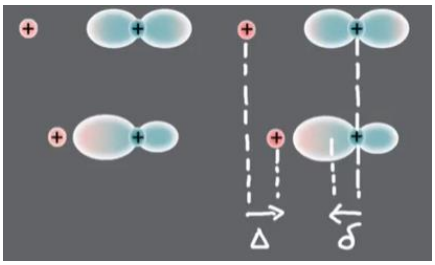

Figure F.2.. The shift in the electron distribution (δ) as a result of a displacement (Δ). Adapted from [57].

While the origin of Born Effective Charges is somewhat indirectly related to the quantification of charge on atoms, they are important quantities elucidating the physical understanding of bonding, as they describe the coupling between lattice displacements and the electric field. This is because the Born charges are only strongly affected by atom positions if the resulting electric field change is significant. For ionic bonds, where the atoms in questions have a more closed shell-like nature, the Born charge carried by an ion would be close to its nominal charge, as the electron shell is less affected by the displacement of ions[59]. On the other hand, if a covalent character is present, a significant amount of charge flows through the bond when ions are displaced and the resulting change in electric field is significant. The Born charge of an atom participating in a covalent bond is therefore usually significantly different from its nominal charge[59].

Computing the Born Effective Charge using VASP

The Born Effective Charges (BEC) can be determined fairly straightforward using VASP. To do so however, it is important to have a fully relaxed structure, which should therefore be the first step. Copy the CONTCAR from this relaxation to the POSCAR of a new (born charge calculation) folder. Subsequently, there are three important things to take into account for calculating the Born charges.

Firstly, it is necessary to set IBRION [f] to 8 and NSW = 0 in your INCAR file. This is required because to determine the Born charges, the second derivatives of the energy with respect to position are needed. To determine these second derivatives, a perturbation matrix needs to be applied to the ions, which is done for IBRION = 8. NSW = 0 is required because no ion displacement other than the perturbations is needed to calculate the Born charges. Secondly, it is important to ensure NPAR is not specified in the INCAR. Why this is exactly seems unclear (it likely has to do with the parallelization of the computation on different nodes), yet not doing so will result in the computation crashing and a fairly angry warning from the VASP output. With these settings, the only other step needed to calculate the Born charges is setting LEPSILON = .TRUE in the INCAR. This will make sure VASP writes the static dielectric matrix and Born Effective Charges to the OUTCAR file.

With these settings, the Born Effective Charges can be found near the end of the OUTCAR file, accessible by writing *grep Born OUTCAR*.

Note: the IBRION = 8 setting requires more computational power than for example IBRION = 2. Therefore, it can be useful to use settings that allow for easy convergence when calculating Born charges. It is recommended to set ISMEAR = 0 and SIGMA = 0.05 and can be useful to set LREAL = .FALSE. If these settings are used however, make sure that the original relaxation was also performed using these settings.

➔ Bader Charges

A different wat to get an estimate of the amount of charge on an atom (sometimes also referred to as the Net Atomic Charge, or NAC), it is possible to devise a method to split the charge density up in different sections and attribute the charge in a certain volume to the corresponding atom. However, where the charge density should be split is not an arbitrary choice. There are several different approaches to do so; there are different electrostatic potential fitting methods, several versions of a Density Derived Electrostatic and Chemical approach (the newest of which is known as DDEC6), and Bader's Quantum Chemical Topology (QCT)[60,61,62]. In the field of solid electrolytes the most commonly used of these methods is the Bader approach, where the integrated charge inside the calculated volume is known as Bader charge.

Bader charge uses what are called zero flux surfaces to divide the electron density into volumes, each belonging to a certain atom[62]. A zero-flux surface is a 2D surface where the gradient of the charge density perpendicular to the surface is zero. Typically, the charge density reaches a minimum between atoms and this is therefore a natural place to separate atoms from each other. The charge subsequently enclosed within the Bader volume is a good approximation for the total electronic charge belonging to the atom. Comparing the Bader charge to the nominal ionic charge also gives a reasonable indication of the nature of a bond between two atoms, yet because the entire charge density is included in the sum of the Bader volumes it is not as accurate an indicator as the Born charge. The Bader charge in turn

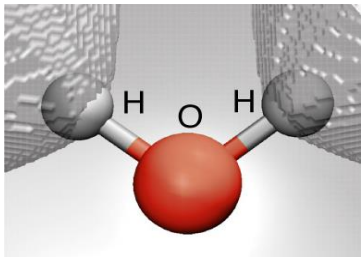

Figure F.3. The zero flux surfaces for an H_2O molecule, with which the shifted electron distribution as a result of the covalent bond can be observed. Adapted from [62].

[f] IBRION = 7 would also work, but IBRION = 8 is preferred since here only the symmetrically non-equivalent perturbations are taken into account.

is a more accurate descriptor of the charge belonging to an atom than the Born charge.

Computing the Bader charge using VASP

Contrary to the Born charges, calculating Bader charge using VASP is not straightforward and requires you to follow five steps, as well as Perl scripts written by the Henkelman group from the University of Texas.

The required Perl script is the chgsum.pl script, available from:
http://theory.cm.utexas.edu/vtsttools/scripts.html
The Bader code is available from:
http://theory.cm.utexas.edu/henkelman/code/bader/

Put the scripts in a folder in your home directory. To use the scripts, you must first activate them using chmod. Generally, the command: *"chmod -R 740 /heretypeyourpath*" will work. Once they've been activated, they will appear as green in the list.

To perform the Bader charge analysis using this code, there are two options:

1) Copy the scripts to the computation folder after the relaxation has been performed. This allows you to use the scripts, but only for this specific folder.
2) It is also possible to add the scripts directly to your path. This means that the scripts will be available from every directory you access. To do so, you must create or edit the .bash_profile file in your home directory (possible with "*nano .bash_profile"*). The commands in this .bash_profile file will be executed each time you log-in onto the system.

   In the .bash_profile file, add the line "*export PATH="/heretypeyourpath:$PATH",* where "heretypeyourpath" is the path to the directory containing the scripts.

With all scripts ready, it is possible to perform Bader charge analysis. This will require five steps[61].

Step 1:
To perform Bader analysis, as with calculating the Born Effective Charges, you will need to start from a properly relaxed structure. Copy the CONTCAR from your relaxation to the POSCAR of a new (Bader charge calculation) folder.

Step 2:
Set the following tags in your INCAR for the relaxation:
NSW = 0
LCHARG = .TRUE
LAECHG = .TRUE

The LCHARG tag will ensure that the charge density is written to the CHGCAR file, whereas the LAECHG tag will restructure the all-electron charge density. The all-electron charge density will be written to three separate files:

- AECCAR0; which contains the core electron density
- AECCAR1; which contains the proto-atomic valence density (essentially the overlapping atomic charge density)
- AECCAR2: which contains the self-consistent (SC) valence density

The separation of the all-electron charge density into different categories is essential for Bader charge analysis, since only the core charge and valence charge density are needed for calculating the zero flux surfaces.

With these settings and a proper KPOINTS distribution, it is possible to perform the relaxation and get the needed output files.

Note: it is important to use a fine fast Fourier transform grid when performing Bader charge analysis. This is generally set using the PREC = Accurate setting, which determines the NG(X,Y,Z)F settings. Without an accurate FFT grid, the total core charge will not be reproduced accurately!

Step 3:
After performing the relaxation, it is required to process the output further to get to the Bader charges. To get the correct electron charge density, we need to sum the core charge and the valence charge densities. Doing so manually would in principle be possible but is very tedious. Therefore, it is easiest to use the chgsum.pl scripts. By using the command "*chgsum.pl AECCAR0 AECCAR2",* the CHGCAR_sum file is created.

Step 4:
Next, it is possible to finally perform the Bader charge calculation itself. To calculate the Bader charges, make sure you have all the Bader script added to your path or in the folder and have all other required files (CHGCAR, CHGCAR_sum) available. To calculate the Bader charges, simply type the command "*bader CHGCAR -ref CHGCAR_sum"*.

With the bader script, three output files are created: ACF.dat, AVF.dat & BCF.dat

- ACF.dat contains the coordinates of the atom, the charge associated with the atom, the minimum distance to zero flux surface and atomic volume (should be compared to max cut-off radius for core radius)
- BCF.dat contains the coordinates of bader maxima
- AVF.dat contains the number of each volume

Step 5.
With the calculated charges of each atom, we are almost at the Bader charges of the atoms. One final correction is required to get to the Bader charges: the calculated charges need to be corrected for the nominal number of valence electrons. This can be found as the ZVAL value printed in the POTCAR file ("*grep ZVAL POTCAR")*. By doing "ZVAL – Bader population (printed in ACF.dat)", you get the Bader charge.

With these five steps, the Bader charge can be computed for all atoms in the system.

➔ Electron Localization Function

A less quantitative but more qualitative way of quantifying charge is the so-called Electron Localization Function (ELF). The ELF is a function of the electron localization in the system and is defined as:

$$n(\vec{r}) = \frac{1}{1+\chi(\vec{r})} \qquad 34\ )$$

where n(**r**) is the ELF and χ(r) is the ratio between the electron localization in the system and the electron localization in a uniform electron gas (fully delocalized)[63]. The ELF is therefore a number between 0 and 1 and expresses the probability of finding another Pauli exclusive electron (same spin) near a chosen reference electron. Since the ELF is a direct measure of the localization of electrons in the system, it is very useful for identifying shared-electron and unshared-electron interactions. The ELF is close to unity in regions which are occupied by paired electrons; these electrons have opposite spin and as such a third reference electron would be Pauli exclusive with one of the paired electrons.

In general, the rule of thumb applies that where the ELF is high (> 0.7), the electrons are characterized as localized, meaning they constitute core, bonding or paired electrons. On the other hand, when the ELF is between 0.7 and 0.2, the electron localization is similar to that of an electron-gas and is characteristic of metallic or ionic bonds. In the absence of electron density, the ELF becomes 0.[63]

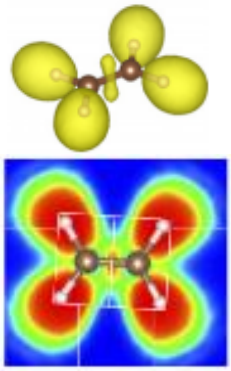

Figure F.461. The charge distribution and the ELF of an ethene (C_2H_4) molecule.

The relation to the Bader charge can easily be seen when one realises that the Bader charge is based on partition of the electron density based on the criterion $\nabla n(\vec{r}) = (0, 0, 0)$. The Bader charge and ELF can therefore function nicely as complementary methods, where the Bader charge quantifies the charge on an atom and the ELF provides an indication of the type of bonding interaction.

Computing the Electron Localization Function using VASP

Contrary to Born charge of Bader charge calculation, getting the ELF using VASP is extremely easy. The only thing to do to get the ELF from a VASP calculation, is by turning on the tag LEFL = .TRUE in the INCAR file. This will write the complete ELF to the ELFCAR file, which is all there is to it.

To open and investigate the ELF, it is useful to use a visualisation software such as VESTA. VESTA is capable of directly opening the ELFCAR file. Opening the ELFCAR file with VESTA will give you the structural model of your system. By going to 2D-visualization, it is possible to see and investigate the ELF. Choose a plane in which you want to evaluate the structure (based on the atomic locations) and you get all information you need!

Note: although not shown directly by VESTA, the scale of the ELF is simply 0 to 1.

➔ Appendix A. - Useful LINUX Commands

The following commands should be followed by a folder or file name. -r can generally be used to apply commands to folders.

cd - Enter a certain folder

cd .. - Leave a certain folder

cp - Copy a file to another file or folder

e.g. *cp CONTCAR POSCAR_new* copies the file CONTCAR to a new file POSCAR_new

cp -r - Copy a folder

~/ - Refer to a specific folder

mv - Re-name the file

rm - Remove a file

rm -r - Enter a folder and remove subfiles or folder (choose which)

rm -rf - Forcefully delete entire folder

mkdir - Makes a new folder

qsub - Submits a folder to a program (e.g. vasp8)

qdel [job] - Deletes a job

cat - Connects several files.

e.g. *cat POTCAR_Ti POTCAR_O > POTCAR* Makes a combined POTCAR of Ti & O

nano - Goes into the file (to edit or read)

nano +999 - Goes into the file at line 999

vi - Makes new file

ls - Shows contents of folder

qstat -u [ID] - Shows jobstatus

tail - Shows last 10 lines of file

grep [item] - Displays lines that contain [item] inside the file

pwd - Checks current directory

cd ~ - Go to home directory

➔ Appendix B. – Example INCAR file

Below an example of the input for the INCAR file for a simple geometry optimization can be found.

#INCAR

ENCUT = 520

IBRION = 3

ISIF = 3

ISPIN = 1

ISMEAR = -5

SIGMA = 0.002

ICHARG = 2

ISTART = 0

ISYM = 0

LREAL = Auto

NELMIN = 4

NPAR = 4

NSW = 500

PREC = Accurate

GGA = PS

EDIFF = 0.000001

EDIFFG = -0.005

Guideline NEB using VASP

T. J. Alders

➔ Introduction

This document describes how to perform the Nudged Elastic Band method using the Vienna Ab-initio Stimulation Package (VASP), using the projected augmented wave (PAW) approach. A basic understanding of Density Functional Theory (DFT) in VASP is assumed, i.e., the user should be able to perform a simple geometry optimization and have the skills to make POSCAR, INCAR, KPOINTS and POTCAR files.

The Nudged Elastic Band (NEB) method is a useful tool to investigate the energy landscape between two different states of a system. NEB can be applied to a variety of systems; from investigating the energy profile of a reaction from reagents to products, to ion migration through a crystal lattice. An example of what can be investigated using NEB is shown below[28]; an illustrative energy profile of Na-migration through a crystal lattice.

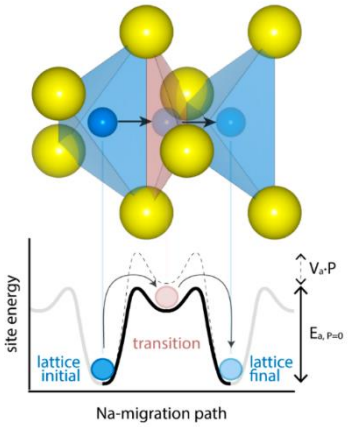

Figure G.1.. Illustration of the energy profile of ion-migration, which can be determined using NEB.

The first section describes the background and theory behind NEB. Subsequently, the implementation of NEB in VASP will be explained. Finally, an example of a complete NEB run including INCAR and results will be shown.[g]

[g] All information in this guideline, if not referenced specifically, comes from the online tutorials by Kunaseth[68] and Iannuzzi[69].

➔ What is the Nudged Elastic Band (NEB) method?

There are many situations where calculating the minimum energy path between two states is very interesting. This could for example be when investigating the reaction path from reagents to products, phase transitions or ion migration through a crystal lattice. To find the minimum energy path however can be tricky, especially when the potential energy landscape is unknown. So, what is needed is an easy method to find the minimum energy path between two known states, an initial and final state.

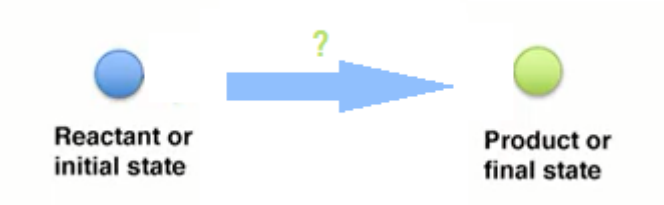

Figure G.2. The objective of NEB is to find the minimum energy path from an initial to a final state. [68]

A logical first step to find such a minimum energy path, is to simply "guess" the intermediate states that could exist. Especially when there is some understanding of what the reaction path might look like, it is fairly straightforward to construct several intermediate "guessed states". The easiest way to construct such states is through linear interpolation between the initial and final state. In most scenarios this will prove an apt approximation to continue on from, although one must ensure that the guessed states are physically possible. If for example ion migration through a lattice is studied, the linear interpolation is only a good method as long as the guessed states do not coincide with other particles in the system (or: moving through free space in the lattice).

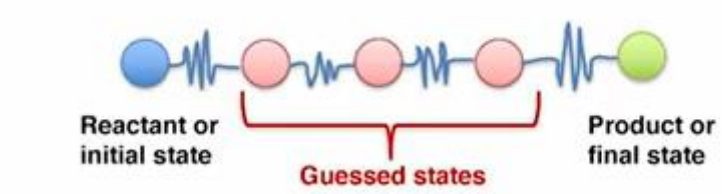

Figure G.3. By constructing guessed states and calculating the energy of these states, the minimum energy path can be modelled. [68]

While useful, the states guessed through linear interpolation are usually still fairly far away from the minimum energy path. Consider for example the potential energy map below: with such a landscape, the blue line would show the minimum energy path, whereas linear interpolation would provide us with the green line. We therefore need to still relax the guessed states, so that they fall in the minimum energy positions along the guessed path.

However, we cannot relax the states directly: since we know that the initial and final states are stable states, the guessed states will likely simply fall back to either the initial or final state. It is therefore important to include a measure to prevent the guessed states from falling back to the end states. For this, there is a simple solution: by connecting the states with springs that keep them at fixed distance from each other, we prevent them from falling back to the end states. This approach is known as the Elastic Band method, because the resulting string of states (also referred to as images) behaves similar to an elastic band.

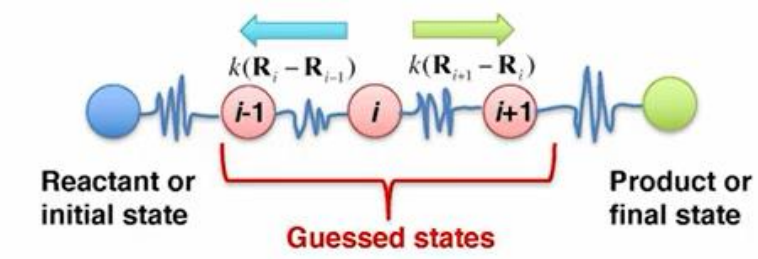

Figure G.4. Connecting the images with strings prevents them from falling back to the initial or final state. [68]

What essentially happens as a result of the added springs, is that we add a component to the effective force on the ion (i)[68]:

$$\vec{F}_i^{EB} = \vec{F}_i^{potential} + \vec{F}_i^{spring} \quad (35)$$

where

$$\vec{F}_j^{spring} = k\left(\vec{R}_{i+1} - \vec{R}_i\right) - k\left(\vec{R}_i - \vec{R}_{i-1}\right) \quad (36)$$

$$\vec{F}_i^{potential} = -\nabla V(\vec{R}_i) \quad (37)$$

By relaxing the images connected through the springs, they tend to relax to the minimum energy path. The Elastic Band method however comes with two potential pitfalls. Firstly, if the spring constant is set too rigid, the springs will pull on the images "too strongly", causing them to cut corners in the energy path (see figure below, left). Alternatively, if the spring constant is set too soft, the springs will not keep the images spaced equidistantly, leading to the images sliding back down towards the end states (see figure below, right).

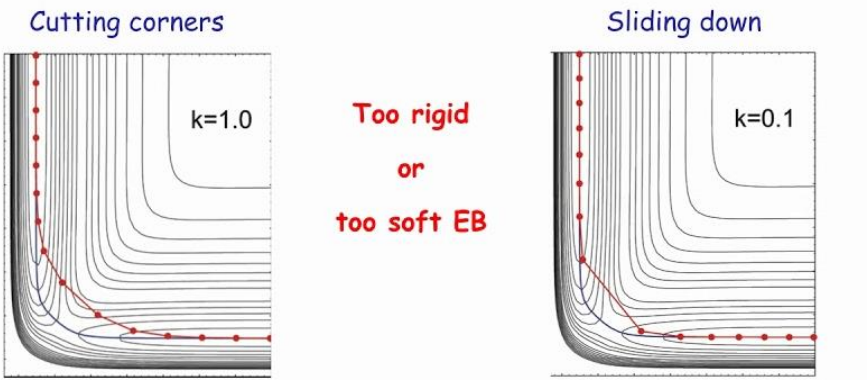

Figure G.5. The two shortcoming from the Elastic Band method are based on a too rigid spring constant (left) or too soft spring constant (right). [69]

This is cutting of corners and sliding down is the result of respectively a) the force of the spring perpendicular to the path being too high and b) the force of the potential along the spring being too strong. To solve this problem, the Nudged Elastic Band (NEB) method was developed. With the NEB method, we project out the perpendicular component of the spring force and the parallel component of the potential energy force. Through this we effectively decouple the energy minimisation (now dependent on the potential force) and the image distribution (now dependent on the spring force alone). The NEB force then becomes:

$$\vec{F}_i^{NEB} = -\nabla V(1 - (\vec{\tau}_i)\vec{\tau}_i) + \left(\vec{F}^{spring} \cdot \vec{\tau}_i\right)\vec{\tau}_i \quad (38)$$

where we define the tangent:

$$\vec{\tau}_i = \frac{\vec{r}_{i+1} - \vec{r}_{i-1}}{|\vec{r}_{i+1} - \vec{r}_{i-1}|} \quad (39)$$

The images will now relax to the point where the sum of these forces is zero (or drops below a given convergence criterion), giving an accurate estimate of the minimum energy path. The decoupling of the forces and subsequent NEB relaxation are visualised in the figure below.

With this method, the minimum energy path can be approximated nicely and the energy associated with the transition calculated. One challenge that might still occur however relates to the transition state or saddle point; because the distance between the images is fixed, it is not certain that an image will be located at the saddle point. The energy of the saddle point will therefore have to be estimated using a fit.

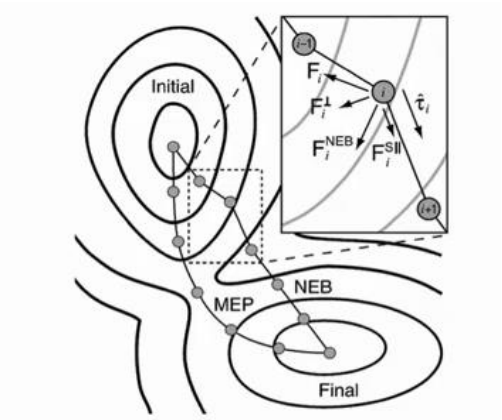

Figure G.6. Using the NEB method, the guessed states are relaxed to the minimum energy path, with which the transition state energy can be found.

To improve on this, the Henkelman group from the University of Texas developed an addition to the NEB method, the so-called Climbing Image NEB (CINEB). With the Climbing Image NEB method, the force formula is changed to allow the highest energy image to be pushed towards the saddle point. To do this, two changes are applied: 1) for the highest energy image, the spring forces are removed and 2) the inverted force parallel to the band is added.

$$\vec{F}_{i,max}^{NEB} = -\nabla V(\vec{R}_{i,max}) + 2\nabla V(\vec{R}_{i,max})\hat{\tau}_i \cdot \hat{\tau}_i \quad (40)$$

As a result, the image will move up the potential energy surface along the band and down in energy perpendicular to the band. Effectively, this meant that the image will be pushed towards the highest energy along the band, which will be located exactly at the saddle point / transition state (as shown in the figure below[62]).

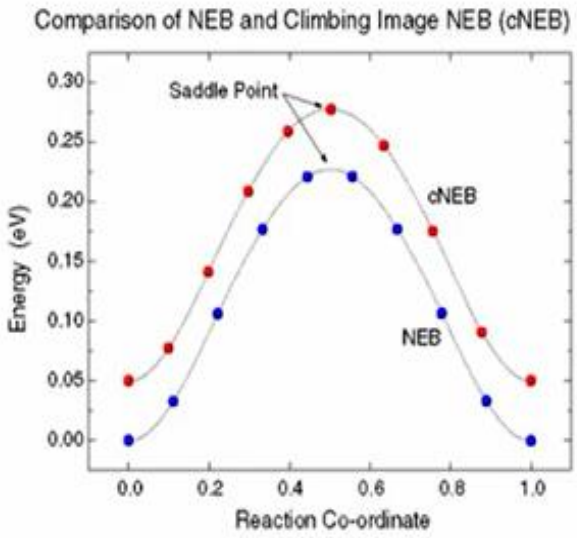

Figure G.7. Comparison between the energy paths found using the NEB and ciNEB methods. With the climbing image, the topmost image is pushed towards the saddle point.

In summary, the NEB method is a very suitable method for finding the minimum energy path between a known initial and final state. The resulting energies of the images along the path provide a valuable insight into the energy profile of the transition and by applying the Climbing Image NEB method, an accurate energy for the transition state / saddle point can be acquired.

➔ How to apply the NEB method in VASP?

The VASP package for Density Functional Theory is readily equipped with the means to perform NEB calculations. Doing so however, requires several steps and needs to be executed carefully. To perform CINEB calculations, an additional piece of code written by the Henkelman group needs to be installed and added to your VASP program. Furthermore, preparing the input files and analysing the output files of your NEB run can be a fair bit of work. To facilitate this, the Henkelman group also developed a VTST tools software package containing Perl / Python scripts which aid in preparing and analysing NEB runs.

This section will focus on how you can perform NEB runs in VASP. Firstly, the necessary steps to prepare your system for easy NEB calculations, such as installing the VTST tools, will be outlined. Then, the NEB procedure for VASP itself will be explained. Furthermore, some examples of how to gather NEB output will be presented, to illustrate what the NEB runs can provide you with. Finally, an example of an INCAR file and possible output will be presented.

➔ Preparing your system for NEB

For working with NEB, the VTST code and scripts developed by the Henkelman Group (University of Texas) are incredibly useful. It is therefore recommended to get both before starting with NEB calculations.

The VTST code which needs to be compiled in VASP, as well as the data processing scripts, can be found here:

https://theory.cm.utexas.edu/vtsttools/index.html

Note: It is very well possible that VASP is already compiled with the VTST code. To check this, simply perform a normal NEB run (you only need the VTST code for the CINEB method, as will be described later), and type "grep VTST OUTCAR" to see whether the VTST code is already installed.

To install the VTST code (only when necessary), download the code from the link above and follow the instructions provided on the webpage.

Besides the VTST code, the Henkelman group has created several scripts for preparing your files for a NEB run and processing the output data. This package of scripts can also be downloaded from the link above. Once downloaded, unpack the zipped file and put the folder containing the scripts in your home directory. To use the scripts, you must first activate them using the *chmod* command. To activate all files at once use the command "*chmod -R 740 /heretypeyourpath"*. Once activated, it is possible to use the scripts by copying them to the desired folder and using them (simply calling the name of the script should then work). However, since many of the scripts and functions require each other to work, this can be quite tedious. It is therefore recommended to add the folder with the scripts to your path, which will make them accessible from anywhere on the system.

To do so, you must create or edit the .bash_profile file in your home directory (possible with "*nano .bash_profile"*). The commands in this .bash_profile file will be executed each time you log-in onto the system. In the .bash_profile file, add the line "*export*

PATH=”/heretypeyourpath:$PATH”, where “heretypeyourpath” is the path to the directory containing the scripts. With this, you will be able to call the scripts from everywhere.
The overview on the webpage above provides information on all different scripts included in the VTST tools package. For NEB, the most interesting ones are listed below:

- *nebmake.pl [POSCAR_IS][POSCAR_FS][# images]*

  The nebmake.pl script assist with preparing the POSCARS needed for the NEB run. As input, supply the POSCARS of the initial and final structure and the # of images (N) desired. The output will consider of several folders **00 to N + 1**, containing the created POSCARS.

- *nebefs.pl*

  Nebefs.pl can be used to check the forces on the atoms and energies of the images during the NEB run. By typing “*nebefs.pl”* a table will be provided containing these metrics. Use nebefs.pl to monitor the progress of the NEB run whilst running.

- *nebconverge.pl*

  Nebconverge.pl serves a similar purpose as nebefs.pl, namely monitoring the progress of the NEB calculation during the run. Nebconverge.pl will output graphs for each image displaying the energy of the image as a function of computation step.

- *nebmovie.pl [0/1]*

  Nebmovie.pl is a very useful tool to visualize the NEB images. Nebmovie.pl will make a “movie” file which contains a concatenation of the POSCARS of the images. This file can then be viewed using different visualization softwares (e.g. JMOL or OVITO) to investigate how the structure changes during the NEB run. Using “*nebmovie.pl 0”* will make the script use the POSCARS in the folders, whereas “*nebmovie.pl 1”* will make the script use the CONTCARs (if available). This way, an easy comparison between the relaxed and unrelaxed NEB images can also be made.

- *nebresults.pl*

  Nebresult.pl is a script that runs many other analysis scripts, including nebefs.pl, nebconverge.pl and nebmovie.pl, but also several others. Nebresults.pl is the easiest method to gather the most important output of the NEB run in one go. An important addition to the previously mentioned functions is that nebresults.pl also runs the nebspline.pl script. This script creates a plot and spline of the minimum energy path (saved to mep.eps), which very clearly show the energy profile of the MEP. A simple was to open this file (for inexperienced users) is to use the Linux command “*epstopdf mep.eps”,* which will convert the .eps file to an easily openable .pdf file.

➔ Performing the NEB analysis

With or without the VTST tools available, performing the NEB relaxation requires only three steps: 1) relaxing the initial and final structure, 2) creating the images and 3) setting the NEB parameters. Each of these steps will be explained in more detail below. For these steps, access to the VTST tools will be assumed; the general procedure however still applies without these scripts.

➔ *Step 1: creating the initial and final structure*

To perform a NEB calculation, it is essential to have the more accurate initial and final states as possible. The first step of doing a NEB is therefore creating your initial and final states. How to do this depends slightly on what kind of transition you are investigating but is generally the same for most calculations.

The first thing to do is to properly relax the structure you want to use. This can simply be the unit cell of a crystal but also a system under applied pressure (using for example the tag PSTRESS) or an organic structure. At this point, you don't need to create your initial and final states yet; simply relax the structure on which you want to base the initial and final structures. When relaxing your structure, there are a few things to consider:

1) For NEB, it is important to have a sufficiently large cell. When you are performing a NEB, the initial and final states usually differ from each other by some defect or vacancy. Imagine for example that you are investigating the energy of hopping through a crystal lattice. In this case, your initial and final states will likely consist of two crystal structures with neighbouring vacancies, so that the images follow the path from one vacancy to the other. However, because of the periodic boundary conditions in DFT, the vacancies will also be present in the unit cells beyond the boundary. As a result, it is likely that the vacancy will interact with the other vacancies, which will cause the initial and final states to relax to the incorrect states.

   Therefore, it is important to use a large enough cell or supercell. The rule of thumb applies that the distance between two defects should be approximately 10 angstroms; for most structures this means a supercell is required (e.g., 2 x 2 x 2).

   Note: when using a large cell or supercell, it is recommended to use the Gamma package for the KPOINTS distribution with 1 x 1 x 1, to ensure convergence. If the structure does not converge in the initial relaxation, it will certainly not converge in the NEB run. It is also strongly recommended to set LWAVE = .FALSE and LCHARG = .FALSE, since the respective output files WAVECAR and CHG / CHGCAR would take up a significant amount of storage space.

2) Make sure you relax your structure with the same parameters you will use for the relaxation of the initial and final states, as well as the NEB calculation. By changing the relaxations parameters throughout the complete NEB procedure, the calculated energies of the relaxed structures and their convergence criteria can deviate. By for example switching from using PREC = Normal for the initial and final states and PREC = Accurate for the NEB, you will end up with incorrect and inaccurate energies and likely a strange minimum energy path.

It is recommended to relax your desired structure with IBRION = 1 (POTIM = 0.05) or IBRION = 3 (POTIM = 0, TIMESTEP = 0.2, MAXMOVE = 0.1) (because the NEB run is based on force optimization), PREC = Accurate, ISIF = 3 and EDIFFG < -0.01[h]. For easier convergence, it is recommended to set ISMEAR = 0 (Gaussian smearing) and SIGMA = 0.05. Optionally LREAL can be set to .FALSE.

Note: an example of an INCAR for the relaxation of the structure / initial and final structures can be found in one of the next sections.

Once you have your general structure relaxed, it is time to create the structures for the initial and final states. To determine what the initial and final states will look like is mainly a question of understanding the underlying process. To investigate ion conduction through a solid electrolyte, creating the initial and final states would require the removal of one atom in two different locations. For the conduction of an ion in a host framework, it can be desirable to remove all "hosted" ions and insert one ion back into the framework, at two different locations. **In general, use your brain when creating to initial and final structures.**

When making the initial and final structures, keep in mind that the POSCARS of the initial and final structure will be related to each other through the order of the atoms in the POSCAR. That means that when creating the image, a linear interpolation will be performed between the coordinates of atom 1 in the POSCAR of the initial structure and atom 1 in the POSCAR of the final structure. Therefore, when you want to model the hopping of an atom from one vacancy to another, make sure that this atom in the initial structure is interpolated to correct equivalent atom in the final structure!

With your initial and final states created, one important step remains: relaxing the initial and final structures. As a result of the created defect / change, the relaxed structure will no longer be in the optimal configuration. Since well relaxed states are essential for your NEB run, we need to re-relax the structures. *There are two important things to note when re-relaxing the structures. Firstly, it is important to use the same parameters (e.g., IBRION, ISMEAR, POTIM) as for the original relaxation. Secondly, it is important to set ISIF = 2. After all, you don't want to change the shape and size of your unit cell anymore, since that might result in the unit cells of the initial and final structures mismatching.*

Now that you've relaxed your initial and final states, you are ready to continue on with the NEB process! Save the CONTCARs of your initial and final states relaxations as POSCAR_IS and POSCAR_FS (or similar names), and copy them to a new folder, which will be used for the NEB run. Also copy the OUTCARs of the relaxations of the initial and final states to this same folder, for example under the names OUTCAR_IS and OUTCAR_FS. These will also be needed for the NEB run. With the initial and final structures complete, we can construct the images needed for the NEB run.

➔ ***Step 2: creating the images***

The next step in the NEB run is fairly straightforward: key for the NEB run is the creation of the guessed states / images. In most cases, a linear interpolation between the initial and final states will suffice. Do keep in mind that this should be possible with the system that is being

[h] It can be useful to run the relaxation with less strict criteria in first relaxations, to find settings that provide convergence. For accurate results in the NEB however, a well relaxed structure is essential, thus requiring stricter criteria.

used: if for example a linear interpolation leads to a path that goes through an existing atom, the path must be chosen differently (e.g., by splitting the path in two sections and performing a linear interpolation twice). Making the images can be done manually (updating the POSCAR with linear steps) but is much easier using the VTST tools. With the nebmake.pl script, all that is needed is an initial and final POSCAR file. Luckily, that is exactly what we created during the previous step!

By typing "*nebmake.pl POSCAR_IS POSCAR_FS #",* the script will make POSCARs of the images automatically. Here, POSCAR_IS is the initial structure we created earlier, and POSCAR_FS the final structure. # Is the number of images N you want to create. When this script is used, the output will be a series of folders, **00 to N + 1**, (for 4 images: 00 to 05), where each folder contains the POSCAR of one image. **00** contains the POSCAR_IS, and the **N + 1** folder contains the POSCAR_FS. To finish preparing the folder for the NEB run, all that is left to do is copying the OUTCARs of the initial and final structure to the respective folders; copy OUTCAR_IS to **00/OUTCAR** and OUTCAR_FS to **N+1/OUTCAR.**

Congratulations, you created your initial guesses for the NEB run!

Although creating the images is not the most difficult step, two important remarks must be made:

1) At this point, it is worth it to verify whether creating the images worked properly. To do so, you can use the *nebmovie.pl* script from the VTST tools[i]. By typing "*nebmovie.pl 0"* in the main NEB folder, a "movie" file will be created containing a concatenation of the POSCARS of the images. This movie file can be opened with various visualization softwares, such as JMOL or OVITO. Open the file and see whether the guessed pathway makes sense and if not, review what might have gone wrong.
2) In principle, any number of images can be used for an NEB run. Generally, start with a lower number of images and use more images once the computation seems to be running properly. **However,** depending on the submitting script used for VASP, the NEB run can crash when using a certain number of images. The number of images N **must be** a multiple of the # of ppn you use for the calculation. This is the number set in the VASP executable: e.g., vasp8 → ppn = 8, or vasp32 → ppn = 32. So vasp8 would be able to run with 4 images, but **not with 5 images.** Therefore, if an odd number of images is desired, you must update the submitting script.

   To do so, open the vasp8 executable in a text editor (or using "nano") and change the ppn = 8 to ppn = x (x being the desired value). Save this as vaspx and submit to this new executable.

[i] It is recommended to make one small change to the nebmovie.pl script before using it: open the file using "*nano nebmovie.pl"* and locate the ".xyz" option. Turn this on (0 to 1). Doing so will make the script generate both a "movie" file and a "movie.xyz" file, the latter of which can be used by more different softwares.

➔ ***Step 3: setting the NEB parameters***

After creating the images and preparing the folders, we are almost ready to run our NEB calculation. As with a normal VASP calculation, we require a KPOINTS file, a POTCAR file and an INCAR file. For the KPOINTS file it is necessary to use the same KPOINT distribution as was used for the relaxations of the initial and final structure; otherwise, the relaxations of the images will not be comparable to those of the initial and final states. It is recommended, since we are using a supercell for NEB calculations, to use a KPOINT distribution of 1 x 1 x 1, using the Gamma package. For the POTCAR file, it is also important to simply use the same POTCAR as was used for the initial and final structure relaxations.

When it comes to the INCAR file, for the most part the same INCAR as for the initial and final structures can (and should!) be used. Especially tags which influence the relaxation steps, such as IBRION, ISMEAR / SIGMA, PREC and POTIM, should be kept the same. It is recommended to use a fairly small EDIFFG for the first relaxations, to check whether the calculation converges at all (an initial EDIFFG of -0.1 or -0.05 should suffice). So, the recommended settings for the usual tags during the NEB run are:

- IBRION = 3
- POTIM = 0
- MAXMOVE = 0.2
- TIMESTEP = 0.1
- ISIF = 2
- ISMEAR = 0 / SIGMA = 0.05
- EDIFFG = -0.05
- LWAVE = .FALSE
- LCHARG = .FALSE

Furthermore, to run a NEB calculation, it is important to specify a few special tags in your INCAR file:

- ICHAIN = 0. This tag must be set to enable the NEB calculation.
- IMAGES = integer. This tag specifies how many images are between the initial and final states. Make sure this number matches with the number of images you created.
- SPRING = -5.0. This tag specifies the spring constant between the images (eV / A^2). A positive value selects the Elastic Band method, a negative value the Nudged Elastic Band method. For most calculations, a spring constant of -5.0 should be fine.
- LCLIMB = .TRUE / .FALSE. This tag determines whether or not the Climbing Image method is selected. This requires the VTST code to be installed. It is recommended to always start with a regular NEB calculation, before attempting a CINEB calculation, for arguments of convergence. If you want to check whether the VTST code is enabled, run a normal NEB calculations and type "*grep VTST OUTCAR"*. If the VTST code is already installed, this will provide you with the version number of the VTST software.

With these tags set, you are good to go! Submit your main NEB folder to VASP (using the qsub command) and sit back while the computer does the work for you.

Well done!

➔ Processing NEB Output

It can be very important and interesting to monitor the output of a NEB run, both during the calculation and afterwards. There are several output variables which are worth monitoring during the run and there is a lot of data available for analysis at the end of the run. It is therefore good to know how the output of a NEB run can be monitored / gathered easily.

➔ *Monitoring the NEB run*

Besides the regular ways to monitor a VASP run (e.g., grabbing the E0 or RMS from respectively the OSZICAR or OUTCAR), there are two scripts written by the Henkelman group which provide alternative means to monitor the progress of the run.

Firstly, the nebefs.pl function is a very useful way to monitor the forces on all atoms during the run. By using the nebefs.pl scripts (if you have it added to your PATH, simply type "*nebefs.pl*") you are provided with a list of images, with for each image the maximum force as well as the relative energy of the image compared to the previous image. This way, you can both monitor how far the run is from converging (since we specified EDIFFG with a minus sign, indicating a force convergence criterium) as well as get a previous of what the energy profile of the MEP will look like.

Secondly, using the script nebconvergence.pl, you can see for each image how the energy of the image has changed each cycle. The nebconvergence.pl script can also simply be used by (if added to the PATH) typing "*nebconvergence.pl"*, which will create a folder called vaspgr. Vaspgr contains graphs for each of the images, showcasing how the energy and max force change with each ionic step. By investigating these graphs, you can easily see whether it is likely that your NEB run will reach convergence or not, as well as how soon.

➔ *Evaluating the NEB results*

For evaluating the outcome of the entire NEB run, the easiest way is again to use the scripts available in the VTST tools package. The most interesting of these scripts is the nebresults.pl script, which runs a set of other analysis scripts all at once, including nebmovie.pl, nebspline.pl and nebbarrier.pl. Simply run nebresults.pl (if added to the PATH) by typing "*nebresults.pl*".[j] A more detailed description of what these scripts do can be found in the previous section.

The output of nebresults.pl contains a lot of information, but there are three things we are usually mainly interested in. Firstly, it can be very insightful to investigate the movie created by nebmovie.pl. This can be done by opening the movie (or movie.xyz) file using a visualisation software such as JMOL or OVITO and play the file.

Secondly, the mep.eps file contains a plot of the energy profile of the images, including a spline fit. This mep.eps file is easily converted to a more accessible format using the epstopdf function built into Linux. Simply type "*epstopdf mep.eps"* to end up with a mep.pdf file of the energy profile.

[j] While for most uses of the VTST scripts it is also possible to copy them to the relevant folder and use them there, for this script it is strongly recommended to have the scripts added to your PATH. The reason for this is that many of the scripts require other functions and scripts in the package to run, meaning that you'd have to copy a lot of separate files to your directory of choice each time you want to use nebresults.pl.

Third and finally, the nebresults.pl provides you with the data of the energy barrier in the neb.dat file. This file contains the energy values of each image and can be used to compare different transition or for further analysis.

Besides these results, there is a lot of valuable information stored within the output of the NEB run. Think for example of structural information of the system during the transition, changes in local charge density or indications of intermediate stable states. While these results are equally interesting, how to analyse them is beyond the scope of this guideline.

So, there you go; hopefully this guideline has provided you with some valuable information on the background of NEB and with all necessary tools to perform your own NEB analysis. As a final addition, the last section contains an example of an INCAR for an NEB run and some of output from a fairly straightforward NEB calculation. For further questions, please refer to ResearchGate or the VTST forum by the Henkelman group.

Good luck!

➔ Example NEB run

This section contains examples of the input and output of a NEB run. The NEB run below was performed on a structure of Na_3PS_4, space group I-43m. For the calculation a supercell was used of 2 x 2 x 2. A vacancy was created for Na-atom 10 in the initial structure and Na-atom 28 in the final structure. A Gamma-centred KPOINTS grid of 1 x 1 x 1 was used. The POTCAR used contained the pseudopotentials Na_pv and the standard forms of the P and S pseudopotentials.

➔ Example INCAR

```
# Basic settings & initialization
ENCUT = 520
ICHARG = 2
ISIF = 2
ISYM = 0
ISPIN = 1
ISTART = 0

# Relaxations parameters
ISMEAR = 0
SIGMA = 0.05
LREAL = Auto
NELMIN = 4
NPAR = 4
NSW = 100
PREC = Accurate
GGA = PS
EDIFF = 0.000001
EDIFFG = -0.05

# NEB specific settings
ICHAIN = 0
IMAGES = 9
SPRING = -5.0
LCLIMB = .FALSE
IBRION = 3
POTIM = 0
IOPT = 3
MAXMOVE = 0.2
TIMESTEP = 0.1
LWAVE = .FALSE
LCHARG = .FALSE
```

➔ **Example Output**

NEBefs: The energy output of a completed NEB run.

Image	Force	Stress	Volume	Magnet	Rel Energy
0	0.00494500	1.25650700	2659.89	0.00000000	0.00000000
1	0.02484700	1.30614900	2659.89	0.00000000	0.00790000
2	0.04090400	1.30316200	2659.89	0.00000000	0.02590000
3	0.04939500	1.25483500	2659.89	0.00000000	0.04730000
4	0.04915000	1.22197700	2659.89	0.00000000	0.06320000
5	0.04617400	1.19852000	2659.89	0.00000000	0.06910000
6	0.04910500	1.22412400	2659.89	0.00000000	0.06320000
7	0.04939000	1.25598700	2659.89	0.00000000	0.04730000
8	0.04089600	1.30343300	2659.89	0.00000000	0.02590000
9	0.02492700	1.30619200	2659.89	0.00000000	0.00790000
10	0.00498600	1.26039200	2659.89	0.00000000	0.00000000

NEB movie - POSCAR: The green atom is the moving Na atom. As can be seen, the other atoms move slightly as a result of the energy-minimisation following the vacancy creation.

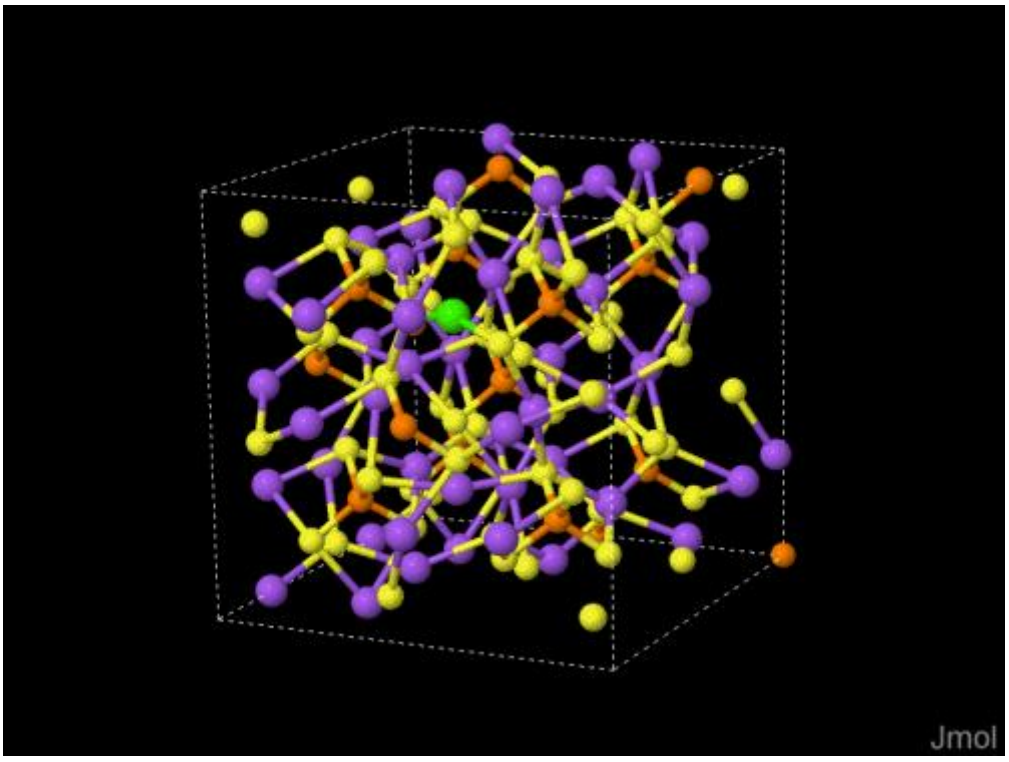

NEBconvergence: The graph of the convergence of the middle image of the run.

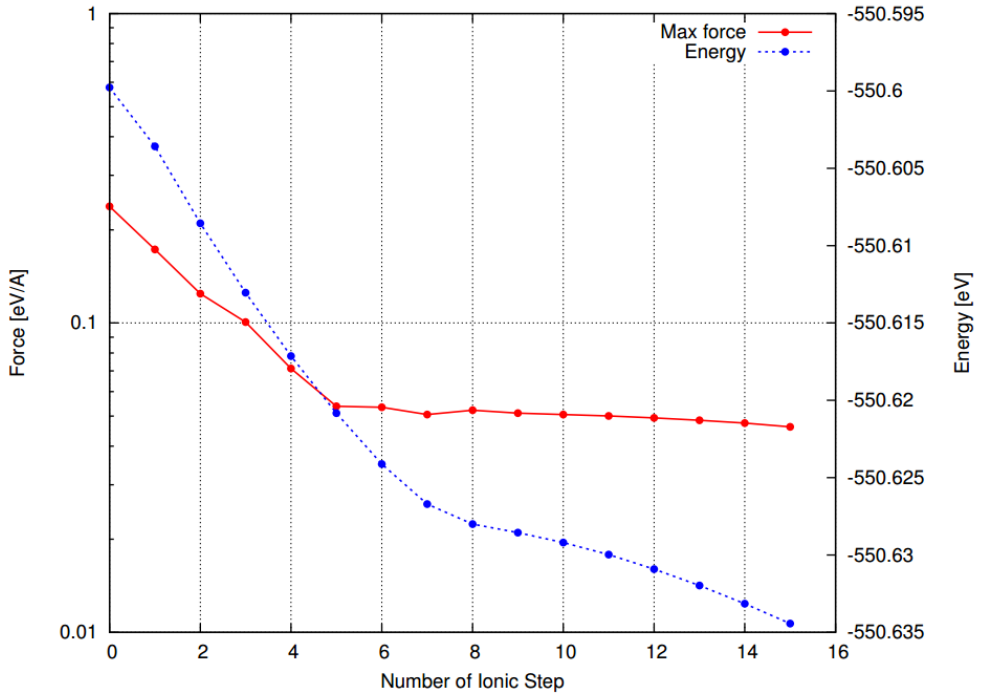

NEB spline: The energy profile along the conduction pathway.